

Low Dimensional Supersymmetric Field Theories on the Lattice

Dissertation

zur Erlangung des akademischen Grades
doctor rerum naturalium (Dr. rer. nat.)

vorgelegt dem Rat der Physikalisch-Astronomischen Fakultät
der Friedrich-Schiller-Universität Jena

von Dipl.-Phys. Christian Wozar
geboren am 13. September 1981 in Lauterbach (Hessen)

Gutachter:

1. Prof. Dr. Andreas Wipf, Jena
2. Dr. habil. Karl Jansen, Zeuthen
3. Prof. Dr. Simon Catterall, Syracuse, NY, USA

Tag der Disputation: 26. Oktober 2010

1	Introduction	3
2	Broken supersymmetric quantum mechanics	7
2.1	Operator formalism	7
2.1.1	Supersymmetry breaking and the Witten index	8
2.1.2	Specifying the model	9
2.2	Lattice regularised path integral	11
2.2.1	Sign of the fermion determinant	13
2.2.2	Ground state structure	14
2.2.3	Thermal field distribution	15
2.2.4	Effective potential	15
2.2.5	Two-point functions and spectrum	16
2.2.6	Ward identity	17
2.3	Conclusions	18
3	$\mathcal{N} = 2$ Wess-Zumino model	19
3.1	Lattice models	19
3.1.1	Supersymmetrically improved lattice actions	19
3.1.2	Lattice fermions	20
3.1.3	Discrete symmetries	21
3.2	Numerical results	23
3.2.1	Dynamical properties of improved lattice actions	23
3.2.2	Setting the stage	26
3.2.3	Determination of masses from correlators	28
3.2.4	Continuum extrapolation	30
3.2.5	Weak coupling	31
3.2.6	Intermediate coupling results	34
3.2.7	Measurement induced supersymmetry breaking	36
3.3	Conclusions	39
4	Algorithmic aspects	41
4.1	Recapitulating the hybrid Monte-Carlo algorithm	41
4.2	Fourier acceleration	42
4.3	Γ distributed integration lengths	44
4.4	Deflated rational hybrid Monte-Carlo	45
4.4.1	Eigenvalue deflation	47
4.4.2	Effects on the Markov chain	48
5	$\mathcal{N} = 1$ Wess-Zumino model	49
5.1	Quenched model	51
5.1.1	The \mathbb{Z}_2 phase transition on the lattice	52
5.1.2	Regulator independence of the renormalised critical coupling	53

5.2	Full dynamical model	54
5.2.1	Renormalised lattice parameters	54
5.2.2	The Pfaffian	55
5.2.3	Symmetries, boundary conditions, and ground states	57
5.2.4	\mathbb{Z}_2 breaking	58
5.2.5	Supersymmetry breaking	58
5.2.6	Masses	61
5.3	Conclusions	64
6	Nonlinear sigma models	65
6.1	Instantons and fermionic zero modes in twisted $\mathbb{C}P^N$ models	65
6.1.1	The $\mathbb{C}P^N$ model in the continuum and on the lattice	66
6.1.2	Instantons at finite temperature	68
6.1.3	Zero modes of the Dirac operator	74
6.1.4	Conclusions	80
6.2	Supersymmetric $O(3)$ sigma model on the lattice	81
6.2.1	Quenched model	82
6.2.2	Supersymmetric model	87
6.2.3	Conclusions	98
7	Summary and outlook	99

Symmetries are one of the guiding principles in contemporary theoretical physics. Already the formulation of quantum mechanics is invariant under a local electromagnetic gauge transformation [1] and its unification with special relativity, quantum electrodynamics [2], still incorporates this symmetry. The extension of this abelian gauge symmetry to non-abelian gauge groups has led to a description of isospin [3] and built the theoretical framework for modern particle physics. By a unification of electroweak interaction [4–6] with strong interaction [7] the standard model of particle physics is constructed. Based on the underlying symmetries bottom and top quark as well as the τ neutrino have been predicted and the experimental discoveries, the last one more than two decades after the prediction [8], substantiated the success of the standard model to describe the physics on energy scales below 1 TeV.

Thereafter it has been aimed at constructing more general theories to gain a unified description of nature. These attempts were based on extending the standard model's symmetries by further ones. However, additional symmetries put further constraints on the scattering matrix. Which symmetries still allow for experimentally reasonable scattering amplitudes has been analysed in the Coleman-Mandula theorem [9] and an extension of the spacetime symmetries is only possible with *internal* symmetries that do not change the spin or the mass of particles. The only way to circumvent this restriction is given by extending the Poincaré algebra with anti-commuting *supersymmetry* generators [10] that relate particles with integer spin to ones with half-integer spin.

The first field theoretical realisation of a renormalisable model with supersymmetry algebra is the Wess-Zumino model [11] in four spacetime dimensions with a field content of two (real) scalars and a Majorana fermion. Since then a variety of supersymmetric models have been constructed, e.g. supersymmetric gauge theories, supersymmetric sigma models, and models with extended supersymmetries. By using supersymmetric extensions of the well established standard model conceptual shortcomings that cannot be explained within the setting of the standard model, such as the hierarchy problem, the occurrence of dark matter, and the strong CP problem, can be solved or weakened [12–14]. Within the minimal supersymmetric standard model even the gauge couplings will be unified at high energy scales.

Supersymmetric models have further the advantage that divergences in the perturbation series are in most cases less severe than in models without supersymmetry and that the supersymmetry algebra induces a vanishing ground state energy, as long as supersymmetry is unbroken. If the ground state is invariant under the supersymmetry mass degenerate multiplets of bosonic and fermionic particles are predicted, and it has been analysed that in certain classes of supersymmetric theories a spontaneous breaking of supersymmetry is not possible [15]. But in the experimental findings so far no such degeneracy has emerged, and the masses of bosonic and fermionic particles appear unrelated. At first sight these results hinder supersymmetry from describing the particle spectrum. However, as was analysed by O'Raiheartaigh [16] this non-degeneracy of masses is naturally expected if supersymmetry is dynamically broken.

In a theory with dynamical supersymmetry breaking the ground state is not invariant under the supersymmetry, and the ground state energy is lifted above zero [17]. But the supersymmetry algebra is still present, which has implications on the physics in the dynamically broken sector. To date the Large Hadron Collider has just started operating and it is expected to measure, apart from many

other interesting predictions (e.g. the Higgs boson), remnants of supersymmetry in the collision events within a few years. If the description of nature includes supersymmetry, what large parts of the physics community expect, it is necessary to have not only a perturbative description of supersymmetric theories at hand but to explore them by using non-perturbative methods that go beyond the perturbatively accessible regime.

Among those methods the lattice regularisation in combination with importance sampling based statistical ‘Monte-Carlo’ methods has become successful over the last decades. Lattice methods often provide the only viable way to gain information about the non-perturbative sector of quantum field theories. E.g. early simulations that aimed at an understanding of the pure $SU(2)$ Yang-Mills theory [18] built the basis for recent computations from first principles of the Hadron spectrum in full quantum chromodynamics [19], which is only possible due to increasing computing power and algorithmic improvements. As non-perturbative effects are automatically taken into account, it is desirable to apply the lattice approach also to supersymmetric theories. This has been the subject of a number of publications, see, e.g., [20–24] and for recent progress in supersymmetric Yang-Mills theories [25–28] and references therein.

In all the lattice regularised versions of field theories symmetries are again of particular interest. If a symmetry of the continuum theory is not implemented in the lattice version it is possible that the symmetry is not restored in the continuum limit. E.g. for simulations of gauge theories it is important to implement the lattice version of the continuum gauge symmetry [29]. But not every symmetry can be directly implemented in the lattice regularised theory. The Nielsen-Ninomiya theorem [30–32] forbids the exact implementation of chirally symmetric fermions with a local fermion interaction and without introducing additional fermion flavours on the lattice. Nevertheless, it is possible to construct a (deformed) lattice version of the chiral symmetry, which is given by the Ginsparg-Wilson relation [33], so that a restoration of the continuum chiral symmetry is ensured in the continuum limit of the lattice action.

For supersymmetry as extension of the Poincaré algebra a fully realised supersymmetry algebra on the lattice must inevitably contain the generators of translations which would imply arbitrary translations to be part of the symmetry group of the lattice theory. By contrast, lattice regularised theories are only symmetric under translations by the lattice spacing. Therefore a complete realisation of the continuum supersymmetry algebra on the lattice is impossible and the full supersymmetry can only be realised as an accidental symmetry in the continuum limit of the lattice regularised theory. Technically, the reason for this can be traced back to the failure of the Leibniz rule on the lattice [34].

It has been shown that even in supersymmetric quantum mechanics the naive discretisation does not lead to a supersymmetric continuum limit [35]; generically, such a limit can at best be achieved by fine-tuning the bare coefficients of all supersymmetry-breaking counterterms [36]. This, however, requires much knowledge of the theory in advance. In some cases the relevant operators can be determined perturbatively, cf. [37]. To circumvent the fine-tuning process several attempts are possible. Firstly a partial realisation of supersymmetry on the lattice is possible for theories with extended supersymmetry (for a recent review see [38]). Secondly recent developments aim at the construction of a Ginsparg-Wilson inspired relation for supersymmetric theories to obtain a lattice version of supersymmetry such that the continuum supersymmetry is broken in a controlled way [39]. Alternatively for scalar theories a deformed supersymmetry algebra on the lattice can be constructed by using a non-local product

operator such that the theory is invariant under the full (deformed) lattice supersymmetry [40].

Apart from an explicit supersymmetry breaking by the finite lattice spacing there exist further supersymmetry breaking effects that must be controlled in the analysis of supersymmetric theories. Firstly a finite temperature breaks the Lorentz invariance and therefore supersymmetry as extension of the Poincaré algebra must be broken, too. Secondly a finite spatial volume may allow for tunnelling processes between two formerly separate ground states such that the finite volume ground state energy is raised above zero. As it is inevitably to use finite lattices for numerical simulations these explicit supersymmetry breaking effects must also be accounted for seriously.

It is the purpose of this work to analyse different models in one and two spacetime dimensions each of which covering main ingredients of more realistic theories like the minimal supersymmetric standard model. By considering the specific aspects separately it is possible to scrutinise the drawbacks and opportunities provided by the given lattice methods. In addition the low dimensionality of these models allows for precise numerical results which can uncover conceptual and technical problems that arise in the lattice treatment of supersymmetric theories.

The analysis of supersymmetric theories on the lattice starts with the more pedagogic example of a supersymmetric quantum mechanics with dynamically broken supersymmetry in Chapter 2. In this setting the basic concepts of supersymmetric theories are explained and reference results for certain observables are computed via the operator formalism, thus allowing to understand the physics behind supersymmetry breaking on solid grounds. The corresponding lattice regularisation is based on a formulation that has been used in the unbroken supersymmetric quantum mechanics with great success [41]. The applicability of a lattice regularisation for theories with broken supersymmetry is verified and it is described how signatures of the low lying energy spectrum are visible in observables that are accessible in the lattice theory.

In Chapter 3 the $\mathcal{N} = 2$ Wess-Zumino model in $1 + 1$ dimensions, which is a dimensionally reduced version of the four dimensional $\mathcal{N} = 1$ Wess-Zumino model, is discussed. This model is build upon a holomorphic superpotential which forbids a supersymmetry breaking in the continuum. Here, different lattice formulations are compared, some of which allowing for a part of the supersymmetry to be realised on the lattice. It will turn out that these ‘Nicolai improved’ formulations have inherent stability problems that hinder the simulations from probing the strong coupling regime. For weak couplings continuum extrapolated lattice results are compared to perturbative one-loop calculations. For intermediate couplings the finite volume induced apparent supersymmetry breaking, measurable in certain observables, is analysed with the help of Ward identities.

Performing high-precision measurements poses a numerical challenge already in two dimensional theories. For that reason the algorithmic improvements that have been gained throughout the simulations are exemplified on the $\mathcal{N} = 2$ Wess-Zumino model in Chapter 4. However, most of the technical advances are not only limited to this specific model but can directly be applied to every other model in this work.

The minimal setting for a field theory with supersymmetry breaking phase transition is given by the $\mathcal{N} = 1$ Wess-Zumino model in $1 + 1$ dimensions, which is analysed in Chapter 5. In the context of the quenched model a particular renormalised critical coupling for the \mathbb{Z}_2 symmetry breaking is shown to be independent of the chosen lattice regulator. The corresponding critical coupling in the full theory is determined and the relation between \mathbb{Z}_2 and supersymmetry breaking is worked out.

Eventually (supersymmetric) nonlinear sigma models are considered in Chapter 6. They share important features with non-abelian gauge theories, such as asymptotic freedom, dynamical mass generation, and the presence of topological objects [42]. In that context the instanton structure of the bosonic $\mathbb{C}P^N$ nonlinear sigma models with twisted boundary conditions is determined, zero modes of the Dirac operator for minimally and supersymmetrically coupled fermions are constructed, and a corresponding index theorem is given. The work concludes with an analysis of the supersymmetric $O(3)$ nonlinear sigma model on the lattice. Proposed supersymmetric lattice models [43, 44] break the target space symmetry on the lattice as well as in the continuum limit. Therefore an explicitly $O(3)$ invariant lattice model is constructed, the analytically determined ground state structure is verified, and a restoration of supersymmetry in the continuum limit is analysed with the non-local SLAC derivative.

The compilation of this work is solely due to the author. However, parts of this work have been done in collaboration with colleagues from the research groups on quantum field theory in Jena and Regensburg. The numerical programming that led to Sec. 3.2.1 – 3.2.5 was done together with Tobias Kästner while the analytical results of Sec. 3.2.5 have been developed in collaboration with Georg Bergner. The corresponding results have already been reported in [45, 46] and went partially into the PhD theses of Tobias Kästner [47] and Georg Bergner [48]. Explicit analytical calculations of Sec. 6.1 result from the combined effort together with Lukas Janssen, Wieland Brendel, Falk Bruckmann and Andreas Wipf, are published in [49], and went into the diploma thesis of Lukas Janssen [50]. The $O(3)$ invariant lattice formulation in Sec. 6.2.2 has been constructed in collaboration with Raphael Flore.

Broken supersymmetric quantum mechanics

An extensive analysis of quantum mechanical systems, such as the anharmonic oscillator, with lattice regularised path integrals has been performed almost three decades ago [51]. Although the used methods can directly be applied to bosonic theories there has been renewed interest in the quantum mechanical systems on the lattice in the context of supersymmetric quantum mechanics (SQM). In several works SQM has been used as a toy model to study the supersymmetry breaking induced by a naive lattice formulation [52] and to explore lattice regularisations with partially [35, 41, 53, 54] or fully [40] conserved supersymmetries. It has been pointed out that a discretisation without any conserved supersymmetries may not be free of finite supersymmetry breaking renormalisation terms in the continuum limit [55] and a careful treatment of supersymmetry restoration is necessary. Most of the lattice studies of SQM so far have been carried out for the case of an unbroken supersymmetry and only few of them [56, 57] consider the case of the dynamically broken supersymmetry. In this work the case of a SQM with dynamically broken supersymmetry is considered to explain the concepts and effects of supersymmetry breaking in a setting that allows for high precision measurements in the lattice theory and provides the possibility to compare to exactly calculable reference values from the operator formalism.

2.1 Operator formalism

SQM in one dimension is a generalisation of the supersymmetric harmonic oscillator.¹ In analogy to supersymmetric field theories *nilpotent* supercharges \mathcal{Q} and its adjoint \mathcal{Q}^\dagger are introduced,

$$\mathcal{Q}^\dagger = \begin{pmatrix} 0 & 0 \\ A & 0 \end{pmatrix} = A\Psi^\dagger, \quad \mathcal{Q} = \begin{pmatrix} 0 & A^\dagger \\ 0 & 0 \end{pmatrix} = A^\dagger\Psi, \quad (2.1)$$

with fermionic creation and annihilation operator Ψ^\dagger and Ψ and

$$A = \frac{d}{d\phi} + P(\phi), \quad A^\dagger = -\frac{d}{d\phi} + P(\phi). \quad (2.2)$$

with *prepotential* $P(\phi)$.² The Hamiltonian is constructed via

$$\frac{1}{2}\{\mathcal{Q}, \mathcal{Q}^\dagger\} = \begin{pmatrix} H_B & 0 \\ 0 & H_F \end{pmatrix} = \frac{1}{2} \left(-\frac{d^2}{d\phi^2} + P^2(\phi) + [\Psi^\dagger, \Psi] P'(\phi) \right) \equiv H, \quad (2.3)$$

and acts on two-component state vectors $|\psi\rangle = (|\psi\rangle_B, |\psi\rangle_F)^\top$ where, for convenience, the first component is called ‘bosonic’ and the second one ‘fermionic’. The supersymmetry algebra is completed by the nilpotency of \mathcal{Q} and \mathcal{Q}^\dagger and the commutation with H ,

$$\{\mathcal{Q}, \mathcal{Q}\} = 0, \quad \{\mathcal{Q}^\dagger, \mathcal{Q}^\dagger\} = 0, \quad [\mathcal{Q}, H] = 0. \quad (2.4)$$

¹The introduction to the operator formalism is based on [58].

²In accordance to the field theory language ϕ denotes the position operator of the quantum mechanical system

If P is a linear function of ϕ then A and A^\dagger are the bosonic annihilation and creation operators of the (supersymmetric) harmonic oscillator. Accordingly the bosonic and fermionic Hamiltonian is given by

$$H_B = \frac{1}{2}A^\dagger A = -\frac{1}{2}\frac{d^2}{d\phi^2} + V_B, \quad H_F = \frac{1}{2}AA^\dagger = -\frac{1}{2}\frac{d^2}{d\phi^2} + V_F, \quad V_{B/F} = \frac{1}{2}(P^2(\phi) \mp P'(\phi)). \quad (2.5)$$

Both Hamiltonians are by construction non-negative. The bosonic sector of a zero energy state is annihilated by A and a fermionic one is annihilated by A^\dagger ,

$$H_B|0\rangle_B = 0 \Leftrightarrow A|0\rangle_B = 0, \quad H_F|0\rangle_F = 0 \Leftrightarrow A^\dagger|0\rangle_F = 0. \quad (2.6)$$

The supersymmetry algebra implies a strict pairing of excited states, i.e. for every bosonic eigenstate $|\psi_B\rangle$ with energy $E > 0$ there is a fermionic partner state

$$|\psi_F\rangle = \frac{1}{\sqrt{2E}}Q^\dagger|\psi_B\rangle, \quad |\psi_B\rangle = \frac{1}{\sqrt{2E}}Q|\psi_F\rangle \quad (2.7)$$

with identical norm and energy.

The zero energy state(s) of the super Hamiltonian H can be given explicitly (in position space) as solutions of first order differential equations. If one of these functions is normalisable, then the supersymmetric ground state exists and supersymmetry is *unbroken*. Since the product of possible zero energy states $\langle x|0_B\rangle \cdot \langle x|0_F\rangle$ is constant, there is at most *one normalisable* state with zero energy. The explicit form of solutions implies that for a polynomial $P(\phi) = \prod_{n=0}^N c_n \phi^n$ with $c_N \neq 0$, $N > 0$ supersymmetry is unbroken iff N is odd. In that case one normalisable zero energy state is present and the spectrum is similar to the case depicted in Fig. 2.1.

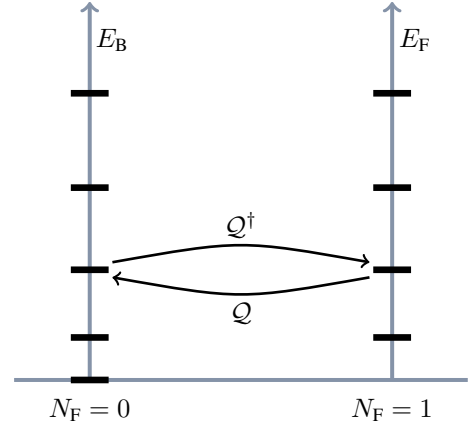


Figure 2.1: Energy spectrum for the unbroken supersymmetric quantum mechanics discussed in [41]. Q and Q^\dagger map between bosonic and fermionic sector.

2.1.1 Supersymmetry breaking and the Witten index

An existing and unbroken supersymmetry is defined by the existence of a normalisable ground state $|0\rangle$ with $Q|0\rangle = Q^\dagger|0\rangle = 0$, which implies $H_B|0\rangle_B = H_F|0\rangle_F = 0$. Witten defined *indices* [15] to determine whether supersymmetry can be broken dynamically in supersymmetric field theories. The simplest of those is given by a trace over all eigenstates of H ,

$$\Delta = \text{Tr}(-1)^{N_F}. \quad (2.8)$$

where (for the supersymmetric quantum mechanics discussed here) $N_F = \begin{pmatrix} 0 & 0 \\ 0 & 1 \end{pmatrix}$ is the *fermion number* operator that commutes with H .³ Now, two cases are possible.

- For *broken* supersymmetry there is no normalisable zero energy state. All eigenstates of H have positive energies and must be paired, which implies $\Delta = 0$.
- For *unbroken* supersymmetry there are n_B bosonic and n_F fermionic ground states with zero

³As it stands, Δ is not well defined and requires a normalisation, e.g. $\Delta = \lim_{\beta \rightarrow 0} \text{Tr}[e^{-\beta H}(-1)^{N_F}]$.

energy. They contribute with $n_B - n_F$ to the Witten index. All contributions from the excited states cancel, which gives $\Delta = n_B - n_F$.

Therefore a non-vanishing Witten index implies an unbroken supersymmetry, but not necessarily vice versa. It is still possible that supersymmetry is unbroken while there are the same number of bosonic and fermionic zero energy states. For a one dimensional supersymmetric quantum mechanics only one zero energy state is possible and $\Delta \neq 0$ is equivalent to unbroken SUSY.

2.1.2 Specifying the model

The minimal modification of the supersymmetric harmonic oscillator with broken supersymmetry is given by the prepotential $P(\phi) = m\phi + h\phi^2$ with vanishing Witten index. In consequence there exists *no normalisable* ground state with zero energy. The spectrum is completely degenerate and acting with the supercharges on one finite energy ground state will give the corresponding superpartner of this ground state.⁴

This model depends on the dimensionful parameters m and h and corresponding to the supersymmetric harmonic oscillator m is used to set the scale. Therefore $f = h/m^{1.5}$ provides a scale independent dimensionless coupling. In presence of a finite temperature a dimensionless temperature is given by $T = (m\beta)^{-1}$ with β as dimensionful inverse temperature. Eventually coordinates are made dimensionless by setting $\Phi = \phi\sqrt{m}$.

The energy spectrum and corresponding states can be computed directly by a discretisation in position space and replacing of $\frac{d}{d\phi}$ by a discretised derivative. After the analysis of different possible discretisations in [59] the most stable choice was found to be the SLAC derivative [60], which is given for periodic boundary conditions on a lattice with an odd number of points N and lattice spacing a by

$$a(\partial^{\text{SLAC}})_{xy} = \begin{cases} 0 & : x = y \\ \frac{\pi}{N} (-)^{x-y} \frac{1}{\sin(\pi(x-y)/(Na))} & : x \neq y \end{cases},$$

$$-a^2(\partial^{\text{SLAC}})^2_{xy} = \begin{cases} \frac{\pi^2}{N^2} \frac{N^2-1}{3} & : x = y \\ \frac{2\pi^2}{N^2} (-)^{x-y} \frac{\cos(\pi(x-y)/(Na))}{\sin^2(\pi(x-y)/(Na))} & : x \neq y \end{cases}. \quad (2.9)$$

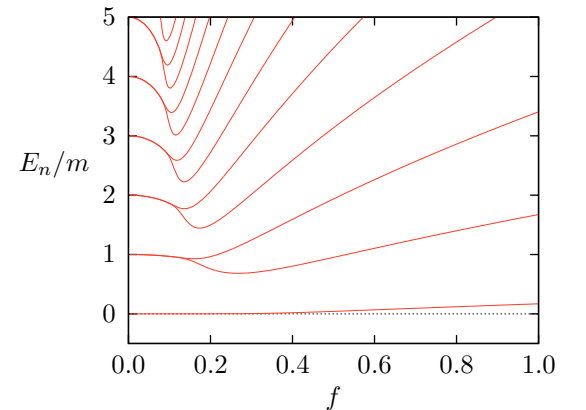


Figure 2.2: Energy levels for the broken supersymmetric quantum mechanics. Each level is doubly degenerate with one bosonic and one fermionic eigenstate.

The spectrum of the diagonalised Hamiltonian is shown in Fig. 2.2. For couplings $f \lesssim 0.1$ there is an additional (approximate) degeneracy of the excited spectrum corresponding to the perturbed energy levels of two harmonic oscillators with energies $\mathbb{N}m$ residing at the minima of the bosonic and fermionic potential $V_{B/F}$ (see Fig. 2.3).

Interpretation as a physical system

The naming ‘bosonic’ and ‘fermionic’ sector may sound misleading because of the complete degeneracy of the spectrum. The system can be interpreted as a particle with spin 1/2 moving in an external potential that depends on the spin orientation. So ‘bosonic’ may refer to ‘spin down’ and ‘fermionic’ to ‘spin up’, respectively. Supersymmetry in this case is represented as degeneracy between an up and

⁴If not otherwise stated, “ground states” may also have a positive energy.

a down state. For the case of unbroken supersymmetry the ground state is unique and is invariant under application of supersymmetry although it is in a definite spin state given by the interaction potential. For the broken supersymmetry there are (in the present case) two different ground states none of which is energetically preferred (see Fig. 2.3). There is no interaction given by the Hamiltonian between bosonic and fermionic sector and one ground state will be preserved if no external interaction is applied (e.g. by interacting with a heat bath at finite temperature). Applying the supercharge will give the partner ground state and amounts to the symmetry between spin up and spin down state. Furthermore no linear combination of the ground states is invariant under the supersymmetry.

Physics at $T = 0$

At vanishing temperature physics is given by ground state (vacuum) expectation values. Since supersymmetry is broken the system will stay in one of the degenerate ground states and expectation values are defined by this particular ground state.⁵ Without loss of generality results are given for the bosonic (finite energy) ground state $|0_B\rangle$ and the expectation value of an observable \mathcal{O} is thus given by $\langle\mathcal{O}\rangle_0 = \langle 0_B|\mathcal{O}|0_B\rangle$.

As reference values for lattice computations in the next section observables can be computed from the diagonalised Hamiltonian. On the lattice the primary focus lies on one- and two-point functions and the probability density of the coordinate Φ given by $\rho_0(\Phi) = |\langle\Phi|0\rangle|^2$. The one-point function is then given by $\langle\Phi\rangle_0 = \int d\Phi \rho_0(\Phi)\Phi$.

The bosonic two-point function (in the bosonic ground state) is defined through the Euclidean time evolution,

$$\langle\Phi(t)\Phi(0)\rangle_0 = \langle 0_B|\Phi(t)\Phi(0)|0_B\rangle = \langle 0_B|e^{tH}\Phi e^{-tH}\Phi|0_B\rangle = \langle 0_B|\Phi e^{-t(H-E_0)}\Phi|0_B\rangle. \quad (2.10)$$

Equivalently the fermionic correlation function is computed by

$$\langle\Psi(t)\Psi^\dagger(0)\rangle_0 = \langle 0_B|\Psi e^{-t(H-E_0)}\Psi^\dagger|0_B\rangle. \quad (2.11)$$

In each case tm defines the dimensionless ‘time’.

The last quantity of interest is the effective potential which may be either defined by a Legendre transform of the Schwinger function⁶ or more directly at vanishing temperature by

$$V_{\text{eff}}(\Phi_0) = \min_{\langle\psi|\Phi|\psi\rangle=\Phi_0} \langle\psi|H|\psi\rangle. \quad (2.12)$$

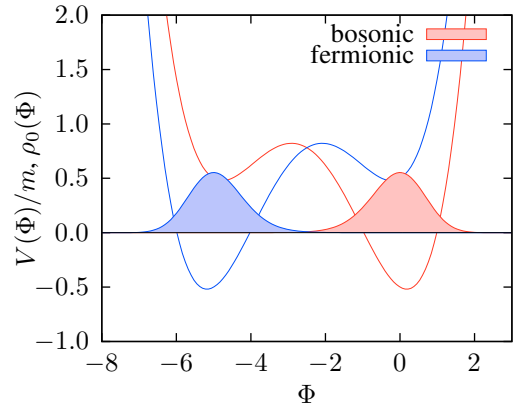


Figure 2.3: Probability density $\rho_0(\Phi)$ (shaded areas) for bosonic and fermionic ground state and potentials $V_{B/F}$ (lines) of the corresponding Hamiltonian at coupling $f = 0.2$.

⁵This is similar to the \mathbb{Z}_2 symmetry in the Ising chain. There, at any finite temperature the symmetry is restored. Only for $T = 0$ the system will take (and preserve) one of the possible ‘‘ground states’’.

⁶The Schwinger function is naturally defined in a path integral formulation.

Finite temperature physics

For any finite temperature there is a Boltzmann distribution with the same contribution of bosonic and fermionic partner states, including the lowest energy ground states. Again, with high precision calculations of the low lying spectrum provided by the diagonalised Hamiltonian it is possible to compute the thermal field distribution and expectation values

$$\rho_T(\Phi) = Z^{-1} \sum_E e^{-E/T} |\langle \Phi | \psi_E \rangle|^2, \quad \langle \mathcal{O} \rangle_T = Z^{-1} \sum_E \langle \psi_E | e^{-\beta H} \mathcal{O} | \psi_E \rangle, \quad Z = \sum_E e^{-E/T}, \quad (2.13)$$

where the sums run over both bosonic and fermionic states.

2.2 Lattice regularised path integral

With the methods given in the previous section it is possible to give exact results against which the path integral based calculations can be compared. Therefore the applicability of the lattice regularisation even for the case of a broken supersymmetry can be investigated. The corresponding Euclidean path integral is given by

$$\mathcal{Z} = \int \mathcal{D}\phi \mathcal{D}\psi \mathcal{D}\bar{\psi} e^{-S[\phi, \psi, \bar{\psi}]}, \quad (2.14)$$

with Euclidean action

$$S = \int d\tau \left(\frac{1}{2} (\partial\phi)^2 + \frac{1}{2} P^2(\phi) + \bar{\psi} (\partial + P'(\phi)) \psi \right). \quad (2.15)$$

Expectation values are computed via

$$\langle A \rangle = \mathcal{Z}^{-1} \int \mathcal{D}\phi \mathcal{D}\psi \mathcal{D}\bar{\psi} A[\phi, \psi, \bar{\psi}] e^{-S[\phi, \psi, \bar{\psi}]}. \quad (2.16)$$

Supersymmetry appears as a symmetry of the action, where one transformation is given by

$$\delta^{(1)}\phi = \bar{\varepsilon}\psi, \quad \delta^{(1)}\bar{\psi} = -\bar{\varepsilon}(\dot{\phi} + P(\phi)), \quad \delta^{(1)}\psi = 0 \quad (2.17)$$

and a variation of the action gives $\delta^{(1)}S = \int d\tau [\partial(\bar{\varepsilon}P\psi)] = 0$. In the same way the action allows for a second supersymmetry transformation

$$\delta^{(2)}\phi = \bar{\psi}\varepsilon, \quad \delta^{(2)}\bar{\psi} = 0, \quad \delta^{(2)}\psi = (\dot{\phi} - P)\varepsilon. \quad (2.18)$$

For the above supersymmetries to hold it is necessary that the fields vanish at infinity or that they are periodic in the Euclidean time. In the case of a thermal path integral at inverse temperature β with the above action the fields naturally obey boundary conditions given by

$$\phi(0) = \phi(\beta), \quad \psi(0) = -\psi(\beta), \quad \bar{\psi}(0) = -\bar{\psi}(\beta), \quad (2.19)$$

i.e. the fermionic field is *antiperiodic* in time. Since the fields need not vanish anymore the variation of the action then reads

$$\delta^{(1)}S = [\bar{\varepsilon}P\psi]_{\tau=0}^{\beta} = -2[\bar{\varepsilon}P\psi]_{\tau=0} \quad (2.20)$$

which can be non-vanishing so that supersymmetry is broken by the finite temperature. In [41, 52] for an unbroken supersymmetric quantum mechanics periodic boundary conditions have been used. For temperature going to zero a change in boundary conditions is equivalent to an insertion of $(-1)^{N_F}$ into the path integral,

$$\mathcal{Z}_p = \int \mathcal{D}\phi \mathcal{D}\psi_p \mathcal{D}\bar{\psi}_p e^{-S[\phi, \psi, \bar{\psi}]} = \int \mathcal{D}\phi \mathcal{D}\psi_{ap} \mathcal{D}\bar{\psi}_{ap} (-1)^{N_F} e^{-S[\phi, \psi, \bar{\psi}]} = \mathcal{Z}_{ap} \Delta. \quad (2.21)$$

Here, the periodic path integral is vanishing due to $\Delta = 0$ for a broken supersymmetry. Thus, for a theory allowing supersymmetry breaking, periodic (supersymmetry preserving) boundary conditions cause a severe sign problem. This does not completely rule out the choice of these boundary conditions, as will be discussed on the case of the two dimensional $\mathcal{N} = 1$ Wess-Zumino model in Chapter 5, but puts constraints on the range of applicability.⁷ To have a well defined (non-vanishing) path integral antiperiodic (thermal) boundary conditions for the fermionic fields are chosen and the path integral coincides with the thermal partition function.

For a construction of the model's lattice representation the choice of the lattice regularised derivative is crucial.⁸ The canonical choice for scalar theories would be the forward (or equivalently backward) derivative. For derivatives appearing in the fermionic action a popular choice is given by Wilson's prescription [29]. Nevertheless, these simple discretisation rules are not applicable to supersymmetric theories as analysed in [41, 52, 55] for the case of an unbroken supersymmetric quantum mechanics. These results show the need for a more careful treatment of the discretisation of supersymmetric theories. In the comparative study of six different discretisations [41] the one based on the SLAC derivative is found to be best suited for the needs of this work by giving results close to the continuum limit even at finite lattice spacing. For an odd number of lattice points with periodic boundary conditions the matrix representation is already given in Eq. (2.9). Antiperiodic boundary conditions (necessary for fermionic fields) are best realised on an even lattice with N points

$$a(\partial^{\text{SLAC}})_{xy} = \begin{cases} 0 & : x = y \\ \frac{\pi}{N} (-)^{(x-y)/a} \frac{1}{\sin(\pi(x-y)/(Na))} & : x \neq y \end{cases}, \quad (2.22)$$

while the squared SLAC derivative for an even number of lattice points and periodic boundary conditions (as needed for the bosonic fields) reads

$$-a^2(\partial^{\text{SLAC}})_{xy}^2 = \begin{cases} \frac{\pi^2}{N^2} \frac{N^2+2}{3} & : x = y \\ \frac{2\pi^2}{N^2} (-)^{(x-y)/a} \frac{1}{\sin^2(\pi(x-y)/(Na))} & : x \neq y \end{cases}. \quad (2.23)$$

Although it was analysed [61] that this prescription will lead to a non-covariant and non-local continuum limit in lattice QED it can be proven [41, 48] that for scalar theories in one or two dimensions with Yukawa interactions a local renormalisable continuum limit is reached. For that reason the SLAC derivative is used in this work to regularise the supersymmetric quantum mechanics on the lattice with

⁷For a phase with unbroken supersymmetry in models with $\Delta = 0$ only one specific ground state belongs to the physical spectrum and periodic boundary conditions may be imposed.

⁸In contrast to the operator formalism where the field space is discretised, the lattice path integral is based on a discretisation in the Euclidean time.

corresponding action

$$S = - \sum_{x,y} \frac{1}{2} \hat{\phi}_x (\hat{\partial}_{xy}^{\text{SLAC}})^2 \hat{\phi}_y + \frac{1}{2} \sum_x P(\hat{\phi}_x)^2 + \sum_{x,y} \bar{\psi}_x (\hat{\partial}_{xy}^{\text{SLAC}} + P'(\hat{\phi}_x) \delta_{xy}) \psi_y \quad (2.24)$$

on lattices with an even number of sites, where field $\hat{\phi}$ and derivative $\hat{\partial}^{\text{SLAC}}$ are dimensionless and arise from rescaling of the dimensionful quantities with the lattice spacing.⁹

Access to the non-perturbative sector of the lattice model is gained from Monte-Carlo simulations which have become a powerful tool due to increasing computer power and algorithmic improvements that allow for the inclusion of dynamical fermions in simulations. These statistical methods are based on importance sampling and the interpretation of the lattice regularised path integral

$$\mathcal{Z} = \int D\hat{\phi} D\psi D\bar{\psi} e^{-S[\hat{\phi}, \psi, \bar{\psi}]} \quad (2.25)$$

as probability distribution. To construct the probability density the action is then split into a bosonic and fermionic part according to

$$S[\hat{\phi}, \psi, \bar{\psi}] = S_{\text{B}}[\hat{\phi}] + \sum_{x,y} \bar{\psi}_x M_{xy}[\hat{\phi}] \psi_y. \quad (2.26)$$

Due to the rules of Grassmann integration the fermionic part of the path integral can (for every fixed $\hat{\phi}$) be integrated out to yield

$$\mathcal{Z} = \int D\hat{\phi} \det M[\hat{\phi}] e^{-S_{\text{B}}[\hat{\phi}]} \quad (2.27)$$

In this way (bosonic) expectation values are computed by

$$\langle \mathcal{O}[\hat{\phi}] \rangle = \mathcal{Z}^{-1} \int D\hat{\phi} \mathcal{O}[\hat{\phi}] \det M[\hat{\phi}] e^{-S_{\text{B}}[\hat{\phi}]} \quad (2.28)$$

In a Monte-Carlo simulation the lattice regularised fields $\hat{\phi}$ are generated according to the distribution

$$\rho[\hat{\phi}] = e^{-S_{\text{B}}[\hat{\phi}] + \ln |\det M[\hat{\phi}]|} \quad (2.29)$$

After a number of N_{MC} samples one obtains a time series $\hat{\phi}^{(k)}$, $k = 1, \dots, N_{\text{MC}}$, and expectation values are evaluated using

$$\langle \mathcal{O} \rangle \stackrel{N_{\text{MC}} \rightarrow \infty}{\equiv} N_{\text{MC}}^{-1} \sum_{k=1}^{N_{\text{MC}}} \mathcal{O}[\hat{\phi}^{(k)}]. \quad (2.30)$$

This expression is only exact iff $\det M \geq 0$. If $\det M$ is negative the sign has to be taken into account by reweighting. However, the emphasis lies on the physical questions and further simulation details will be given in Chapter 4.

2.2.1 Sign of the fermion determinant

For periodic fermionic boundary conditions $\mathcal{Z}_{\text{p}} \propto \Delta$ will vanish in the continuum and a severe sign problem is expected to arise in reweighted expectation values. For thermal boundary conditions it is a priori unknown if there are configurations with $\det M < 0$ and if there is any dependence on

⁹The fermionic fields $\psi, \bar{\psi}$ are already dimensionless and need not to be rescaled.

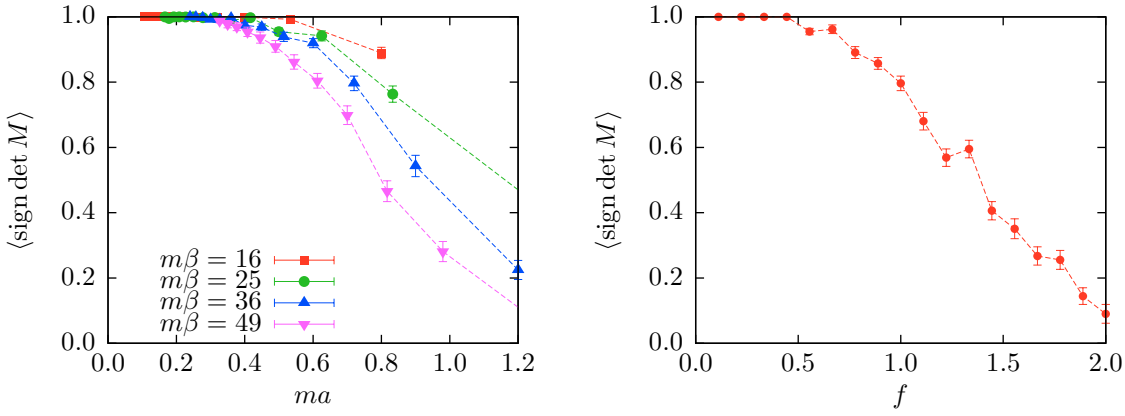


Figure 2.4: Sign of the fermion determinant measured at fixed $f = 1$ (left panel) and at fixed $m\beta = 36$ and $N = 50$ lattice points (right panel) with 10^5 configurations per data point.

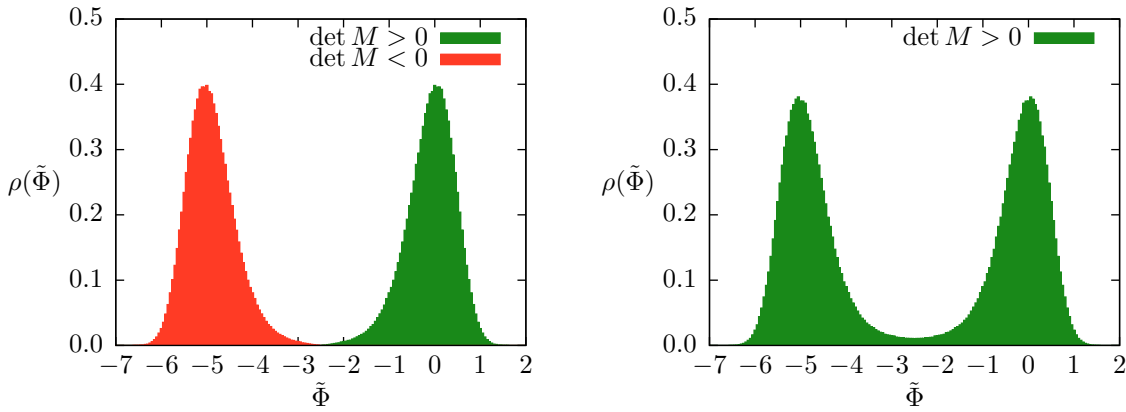


Figure 2.5: The distribution of the averaged field $\tilde{\Phi}$ for $m\beta = 4$ at coupling $f = 0.2$ with respect to the sign of the determinant for periodic (left panel, $N = 101$) and antiperiodic (right panel, $N = 100$) fermionic boundary conditions obtained from 10^6 configurations.

lattice spacing, temperature, or coupling. For that reason $\langle \text{sign det } M \rangle$ has been measured in the sign quenched ensemble with the distribution given by Eq. (2.29) for different parameter sets (see Fig. 2.4). These results imply a complete absence of the sign problem in the continuum limit for *every* coupling and temperature. The sign problem will be present for large couplings f at fixed lattice spacing and temperature.

2.2.2 Ground state structure

With thermal and supersymmetry preserving boundary conditions for small temperature $T = 0.25$ the ground state structure is analysed. Simulations at $f = 0.2$ are performed and the distribution of the lattice averaged field $\tilde{\Phi} = N^{-1} \sum_x \Phi_x$ is analysed with respect to the sign of $\det M$ (see Fig. 2.5). Configurations with $\tilde{\Phi} > -\frac{1}{2f}$ are unaffected by a change of boundary conditions whereas the sign of $\det M$ changes for $\tilde{\Phi} < -\frac{1}{2f}$. This behaviour can be seen explicitly on the level of the discretised action. For the chosen prepotential bosonic and fermionic ground state are related by a \mathbb{Z}_2 symmetry $\Phi_x \rightarrow -\Phi_x - \frac{1}{f}$. S_B is invariant under the symmetry operation whereas the effect on the fermionic contribution depends on the used derivative. The SLAC derivative has an antisymmetric matrix representation, $\partial_{xy}^{\text{SLAC}} = -\partial_{yx}^{\text{SLAC}}$. $P'(\phi)$ enters on the diagonal of the fermion matrix M . Applying the \mathbb{Z}_2 symmetry gives $P'(\phi) \rightarrow -P'(\phi)$ and changes the sign of the diagonal elements of the fermion matrix. Altogether, the symmetry operation changes $M(\hat{\phi}) \rightarrow -M^T(\hat{\phi})$. For antiperiodic (periodic) fermions the fermion matrix size will be even (odd, respectively) and the determinant will keep the modulus

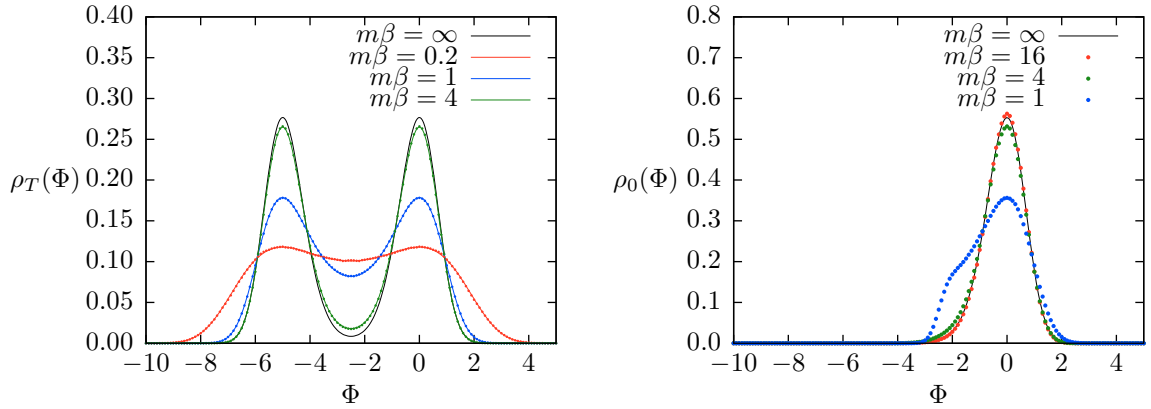


Figure 2.6: Probability distribution $\rho(\Phi)$ for for different temperatures at coupling $f = 0.2$ on a $N = 100$ lattice. Lines depict the exact results, points arise from the lattice calculations. For comparison the distribution at $T \rightarrow 0$ is also drawn. Left panel: Thermal distribution. Right panel: Exact distribution for the bosonic ground state and distribution measured on configurations with $\tilde{\Phi} > -\frac{1}{2f}$.

but changes its sign for periodic boundary conditions. For antiperiodic fermions the sign is preserved. Therefore periodic SLAC fermions imply $\mathcal{Z}_p = 0$ exactly. The boundary condition dependence of the distribution coincides with introducing $(-1)^{N_F}$ into the path integral for periodic boundary conditions and configurations with $\tilde{\Phi} > -\frac{1}{2f}$ correspond to the bosonic ground state whereas the other ones correspond to the fermionic ground state, respectively. This is in accordance with results from the operator formalism shown in Fig. 2.3.

2.2.3 Thermal field distribution

At finite temperature the single site distribution $\rho_T(\Phi)$ of Eq. (2.13) is computed on a lattice with $N = 100$ points at fixed coupling $f = 0.2$ in the temperature range $m\beta \in [0.2, 4]$ with 10^6 configurations. Even for this finite lattice spacing the results match almost perfectly with the reference values from the diagonalised Hamiltonian (see Fig. 2.6, left panel). Further it is possible to extract at small temperatures $m\beta = 16$ the probability distribution in the bosonic ground state by considering only configurations with $\tilde{\Phi} > -\frac{1}{2f}$. Even at this finite (but small) temperature the probability distribution matches up with the exact result, see Fig. 2.6 (right panel). In consequence, for $T \rightarrow 0$ a thermal mixture of bosonic and fermionic ground state is found whereas at exactly vanishing temperature the system can be triggered to stay in one chosen ground state.

2.2.4 Effective potential

The effective potential as introduced in the Sec. 2.1.2 is not directly accessible in lattice simulations. A better suited quantity is given by the constraint effective potential [62]

$$U(\tilde{\Phi}_0) = -\frac{1}{\beta} \ln \left(\int D\hat{\phi} \det M[\hat{\phi}] e^{-S_B[\hat{\phi}]} \delta(\tilde{\Phi} - \tilde{\Phi}_0) \right), \quad (2.31)$$

which can be easily computed on the lattice.¹⁰ In the limit of infinite volume (or equivalently vanishing temperature) it coincides with the effective potential, $\lim_{m\beta \rightarrow \infty} U(\tilde{\Phi}) = \lim_{m\beta \rightarrow \infty} V_{\text{eff}}(\tilde{\Phi})$. In Fig. 2.7 the constraint effective potential has been determined for various volumes $m\beta$ at fixed coupling $f = 0.2$. The minimum of the potential is normalised to 0. For large volumes the peak at $\tilde{\Phi} = \frac{1}{2}f^{-1}$

¹⁰Only an additive normalisation constant of the constraint effective potential is left undetermined.

cannot be resolved because corresponding configurations are exponentially suppressed with the volume $m\beta$. However, a slow flattening with increasing volume is visible and the positions of the minima correspond to the bosonic and fermionic ground state.

Although it is often stated that the effective potential for a quantum mechanical system is strictly convex, this only applies to $L^2(\mathbb{R}^d)$ Hilbert spaces. Here the bosonic and fermionic sector form an $L^2(\mathbb{R}) \otimes \mathbb{C}^2$ Hilbert space, such that every linear combination of bosonic and fermionic ground state has the same energy, which implies a flat region in the effective potential as defined in (2.12).

2.2.5 Two-point functions and spectrum

Lattice based path integral methods provide a non-perturbative way to gain information about the spectrum of the theory. Via the long distance behaviour of correlators $C(t) \xrightarrow{t \rightarrow \infty} \exp(-m_{\text{phys}}t)$ it is possible to extract the physical ‘pole mass’ m_{phys} which is given by the imaginary part of the pole of the propagator $G(p) = (\mathcal{F}C)(p)$, the Fourier transform of the correlator, and describes the energy difference between ground state and first excited state of the theory. For that reason connected correlation functions in the thermal ensemble have been computed for bosonic and fermionic fields (see Fig. 2.8) with $C_B(t) = \langle \Phi(t)\Phi(0) \rangle - \langle \Phi \rangle^2$ and $C_F(t) = \langle \psi(t)\bar{\psi}(0) \rangle$. The correlators take non-vanishing constant values for large distances in a region where the exponential falloff drops below the visibility scale.¹¹ Correlators computed from the lattice regularised theory fit nicely to the ones computed by the diagonalised Hamiltonian. Fluctuation are still visible around the continuum values with the size of fluctuations vanishing for smaller lattice spacings. Further it is possible from the fermionic correlator at small (but non-vanishing) temperature to compute the overlap of bosonic and fermionic ground state $|\langle 0_F | \Psi^\dagger | 0_B \rangle|^2 = 0.41174$ by the approximation $C_F(m\beta/2) = 0.427(12)$ for $m\beta = 16$ and $N = 400$.

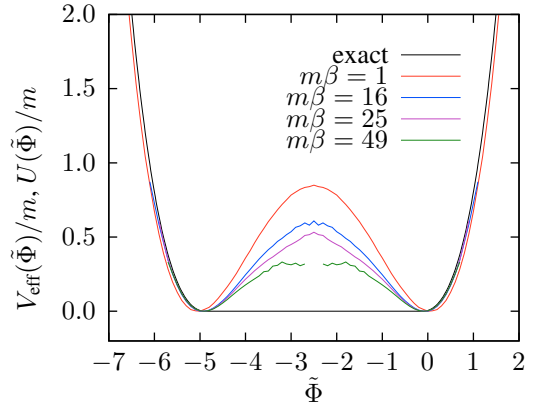


Figure 2.7: Effective potential for $T = 0$ (exact) and constraint effective potential from lattice simulations at various $m\beta$ for coupling $f = 0.2$ and $N = 150$ lattice points measured with up to 10^8 configurations.

¹¹This is *not directly* related to any unconnected part. Here only connected correlators are considered.

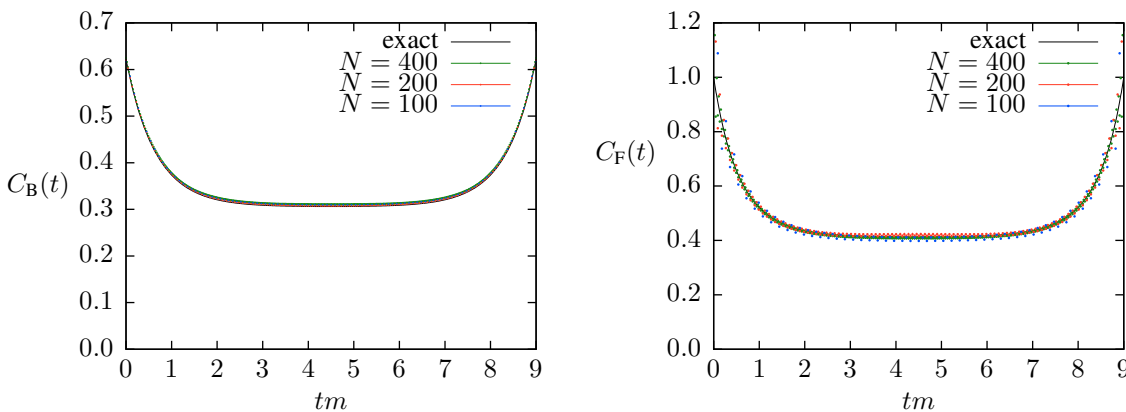


Figure 2.8: The two-point function (left panel: bosonic, right panel: fermionic) for the thermal ensemble given by $m\beta = 9$ and coupling $f = 1$ computed by the diagonalised Hamiltonian and on a lattices with $N \in \{100, 200, 400\}$ points. For the bosonic case the data points completely cover the reference line. A statistics of up to 10^7 configurations has been used.

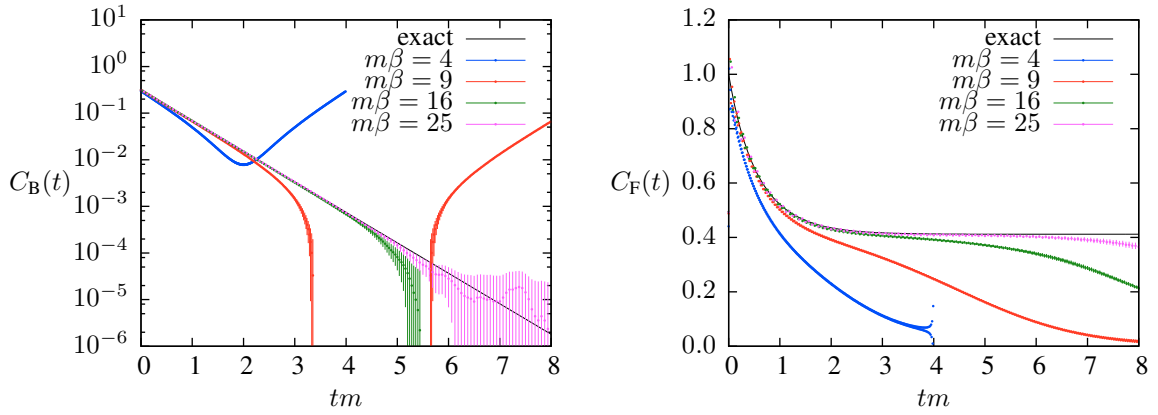


Figure 2.9: Bosonic (left panel) and fermionic (right panel) correlator in the ensemble projected to one ground state as obtained from the diagonalised Hamiltonian and from lattice simulations with $N = 400$ sites at coupling $f = 1$.

With nearly vanishing temperature the system will mainly reside in the ground states and with the results of Sec. 2.2.2 it is possible to compute the correlation function present at $T = 0$ by projecting to one of the ground states (see Fig. 2.9). In that case the bosonic correlator shows no constant part and the exponential behaviour completely coincides with the one resulting from the first excited (bosonic) state. From the lattice values at $N = 400$ a mass of $m_{\text{phys}} = 1.5064(26) m$ is extracted through an exponential fit in the range $tm \in [1, 3]$ from a simulation at $m\beta = 25$ coinciding within error bars with the exact result $E_1 - E_0 = 1.5046 m$. Of course this method is only applicable for $t < \beta/2$ and there will be large deviations for t close to $\beta/2$.

All these results clearly show that it is possible to extract correlators at finite and vanishing temperature with a lattice discretisation in complete coincidence with exact results in the continuum limit. In addition the degenerate ground states are visible as a constant part in the fermionic correlator and a projection to one ground state allows to extract the energy difference between ground state and first excited state in the bosonic energy spectrum (see Fig. 2.10).

2.2.6 Ward identity

For field transformations $\Phi' = \Phi + \delta\Phi$ that do *not* change the path integral measure¹² ($\mathcal{D}\Phi = \mathcal{D}\Phi'$) Ward identities arise naturally on the level of observables as

$$\langle \mathcal{O} \rangle = \mathcal{Z}^{-1} \int \mathcal{D}\Phi' \mathcal{O}[\Phi'] e^{-S[\Phi']} = \mathcal{Z}^{-1} \int \mathcal{D}\Phi (\mathcal{O}[\Phi] + \delta\mathcal{O}[\Phi]) (1 - \delta S[\Phi]) e^{-S[\Phi]} = \langle \mathcal{O} + \delta\mathcal{O} - \mathcal{O} \delta S \rangle \quad (2.32)$$

implying $\langle \delta\mathcal{O} \rangle = \langle \mathcal{O} \delta S \rangle$. If further the action *and* the ground state is invariant under the transformation given by δ then $\langle \delta\mathcal{O} \rangle$ vanishes for every observable \mathcal{O} .

For unbroken supersymmetric theories Ward identities are used to test the supersymmetry restoration in the continuum limit by analysing the continuum limit of $\langle \delta\mathcal{O} \rangle$ for given observables \mathcal{O} . If

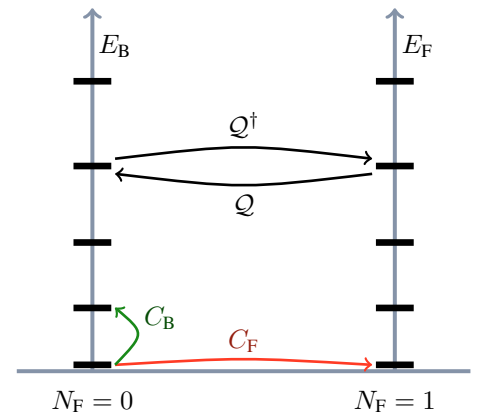


Figure 2.10: Excitations visible as $t \rightarrow \infty$ behaviour of the correlators evaluated on configurations projected to the bosonic ground state.

¹²Here only the anomaly free case is considered. If the path integral measure is changed under the transformation additional contributions must be taken into account.

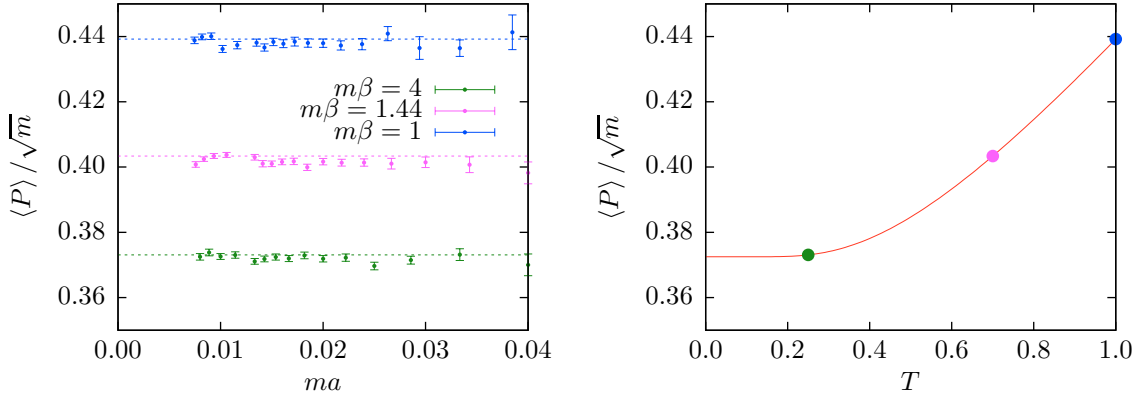


Figure 2.11: Prepotential for coupling $f = 1$. Left panel: Continuum limit of the prepotential $\langle P \rangle / \sqrt{m}$ which serves as simplest Ward identity for the supersymmetric quantum mechanics. Right panel: Temperature dependence of $\langle P \rangle / \sqrt{m}$ computed from the diagonalised Hamiltonian (data from the left panel is marked by points).

supersymmetry is broken then Ward identities will *not* be fulfilled in the continuum limit, $\langle \delta \mathcal{O} \rangle \neq 0$. On the lattice supersymmetry will be further broken explicitly by a finite lattice spacing and by finite temperature.

A simple Ward identity is provided by

$$(m\beta)^{-1} \int dt \langle \delta^{(1)} \bar{\psi} \rangle = -\bar{\varepsilon} (m\beta)^{-1} \int dt \langle \dot{\phi} + P(\phi) \rangle = -\bar{\varepsilon} \left\langle (m\beta)^{-1} \int dt P(\phi) \right\rangle = -\bar{\varepsilon} \langle P(\phi) \rangle, \quad (2.33)$$

and a dimensionless identity is given by $\langle P \rangle / \sqrt{m} = 0$ iff the ground state is invariant under the supersymmetry. The impact of the explicit supersymmetry breaking on the continuum result at vanishing temperature is analysed in Fig. 2.11 for coupling $f = 1$. At the given lattice spacings finite a effects are rather small and provide results in accordance with the continuum limit. Finite temperature effects are nearly absent for $T < 0.2$ and a non-zero value of $\langle P \rangle / \sqrt{m} = 0.37251$ is reached which corresponds to the non-supersymmetric ground states. In addition this quantity is invariant under the \mathbb{Z}_2 symmetry $\Phi \rightarrow -\frac{1}{f} - \Phi$ and is not sensitive to the specific ground state chosen at $T = 0$.

2.3 Conclusions

For the case of a supersymmetric quantum mechanics with dynamically broken supersymmetry observables that are computed using a lattice regularisation with the SLAC derivative completely coincide with results obtained from the diagonalised Hamiltonian. The (bosonic/fermionic) nature of both ground states can be explained with the the impact of a change in boundary conditions on the fermionic determinant. Correlators computed in the thermal ensemble show a constant part for large t which is a remnant of the degenerate ground states. With a projection to one ground state the constant part is still visible in the fermionic correlator, which goes at hand with the massless fermionic excitation implied by the degeneracy. In the bosonic correlator the constant part vanishes and the remaining exponential falloff corresponds to the first excited state in the bosonic spectrum. On the level of Ward identities it is checked that the ground state is not invariant under the supersymmetry and a simple Ward identity is not fulfilled in the limit of vanishing lattice spacing and temperature, as predicted from diagonalising the Hamiltonian. Altogether it is possible to analyse the broken supersymmetric quantum mechanics with lattice methods based on the SLAC derivative and physical properties can be determined reliably.

Chapter 3

$\mathcal{N} = 2$ Wess-Zumino model

The numerical analysis of the $\mathcal{N} = 2$ Wess-Zumino model started with the works [53, 63] which covered the perturbative region of this model. With algorithmic and analytical improvements based on the analysis of the unbroken SQM in [41] it is possible to analyse the lattice theory in a much enlarged parameter space beyond the perturbative region and to analyse artificial supersymmetry breaking introduced by the lattice regularisation and the measurement process.

This model is of particular interest because of the non-vanishing Witten index which implies an unbroken supersymmetry in the continuum theory. Further all divergences in the perturbation series in superspace cancel and the model obtains only finite renormalisation terms. Finally the model allows for a partial realisation of the supersymmetry algebra on the lattice as discussed e.g. in [64, 65]. An elegant suggestion uses a Nicolai map [66] to create lattice improvement terms that guarantee a partial realisation of supersymmetry, cf. e.g. [63]. With this partially realised supersymmetry the number of relevant operators in the continuum is reduced and the standard lore is that it is sufficient to realise just a part of the supersymmetry on the lattice in order to ensure the correct continuum limit.

In a systematic study the effects of the above-mentioned improvement terms introduced by the Nicolai map [63] will be analysed and comparisons are done with models without such terms. In previous works [41, 59] and the previous chapter it has been demonstrated that lattice models based on the SLAC derivative [60] and on the twisted Wilson formulation (as introduced in [41]) are particularly well-behaved as far as the continuum limit is concerned. Even at large lattice spacing the continuum result is approximated very well. Therefore the numerical analysis covers different lattice discretisations that can be directly compared in the continuum limit.

3.1 Lattice models

3.1.1 Supersymmetrically improved lattice actions

The lattice models under consideration have been discussed at length in [41]. Therefore, only briefly the definitions of the corresponding continuum and lattice actions are recalled. In terms of complex coordinates z and \bar{z} for the two dimensional Euclidean spacetime together with the corresponding holomorphic and anti-holomorphic differentials ∂ and $\bar{\partial}$ the continuum action of the $\mathcal{N} = 2$ Wess-Zumino model reads

$$S_{\text{cont}} = \int d^2x \left(2\bar{\partial}\bar{\varphi} \partial\varphi + \frac{1}{2}|W'(\varphi)|^2 + \bar{\psi}M\psi \right). \quad (3.1)$$

The bosonic potential is given by the absolute square of the derivative of the holomorphic superpotential $W(\varphi)$ with respect to its argument $\varphi = \varphi_1 + i\varphi_2$. Apart from the standard kinetic term for the (two-component) Dirac spinors, the Dirac operator M contains a Yukawa coupling,

$$M = \gamma^z \partial + \gamma^{\bar{z}} \bar{\partial} + W'' P_+ + \bar{W}'' P_-. \quad (3.2)$$

The chiral projectors $P_{\pm} = \frac{1}{2}(\mathbb{1} \pm \gamma_*)$ in the Weyl basis with $\gamma^1 = \sigma_1$, $\gamma^2 = -\sigma_2$, $\gamma_* = i\gamma^1\gamma^2$ project onto the upper and lower components of ψ . In the form (3.1) the action is invariant under four real supercharges. Taken together they satisfy the $\mathcal{N} = (2, 2)$ superalgebra, and it has been argued that at most one supersymmetry can be preserved on the lattice [63]. With the help of the explicitly known form of the Nicolai map it is possible to construct such a lattice model straightforwardly. In terms of

the Nicolai variable $\xi_x = 2(\bar{\partial}\bar{\varphi})_x + W_x$ on the lattice, the discretised Wess-Zumino action reads

$$S = \frac{1}{2} \sum_x \bar{\xi}_x \xi_x + \sum_{x,y} \bar{\psi}_x M_{xy} \psi_y \quad (3.3)$$

with W_x as the lattice counterpart of the continuum operator $W'(\varphi)$, i.e. $W_x = W'(\varphi_x)$.¹ The matrix M is given by

$$M_{xy} = \begin{pmatrix} W_{xy} & 2\bar{\partial}_{xy} \\ 2\partial_{xy} & \bar{W}_{xy} \end{pmatrix} = \begin{pmatrix} \frac{\partial \xi_x}{\partial \varphi_y} & \frac{\partial \xi_x}{\partial \bar{\varphi}_y} \\ \frac{\partial \bar{\xi}_x}{\partial \varphi_y} & \frac{\partial \bar{\xi}_x}{\partial \bar{\varphi}_y} \end{pmatrix}. \quad (3.4)$$

All lattice difference operators are here required to be antisymmetric, $\partial_{xy} = -\partial_{yx}$. From the second equality in (3.4) one reads off that $W_{xy} = \frac{\partial W_x}{\partial \varphi_y}$.

One easily checks that (3.3) is invariant under the following (supersymmetry) variation,

$$\delta\varphi_x = \bar{\varepsilon}\psi_{1,x}, \quad \delta\bar{\psi}_{1,x} = -\frac{1}{2}\bar{\xi}_x\bar{\varepsilon}, \quad \delta\psi_{1,x} = 0, \quad (3.5a)$$

$$\delta\bar{\varphi}_x = \bar{\varepsilon}\psi_{2,x}, \quad \delta\bar{\psi}_{2,x} = -\frac{1}{2}\xi_x\bar{\varepsilon}, \quad \delta\psi_{2,x} = 0. \quad (3.5b)$$

In terms of the original fields, (3.3) takes the form

$$S = \sum_x \left(2(\bar{\partial}\bar{\varphi})_x (\partial\varphi)_x + \frac{1}{2}|W_x|^2 + W_x(\partial\varphi)_x + \bar{W}_x(\bar{\partial}\bar{\varphi})_x \right) + \sum_{x,y} (\bar{\psi}_{1,x}, \bar{\psi}_{2,x}) \begin{pmatrix} W_{xy} & 2\bar{\partial}_{xy} \\ 2\partial_{xy} & \bar{W}_{xy} \end{pmatrix} \begin{pmatrix} \psi_{1,y} \\ \psi_{2,y} \end{pmatrix}. \quad (3.6)$$

This supersymmetrically improved lattice action differs from a straightforward discretisation of (3.1) by the *improvement term*

$$\Delta S = \sum_x \left(W_x(\partial\varphi)_x + \bar{W}_x(\bar{\partial}\bar{\varphi})_x \right), \quad (3.7)$$

a discretisation of a surface term in the continuum theory (which is therefore expected to vanish in the continuum limit for suitably chosen boundary conditions). For the free theory ($W_x = m\varphi_x$) $\Delta S = 0$ readily follows from the antisymmetry of the difference operator ∂_{xy} while for interacting theories (3.7) guarantees the invariance of the action under (3.5) without the need of the Leibniz rule. To study the impact of this supersymmetry improvement the improved action will be compared with the *unimproved* straightforward discretisation of (3.1) (without ΔS).

3.1.2 Lattice fermions

For the symmetric difference operator

$$a(\partial_\mu^S)_{xy} = \frac{1}{2}(\delta_{x+\hat{\mu},y} - \delta_{x-\hat{\mu},y}), \quad (3.8)$$

doublers are inevitably introduced into both the bosonic and fermionic sector. In order to get rid of them a Wilson term may be added to the superpotential so as to maintain the invariance of the action under (3.5). Within this context two different choices have been discussed previously [41],

$$W_x = W'(\varphi_x) - \frac{r}{2}(\Delta\varphi)_x \quad (3.9)$$

¹The lattice fermion fields are made dimensionless by rescaling the continuum ones with the lattice spacing.

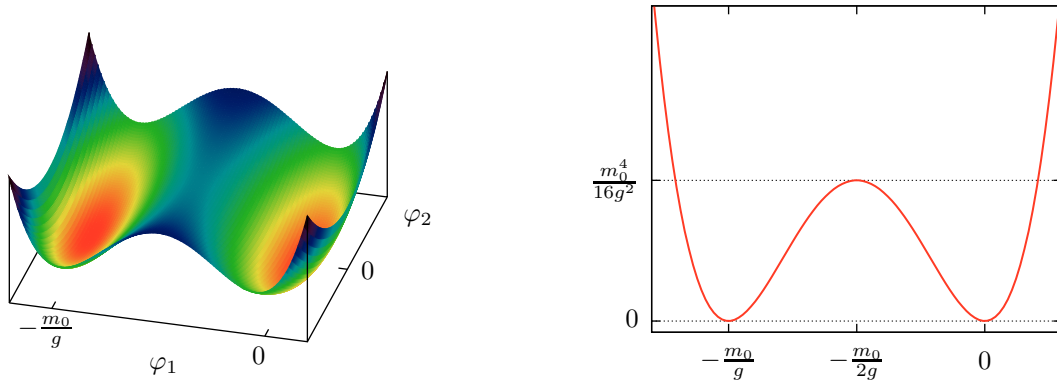


Figure 3.1: Classical bosonic potential $V(\varphi) = \frac{1}{2}|W'(\varphi)|^2$ from (3.11) in the complex φ plane (left panel) and for vanishing imaginary part ($\varphi_2 = 0$, right panel). In the free theory limit ($g \rightarrow 0$) the left minimum is pushed towards minus infinity.

and

$$W_x = W'(\varphi_x) + \frac{ir}{2}(\Delta\varphi)_x. \quad (3.10)$$

For Wilson fermions, the derivative of the superpotential is now shifted as compared to the situation after (3.3). From the first expression the standard Wilson term for the fermions is recovered, i.e. $W_{xy} = W''(\varphi_x)\delta_{xy} - \frac{r}{2}\Delta_{xy}$. The operator Δ_{xy} is the usual two dimensional (lattice) Laplacian $2\partial\bar{\partial}$. The second possibility (3.10) leads in (3.4) to $M_{xy} = \gamma^\mu(\partial_\mu)_{xy} + W''(\varphi_x)\delta_{xy} + \gamma_*\frac{r}{2}\Delta_{xy}$. Here, the appearance of γ_* motivates the name *twisted* Wilson fermions (not be confused with the twisted mass formulation of lattice QCD [67]). It was already shown for the free theory [41] that *twisted* Wilson fermions suffer far less from lattice artefacts than their standard Wilson cousins. In the following it will be shown that they remain superior even for (strongly) interacting theories.

Besides these two (ultra-)local difference operators also the SLAC lattice derivative is used for the present model. In higher dimensions the SLAC derivative is a straightforward generalisation of the one introduced in Chapter 2 and amounts to forming suitable tensor products of Eq. (2.9).² For SLAC fermions no further modifications to the superpotential are necessary. It is due to this fact that they constitute an interesting alternative to Wilson fermions.

3.1.3 Discrete symmetries

For the upcoming numerical analysis the superpotential

$$W(\varphi) = \frac{1}{2}m_0\varphi^2 + \frac{1}{3}g\varphi^3 \quad (3.11)$$

is chosen which coincides with that in earlier simulations of the Wess-Zumino model [53, 63]. The coupling constants m_0 and g are assumed to be real and positive. The superpotential (3.11) allows for discrete symmetries $\mathbb{Z}_2^R \times \mathbb{Z}_2^C$ which act as reflections interchanging the two vacua and as complex conjugations on the complex scalar field,

$$\mathbb{Z}_2^R: \varphi \mapsto -\frac{m_0}{g} - \varphi \quad \text{and} \quad \mathbb{Z}_2^C: \varphi \rightarrow \bar{\varphi}, \quad (3.12)$$

so that also the potential $\frac{1}{2}|W'(\varphi)|^2$ is invariant under both transformations, cf. Fig. 3.1.

²Here only periodic boundary conditions are applied and an odd number of lattice points is used.

	(1) Wilson impr.	(2) Wilson unimpr.	(3) twisted Wilson ^a	(4) SLAC impr.	(5) SLAC unimpr.
lattice derivative	local	local	local	non-local	non-local
lattice artefacts	$\mathcal{O}(a)$	$\mathcal{O}(a)$	$\mathcal{O}(a)^b$	'perfect'	'perfect' ^c
modifications to superpot.	yes	yes	yes	no	no
discrete symmetries	\mathbb{Z}_2^{PC}	$\mathbb{Z}_2^{\text{T}} \times \mathbb{Z}_2^{\text{P}} \times \mathbb{Z}_2^{\text{C}}$	\mathbb{Z}_2^{TR}	$\mathbb{Z}_2^{\text{TPR}} \times \mathbb{Z}_2^{\text{PC}}$	$\mathbb{Z}_2^{\text{T}} \times \mathbb{Z}_2^{\text{P}} \times \mathbb{Z}_2^{\text{R}} \times \mathbb{Z}_2^{\text{C}}$
supersymmetries	one	none	one	one	none

^aOnly improved considered.

^bIn the interacting case the good scaling properties are lost. However the overall size of lattice artefacts is still much smaller when compared to Wilson fermions.

^cThe dispersion relation is up to the cut-off the same as in the continuum.

Table 3.1: Comparison of various lattice models with respect to their symmetries. All statements refer to the interacting theory, i.e. $g \neq 0$. The notion \mathbb{Z}_2^{PC} denotes the combined action of a field and parity transformation as discussed in the text.

From the explicit form of the fermion matrix M and its adjoint M^\dagger ,

$$\begin{aligned} M &= \gamma^\mu \partial_\mu + m_0 + 2g(\varphi_1 + i\gamma_* \varphi_2), \\ M^\dagger &= -\gamma^\mu \partial_\mu + m_0 + 2g(\varphi_1 - i\gamma_* \varphi_2), \end{aligned} \quad (3.13)$$

one finds that

$$\mathbb{Z}_2^{\text{R}}: M \mapsto -\gamma_* M \gamma_*, \quad \mathbb{Z}_2^{\text{C}}: M \mapsto \gamma_* M^\dagger \gamma_*, \quad (3.14)$$

which shows the invariance of the determinant.³

Apart from Lorentz transformation, the continuum model is (irrespective of the concrete form of the superpotential) also invariant under time reversal and parity transformations

$$\mathbb{Z}_2^{\text{T}}: (z, \bar{z}) \mapsto (-\bar{z}, -z), \quad \mathbb{Z}_2^{\text{P}}: (z, \bar{z}) \mapsto (\bar{z}, z). \quad (3.15)$$

Barring possible Wilson terms, the unimproved lattice models obviously inherit all discrete symmetries from the continuum. By contrast, the supersymmetrically improved lattice models are invariant only under a combination of all symmetries. With

$$\mathbb{Z}_2^{\text{R}}: W'_x(\partial\varphi)_x \mapsto -W'_x(\partial\varphi)_x, \quad \mathbb{Z}_2^{\text{C}}: W'_x(\partial\varphi)_x \mapsto \overline{W}'_x(\partial\bar{\varphi})_x. \quad (3.16)$$

for the improved models (with SLAC fermions) the continuum symmetry is reduced,

$$\mathbb{Z}_2^{\text{T}} \times \mathbb{Z}_2^{\text{P}} \times \mathbb{Z}_2^{\text{R}} \times \mathbb{Z}_2^{\text{C}} \longrightarrow \mathbb{Z}_2^{\text{TPR}} \times \mathbb{Z}_2^{\text{PC}} = \text{diag}(\mathbb{Z}_2^{\text{T}} \times \mathbb{Z}_2^{\text{P}} \times \mathbb{Z}_2^{\text{R}}) \times \text{diag}(\mathbb{Z}_2^{\text{P}} \times \mathbb{Z}_2^{\text{C}}). \quad (3.17)$$

Here, the diagonal subgroup $\text{diag}(\mathbb{Z}_2^{\text{P}} \times \mathbb{Z}_2^{\text{C}})$ is a group \mathbb{Z}_2^{PC} generated by the product of the generators of \mathbb{Z}_2^{P} and \mathbb{Z}_2^{C} (analogous notations are used for the other groups). It readily follows that the improvement term must have a vanishing expectation value in the original ensemble without improvement and this has been checked with large numerical precision. For Wilson and twisted Wilson fermions with improvement the right hand side of (3.17) is even further broken down due to the presence of the (twisted) Wilson term in the superpotential. For Wilson fermions, the bosonic action can be read off from (3.6)

³This is true at least up to an irrelevant sign. On the lattice the fermion matrix M always has an even number of rows and columns, hence this phase does not appear.

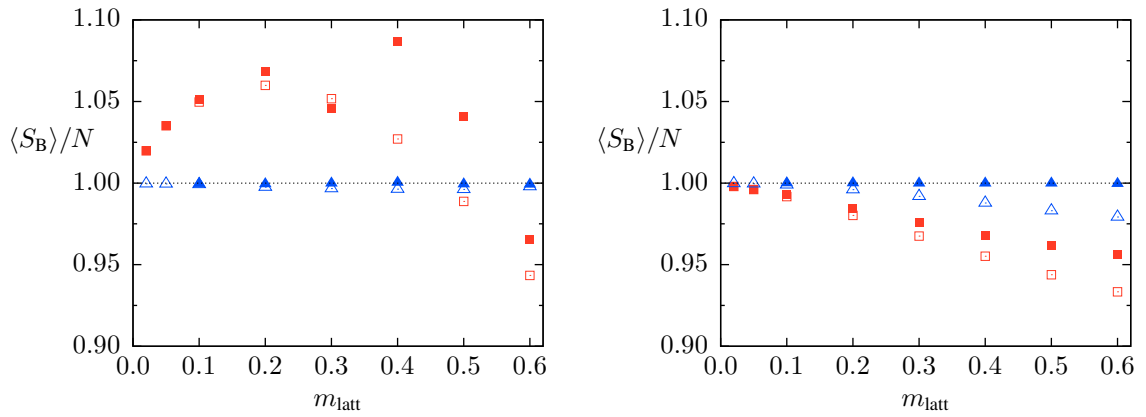


Figure 3.2: Normalised bosonic action as a function of the bare mass lattice parameters using Wilson fermions (left panel, $N = 16 \times 16$) and SLAC fermions (right panel, $N = 15 \times 15$) with the improved (filled symbols) and unimproved (empty symbols) actions from either quenched (red squares) or dynamical fermion (blue triangles) simulations at dimensionless coupling $\lambda = 1$.

and (3.9),

$$S_B = \frac{1}{2} \sum_x \left| (2\bar{\partial}\bar{\varphi})_x + W'_x - \frac{\tau}{2}(\Delta\varphi)_x \right|^2. \quad (3.18)$$

Since Δ_{xy} is invariant under both time reversal and parity, (3.16) cannot be preserved; the Wilson term inevitably changes sign. Conversely, from the bosonic action with twisted Wilson fermions

$$S_B = \frac{1}{2} \sum_x \left| (2\bar{\partial}\bar{\varphi})_x + W'_x + \frac{i\tau}{2}(\Delta\varphi)_x \right|^2. \quad (3.19)$$

only ($\varphi \rightarrow -\frac{m_0}{g} - \bar{\varphi}$, $\partial \rightarrow -\bar{\partial}$) can be shown to yield a symmetry. In either case the breaking of the other symmetries is induced by a higher-dimensional operator and may be expected to be at most $\mathcal{O}(a)$ [63,68]. Nevertheless, at finite lattice spacing, the physics might be affected since the overall size of the breaking terms is a dynamical question. By contrast, SLAC fermions with the larger symmetry (3.16) are again favoured. Tab. 3.1 summarises all discrete symmetries of the lattice models used for simulations.

3.2 Numerical results

For the numerical simulations the hybrid Monte-Carlo algorithm with a stochastic estimation of the fermion determinant using *real* pseudo-fermion fields is used. The algorithmic details and improvements are discussed in Chapter 4.

3.2.1 Dynamical properties of improved lattice actions

Before physical observables are discussed in the next section the first focus lies on the improvement term (3.7) to understand the difference between improved and unimproved lattice models with respect to predictions of supersymmetry. The simplest test is a measurement of the bosonic action itself. With the help of the Nicolai map appearing in (3.3) one can show that

$$\langle S_B \rangle = N. \quad (3.20)$$

Here, $N = N_t \times N_s$ denotes the total number of lattice points, and (3.20) is only expected to hold when fermions are included dynamically. Then, however, this prediction holds irrespectively of the concrete

value of the coupling constants. With a slightly different argument the same was also found in [63]. Eq. (3.20) provides a test observable distinguishing improved from unimproved lattice models as well as quenched from dynamical fermion simulations. To accomplish this, simulations with both (standard) Wilson and SLAC fermions have been performed. The results are shown as a function of the bare lattice mass parameter $m_{\text{latt}} = m_0 a = m_0 L/N_s$. Since the continuum limit for this theory is obtained from $m_{\text{latt}} \rightarrow 0$, smaller values of m_{latt} likewise mean a finer lattice spacing (and for fixed N a smaller space-time volume). The dimensionless coupling strength $\lambda = g/m_0$ was set to $\lambda = 1$. The lattice sizes used for the numerical simulations were $N = 16 \times 16$ for Wilson and $N = 15 \times 15$ for SLAC fermions. For the quenched simulations 500 000 (independent) configurations were evaluated, and 30 000 configurations with dynamical fermions were analysed. The results are shown in Fig. 3.2. One clearly observes that the quenched data significantly deviate from the predicted value which illustrates the necessity of dynamical fermion contributions in order to retain supersymmetry. Using an unimproved action with dynamical fermions much smaller deviations are found which in case of the Wilson fermions are already hard to distinguish from the improved results. For SLAC fermions the deviations are somewhat more systematic and remain also clearly distinguishable from other dynamical fermion simulations. A second difference between Wilson and SLAC fermions may be inferred from Fig. 3.3. Namely, there is a distinct correlation between the ground state around which the field φ_1 fluctuates on the one hand and size and variance of the improvement term on the other hand. This may be taken as direct manifestation of the additionally broken $\mathbb{Z}_2^{\text{TPR}}$ -symmetry due to the Wilson term which will also play a role when discussing the failure of improvement in the next paragraphs.

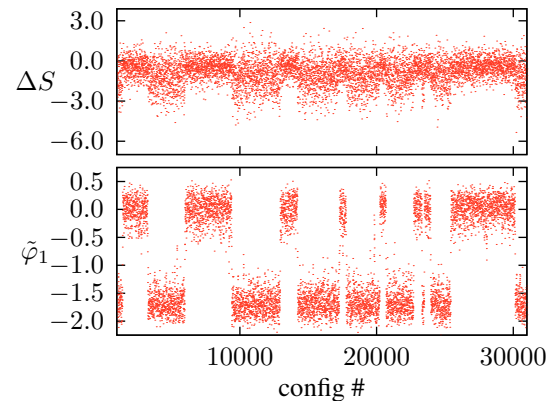


Figure 3.3: Monte-Carlo history of the lattice mean $\tilde{\varphi}_1 = N^{-1} \sum_x \varphi_{1,x}$ and size of the improvement term for Wilson fermions ($N = 16 \times 16$, $\lambda = 0.6$, $m_{\text{latt}} = 0.3$).

Limitations of improved lattice actions

By studying the improvement term ΔS for models with either Wilson or SLAC fermions it is observed that the system is ultimately pushed into an unphysical region of configuration space, at least for strong couplings. The simulations have revealed that this instability is controlled by the actual size of the bare mass parameter and the coupling strength λ . Simulations tend to fail more often as either of them grows. The study of this phenomenon with Wilson fermions turns out to be clumsy since there is no clear correlation between the value of the coupling and the number of configurations where the instability occurs. For that reason the analysis based on SLAC fermions is presented. However, it should be emphasised again that for either Wilson or twisted Wilson fermions the qualitative picture is the same as described below.

It is to be expected that the improvement term grows with the coupling strength λ and vanishes continuously in the continuum limit (at $m_{\text{latt}} = 0$). This has been checked numerically and a good scaling behaviour with respect to the lattice size is observed (see Fig. 3.4). For all couplings λ and m_{latt} the improvement term is found to be smaller than 14% of the total bosonic action. Depending on the coupling strength λ , this ratio is reached sooner or later. Actually, this represents a threshold above which the

simulation fails. The situation is depicted in Fig. 3.5. At some instant, the improvement term blows up and settles again at a value about 40 times the size of the bosonic action. At the same time also the fermion determinant grows drastically and so hinders the system from returning into the original (and desired) region of configuration space. A reason for this instability may be found by reconsidering the improved action

$$S_B = \frac{1}{2} \sum_x \left| 2(\partial\varphi)_x + \overline{W}_x \right|^2. \quad (3.21)$$

In this form the action allows for two distinct behaviours of the fluctuating fields. The physically expected behaviour consists of small fluctuations around the classical minima of the potential. Alternatively, (3.21) allows for large fluctuations of φ to be compensated by large values of \overline{W}_x . The latter would be dominated by UV contributions, and this is actually observed, cf. Fig. 3.6. In this situation, it is definitely no longer possible to extract meaningful physics. Another view on this “broken phase” is again taken in Fig. 3.5. While the ensemble with $\lambda = 1.4$ exhibits the expected behaviour at the only slightly larger value of $\lambda = 1.7$ the simulation breaks down after about 5 000 configurations and for $\lambda = 1.9$ the simulation instantly slides into the broken phase.

This seems not to be directly related to the violation of reflection positivity by the improvement term. Namely, as a counterexample without improvement term, which also violates reflection positivity and does not display such a broken phase, one might consider a free model with SLAC fermions (with the typical oscillatory behaviour of two-point functions in theories violating reflection positivity [41]).

To sum up, it has been observed that the improved lattice models may become unstable at any finite m_{latt} and hence any finite lattice spacing. If and when this happens depends on several factors. Wilson fermions are affected in a stronger way while SLAC fermions remain stable for a much wider range of coupling constants. Apart from that, one should ensure by monitoring the improvement term or any other observable discussed above explicitly that a simulation is not subject to this phenomenon. Pro-

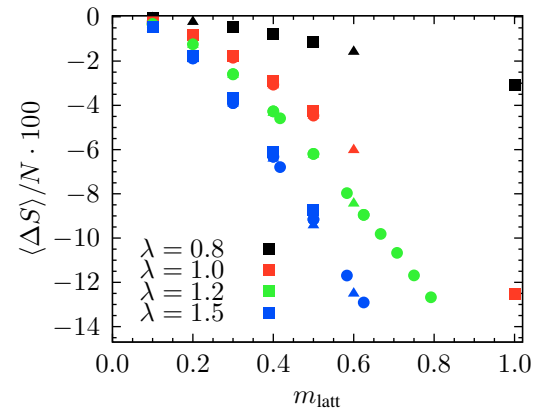


Figure 3.4: Reduced improvement term $\Delta S/N$ for different lattice sizes: 9×9 (squares), 15×15 (triangles) and 25×25 (circles).

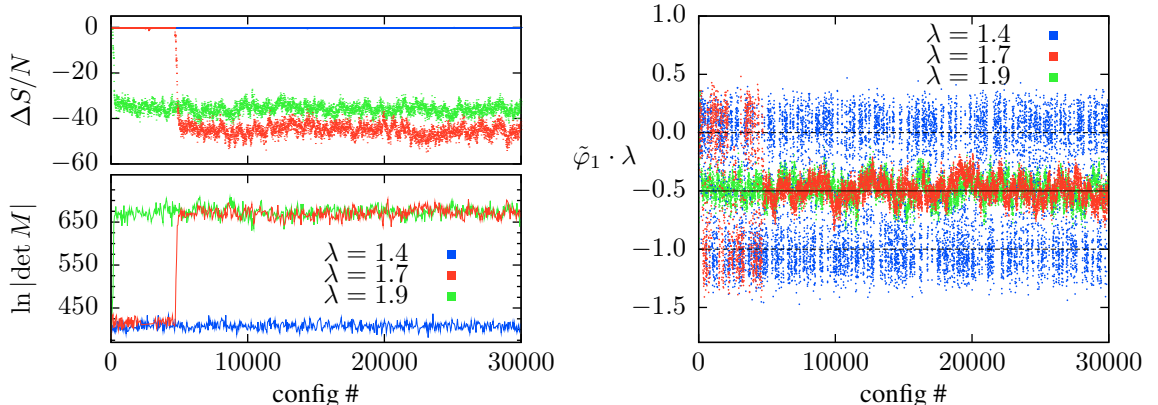


Figure 3.5: Monte-Carlo history of improvement term and fermion determinant (left panel) and normalised lattice mean $\tilde{\varphi}_1 \cdot \lambda$ (right panel) for the improved model with SLAC fermions ($N = 15 \times 15$, $m_{\text{latt}} = 0.6$).

vided that one is confined to lattices smaller than 64×64 but demands the absence of finite size effects, improved lattice models with Wilson fermions can be used for the continuum extrapolation of masses only up to $\lambda < 0.4$. SLAC fermions can be used in the greater range of $\lambda < 1.5$; the corresponding results will be presented further below.

3.2.2 Setting the stage

In Monte-Carlo simulations, importance sampling is only meaningful with respect to a positive measure. Including dynamical fermions the measure is $\det M \exp(-S_B)$. While the exponential factor is strictly positive (S_B is real), the positivity of the determinant cannot be guaranteed for an interacting theory and a possibly emerging sign problem has to be addressed similar to the situation in Sec. 2.2.1. In order to make sensible comparisons with continuum cal-

culations (which are most conveniently performed in an infinite spacetime) it must be ensured that physical observables are free of finite size effects. In order to check this, all simulations in this section are repeated for different physical volumes $m_0 L$ on square lattices with $N = N_t \times N_s$ lattice points.

Negative fermion determinants

The Nicolai map in a supersymmetric theory is a change of bosonic variables which renders the bosonic part of the action Gaussian; at the same time, the Jacobian of this change of variables has to cancel the fermion determinant. For the present model this means

$$\det M = \det \left(\frac{\delta}{\delta \varphi} (2(\bar{\partial} \bar{\varphi}) + W') \right). \quad (3.22)$$

In this light, an indefinite fermion determinant obviously corresponds to a non-invertible change of variables in the continuum,

$$\varphi \mapsto \xi = 2\bar{\partial} \bar{\varphi} + W'. \quad (3.23)$$

This map is globally invertible iff the superpotential is of degree 1 (the Nicolai map in this case has winding number 1), i.e., for the free theory [69]. For the choice $W'(\varphi) = m_0 \varphi + g \varphi^2$ the map is *not globally* invertible, and there exists at least one point where $\det M$ vanishes iff $g \neq 0$. By this line of argument (for the continuum formulation of the model) negative determinants cannot be ruled out.

One way to cope with this in practical simulations is to use $|\det M| \exp(-S_B)$ for the generation of configurations instead and to reweight with the sign afterwards. Unfortunately, calculating the sign of $\det M$ is as costly as the computation of the whole determinant. Hence, this method becomes unfeasible for large lattices. A way out is to avoid reweighting within certain bounds for the parameters in which the ensuing systematic errors are negligible. Thus an estimate of the frequency of occurrence of negative determinants as a function of the parameters is necessary. To obtain more reliable results this subject is studied with a naive inversion algorithm which computes the determinant from a LU decomposition and takes its contributions exactly into account. This is numerically much more involved

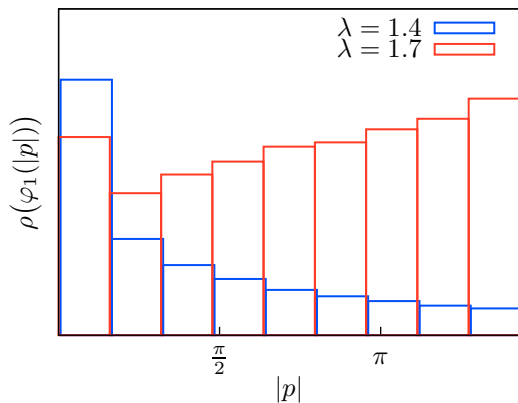


Figure 3.6: Mode analysis of ensembles in the physical ($\lambda = 1.4$) and unphysical ($\lambda = 1.7$) phase. Here ρ is the distribution function for the modulus of the lattice momentum averaged over 25 000 configurations (SLAC improved, $N = 15 \times 15$, $m_{latt} = 0.6$).

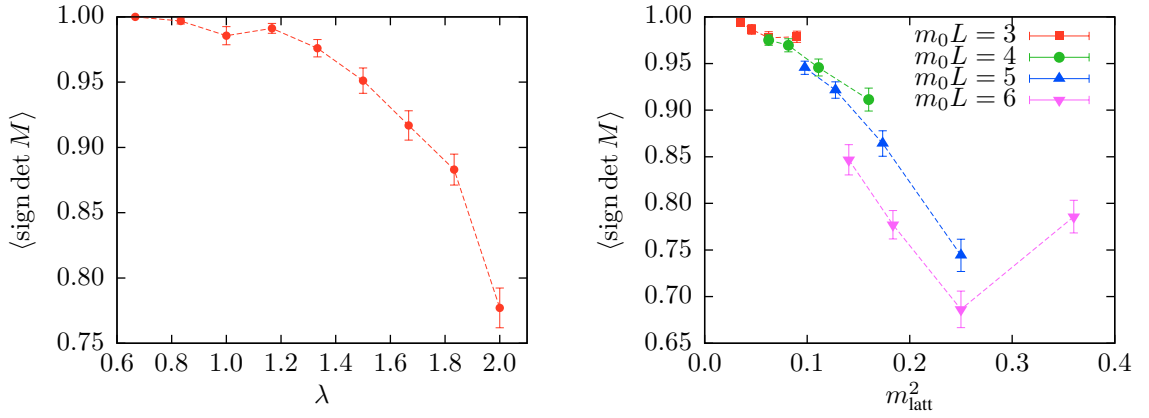


Figure 3.7: Average sign of the determinant for the unimproved model with Wilson fermions for fixed lattice spacing and volume (left panel, $N = 14 \times 14$, $m_0L = 6$) and for fixed coupling (right panel, $\lambda = 2.0$).

than the standard pseudo-fermion algorithm, thus, this method is only applicable to small lattice sizes with up to 16×16 lattice sites. For fixed scale m_0a or m_0L it can be gleaned from Fig. 3.7 (left panel) that configurations with a negative sign of the determinant show up only for $\lambda \geq 1.0$. Furthermore, in order to understand the dependence on the lattice size and the lattice spacing the coupling is fixed to $\lambda = 2.0$ and simulations on different physical volumes m_0L and lattice spacings m_{latt} are performed. The results displayed in Fig. 3.7 (right panel) clearly show that the problem dissolves in the continuum limit but becomes worse at every finite lattice spacing when the physical volume is increased. For both figures, for each data point about 50 000 configurations were evaluated. Eventually, to estimate the impact on actual measurements the bosonic action has been measured with $m_0L = 5$, $\lambda = 2$ on a 12×12 lattice with about 7% of configurations with a negative sign for the fermion determinant. The expectation values considered here are $\langle S_B \rangle_{\text{non-reweighted}} = 149.94(12)$ and $\langle S_B \rangle_{\text{reweighted}} = 149.49(10)$. Hence even at large coupling (far larger than what is targeted at in the next section) effects may be assumed to be at most of marginal relevance for actual measurements.

Finite size effects

For the present model the bare lattice mass m_{latt} also sets the scale of the overall spacetime volume. As with all lattice simulations a balance between finite size and discretisation errors must be achieved. If the lattice spacing is chosen too large, lattice artefacts may grow; on the other hand if, say, the Compton wavelength of a particle is larger than the spacetime volume the extraction of masses will eventually suffer from finite size effects. One way to test for the presence of such finite size violations is to study the model at different spacetime volumes. Comparing the fermion species introduced earlier Wilson fermions may be expected to be most affected. Here, lattice artefacts further increase the correlation lengths so that measurements are much more sensitive to the finite box size. The setup for this analysis is as follows. At first the improved lattice model is simulated using Wilson fermions at fixed coupling parameters $m_0L = 15$ and $\lambda = 0.3$ for five different lattices with $N_t = N_s \in \{20, 24, 32, 48, 64\}$ lattice points in each direction ($N = N_t \times N_s$). Then it is *assumed* that with this choice of coupling constants the spacetime volume is large enough to allow for a sufficiently good identification with the thermodynamic limit. The masses obtained from these simulations were extrapolated to the continuum as described in Sec. 3.2.4. This is also shown in Fig. 3.8 where the resulting fit (and its uncertainty) is depicted with a gray shaded area. The next step is to decrease the volume using $m_0L \in \{9, 7, 5, 3\}$.

As long as no finite size effects are visible the masses extracted at these smaller and smaller volumes are expected to lie on top of the fit from the original lattice. Down to a volume of $m_0L = 7$ this scaling may be easily inferred from Fig. 3.8 which justifies a posteriori the correctness of the earlier assumption.

However, since by perturbation theory the physical masses decrease for growing coupling (see next section), growing Compton wavelengths are expected and simulations are performed on a reference volume $m_0L = 15$ for most of the further measurements to exclude finite size effects.

3.2.3 Determination of masses from correlators

One important observable of a quantum field theory is the energy gap between the ground state and the first excited state. This energy gap corresponds to the mass of the lightest particle in the spectrum. As this chapter aims a high precision measurements, the determination of masses is explained in detail.

To obtain the masses in the Wess-Zumino model one has to consider the propagators of fermions and bosons. At vanishing spatial momentum $p_1 = 0$, the free bosonic continuum propagator in momentum space reads

$$G_B(p) = \frac{1}{m_0^2 + p_0^2}. \quad (3.24)$$

The real and imaginary parts φ_1 and φ_2 of φ decouple (the propagator is diagonal and even equal for φ_1, φ_2). The Fourier transform of $G_B(p)$ shows the well known exponential decay

$$C_B(t) \propto \exp(-m_0 |t|), \quad (3.25)$$

where m_0 is the above mentioned mass of the lightest particle.⁴ In the interacting case this quantity can be obtained on the lattice by measuring the two-point function. The projection onto $p_1 = 0$ can be achieved by averaging over the spatial lattice sites,

$$C_{B,\alpha\beta}(t) = \frac{1}{N_s} \sum_x \langle \varphi_\alpha(0,0) \varphi_\beta(t,x) \rangle, \quad (3.26)$$

with α, β labelling components of the bosonic field.

The free fermionic continuum correlator for $p_1 = 0$ is

$$\langle \psi_\alpha \bar{\psi}_\beta \rangle = G_{F,\alpha\beta}(p_0) = \frac{m_0 - i\gamma_{\alpha\beta}^0 p_0}{m_0^2 + p_0^2}. \quad (3.27)$$

Using the representation of the γ matrices as described after (3.4) one can read off a direct connection

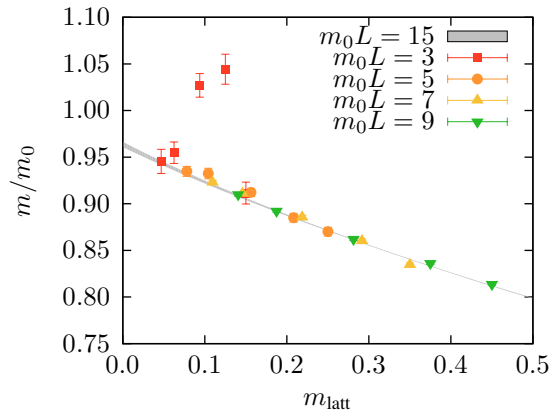


Figure 3.8: Lattice masses for $\lambda = 0.3$ on box sizes $m_0L \in \{3, 5, 7, 9\}$. Systematic deviations from the $m_0L = 15$ reference result are visible below $m_0L \approx 7$.

⁴The space coordinates corresponding to p_1 and p_0 are called x and t , respectively. $\hat{t} = t/a$ gives the temporal coordinate in lattice units.

with the bosonic correlator using

$$G_F(p_0) = G_{F,11}(p_0) + G_{F,22}(p_0) = \frac{2m_0}{m_0^2 + p_0^2}. \quad (3.28)$$

As in the bosonic case on the lattice a summation over the spatial lattice sites yields the projection onto $p_1 = 0$. $C_F(t)$ defines the Fourier transform of this object.

Fermionic masses

The fermionic correlator $C_{F,\alpha\beta}$ is given by $\langle \psi_\alpha \bar{\psi}_\beta \rangle = \langle M_{\alpha\beta}^{-1}[\varphi_1, \varphi_2] \rangle$, where M is the fermion matrix. The calculation of this quantity requires a high numerical effort for the inversion of large matrices. Fortunately in the weak-coupling limit the fermion matrix is approximately the same as that of the free theory and the statistical fluctuations are rather small. Therefore the necessary statistics to read off a reasonable fermionic correlator is much smaller than for bosons.

After the fermionic correlator in position space is computed the masses can be determined from its long range behaviour. Inspired by the continuum connection between fermionic and bosonic correlators, (3.28), and the behaviour at large distances, (3.25), one can consider

$$m_{\text{eff}}a = \ln \left(\frac{C_F(\hat{t})}{C_F(\hat{t} + 1)} \right) \quad (3.29)$$

with \hat{t} in a region between zero and $N_t/2$. The mass can then be determined from the average of m_{eff} .

A more elaborate way is a least square fit of the fermionic correlator $C^{\text{fermion}}(t)$ with the function

$$f_{A,m_F}(t) = A \cdot \cosh(m_F a(\hat{t} - N_t/2)) \quad (3.30)$$

One better not take the full range of t into account for this fit because it is valid only for large distances (from both boundaries of the lattice). One should therefore constrain \hat{t} to be in $\{1 + t_{\text{skip}}, \dots, N_t - 1 - t_{\text{skip}}\}$. The choice of t_{skip} is determined by the fringe of the plateau in a plot of the fitting result vs. t_{skip} .

The differences of the different methods to determine the masses are illustrated in Fig. 3.9. One clearly observes that the effective masses determined according to (3.29) do not show a plateau from which the mass can be read off. By contrast, the masses obtained from a cosh fit clearly show this behaviour at large t_{skip} . As mentioned above, the effective mass of the bosonic correlator is subject to much larger statistical errors.

Bosonic masses

In order to calculate the bosonic correlators for the determination of the masses the connected two-point function is considered. At large distances, where the masses can be extracted, the relative statistical error of the correlator grows exponentially. Therefore, one must achieve a balance between this statistical error and the systematic errors due to the evaluation at small distances.

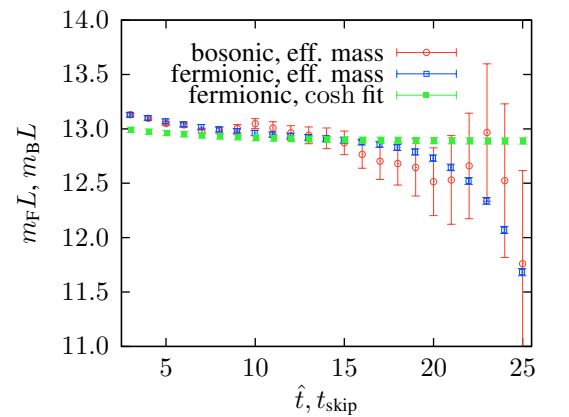


Figure 3.9: Bosonic and fermionic masses obtained via a cosh fit (3.30) and the effective mass definition (3.29) for the improved Wilson model ($\lambda = 0.4$, $N = 64 \times 64$). The fermionic masses with a statistics of about 5000 independent configurations are much sharper and more reliable than the bosonic ones from about 10^6 independent configurations.

$\ln(C_B(t))$ was fitted against the function $A + \ln(\cosh(m_B a(\hat{t} - N_t/2)))$ to determine A and the mass m_B . In order to exclude the points with the largest statistical and systematic errors from this fit, only the points in the interval $([t_{\text{skip}}, t_{\text{st}}] \cup [N_t - t_{\text{st}}, N_t - t_{\text{skip}}])$ have been taken into account. As a tradeoff between statistical noise and the effects of higher excited states $t_{\text{skip}} = \lceil 0.2N_t \rceil$ and $t_{\text{st}} = \lfloor 0.4N_t \rfloor$ was used.

If the SLAC derivative is used an oscillatory behaviour of m_B as a function of t_{skip} can be observed. In the bosonic case it is slightly smaller than the statistical error. Therefore, it is sufficient to measure a ‘‘smeared’’ mass, $m_{\text{SLAC}} = 0.5m_B(t_{\text{skip}}, t_{\text{st}}) + 0.25m_B(t_{\text{skip}} + 1, t_{\text{st}}) + 0.25m_B(t_{\text{skip}} - 1, t_{\text{st}})$, where the error of the oscillations is negligible as compared to the statistical one.

3.2.4 Continuum extrapolation

For the continuum extrapolation the focus lies on the fermionic masses because of their much smaller statistical error in the perturbative regime. The explicit extrapolation procedure is guided by analytic results and observations for the free theory. The three different discretisations investigated in this chapter require different strategies for this procedure.

Wilson derivative

Compared with the continuum formula, (3.28), the free momentum space correlation function for the Wilson derivative gets a momentum dependent mass,

$$G_F(p_0) = \frac{m_{\text{latt}} + 1 - \cos(p_0 a)}{\sin^2(p_0 a) + (m_{\text{latt}} + 1 - \cos(p_0 a))^2}. \quad (3.31)$$

The pole of this correlator coincides with the above mentioned cosh fit within the error bars.

To extrapolate the continuum limit an expansion in powers of the lattice spacing is used. Exact results for the free theory were derived to check this extrapolation. In this case an expansion up to a linear order in a is not enough to obtain the known result within the high precision of the numerical measurements at weak coupling. Therefore the first correction to this expansion is naively of quadratic order and yields a better result; but still the error is too large for high precision measurements.

The functional behaviour of the masses m_F , obtained by the fit as a function of the lattice spacing is well *approximated* by

$$m_F(a) \approx m_{\text{cont}} + A \cdot a + B \cdot a^{\frac{3}{2}} \quad (3.32)$$

for all $a/L \in [0, 0.05]$ at lattice volume $m_0 L = 15$. The deviation from this behaviour is negligible with respect to the statistical errors in the weak coupling case. In addition the expected continuum result is achieved with the necessary precision. Motivated by these results this formula is also used in the interacting case.

Twisted Wilson derivative

A Wilson parameter of $r = \sqrt{\frac{4}{3}}$ for the twisted Wilson fermions in the free theory leads to discretisation errors of $\mathcal{O}(a^4)$ as discussed in [41]. For the weakly coupled regime ($\lambda \leq 0.3$) these errors are expected to dominate the lattice artefacts. Nevertheless for an intermediate coupling corrections of $\mathcal{O}(a)$ arise. Taking this into account the masses are extrapolated to the continuum assuming a functional behaviour of

$$m_F(a) = m_{\text{cont}} + A \cdot a + B \cdot a^4. \quad (3.33)$$

For $\lambda > 0.3$ the $\mathcal{O}(a)$ terms dominate. Therefore a linear extrapolation is sufficient.

SLAC derivative

It has become apparent in previous investigations [41] and in Chapter 2 that the SLAC derivative shows an almost perfect behaviour. That means the extrapolated masses coincide with their continuum counterparts already at finite lattice spacings. On the other hand an oscillatory behaviour of the correlation function is observed. This was shown to be connected with the exact reproduction of the continuum dispersion relation by the SLAC derivative. To handle this problem the free theory is studied first. As in the bosonic case the plot of $m_{\text{F}}L$ versus t_{skip} does not show a clear plateau but rather oscillates around the expected continuum value, cf. Fig. 3.10.

Guided by these observation of the free theory a suitable averaging can lead to the extraction of the correct continuum results at finite lattice spacing. Starting with the ansatz

$$m_{\text{F}}(N_s, \mathbf{c}) = c_0 m_{\text{F}}(t_{\text{skip}}) + c_1 m_{\text{F}}(t_{\text{skip}} - 1) + c_2 m_{\text{F}}(t_{\text{skip}} - 2). \quad (3.34)$$

the difference to the known continuum result of the free theory

$$\Delta(N_s, \mathbf{c}) = |m_{\text{F}}(N_s, \mathbf{c}) - m_{\text{cont}}| \quad (3.35)$$

is minimised for lattice sizes of $N_s = N_t \in \{35, 37, \dots, 75\}$ and $t_{\text{skip}} = \lfloor 0.4N_s \rfloor$. A least square fit yields

$$c_0 = 0.11791, \quad c_1 = 0.47877, \quad c_2 = 0.40332, \quad (3.36)$$

leading to $\max \Delta(N_s, \mathbf{c}) = 5.282 \times 10^{-4}$. A smaller t_{skip} does not change this result considerably. Using this approximation scheme the systematic error based on the oscillatory behaviour of the SLAC derivative can be neglected compared to the statistical errors at least for the weak coupling case.

3.2.5 Weak coupling

The main observable for comparing lattice results with continuum physics is the mass of the lightest excited state, i.e. the energy gap. Since unbroken supersymmetry in the continuum predicts that bosonic and fermionic masses coincide it also provides a possibility to check the supersymmetric properties of the lattice prescription. The corresponding values can be extrapolated from the lattice masses in the continuum limit. In the weak coupling regime it will be possible to match these results to predictions of perturbation theory. This provides an important test for the numerical results and ensures that also the results at intermediate coupling are reliable.

The reference value is given by a one-loop calculation of the renormalised (physical) mass

$$m_{\text{ren}}^2 = m_0^2 \left(1 - \frac{4\lambda^2}{3\sqrt{3}} \right) + \mathcal{O}(\lambda^4) \quad (3.37)$$

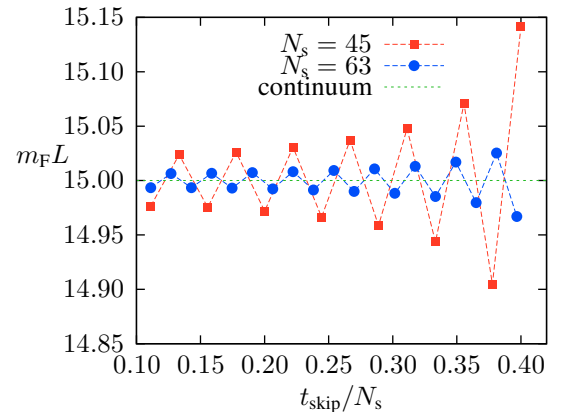


Figure 3.10: Masses obtained via a cosh-fit for the free theory using the SLAC derivative with $m_0L = 15$. At larger lattices the oscillation amplitude around the continuum value gets smaller.

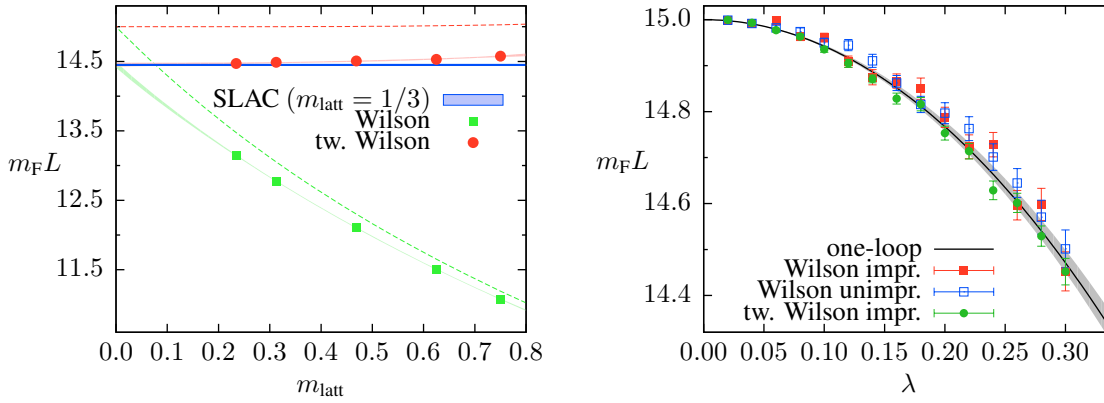


Figure 3.11: *Left panel:* The continuum extrapolation of masses for $\lambda = 0.3$, $m_0 L = 15$ for the improved Wilson and twisted Wilson model. The SLAC result is given for one single lattice spacing $m_{\text{latt}} = 1/3$. For comparison the exact results for the free theory are also shown. *Right panel:* Continuum masses for the weakly coupled regime in comparison to the perturbative result. The shaded area corresponds to the extrapolation provided by the continuum results according to (3.38) with $m_0 L = 15$ and $b = 1.35(13)$.

in the continuum valid for $\lambda \ll 1$ with the bare mass m_0 as used in Eq. (3.11). To obtain this result one first must calculate contributions of the loop diagrams to the propagator. An expansion in λ then yields the above result.

As has been shown above the fermionic masses have lower statistical errors than the bosonic ones. Therefore only the extrapolations for fermionic masses are compared to the perturbative results. This procedure gets justified by the fact that bosonic and fermionic masses coincide even on a finite lattice for the weak coupling regime as described below. If not otherwise stated $m_0 L = 15$ is used in the following.

Continuum limit

The methods to extrapolate to the continuum given in the previous section are based on the free theory with $\lambda = 0$. Since the interest lies in the interacting case it must be made sure that the continuum extrapolation of masses remains stable even for $\lambda = 0.3$.

For that purpose the masses in the improved model with standard Wilson and twisted Wilson fermions at $\lambda = 0.3$ at different lattice spacings a/L are considered. In the perturbative coupling regime square lattices of sizes $N_t = N_s \in \{20, 24, 32, 48, 64\}$ are used. These correspond to lattice spacings of about $a/L \in [0.015625, 0.05]$. A statistics of 10 000 independent configurations is used to extrapolate to the continuum limit.

Using these masses $m_F(a)$ at finite lattice spacing the extrapolation is shown in Fig. 3.11 (left panel). For comparison also the mass for SLAC fermions at a finite lattice size $N_t = N_s = 45$ (corresponding to $m_{\text{latt}} = 1/3$) is marked. All these results indicate that even at $\lambda = 0.3$ the continuum extrapolated masses coincide within error bounds. Even better, the masses of SLAC fermions at finite lattice spacing cannot be distinguished from the continuum result.

Comparison with perturbation theory

As described above the masses for Wilson (improved and unimproved) and twisted Wilson (improved) fermions for $\lambda \in [0, 0.3]$ are extrapolated to the continuum values, cf. Fig. 3.11 (right panel) and Tab. 3.2. The masses coincide within error bars although the twisted Wilson masses are systematically

smaller. This difference has to be interpreted as a systematic error in the continuum extrapolation for the masses but its effect is almost overshadowed by the statistical errors. However this result indicates that for a reliable extrapolation at larger statistics finer lattices can be necessary to yield a better continuum limit.

As a further test these results are used to reproduce the perturbative formula

$$m_F(\lambda)L \approx m_0L \sqrt{1 - \frac{\lambda^2}{b}}. \quad (3.38)$$

Taken this functional form for granted, the parameters m_0L and b can be extracted from a least-square fit to the given data. For this fit the knowledge about the free theory ($m_0L = 15$) as a fixed input may be used or, alternatively, one allows for both m_0L and b as free parameters. The corresponding results are given in Tab. 3.3.

The extrapolated results for m_0L confirm that the extrapolation to the free theory works reliably and that meaningful results for b are expected. Furthermore the results obtained for improved and unimproved Wilson fermions coincide very well and therefore both provide the correct continuum limit.

Additionally the results for standard Wilson and twisted Wilson fermions lead to compatible results when taking systematic uncertainties of the continuum extrapolation into account.

As an important result of these observations, all three models considered in the weak coupling case tend towards the same continuum limit for $\lambda > 0$. The perturbative results can be recovered where the largest error bars (including possible systematic errors) yield $b = 1.35(13)$ in agreement with the one-loop result of $b_{\text{one-loop}} \approx 1.2990$.

Signs of supersymmetry at finite lattice spacing

Apart from all results solely based on fermions the primary focus lies on the restoration of supersymmetry on

the lattice. For this reason it is necessary to check the demand from supersymmetry that the masses of bosonic and fermionic superpartners match. This is checked by computing bosonic and fermionic masses at couplings $\lambda = 0.2$ and $\lambda = 0.4$ with $m_0L = 15$ for all the models on different lattice sizes.

As visible in the whole weak coupling regime the fermionic masses do not suffer from statistical noise. This behaviour derives from the fact that the fermionic correlator for the free theory ($\lambda = 0$) is independent of the bosonic field φ and is obtained by a pure matrix inversion. At small (and finite) λ , corrections to the free propagator are of $\mathcal{O}(\lambda^2)$, and the fluctuations of φ during the simulation are

λ	Wilson unimpr.	Wilson impr.	tw. Wilson
0.02	14.999(2)	14.997(2)	14.999(1)
0.04	14.992(4)	14.993(4)	14.993(3)
0.06	14.982(6)	14.999(7)	14.977(4)
0.08	14.974(8)	14.963(8)	14.963(5)
0.10	14.95(1)	14.96(1)	14.935(6)
0.12	14.94(1)	14.91(1)	14.905(9)
0.14	14.91(1)	14.87(2)	14.871(9)
0.16	14.86(2)	14.87(2)	14.83(1)
0.18	14.82(2)	14.85(2)	14.82(1)
0.20	14.80(2)	14.79(2)	14.75(2)
0.22	14.76(3)	14.72(3)	14.71(2)
0.24	14.70(3)	14.73(3)	14.63(2)
0.26	14.64(3)	14.60(3)	14.60(2)
0.28	14.57(4)	14.60(4)	14.53(2)
0.30	14.50(4)	14.45(4)	14.45(3)

Table 3.2: Continuum extrapolations of fermionic masses m_FL for Wilson and twisted Wilson fermions in the weak coupling regime ($m_0L = 15$).

derivative	b	m_0L
Wilson improved	1.34(6)	15.007(6)
Wilson unimproved	1.39(7)	15.008(6)
twisted Wilson improved	1.26(4)	14.996(4)
Wilson improved	1.37(5)	fixed to 15
Wilson unimproved	1.42(6)	fixed to 15
twisted Wilson improved	1.25(3)	fixed to 15

Table 3.3: Fit for the perturbative mass formula with $\mathcal{O}(\lambda^2)$ corrections to be compared with the one-loop results. For comparison the one-loop result is $b \approx 1.2990$.

suppressed with λ^2 ; a statistics of only 10^4 is needed to obtain reliable results.

On the other hand the bosonic correlator even for the free theory is given by the correlations of the fluctuating field φ . Therefore a much higher statistics is necessary to sample the bosonic two-point function. Here, problems arise by the exponentially growing relative error of the two-point function $C_B(t)$ with respect to t .

Only with the use of an algorithm combining Fourier acceleration with higher order integrators as described in Chapter 4 it was possible to simulate 10^6 to 10^7 configurations for each parameter set $(m_{\text{latt}}, \lambda)$ with an autocorrelation time of the two-point function of $\tau \leq 2$.

The results of these numerical efforts are summarised in Tab. 3.4. They show that independently of the model even for $\lambda \in \{0.2, 0.4\}$ bosonic and fermionic masses correspond to each other and lattice-induced supersymmetry breaking cannot be observed.

Finally in Fig. 3.12 the derived bosonic and fermionic masses are shown for the improved (and unimproved) model with Wilson fermions. Even these high statistics do not allow for a clear cut distinction between the extrapolated continuum masses of bosons and fermions for the improved and the unimproved models. This proves that even at $\lambda = 0.4$ the improvement is not necessary even on a finite lattice. Each model tends towards the supersymmetric continuum limit.

model	N_s	λ	$m_F L$	$m_{B,1} L$	$m_{B,2} L$
Wilson	24	0.2	11.592(2)	11.53(4)	11.59(4)
impr.	24	0.4	11.375(4)	11.39(3)	11.34(3)
	32	0.2	12.224(2)	12.20(3)	12.15(4)
	32	0.4	11.945(5)	11.95(3)	11.88(4)
	48	0.2	12.941(5)	12.87(5)	13.02(5)
	48	0.4	12.548(13)	12.47(4)	12.53(4)
	64	0.2	13.349(10)	13.45(9)	13.32(9)
	64	0.4	12.89(3)	12.73(9)	12.83(9)
Wilson	24	0.2	11.591(2)	11.58(2)	11.63(3)
unimpr.	24	0.4	11.400(4)	11.44(2)	11.39(3)
	32	0.2	12.221(2)	12.20(3)	12.15(4)
	32	0.4	11.965(5)	11.97(3)	11.87(4)
	48	0.2	12.942(5)	12.92(6)	13.00(7)
	48	0.4	12.572(14)	12.54(4)	12.49(4)
	64	0.2	13.347(7)	13.45(9)	13.32(9)
	64	0.4	12.91(2)	12.82(9)	12.79(9)
tw. Wilson	24	0.2	14.811(7)	14.94(11)	14.91(12)
(impr.)	24	0.4	14.13(1)	14.21(9)	14.06(8)
	32	0.2	14.788(6)	14.61(14)	14.94(12)
	32	0.4	14.08(1)	14.39(14)	13.68(13)
	48	0.2	14.789(6)	14.74(11)	14.61(11)
	48	0.4	14.04(1)	14.16(16)	13.98(15)
SLAC	45	0.2	14.768(4)	14.87(10)	14.83(9)
impr.	45	0.4	13.997(13)	14.08(11)	13.92(10)
SLAC	45	0.2	14.769(4)	14.75(6)	14.57(6)
unimpr.	45	0.4	14.047(16)	13.74(8)	13.75(7)

Table 3.4: For different models and lattice sizes bosonic and fermionic masses are computed with bare mass $m_0 L = 15$.

3.2.6 Intermediate coupling results

Earlier attempts to go beyond the perturbative regime could not reliably determine the mass spectrum. Namely, this was hindered by instabilities introduced by improvement terms. For Wilson fermions, this renders simulations at intermediate couplings invalid. Therefore the analysis of coupling constants in the intermediate regime ($0.3 < \lambda \leq 1.1$) is based on actions with twisted Wilson and SLAC fermions (which anyhow yield better results at finite lattice spacing). For twisted Wilson fermions simulations with the improved action have run on lattices with $N_s \in \{32, 40, 48, 56, 64\}$ lattice points in the spatial direction. For the temporal direction $1.25 \cdot N_s$ lattice points were used in order to be able to assess whether contributions from higher excited states are really absent. At the chosen

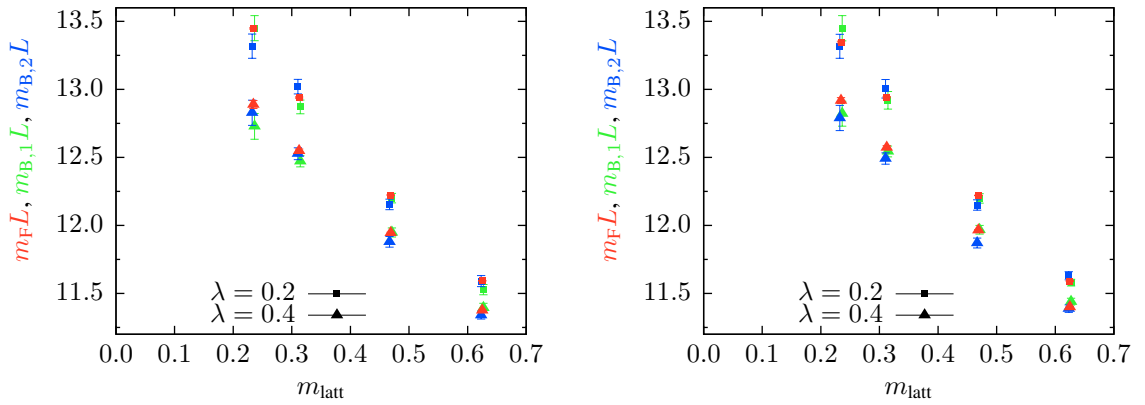


Figure 3.12: Bosonic and fermionic masses for the weakly coupled regime for the improved (left panel) and unimproved (right panel) Wilson model.

value of $m_0 L = 15$ almost every simulation, the respective bare lattice mass parameter m_{latt} confines the attainable coupling strengths to $\lambda \leq 0.7$ for twisted Wilson fermions.⁵ For even larger coupling strengths λ only SLAC fermions have been found to yield sensible results. In the simulations this species is used for both the improved and unimproved lattice models on a fixed lattice size of $N = 45 \times 45$. Apart from that, one further run was done on a 63×63 lattice with $\lambda = 0.8$. Square lattices turned out to be more convenient with SLAC fermions and to be sufficient to clearly read off (within statistical errors) the masses. As for the simulations with twisted Wilson fermions only the masses from the fermionic correlators are determined since with the statistics (50 000 trajectories) achieved so far the bosonic correlators are far too noisy to yield reliable results.

The results may be found in Tab. 3.5 and are depicted graphically in Fig. 3.13. From the comparison with perturbation theory first deviations are seen as soon as $\lambda \geq 0.4$ where the (extrapolated) lattice results are slightly stronger curved. Also clear deviations between the improved and unimproved model using SLAC fermions become apparent for $\lambda \geq 0.6$. It is worthwhile to note that the result from the improved lattice model is closer to the continuum limit which may be inferred from Tab. 3.6. While the lattice data from the improved model almost coincide for both lattice spacings the data from the unimproved model is likely to approach the same value if increasingly finer grained lattices are used.

λ	tw. Wilson	SLAC unimpr.	SLAC impr.
0.20	0.987(2)	0.985(3)	0.985(3)
0.35	0.949(2)		
0.40	0.933(2)	0.937(2)	0.933(1)
0.45	0.908(3)		
0.50	0.887(4)		
0.55	0.853(8)		
0.60	0.813(8)	0.854(3)	0.829(4)
0.65	0.79(1)		
0.70	0.69(3)		
0.80		0.766(6)	0.68(2)
1.00		0.643(5)	0.512(5)
1.10			0.46(2)

Table 3.5: Fermionic masses m_F/m_0 for the intermediate coupling case. Twisted Wilson results are continuum extrapolations whereas the SLAC data is from a 45×45 lattice. $m_0 L = 15$ for $\lambda \leq 0.8$ and $m_0 L = 20$ for $\lambda \geq 1.0$.

N_s	improved	unimproved
45	10.22(26)	11.49(9)
63	10.54(15)	10.70(19)

Table 3.6: Fermionic masses $m_F L$ for the SLAC derivative on two different lattice sizes for $\lambda = 0.8$ and $m_0 L = 15$.

⁵For $\lambda = 0.7$ the simulation failed already on the coarsest lattice and had to be excluded from extrapolations to the continuum limit.

3.2.7 Measurement induced supersymmetry breaking

For a discussion of the measurement procedure a closer look at the properties under $\mathbb{Z}_2^{\text{TPR}}$ is necessary. When using SLAC fermions the action and the fermionic determinant are invariant under application of the symmetry. The impact on the traced fermionic correlator can be calculated using Eq. (3.14),

$$C_F(t) \xrightarrow{\mathbb{Z}_2^{\text{TPR}}} -C_F(t). \quad (3.39)$$

In order to extract masses and to gain a non-vanishing correlator expectation values are only measured on configurations in the vicinity of the perturbative ground state, i.e. only configurations with $\tilde{\varphi}_1 = N^{-1} \sum_x \varphi_{1,x} > -\frac{1}{2\lambda}$ are used. This procedure effectively mimics the thermodynamic limit of the theory where the \mathbb{Z}_2^{R} symmetry is spontaneously broken and only one (bosonic) ground state is present. Tunnelling events to the other ground state (which would lift the ground state energy above zero) are forbidden by supersymmetry.⁶ Equivalently the measurement of the (connected) bosonic correlator is affected once tunnelling between the ground states in one simulation run sets in. In that manner the bosonic correlation function is also computed by using the configurations with $\tilde{\varphi}_1 > -\frac{1}{2\lambda}$.

Strictly speaking the tunnelling probability within simulations is algorithm dependent. E.g. it may be possible to globally flip the field φ at random according to $\mathbb{Z}_2^{\text{TPR}}$ preserving the effective action. However, the simulations in this work are performed using a hybrid Monte-Carlo algorithm which (by construction) makes use of a Hamiltonian evolution which mimics (with final step size) a continuous trajectory in the space of fields φ . As consequence for small couplings λ the used algorithm will show nearly no tunnelling (for a reasonable number of generated configurations) and an effect of the tunnelling on the measurement prescription will be better visible for large couplings.

For small couplings λ it has been checked in Sec. 3.2.5 that bosonic and fermionic masses coincide.

⁶The projection is equivalent to removing external currents after the thermodynamic limit is taken as has been analysed for the case of $O(N)$ models in [70–72].

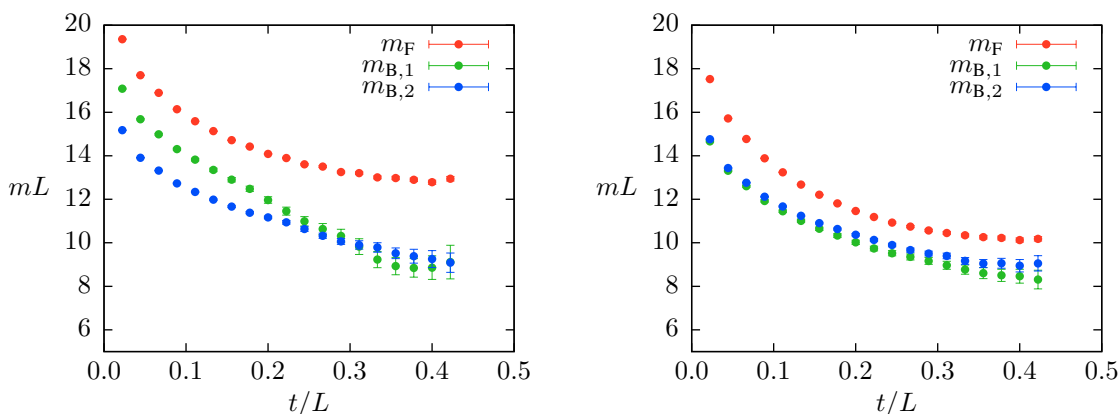


Figure 3.14: Local mass obtained from simulations on a 45×45 lattice with $m_0L = 20$, $\lambda = 1.0$ using the unimproved (left panel) and improved (right panel) formulation with SLAC fermions.

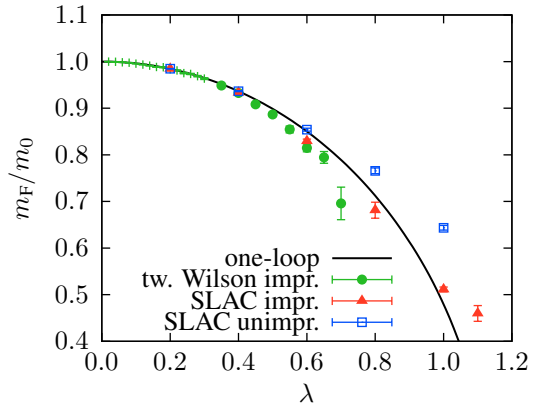


Figure 3.13: Masses of the improved and unimproved model with SLAC fermions on a 45×45 lattice and continuum extrapolated results for twisted Wilson fermions are compared with the perturbative one-loop result in the continuum.

Now, for $\lambda = 1.0$ and $m_0L = 20$ on a 45×45 lattice the *local mass* obtained from a local cosh-fit on configurations around the perturbative classical ground state is analysed using the SLAC derivative with improved and unimproved formulation (see Fig. 3.14). Differences between improved and unimproved formulation become apparent and, more important, there is, even in the improved formulation, a splitting of bosonic and fermionic masses in contradiction to supersymmetry. To exclude that this mass splitting is only due to the finite lattice spacing effective masses at two lattice spacings are compared in Fig. 3.15. Even at $\lambda = 1.1$ a perfect scaling with respect to the lattice spacing is present in the improved model and discretisation effects can be excluded. It may be concluded from the plateau of the effective mass for large t that bosonic and fermionic masses do *not* coincide and supersymmetry is broken.

However, the lattice formulation of the Wess-Zumino model based on the Nicolai map leaves one (real) supersymmetry unbroken in spite of the fact that a finite lattice spacing is present. Therefore a measurement of a Ward identity derived from this symmetry may shed some light on the preservation of this specific supersymmetry.

To construct a Ward identity $\langle \delta A \rangle = 0$ related to the fermionic correlator an operator $A = \varphi_x \bar{\psi}_{1,y} + \bar{\varphi}_x \bar{\psi}_{2,y}$ is used which turns (via a spinor trace) into $\langle F(t) \rangle = \langle B(t) \rangle$ with

$$\begin{aligned} F(t) &= N_s^{-2} N_t^{-1} \sum_{\alpha, x, x', t'} \psi_{\alpha, (t', x)} \bar{\psi}_{\alpha, (t+t', x')}, \\ B(t) &= N_s^{-2} N_t^{-1} \text{Re} \sum_{x, x', t'} \bar{\varphi}_{(t', x)} \xi_{(t+t', x')}. \end{aligned} \quad (3.40)$$

Again, the bosonic part $B(t)$ of the Ward identity is antisymmetric under $\mathbb{Z}_2^{\text{TPR}}$ and a measurement of the Ward identity corresponding to the fermionic correlator turns out to give “ $0 = 0$ ”. Also here the projection to $\tilde{\varphi}_1 > -\frac{1}{2\lambda}$ is applied to gain a non-trivial result.

For the case of $m_0L = 20$ and $\lambda = 1.1$ the fulfilment of the Ward identity given by Eq. (3.40) is tested and corresponding results for lattice sizes 45×45 and 63×63 are shown in Fig. 3.16. Here

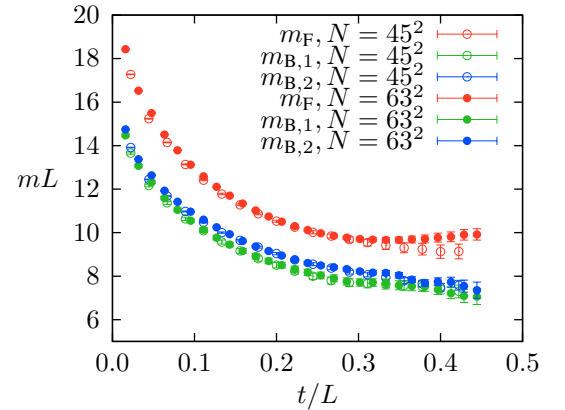


Figure 3.15: Local mass at $m_0L = 20$ and $\lambda = 1.1$ obtained on a 45×45 and 63×63 lattice using the improved formulation with SLAC fermions.

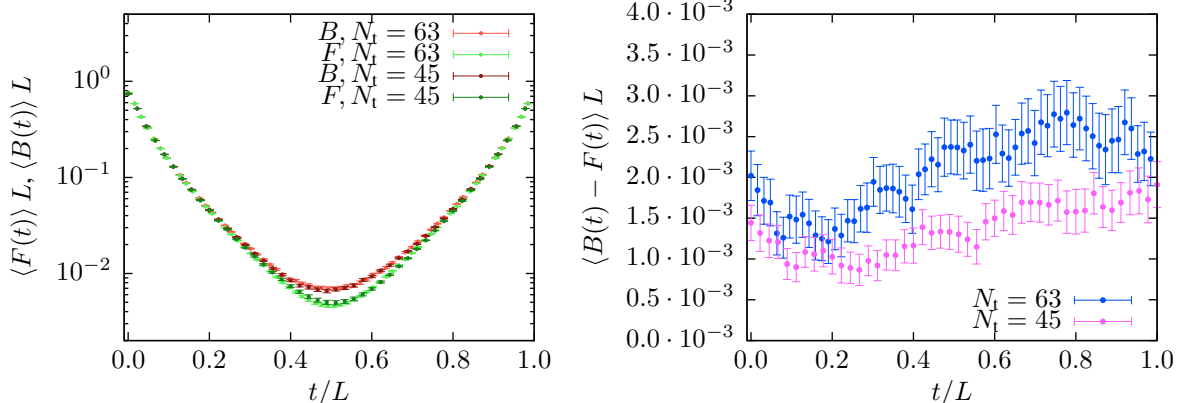


Figure 3.16: Contributions to the Ward identity obtained for $m_0L = 20$ and $\lambda = 1.1$ at two lattice spacings in the improved model with SLAC fermions measured on $2 \cdot 10^6$ configurations.

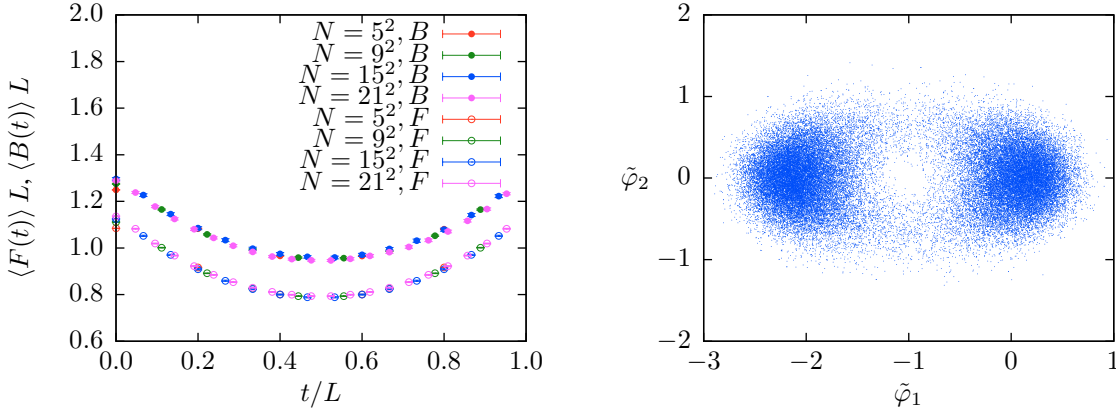


Figure 3.17: Left panel: Contributions to the Ward identity for $m_0L = 1.4$ and $\lambda = 0.5$ at different lattice spacings. Right panel: Field distribution in the complex plane for the volume averaged $\tilde{\varphi}$ on $m_0L = 3$ and $\lambda = 0.5$. Both are computed in the improved model with SLAC fermions.

the breaking of the (by definition unbroken) supersymmetry is apparent and discretisation effects are excluded by the (within error bars) coinciding results for different lattice spacings.

Naively one expects that this inconsistency between a (per definition) supersymmetric action and the broken Ward identity should be pronounced for larger couplings. Nevertheless, this issue can be clarified by considering even smaller couplings. E.g. simulations for $\lambda = 0.5$ but at a smaller volume $m_0L = 1.4$ with the improved model with SLAC fermions share the same breaking of the Ward identity (see Fig. 3.17, left panel). Again the independence of the lattice spacing is clearly visible and the breaking of the Ward identity is a real continuum effect. In the field distribution (see Fig. 3.17, right panel) an overlapping of both ground states is visible (even for a larger volume $m_0L = 3$) which is entirely caused by the finite volume.

The difference $\langle B(t) - F(t) \rangle$ seems to be independent of t and the averaged difference $\langle \tilde{B} - \tilde{F} \rangle$ can be taken as an observable that measures supersymmetry breaking. To clearly identify the volume dependence simulations at fixed $\lambda = 0.5$ have been performed at 15×15 lattices with varying box size m_0L (see Fig. 3.18). It is found that this supersymmetry breaking is exponentially suppressed with the volume according to $\langle \tilde{B} - \tilde{F} \rangle L = 0.73(2)e^{-1.08(2)m_0L}$.

In fact, this supersymmetry breaking can also be seen on the level of the action. The chosen measurement procedure amounts to a suppression of all configurations with $\tilde{\varphi}_1 < -\frac{1}{2\lambda}$. This prescription is equivalent to simulating the theory with changed bosonic action

$$S_B \rightarrow \lim_{\alpha \rightarrow \infty} \left(S_B + \alpha \cdot \theta \left(N^{-1} \sum_x \varphi_{1,x} - \frac{1}{2\lambda} \right) \right). \quad (3.41)$$

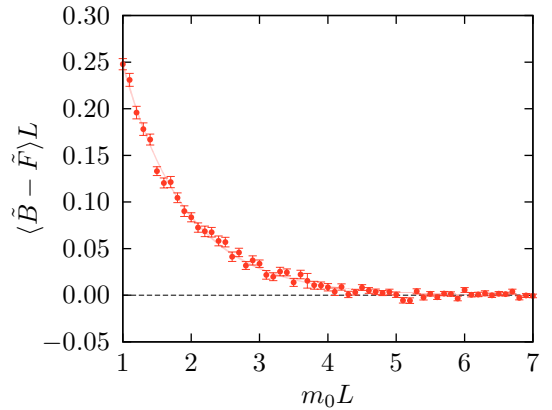


Figure 3.18: Volume dependence of the averaged difference $\langle \tilde{B} - \tilde{F} \rangle L$ for coupling $\lambda = 0.5$ obtained from 15×15 lattices with an improved SLAC model. The shaded line denotes an exponential fit.

Introducing the additional θ function which lifts the action of configurations with $\tilde{\varphi}_1 < -\frac{1}{2\lambda}$ to arbitrary high values cannot be obtained by the construction using Nicolai variables and thus will not preserve the supersymmetry. In this sense the simulation performed with the Nicolai improved action will *not*

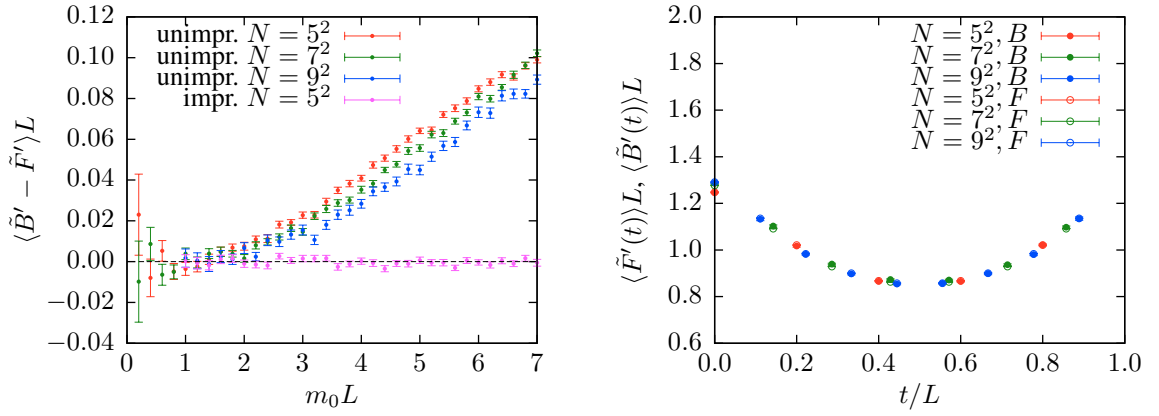


Figure 3.19: Left panel: Ward identity (3.42) calculated for the improved and unimproved model with SLAC derivative for $\lambda = 0.5$. Right panel: Ward identity contributions for the improved model at $m_0 L = 1.4$ and $\lambda = 0.5$. Bosonic and fermionic contributions lie on top of each other.

break one specific supersymmetry but the explicit measurement procedure based on the projection to one classical ground state will break the supersymmetry explicitly.

To finally prove that the supersymmetry is only broken by the projection to one ground state a Ward identity is constructed that contains a non-vanishing part invariant under the $\mathbb{Z}_2^{\text{TPR}}$ symmetry and can therefore be measured without any projection. A simple form of such a Ward identity is given by the operator $A' = (\varphi_{1,x} + \frac{1}{2\lambda})^2 (\bar{\psi}_{1,y} + \bar{\psi}_{2,y})$ which gives rise to equality of bosonic and fermionic part

$$\begin{aligned}
 F'(t) &= N_s^{-2} N_t^{-1} \sum_{\alpha, \beta, x, x', t'} \psi_{\alpha, (t', x)} \left(\varphi_{1, (t', x)} + \frac{1}{2\lambda} \right) \bar{\psi}_{\beta, (t+t', x')}, \\
 B'(t) &= N_s^{-2} N_t^{-1} \text{Re} \sum_{x, x', t'} \left(\varphi_{1, (t', x)} + \frac{1}{2\lambda} \right)^2 \xi_{(t+t', x')}.
 \end{aligned} \tag{3.42}$$

For comparison the supersymmetry breaking can be calculated by using the unimproved as well as the improved model and the corresponding results are shown in Fig. 3.19. These clearly show that the simulation using the improved model preserves the supersymmetry (within error bars) while the unimproved model sets the reference scale to ‘measure the zero’.

The analysis of this finite size induced supersymmetry breaking in the measurement process shows that broken Ward identities may be visible on volumes with $m_{\text{phys}} L \gtrsim 10$ depending on the strength of the coupling λ . Therefore these effects must be accounted for seriously if one aims at simulations at even larger couplings than discussed here. Additionally, the analysis of the local masses in the continuum limit (see Fig. 3.15) shows that the fermionic masses given in Tab. 3.5 for the largest couplings can only be taken as an upper bound of the mass of the supersymmetry multiplet and the difference to the bosonic masses gives the possible systematic error.

3.3 Conclusions

In this chapter a detailed numerical analysis of the two dimensional $\mathcal{N} = (2, 2)$ Wess-Zumino model has been presented. The lattice models have been studied at much larger lattice sizes, i.e. smaller lattice spacings and more importantly at stronger couplings than in previous works. For a comparison with analytical results from perturbation theory finite size effects and other systematic errors such as sign changes of the fermion determinant have been checked explicitly. Both were seen to be under control

for the scrutinised parameter range. Earlier weak coupling results are confirmed and (small) deviations from perturbation theory are resolved for the first time. All three kinds of fermions, Wilson, twisted Wilson, and SLAC fermions, approach the same continuum results. It turned out that lattice artefacts were largest for Wilson and smallest for SLAC fermions. At intermediate coupling supersymmetrically improved lattice actions using Wilson fermions lead to unstable simulations that eventually fail to produce reliable results unless very large lattices are chosen. Simulations with SLAC fermions proved to be much more stable; they allow for improvement terms for a wider parameter range. At finite lattice spacing and weak coupling no significant differences in the measured spectrum between simulations using the improved or unimproved actions could be seen. It is only at larger coupling that deviations become visible, and the improved lattice action in fact suppresses lattice artefacts.

It has been explicitly analysed that the measurement process which mimics the infinite spacetime volume by a projection to one ground state explicitly breaks supersymmetry irrespective of the supersymmetric lattice action used for the simulations. For that reason it is still an open problem to go to even stronger couplings. Practical simulations become considerably more involved due to stronger fluctuations in the sign of the fermion determinant and enlarged finite size effects.

Algorithmic aspects

With increasing computer power over the last years, to date still following Moore's law [73], simulations of realistic physical systems have become feasible. Beginning with small scale simulations of a $SU(2)$ Yang-Mills theory more than three decades ago [18] and simulations of gauged Ising models [74] there has been an ongoing technical evolution. Amongst the biggest achievements in the simulation of lattice regularised theories has been the recent computation of the hadron spectrum [75]. This progress not only benefits from the faster computer resources. The algorithmic developments caused revolutions in the steady progress of technical evolution. Unlike local algorithms [76] contemporary hybrid Monte-Carlo (HMC) algorithms are based on a global evolution and allow now for the inclusion of dynamical fermions [77].

Although the numerical improvements described in this chapter are explained in the setting of the $\mathcal{N} = 2$ Wess-Zumino model the Fourier acceleration and the Γ distributed integration lengths are also applied to every other model discussed in this work.

4.1 Recapitulating the hybrid Monte-Carlo algorithm

Although new developments allow for the efficient simulation of models with dynamical fermions by writing the partition function as a loop gas [78, 79] this method only applies to Wilson fermions¹ and not for discretisations based on the SLAC derivative. Therefore it is natural to use the generic HMC algorithm throughout the present work.

When simulating a system with lattice action $S[\phi]$, where ϕ denotes the set of bosonic fields², a 'Hamiltonian' $H[\phi, \pi] = S[\phi] + P[\pi]$ with a 'momentum' field π_x with as many degrees of freedom as ϕ_x is introduced. The corresponding lattice path integral

$$\mathcal{Z} = \int D\phi D\pi e^{-H[\phi, \pi]} = \int D\phi e^{-S[\phi]} \int D\pi e^{-P[\pi]} \quad (4.1)$$

factorises and expectation values depending only on ϕ fields are not affected by the additional momentum distribution. Equations of motion $\dot{\phi}_x = G_x[\phi, \pi]$ for a Hamiltonian evolution are imposed and $\dot{\pi}_x = F_x[\phi, \pi]$ is derived by the requirement of $H[\phi(t), \pi(t)]$ to be constant on a trajectory. The canonical choice [77] is given by

$$P[\pi] = \frac{1}{2} \sum_x \pi_x^2, \quad G_x = \pi_x, \quad F_x = -\frac{\partial S}{\partial \phi_x}. \quad (4.2)$$

However, in simulations this evolution must be performed in a discretised form and the generalised concept allows for better stability as will be explained in Sec. 4.2. Ergodicity is obtained by a careful choice of G_x , e.g. $G_x = \pi_x^2$ would lead to a monotonically rising ϕ_x and would thus violate ergodicity. To sum up, the HMC algorithm to generate a distribution of ϕ according to the measure $e^{-S[\phi]}$ is performed by repeating the following steps:

1. Choose π_x distributed according to the measure $e^{-P[\pi]}$.
2. Perform a Hamiltonian evolution with integration length τ_{int} .

¹This rewriting may be possible for every nearest neighbour fermionic interaction.

²The action may also be an effective action including contributions from the fermionic determinant.

3. Perform a Metropolis acceptance step with acceptance $p = \min(1, \exp(-H[\phi(\tau_{\text{int}}), \pi(\tau_{\text{int}})] + H[\phi(0), \pi(0)]))$.

For an exact integration the energy H is constant. In practice the integration must be performed numerically with time steps $\delta\tau$ using a symplectic and time reversible integrator. Here a fourth order integration scheme is used [80].

Naive fermionic action

If the action contains Dirac fermions ψ via

$$S[\phi, \psi] = S_{\text{B}}[\phi] + \bar{\psi}M[\phi]\psi \quad (4.3)$$

the fermions can be integrated out according to

$$\mathcal{Z} = \int \text{D}\phi \text{D}\psi \text{D}\bar{\psi} e^{-S_{\text{B}}[\phi] - \bar{\psi}M[\phi]\psi} = \int \text{D}\phi \det M[\phi] e^{-S_{\text{B}}[\phi]}. \quad (4.4)$$

In general this expression has an inherent sign problem because the determinant of M can be negative. To allow for a statistical interpretation and make a Monte-Carlo sampling feasible the sign of the fermion determinant is factored out and is taken into account by reweighting in the measurement process according to

$$\langle A \rangle = \frac{\langle A \cdot \text{sign det } M \rangle_+}{\langle \text{sign det } M \rangle_+}, \quad (4.5)$$

where the expectation values $\langle \cdot \rangle_+$ are taken with respect to the path integral³

$$\mathcal{Z} = \int \text{D}\phi \det^{1/2}(\underbrace{MM^{\text{T}}}_{=Q}) e^{-S_{\text{B}}[\phi]} = \int \text{D}\phi \exp(-S_{\text{B}}[\phi] + \frac{1}{2} \ln \det Q). \quad (4.6)$$

In that way the HMC algorithm can be used directly with the action $S[\phi] = S_{\text{B}}[\phi] - \frac{1}{2} \ln \det Q[\phi]$ and the equations of motion are given for the canonical case (4.2) by

$$F_x = -\frac{\partial S_{\text{B}}}{\partial \phi_x} + \text{tr} \left(M^{-1} \frac{\partial M}{\partial \phi_x} \right). \quad (4.7)$$

The only pitfall of this method arises from the fact that the matrix dimension scales with the lattice volume V . If the determinant (and the inverse, which is involved in the calculation of the force F_x) cannot be computed in a direct way⁴ the algorithm will have a complexity $\mathcal{O}(V^3)$, not taking into account the additional critical slowing down that arises from a growing physical volume. An established method to circumvent these problems is given by introducing (multiple) pseudo-fermions [77] as discussed in Sec. 4.4.

4.2 Fourier acceleration

The effectiveness of the Hamiltonian evolution is affected by the distance covered in phase space per trajectory. To gain a small autocorrelation in terms of computer time it is preferable to obtain the longest possible evolution with the same number of steps and preserved integration error. The

³For the models discussed in this work the matrix M has only real entries.

⁴The direct computation of the determinant is possible for the SQM with Wilson fermions.

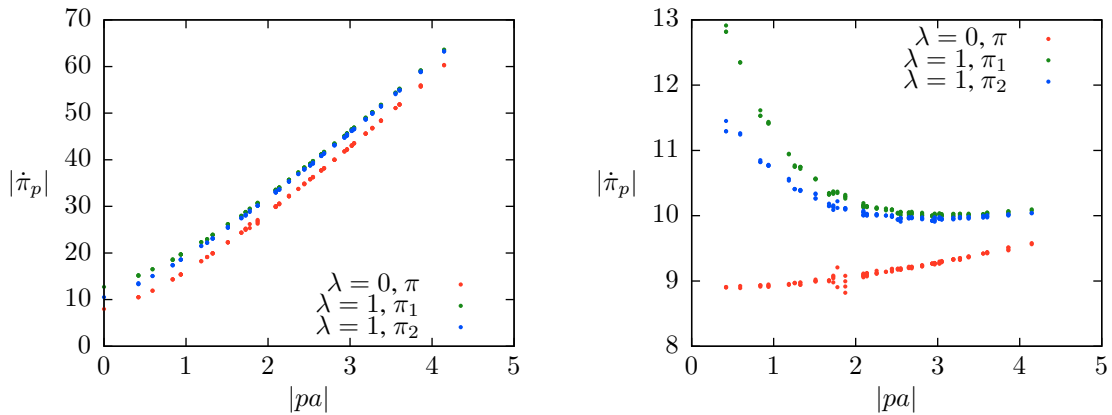


Figure 4.1: Distribution of $\dot{\pi}$ for the $\mathcal{N} = 2$ Wess-Zumino model at $\lambda = 1$ and for the free case on a 15×15 lattice in the unimproved SLAC model and $m_0L = 10$, unscaled (left panel) and rescaled (right panel) using $g(p)$ with $m_{acc} = m_{latt} = 10/15$.

formulation of the evolution equations is in general translation invariant. Instead, in momentum space the distribution of $\dot{\phi}$ and $\dot{\pi}$ is non-uniform (see Fig. 4.1, left panel). Based on this observation the velocity of the Hamiltonian evolution depends on the momentum mode as introduced and calculated for the case of a leap frog integrator in [81] and first exemplified on the unbroken supersymmetric quantum mechanics in [82].

A *Fourier acceleration* is implemented by choosing G_x (or more directly the momentum component) to obey $G_p = g(p) \cdot \pi_p$ with $g(p)$ to be specified later. Equivalently this may be specified in position space as $G_x = \sum_y A_{xy} \pi_y$ with a matrix $A_{xy} = V^{-1} \sum_p e^{ipx} g(p) e^{-ipy}$. The force is then given by $F_x = -A_{yx} \frac{\partial S}{\partial \phi_y}$. Here $g(p) = g(-p)$ is used such that A is symmetric. For the scalar models considered here the largest forces are given for large momenta which cause severe energy violations in the discretised Hamiltonian evolution because the error scales with $(\delta\tau)^4$ for the chosen integrator. Further the physical content should be encoded mainly in the infrared properties of the lattice theory so that a decorrelation of low momentum modes should be preferred. Although various functional forms are possible [83] $g(p)$ will be chosen analogous to [82] by

$$g(p) = \frac{m_{acc}}{\sqrt{(m_{acc})^2 + (pa)^2}} \quad (4.8)$$

so that the zero momentum sector is not affected while larger momenta are damped (see Fig. 4.1, right panel). This choice provides optimal decorrelation for the free theory when choosing the free parameter m_{acc} to be the mass in lattice units. A speedup for the low momentum modes is then achieved by larger possible integration steps. With this prescription it is possible to reach an improved tunnelling behaviour in the interacting $\mathcal{N} = 2$ Wess-Zumino model with preserved numerical effort (see Fig. 4.2). Accordingly the integrated autocorrelation time for the averaged field $\tilde{\varphi}$ and other observables can decrease by orders of magnitude and can be tuned below 5 in almost every case [47].

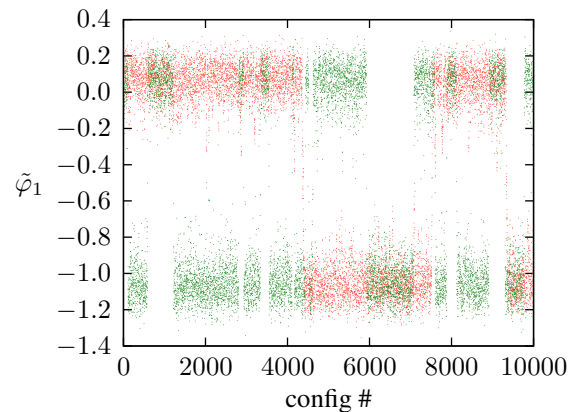


Figure 4.2: Average field $\tilde{\varphi}_1$ in the $\mathcal{N} = 2$ Wess-Zumino model for an acceptance rate of 97% and 5 integration steps without (red) and with (green) Fourier acceleration with $m_{acc} = 5/15$ and on a 15×15 lattice for the unimproved SLAC model at $m_0L = 10$ and $\lambda = 1$

4.3 Γ distributed integration lengths

For systems close to the free theory (e.g. in the perturbative sector of the $\mathcal{N} = 2$ Wess-Zumino model) it is possible to gain further decorrelation by choosing τ_{int} randomly. In the free theory φ_1 and φ_2 decouple and their lattice averages Φ obey a differential equation in the Hamiltonian evolution

$$\frac{d}{d\tau} \begin{pmatrix} \Phi \\ \Pi \end{pmatrix} = \begin{pmatrix} 0 & 1 \\ -m_{\text{latt}}^2 & 0 \end{pmatrix} \begin{pmatrix} \Phi \\ \Pi \end{pmatrix} \quad (4.9)$$

with Hamiltonian $H = \frac{1}{2}(\Pi^2 + m_{\text{latt}}^2 \Phi^2)$. For this reduced system the equations of motion describe an ellipsis and an exact integration is possible. Instead of fixing the integration length, τ_{int} is now chosen randomly for every trajectory. Because of $\tau_{\text{int}} > 0$ the distribution function may only have a positive support. For normalisation it is useful to have a fixed mean integration length $\overline{\tau}_{\text{int}}$. A natural choice for the distribution function is then given by the $\Gamma(k, \theta)$ distribution with two parameters $k, \theta > 0$ describing the shape and the scale of the probability distribution. For a $\Gamma(k, \theta)$ distributed observable the mean is given by $k\theta$ and the variance by $k\theta^2$ which implies to set $\theta = k^{-1}$ and consider the normalised distribution $\Gamma_k = \Gamma(k, k^{-1})$ with mean 1 and variance k^{-1} (see Fig. 4.3).

To compare autocorrelation times Φ is considered for the free theory and the volume averaged $\tilde{\varphi}_2$ for the interacting theory because of its insensitivity to tunnelling events between both ground states. To get rid of systematic errors the step size of the numerical integrator is chosen to be small enough to ensure full acceptance in the Metropolis step. However, considering only the integrated autocorrelation time may be misleading for the case of anti-correlations (e.g. an alternating behaviour $\Phi \leftrightarrow -\Phi$). For that reason the correlation after one trajectory,

$$C(1) = (\langle \Phi^2 \rangle - \langle \Phi \rangle^2)^{-1} (N_{\text{MC}} - 1)^{-1} \sum_{k=1}^{N_{\text{MC}}-1} (\Phi^{(k)} - \langle \Phi \rangle)(\Phi^{(k+1)} - \langle \Phi \rangle), \quad (4.10)$$

is analysed, which is close to 1 for strong correlations and close to -1 for anti-correlations.

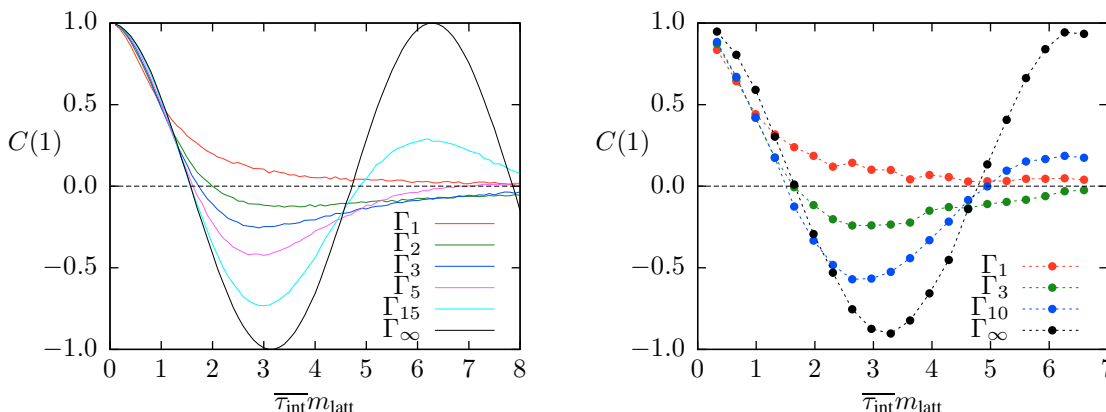


Figure 4.4: Correlation function of $\tilde{\varphi}_2$ after one trajectory for the free theory (left panel) and the full theory (right panel) with $m_0 L = 15$ and $\lambda = 0.5$ on a 15×15 lattice in the unimproved SLAC model using Γ_k distributed integration lengths.

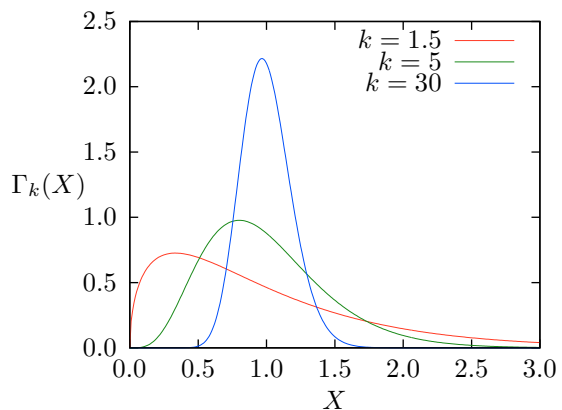


Figure 4.3: Gamma function for different shape parameters. For $k \rightarrow \infty$ the delta distribution $\delta(x - 1)$ is reached.

For the free theory the system shows an oscillatory behaviour (see Fig. 4.4, left panel) over the integration lengths which follows from a trajectory on an ellipsis that leads back to the starting point after $\tau_{\text{int}} m_{\text{latt}} = 2\pi$. For $C(1) < 0$ anti-correlations are present, which imply integrated autocorrelation times smaller than 1 without any real decorrelation in terms of physically distinct configurations. For smaller values of the shape parameter k these oscillations are damped and a real decorrelation is reached for $\overline{\tau}_{\text{int}}$ large enough. To go beyond the free theory computations have been performed for the full model at coupling $\lambda = 0.5$ with the unimproved SLAC formulation and shape parameter $k \in \{1, 3, 10, \infty\}$. The configurations are generated using Fourier acceleration with $m_{\text{acc}} = m_{\text{latt}} = 1$ in order to get a sufficiently high acceptance rate on a 15×15 lattice. Even for the interacting case (Fig. 4.4, right panel) particular choices of the shape parameter suppress the (anti-)correlation for large integration lengths and improve the decorrelation for small $\overline{\tau}_{\text{int}}$. Based on these observations a shape parameter of $k = 3$ was used for all simulations in this work.

4.4 Deflated rational hybrid Monte-Carlo

For systems with dynamical fermions the path integral is calculated as

$$\mathcal{Z} = \int D\phi |\det M|^\kappa e^{-S_B} \quad (4.11)$$

with field dependent fermion matrix $M[\phi]$ and $\kappa = 1$ for Dirac fermions or $\kappa = \frac{1}{2}$ for Majorana fermions. In this work the fermion matrix has only *real* entries and the path integral is rewritten as

$$\mathcal{Z} = \int D\phi |\det Q|^{\kappa/2} e^{-S_B}, \quad Q = MM^T \quad (4.12)$$

with a symmetric matrix $Q[\phi]$ with positive semidefinite spectrum. In the well established rational hybrid Monte-Carlo (RHMC) algorithm [84–86] the path integral is reformulated using *complex* pseudo-fermion fields which are necessary for a complex matrix M . For $M \in \mathbb{R}^{n \times n}$ one can express the path integral (up to a multiplicative normalisation constant) using N_{pf} pseudo-fermions as

$$\mathcal{Z} = \int D\phi \prod_{n=1}^{N_{\text{pf}}} D\chi_n \exp(-S_B - \sum_{m=1}^{N_{\text{pf}}} \chi_m^T r^2(Q) \chi_m) \det(Q^\alpha r(Q))^{N_{\text{pf}}}. \quad (4.13)$$

with $\alpha = \frac{\kappa}{2N_{\text{pf}}}$. Now $r(Q)$ is chosen to be a rational approximation

$$r(Q) = \alpha_0 + \sum_{k=1}^{N_E} \frac{\alpha_k}{Q + \beta_k} \quad (4.14)$$

with order N_E to the function $Q^{-\alpha}$ that can be constructed with the Remez algorithm (for a review see [87], the implementation of [88] is used).⁵ Additionally $r(Q)\chi$ can be computed efficiently using a multishift solver based on the conjugate gradient (CG) method [92]. This approximation will only be accurate within given error bounds if the spectrum of Q lies within a predefined interval $\sigma(Q) \in [a, b]$ and it is necessary for the exactness of the algorithm to ensure this condition. For that reason the bounds a, b must be defined at the beginning of the simulation and are chosen pessimistically to *always* cover the spectrum of Q . Naturally the exactness of the algorithm is limited by the order of the approximation N_E and the exactness of the inverter used. To reduce the condition number of Q a preconditioner P

⁵Alternatively a polynomial approximation is possible that leads to comparable performance [89–91].

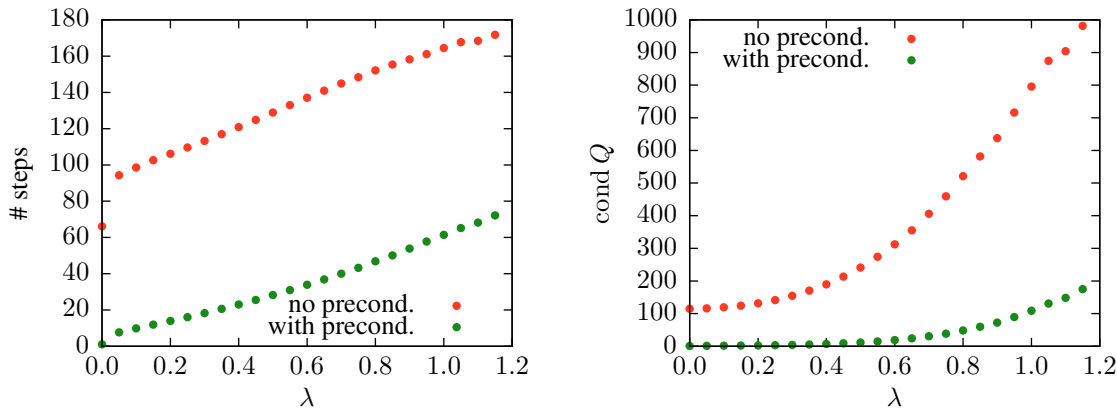


Figure 4.5: Average number of CG steps (left panel) and condition number of Q (right panel) with and without preconditioner for a 25×25 lattice and volume $m_0 L = 10$ in the unimproved $\mathcal{N} = 2$ Wess-Zumino model with SLAC discretisation for a residual error of the CG solver of 10^{-14} .

can be implemented by changing $M \rightarrow MP$ with a constant matrix P . This amounts only to a multiplicative normalisation of the path integral by $|\det P|^\kappa$. For the Wess-Zumino models the free fermion matrix $P = M[\varphi = 0]^{-1}$ is chosen as preconditioner. The advantage is the fast applicability of this matrix through its diagonal form in Fourier space. This preconditioner reduces the condition number and the necessary CG steps considerably not only in the perturbative region (see Fig. 4.5).

In practice the approximation will have smaller errors for fixed N_E if a narrower range $[a, b]$ is chosen. Therefore the spectral bounds are computed in test runs with a very pessimistic parameter setting on about 1 000 configurations to determine reasonable bounds for the production runs. In this work the ARPACK library [93] based on the implicitly restarted Arnoldi method [94] is used for the computation of the spectrum of the (preconditioned) Q .

With the above definitions the action used in the energy calculation is given by

$$S = S_B + \sum_{m=1}^{N_{\text{pf}}} \chi_m^\top r^2(Q) \chi_m. \quad (4.15)$$

with a (numerically) exact approximation $r(Q) = Q^{-\alpha}$. For the computation of the force during the molecular dynamics the full numerical precision is not necessary and the action

$$S = S_B + \sum_{m=1}^{N_{\text{pf}}} \chi_m^\top r_{\text{MD}}(Q) \chi_m \quad (4.16)$$

is used with $r_{\text{MD}}(Q)$ as rational approximation to $Q^{-2\alpha}$ over the same region $[a, b]$. The approximation r_{MD} is used to provide a cost efficient calculation by using a lower degree of approximation N_{MD} which leads to larger shifts β_i and a better conditioned inverter. The exactness of the algorithm still depends only on the exactness of the approximation in the energy calculation which gives room to use a faster but inexact calculation of the force that is given in the canonical scheme (4.2) by

$$F_x = -\frac{\partial S_B}{\partial \phi_x} + 2 \sum_{m=1}^{N_{\text{pf}}} \sum_{i=1}^{N_{\text{MD}}} \alpha_i \eta_{m,i}^\top \frac{\partial M}{\partial \phi_x} \eta'_{m,i} \quad (4.17)$$

with $\eta_{m,i} = (Q + \beta_i)^{-1} \chi_m$, $\eta'_{m,i} = M^\top \eta_{m,i}$ and coefficients α_i, β_i of $r_{\text{MD}}(Q)$.

Using these definition the RHMC algorithm proceeds as follows.

1. Choose π_x according to $e^{-P[\pi]}$ and initial fields γ_i according to $e^{-\gamma_i^\top \gamma_i}$. From these construct the pseudo-fermion fields $\chi_n = r_{E0}(Q)\phi_n$ with $r_{E0}(Q)$ as order N_E approximation to Q^α .
2. Perform a Hamiltonian evolution with integration length τ_{int} using the effective action (4.16).
3. Perform a Metropolis acceptance step with acceptance $p = \min(1, e^{-H[\phi(\tau_{\text{int}}), \pi(\tau_{\text{int}})] + H[\phi(0), \pi(0)]})$ using the action (4.15), where the approximation to $Q^{-\alpha}$ is needed.

4.4.1 Eigenvalue deflation

The RHMC algorithm as described above depends on the known spectral bounds which ensure the exactness of the algorithm. For the present work zero modes of the Dirac operator cannot be excluded in general.⁶ It was analysed [95] that it may be sufficient to choose the spectral range $[a, b]$ pessimistically enough to extract the correct physics. Nevertheless, every chosen spectral range used to construct the approximation within the RHMC will render the algorithm in principle *inexact*.

For the $\mathcal{N} = 2$ Wess-Zumino model the eigenvalues lie in the range $[10^{-7}, 9]$ (see Fig. 4.6) where the largest eigenvalue shows almost no fluctuations and the choice of $b = 10$ is reasonable safe. However the smallest eigenvalue fluctuates in a range $[10^{-7}, 10^{-1}]$ over 50 000 configurations and smaller ones cannot be excluded in general. Therefore the smallest eigenvalues should be treated exactly to get an exact algorithm even if the estimated spectral bounds are too tight.

To compute the force an exact computation is not necessary since deviations will be cured in the *exact* Metropolis step. Additionally the spectral interval for the force calculations can be chosen to cover a wider range than for the energy calculations to provide further stability. Only the heat bath calculation at the beginning of each trajectory and the computation of the energy at the end of each trajectory must be handled exactly. When (e.g. in the heat bath step) approximating $\chi = Q^\alpha \gamma$ the approximation $\chi' = r(Q)\gamma$ is used, which in spectral form reads

$$\chi' = \sum_{\lambda} r(\lambda) \xi_{\lambda} (\xi_{\lambda}^{\top} \gamma) \quad (4.18)$$

with ξ_{λ} as eigenvector of Q to the eigenvalue λ . Using the “exactness” of the approximation for $\lambda > a$ an exact computation over the whole spectrum is gained by

$$\chi = \chi' + \sum_{\lambda < a} (\lambda^{\alpha} - r(\lambda)) \xi_{\lambda} (\xi_{\lambda}^{\top} \gamma). \quad (4.19)$$

The computation of the smallest eigenvalues and eigenvectors is performed by the ARPACK package and can be computed parallel to the multishift CG solver. The deflation (4.19) is performed afterwards in the heat bath and Metropolis step and uses only fast vector-vector operations. During different

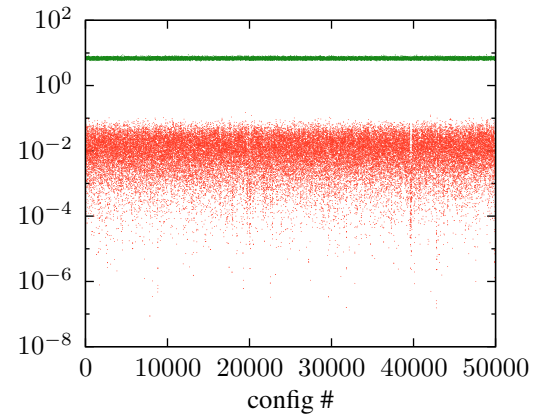


Figure 4.6: Smallest (red) and largest (green) eigenvalue of Q for $mL = 15$, $\lambda = 1.2$ on a 45×45 lattice for the improved $\mathcal{N} = 2$ Wess-Zumino model with SLAC discretisation.

⁶As long as a change in the sign of the fermion determinant is possible zero modes *must* occur.

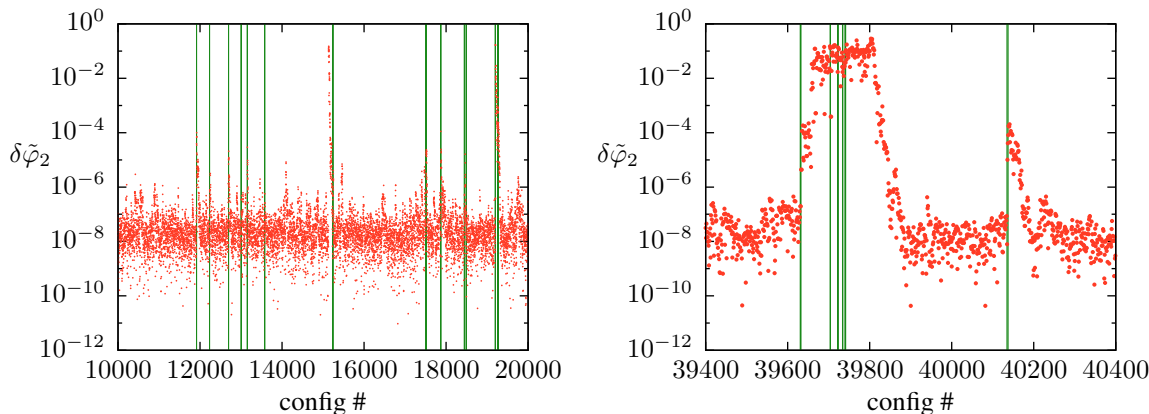


Figure 4.7: Difference in the $\tilde{\varphi}_2$ timeline for $m_0L = 15$, $\lambda = 1.2$ for a run with 3 pseudo-fermions and spectral bounds $[10^{-5}, 10]$ on a 45×45 lattice using the same random numbers for standard and deflated RHMC algorithm. The vertical lines mark configurations with smallest eigenvalues below the bound.

simulations the number of matrix applications in the eigenvalue solver is similar to the ones needed in the CG solver. Therefore the computational cost is increased roughly by the amount that is necessary for one additional pseudo-fermion in the energy calculations.

4.4.2 Effects on the Markov chain

The influence of the deflation on the Markov chain is analysed by starting two simulations with the same random number generator and corresponding seed. If a small eigenvalue occurs the deflation can change the trajectory by accepting/rejecting configurations that otherwise would not have been accepted/rejected. The naive expectation is that the Markov chains from that point on differ considerably. For the improved $\mathcal{N} = 2$ Wess-Zumino model with $m_0L = 15$, $\lambda = 1.2$ on a 45×45 lattice with lower spectral bound of 10^{-5} less than 0.3% of all configurations lie below this bound (see Fig. 4.6). The timelines of observables can indicate differences in the Markov chain. E.g. for the averaged bosonic field about 5.8% of all configurations differ by $\delta\tilde{\varphi}_2 = |\tilde{\varphi}_2^{\text{deflated}} - \tilde{\varphi}_2^{\text{undeflated}}| > 10^{-6}$ (see Fig. 4.7). As naively expected the onset of strong differences in the Markov chain is correlated with the occurrence of small eigenvalues. However, after some

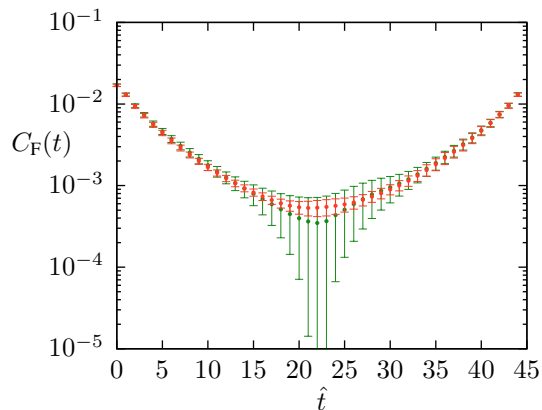


Figure 4.8: Fermionic correlation function for $m_0L = 15$, $\lambda = 1.2$ for a run with 3 pseudo-fermions and spectral bounds $[10^{-5}, 10]$ on a 45×45 lattice with exact deflated RHMC algorithm (red) and inexact standard RHMC algorithm (green).

(for the present case up to a few hundred) configurations, the Markov chains again converge towards each other and the Markov chain will depend up to numerical accuracy of 10^{-8} only on the random numbers and *not the configuration* that was changed by the eigenvalue deflation. Of course the deflation is necessary to obtain an exact algorithm. Without deflation it becomes visible on two-point functions (see Fig. 4.8) that the inexactness of the standard RHMC algorithm leads to much enlarged errors and will eventually give wrong results although the Markov chain seems to be stable with respect to perturbations caused by the deflation.

Chapter 5

$\mathcal{N} = 1$ Wess-Zumino model

Supersymmetry as incorporated in the minimal supersymmetric standard model (MSSM) or extensions thereof can only be a fundamental symmetry if it is spontaneously broken on the experimentally accessible energy scale with a phase transition at a much higher energies. Guided by this observation there is need to study supersymmetry breaking phase transitions using non-perturbative tools. To explore the possibilities provided by lattice regularisations a minimal model is chosen, namely the $\mathcal{N} = (1, 1)$ Wess-Zumino model in two dimensions. Technically, the Wess-Zumino model with $\mathcal{N} = (1, 1)$ supersymmetry is obtained by constraining the fields of the $\mathcal{N} = (2, 2)$ model to be real. This amounts to turning complex scalars into real ones and replacing Dirac fermions with Majorana fermions leading to a minimal field content with only one bosonic and fermionic degree of freedom.¹ Further, at least two dimensions are necessary to obtain a phase transition. The supersymmetric quantum mechanics will only reside in one specific phase depending on the highest power of the superpotential (cf. Sec. 2.1) and is therefore not sufficient to model a phase transition. The physical significance is given via the $\mathcal{N} = 2$ Wess-Zumino model which provides a dimensionally reduced version of the matter sector of the MSSM. Finally, since the seminal work by Witten [15] it is known that the index $\text{Tr}(-1)^{N_F}$ can vanish for a specific choice of the prepotential and supersymmetry may be broken spontaneously depending on the couplings of the prepotential for the $\mathcal{N} = 1$ Wess-Zumino model.

The off-shell continuum formulation is given by the action

$$S = \int d^2x \frac{1}{2} ((\partial_\mu \phi)^2 + \bar{\psi}(\not{\partial} + P'(\phi))\psi + 2FP(\phi) - F^2), \quad (5.1)$$

where F and ϕ denote real scalar fields and ψ is a (real) Majorana spinor with two spinorial components. This formulation is invariant under the supersymmetry transformations

$$\delta\phi = \bar{\epsilon}\psi, \quad \delta\psi = (\not{\partial}\phi - F)\epsilon, \quad \delta F = -\bar{\epsilon}\not{\partial}\psi. \quad (5.2)$$

By eliminating the auxiliary field $F = P(\phi)$ one arrives at the on-shell action

$$S = \int d^2x \frac{1}{2} ((\partial_\mu \phi)^2 + \bar{\psi}(\not{\partial} + P'(\phi))\psi + P(\phi)^2). \quad (5.3)$$

In this work the prepotential P is chosen to be

$$P(\phi) = \frac{\mu_0^2}{\sqrt{2\lambda}} + \sqrt{\frac{\lambda}{2}}\phi^2, \quad (5.4)$$

so that the classical potential (Fig. 5.1) for the scalar part corresponds to a ϕ^4 theory with \mathbb{Z}_2 symmetry ($\phi \rightarrow -\phi$),

$$\frac{P(\phi)^2}{2} = \frac{\mu_0^2}{2}\phi^2 + \frac{\lambda}{4}\phi^4 + \text{const.}, \quad (5.5)$$

while the fermions acquire a Yukawa interaction. An analysis of the Witten index [15] reveals one bosonic and one fermionic ground state that imply $\text{Tr}(-1)^{N_F} = 0$. This ground state structure then

¹From a practical point of view the absence of gauge fields has the advantage that derivatives can be applied in momentum space to speed up Monte-Carlo simulations considerably.

allows for a spontaneous supersymmetry breaking. It is expected that for fixed $\lambda > 0$ and $\mu_0^2 \ll 0$ the system cannot tunnel between both possible ground states so that supersymmetry is unbroken. Accordingly, for $\mu_0^2 > 0$ both ground state energies are lifted above zero and supersymmetry is broken. In consequence there will be a supersymmetry breaking phase transition for some $\mu_0^2 < 0$ and this chapter is devoted to the calculation of a corresponding critical coupling.

There have already been several studies aiming at analysing and understanding supersymmetry breaking in this model. By strong coupling computations [96] the occurrence of a supersymmetry breaking phase transition was predicted. Calculations of the ground state energy with Monte-Carlo methods [97] confirm this expectation. Afterwards lower bounds on the ground state energy have been analysed [98, 99] to obtain a phase diagram of supersymmetry breaking by working in the Hamiltonian formalism and making a numerical analysis with Green's function Monte-Carlo methods. However, the obtained critical lattice couplings so far are only unrenormalised couplings corresponding to one specific lattice spacing. Recently an analysis based on exact renormalisation group methods [100] has been performed [101] where no supersymmetry breaking is introduced during the renormalisation group flow. Again, the phase diagram has been obtained and supersymmetry breaking is found to coincide with a restoration of the \mathbb{Z}_2 symmetry in a *second order* phase transition. A supersymmetric (massive) phase is found for weakly coupled systems as well as a phase of broken supersymmetry with *goldstinos*, the massless Goldstone fermions of the broken supersymmetry², and bosons whose mass vanishes with growing renormalisation group scale.³ But still the critical coupling depends on the chosen regulator which prevents a direct comparison of numerical values.

In general a naive discretisation of a lattice action has to face the problem of broken supersymmetry for finite lattice spacing with the need to fine-tune lattice couplings to reach a supersymmetric continuum limit. However, this model has the advantage that the necessary counterterms have been analysed in lattice perturbation theory [37] and a lattice prescription is given that ensures the supersymmetric continuum limit (perturbatively). Simulations of the given discretisation (that is based on the Wilson derivative) have already been performed [103] and a tunnelling between the possible ground states is found to coincide with the onset of supersymmetry breaking and the appearance of a goldstino. After all there are some open issues. The breaking of a \mathbb{Z}_2 symmetry (which is correlated with the restoration of supersymmetry) has been analysed with a \mathbb{Z}_2 breaking action.⁴ Further the given critical coupling is still regulator dependent and not directly comparable to other methods. For that reason the aim of this chapter is the non-perturbative determination from first principles of a renormalised critical coupling in the continuum limit of this model.

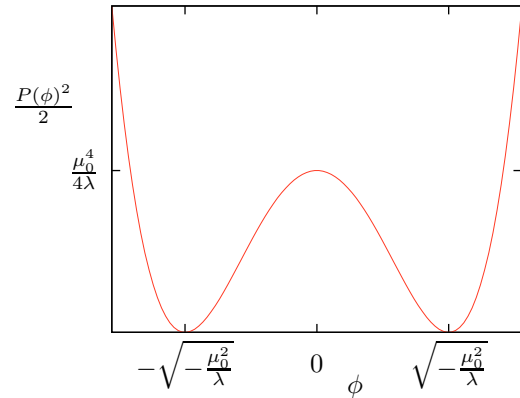


Figure 5.1: The classical bosonic potential of the Wess-Zumino model given in Eq. (5.5).

²This breaking is *not* forbidden by the Mermin-Wagner theorem [102] that only applies to *bosonic* symmetry generators.

³Also the corresponding critical exponents have been determined in [101].

⁴The Wilson term for the fermionic part of the action will break the \mathbb{Z}_2 symmetry as analysed in Sec. 3.1.3.

5.1 Quenched model

Despite the fact that the primary focus lies on the full supersymmetric model it useful to exemplify the definition of a renormalised critical coupling in the setting of the quenched model where fermionic contributions are neglected. This becomes especially important because a non-standard discretisation based on the SLAC derivative is used.

With the prepotential of Eq. (5.4) the quenched model is nothing but the two dimensional ϕ^4 model with bosonic action

$$S_B = \int d^2x \frac{1}{2} \left((\partial_\mu \phi)^2 + \mu_0^2 \phi^2 + \frac{\lambda}{2} \phi^4 \right). \quad (5.6)$$

This model is (classically) invariant under a discrete \mathbb{Z}_2 symmetry ($\phi \rightarrow -\phi$) which can be broken dynamically in the full quantum theory [104]. The unbroken phase is defined by $\langle \phi \rangle = 0$, whereas in the broken phase (in the thermodynamic limit) $\langle \phi \rangle \neq 0$.

In contrast to the full $\mathcal{N} = 2$ Wess-Zumino model the ϕ^4 model (as well as the full $\mathcal{N} = 1$ Wess-Zumino model) is not finite and there is need for a renormalisation of couplings. In the \mathbb{Z}_2 symmetric phase the only divergence arises from the ‘leaf’ diagram (see Fig. 5.2) and the model can be made finite with a mass renormalisation,

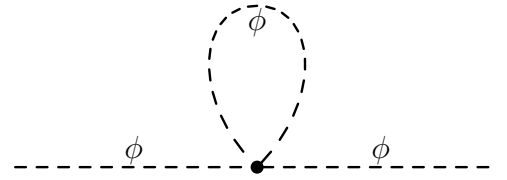


Figure 5.2: The only divergent Feynman diagram for the bosonic ϕ^4 model in the \mathbb{Z}_2 symmetric phase.

$$S_B = \int d^2x \frac{1}{2} \left((\partial_\mu \phi)^2 + \mu^2 \phi^2 + \frac{\lambda}{2} \phi^4 - \delta\mu^2 \phi^2 \right). \quad (5.7)$$

The (one-loop) relation between the inverse propagators is given in terms of renormalised couplings by

$$G^{-1}(p) = p^2 + \mu^2 + \Sigma(p^2), \quad \Sigma(p^2) = 3\lambda A_{\mu^2} - \delta\mu^2, \quad A_{\mu^2} = \int \frac{d^2p}{(2\pi)^2} \frac{1}{p^2 + \mu^2} \quad (5.8)$$

and the only (logarithmically) divergent part is expressed in A_{μ^2} . Therefore all ultraviolet divergences can be removed by a renormalisation of the mass term⁵,

$$\delta\mu^2 = 3\lambda A_{\mu^2} \quad \Leftrightarrow \quad \mu_0^2 = \mu^2 - 3\lambda A_{\mu^2}. \quad (5.9)$$

It was explicitly constructed in [104] that this renormalisation prescription will also be sufficient in the \mathbb{Z}_2 broken phase. As discussed in [105] a dimensionless renormalised coupling f that is able to distinguish between broken and unbroken phase is constructed by $f = \frac{\lambda}{\mu^2}$. By contrast, (naively) possible definitions of a renormalised coupling that are based on the pole mass or the propagator at vanishing momentum are *not sufficient* to distinguish between both phases.

Nevertheless, this renormalisation prescription can only be applied in a given regulator scheme and continuum results will then follow by removing the ultraviolet regulator.⁶

⁵Equivalently this renormalisation can be obtained by a normal ordering of the interaction part in the symmetric phase,

$$S_B = \int d^2x \frac{1}{2} \left((\partial_\mu \phi)^2 + \mu^2 \phi^2 + \frac{\lambda}{2} : \phi^4 :_\mu \right).$$

where $: \cdot :_\mu$ denotes a normal ordering with respect to the mass μ .

⁶There is no need to introduce an infrared regulator.

5.1.1 The \mathbb{Z}_2 phase transition on the lattice

The computation of the critical coupling of the bosonic ϕ^4 model has a long history where several methods and approximations (e.g. based on the Gaussian effective potential or light-cone quantisation) have contributed and a recent overview is given together with the most precise Monte-Carlo results in [106]. The Monte-Carlo results of [106] shall serve as reference values for the discretisation used here. Therefore a short review of these is in order. The lattice regularisation in [105, 106] is based on the ‘‘canonical’’ discretisation utilising the forward derivative and a renormalised critical coupling is computed with high precision. The canonical model is given by

$$S_B = \sum_x \frac{1}{2} \left(\sum_{\nu} (\phi_{x+\nu} - \phi_x)^2 + \hat{\mu}_0^2 \phi_x^2 + \frac{\hat{\lambda}}{2} \phi_x^4 \right) \quad (5.10)$$

with dimensionless lattice parameters $\hat{\lambda} = \lambda a^2$ and $\hat{\mu}_0^2 = \mu_0^2 a^2$. Since λ acquires *no renormalisation* it is used to set the scale. Equivalently $\hat{\lambda}$ determines the lattice spacing with $\hat{\lambda} \rightarrow 0$ in the continuum limit. The (dimensionless) renormalised coupling is again given by $\hat{f} = \frac{\hat{\lambda}}{\hat{\mu}^2}$ and the corresponding $\hat{\mu}_0^2$ can be computed via $\hat{\mu}_0^2 = \hat{\mu}^2 - 3\hat{\lambda}A_{\hat{\mu}^2}$, where $A_{\hat{\mu}^2}$ that enters the normal ordering is given in the infinite volume limit by the lattice propagator for the forward derivative,

$$A_{\hat{\mu}^2} = \lim_{n \rightarrow \infty} n^{-2} \sum_{k_1=1}^n \sum_{k_2=1}^n \frac{1}{\hat{\mu}^2 + 4 \sin^2(\pi k_1/n) + 4 \sin^2(\pi k_2/n)}. \quad (5.11)$$

Because $A_{\hat{\mu}^2}$ diverges only logarithmically for $a \rightarrow 0$ it follows that $\hat{\mu}^2, \hat{\mu}_0^2 \rightarrow 0$ in the continuum limit at fixed \hat{f} . One may argue that at every fixed $\hat{\lambda}$ a second order phase transition appears. However, the continuum physics at these phase transitions corresponds to an *infinite* continuum coupling λ and is therefore only *indirectly relevant* for the continuum ϕ^4 model under consideration.

At finite lattice spacing (given by fixed $\hat{\lambda}$) there will be a \mathbb{Z}_2 breaking phase transition and a critical $\hat{\mu}_c^2$ can be extracted. The renormalised critical coupling in the continuum limit is then determined via

$$f_c = \left[\frac{\lambda}{\mu^2} \right]_{\text{crit}} = \lim_{\hat{\lambda} \rightarrow 0} \hat{f}_c \quad \text{with} \quad \hat{f}_c = \frac{\hat{\lambda}}{\hat{\mu}_c^2}. \quad (5.12)$$

The phase transition itself for finite $\hat{\lambda}$ can be determined from the Binder cumulant $U = 1 - \frac{\langle \bar{\phi}^4 \rangle}{3 \langle \bar{\phi}^2 \rangle^2}$, which becomes *independent* of the lattice volume *at* the second order phase transition point [107].⁷ The critical coupling has been determined from lattices up to a size of 1200^2 and was found to be affected by linear and logarithmic corrections in the lattice spacing. An extrapolation based on the published values in [106] for $\hat{\lambda} \in [0.01, 1]$ to the continuum using a

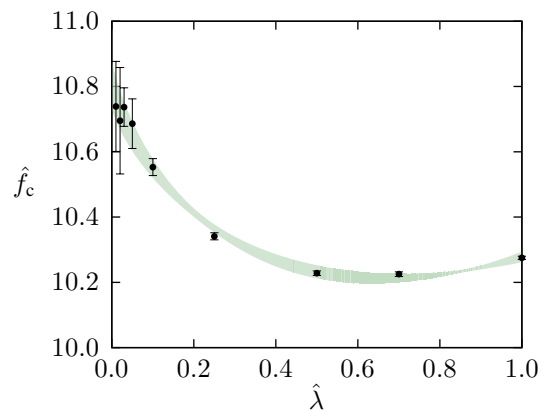


Figure 5.3: Extrapolation of the critical couplings of the bosonic ϕ^4 model to the continuum limit. The shaded region indicates error bands for the extrapolation using the functional form (5.13). Data points are taken from [106] with the canonical discretisation. Confidence bands are computed in this work.

⁷Strictly speaking there is still a slight volume dependence such that the large volume extrapolation of the intersection point for different lattice volumes corresponds to the phase transition.

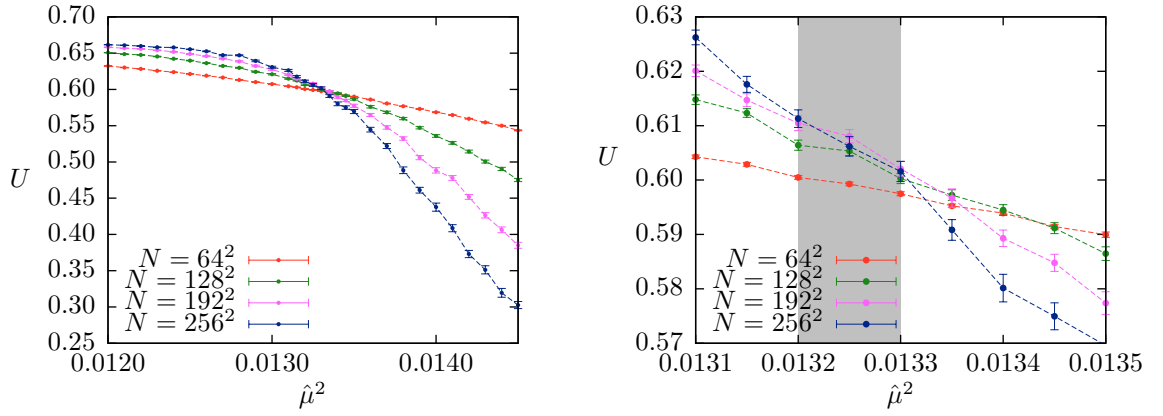


Figure 5.4: Binder cumulants at $\hat{\lambda} = 0.15$ for different lattice sizes. The coarse view is given in the left panel while a close-up view of the critical region is shown in the right panel. From the intersection point for the largest lattices a critical coupling $\hat{f}_c = \frac{0.15}{0.01325(5)} = 11.321(43)$ is extracted. The shaded region gives the error band for the infinite volume extrapolation.

functional form

$$\hat{f}_c(\hat{\lambda}) \approx f_c + a\hat{\lambda} + b\hat{\lambda} \ln \hat{\lambda} \quad (5.13)$$

reveals a renormalised critical coupling in the continuum of $f_c = 10.81(7)$ (see Fig. 5.3).

5.1.2 Regulator independence of the renormalised critical coupling

The results of Chapter 2 and 3 imply that a discretisation based on the SLAC derivative gives results close to the continuum limit and will not break the \mathbb{Z}_2 symmetry of the full supersymmetric model. For that reason the SLAC derivative will also be used to simulate the $\mathcal{N} = 1$ Wess-Zumino model. In contrast to the models considered above it is now necessary to cope with a logarithmic mass renormalisation and the renormalised lattice coupling depends on the chosen renormalisation procedure.

To justify the applicability of the SLAC derivative also for the present case simulations based on the lattice action

$$S = \sum_x \frac{1}{2} \left(\sum_\nu (\partial_\nu^{\text{SLAC}} \phi)_x^2 + \hat{\mu}_0^2 \phi_x^2 + \frac{\hat{\lambda}}{2} \phi_x^4 \right) \quad (5.14)$$

have been performed where the mass parameter is still given by $\hat{\mu}_0^2 = \hat{\mu}^2 - 3\hat{\lambda}A_{\hat{\mu}^2}$. Only now, $A_{\hat{\mu}^2}$ is determined from the propagator based on the SLAC derivative,

$$A_{\hat{\mu}^2} = \lim_{n \rightarrow \infty} (2n)^{-2} \sum_{k_1=-n+1}^n \sum_{k_2=-n+1}^n \frac{1}{\hat{\mu}^2 + (\pi k_1/n)^2 + (\pi k_2/n)^2}. \quad (5.15)$$

Similar to the case of the naive discretisation the crossing of the Binder cumulant U for different lattice volumes at fixed $\hat{\lambda}$ determines the critical $\hat{\mu}^2$ and therefore the critical coupling \hat{f}_c . This procedure is exemplified for $\hat{\lambda} = 0.15$ in Fig. 5.4 where lattice sizes up to 256^2 were used. As an outcome of these calculations critical couplings have been determined for six different $\hat{\lambda}$ (see Tab. 5.1). Again, an extrapolation to the continuum limit $\hat{\lambda} \rightarrow 0$ has been performed according to (5.13) (see Fig. 5.5) and gives the renormalised critical coupling in the continuum of $f_c = 10.92(13)$ which is in complete agreement with the reference value $f_c = 10.81(7)$

$\hat{\lambda}$	\hat{f}_c
0.02	11.035(76)
0.05	11.112(74)
0.10	11.268(57)
0.15	11.321(43)
0.20	11.386(42)
0.25	11.429(29)

Table 5.1: Renormalised critical couplings for the ϕ^4 model as determined from lattice sizes up to 256^2 with the SLAC derivative.

of [106]. This proves that even with the non-local SLAC derivative the lattice ϕ^4 model possesses the correct continuum limit. Further the definition of a renormalised critical continuum coupling is *independent* of the chosen lattice regulator.

5.2 Full dynamical model

By inclusion of dynamical fermions the model is now given in the continuum by the action (5.3). Irrespective of the chosen prepotential $P(\phi)$ the action possesses one (spinorial) supersymmetry. The dynamical breaking of this supersymmetry for the prepotential defined in Eq. (5.4) will be analysed in the following.

5.2.1 Renormalised lattice parameters

Using a discretisation based on the SLAC derivative the lattice action is given by a direct discretisation of the corresponding continuum action,

$$S = \sum_x \frac{1}{2} \left(\sum_\nu (\partial_\nu^{\text{SLAC}} \phi)_x^2 + \hat{\mu}_0^2 \phi_x^2 + \frac{\hat{\lambda}}{2} \phi_x^4 + \sum_y \psi_x^\top \underbrace{C(\partial_{xy}^{\text{SLAC}} + \sqrt{2\hat{\lambda}}\phi_x \delta_{xy})}_{=M[\phi]} \psi_y \right). \quad (5.16)$$

Here, the representation of the Clifford algebra is given by

$$\gamma_0 = \begin{pmatrix} 1 & 0 \\ 0 & -1 \end{pmatrix}, \quad \gamma_1 = \begin{pmatrix} 0 & -1 \\ -1 & 0 \end{pmatrix}, \quad C = \begin{pmatrix} 0 & -1 \\ 1 & 0 \end{pmatrix} \quad (5.17)$$

and turns the fermion matrix M into a real and antisymmetric matrix.

In [37] a lattice model of the $\mathcal{N} = 1$ Wess-Zumino model has been analysed that is built upon the symmetric derivative. To avoid the species doubling problem a Wilson mass term has been added to the prepotential similar to the case of the $\mathcal{N} = 2$ Wess-Zumino model in Chapter 3. With properly renormalised coupling parameter (as described below) it was shown that the supersymmetric continuum limit is reached. Although this restoration was only analysed for a discretisation based on Wilson fermions the whole line of argument is directly applicable for the SLAC derivative. This follows from the fact that the SLAC derivative for two dimensional models with Yukawa interaction needs no non-local or non-covariant counterterms to achieve a local continuum limit and the lattice degree of divergence of Feynman diagrams will simply be the degree of divergence of the corresponding continuum diagram [40, 41, 108].

The analysis of divergent diagrams in [37] starts from the \mathbb{Z}_2 broken phase and shows that a logarithmic renormalisation of the bare mass parameter is necessary to cancel divergent contributions,

$$\hat{\mu}_0^2 = \hat{\mu}^2 + \frac{\hat{\lambda}}{4\pi} (\ln(\hat{\mu}^2) + c), \quad (5.18)$$

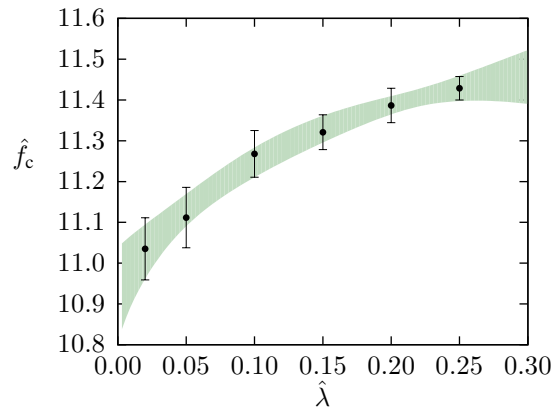


Figure 5.5: Extrapolation of the critical couplings of the bosonic ϕ^4 model based on the SLAC derivative to the continuum limit according to the functional form (5.13).



Figure 5.6: The divergent Feynman diagrams for the full $\mathcal{N} = 1$ Wess-Zumino model in the \mathbb{Z}_2 symmetric phase.

where c may be any constant to fix the renormalisation scale. In analogy to the quenched model this constant is now fixed to obtain

$$\hat{\mu}_0^2 = \hat{\mu}^2 - 1\hat{\lambda}A_{\hat{\mu}^2} \quad (5.19)$$

with $A_{\hat{\mu}^2}$ defined for the SLAC derivative in Eq. (5.15). In contrast to the quenched model only a factor “1” in front of the divergent part is needed that arises from a partial cancellation of the Feynman diagrams shown in Fig. 5.6. Compared to the $\mathcal{N} = 2$ Wess-Zumino model there is *no complete cancellation* but a divergence remains. Again the given renormalisation procedure amounts to a normal ordering of interaction terms with a mass parameter $\hat{\mu}$ in the \mathbb{Z}_2 restored phase. Eventually a renormalised coupling is defined in the continuum limit in the same manner as in the bosonic case according to Eq. (5.12), but now with $\hat{\mu}_0^2$ given through Eq. (5.19).

5.2.2 The Pfaffian

The field content of the $\mathcal{N} = 1$ Wess-Zumino model includes Majorana fermions so that the fermionic part of the path integral may be integrated out to yield

$$\mathcal{Z} = \int D\phi D\psi e^{-S_B[\psi] - \psi^\top M[\phi]\psi} = \int D\phi \text{Pf } M[\phi] e^{-S_B[\phi]}. \quad (5.20)$$

where $M[\phi]$ is an antisymmetric matrix.⁸ The Pfaffian is (up to a sign) the square root of the determinant, $(\text{Pf } M)^2 = \det M$, and follows from Grassmann integration,

$$\text{Pf } M = \frac{1}{2^N N!} \sum_{\sigma \in S_{2N}} \text{sign}(\sigma) \prod_{i=1}^N M_{\sigma_{2i-1}, \sigma_{2i}}. \quad (5.21)$$

In practice the Pfaffian is computed as described in [110] with complexity $\mathcal{O}(N^3)$. Similar to the case of Dirac fermions in Sec. 4.1 this Pfaffian may have a fluctuating sign and Monte-Carlo simulations are carried out with the effective action

$$S_{\text{eff}} = S_B - \ln |\text{Pf } M| = S_B - \frac{1}{2} \ln \det M \quad \Rightarrow \quad \mathcal{Z} = \int D\phi e^{-S_{\text{eff}}[\phi]}. \quad (5.22)$$

Nevertheless, the sign of the Pfaffian must be taken into account by reweighting of measurements.

With the chosen representation of the Clifford algebra the fermion matrix is given by

$$M = \begin{pmatrix} \partial_1^{\text{SLAC}} & \partial_0^{\text{SLAC}} - P' \\ \partial_0^{\text{SLAC}} + P' & -\partial_1^{\text{SLAC}} \end{pmatrix}, \quad (5.23)$$

⁸In general, as it is the case e.g. for supersymmetric Yang-Mills theories [109], the matrix M is not necessarily real. However, it is still antisymmetric but needs not to be anti-Hermitian.

and by using general identities for the Pfaffian of an antisymmetric matrix $A \in \mathbb{R}^{2n \times 2n}$ and general matrix $B \in \mathbb{R}^{2n \times 2n}$,

$$\text{Pf}(A) = (-)^n \text{Pf}(A^\top), \quad \text{Pf}(BAB^\top) = \det(B) \text{Pf}(A), \quad (5.24)$$

transformation properties under the \mathbb{Z}_2 symmetry $\phi \rightarrow -\phi$ of the bosonic potential $P^2/2$ can be derived.

For the general case of a derivative with antisymmetric matrix representation (e.g. for the SLAC derivative) on a lattice with N points

$$\begin{aligned} \text{Pf} \begin{pmatrix} \partial_1 & \partial_0 - P' \\ \partial_0 + P' & -\partial_1 \end{pmatrix} &\stackrel{\text{transpose}}{=} (-)^N \text{Pf} \begin{pmatrix} -\partial_1 & -\partial_0 + P' \\ -\partial_0 - P' & \partial_1 \end{pmatrix} \\ &\begin{pmatrix} 0 & -1 \\ 1 & 0 \end{pmatrix} \\ &= (-)^N \text{Pf} \begin{pmatrix} \partial_1 & \partial_0 + P' \\ \partial_0 - P' & -\partial_1 \end{pmatrix} \end{aligned} \quad (5.25)$$

holds true. Because under the \mathbb{Z}_2 symmetry $P' \rightarrow -P'$ the Pfaffian is *not changed* on even lattice volumes and it is a symmetry of the full model. However, for an odd number of lattice points the Pfaffian changes its sign under $P' \rightarrow -P'$. This (at first sight) inconsistent behaviour where symmetry properties depend on the number of lattice points can be resolved by considering the SLAC derivative. For the SLAC derivative the number of lattice points is directly related to the boundary conditions for the fields. By imposing the natural condition that the spectrum of the lattice derivative operator lies symmetric around the real axis in momentum space an even number of lattice points *must* be used for antiperiodic boundary conditions and an odd number for periodic ones.⁹ In consequence the Pfaffian will change its sign under $P' \rightarrow -P'$ for periodic boundary conditions. Then every field configuration with positive Pfaffian is cancelled in the path integral by a configuration with negative Pfaffian and same bosonic action. This directly implies a vanishing Witten index, which is nothing but the path integral with periodic fermionic boundary conditions. For antiperiodic fermions in the temporal direction the Pfaffian keeps its sign under the \mathbb{Z}_2 symmetry in accordance with the positive definite partition function for the thermal ensemble.

If the lattice derivative would be derived from Wilson fermions the situation changes considerably. In that case the derivative has still an antisymmetric matrix representation but the contribution of the Wilson term leads to

$$\begin{aligned} \text{Pf} \begin{pmatrix} \partial_1 & \partial_0 - P' - \frac{r}{2}\Delta \\ \partial_0 + P' + \frac{r}{2}\Delta & -\partial_1 \end{pmatrix} &\stackrel{\text{transp.}}{=} (-)^N \text{Pf} \begin{pmatrix} -\partial_1 & -\partial_0 + P' + \frac{r}{2}\Delta \\ -\partial_0 - P' - \frac{r}{2}\Delta & \partial_1 \end{pmatrix} \\ &\begin{pmatrix} 0 & -1 \\ 1 & 0 \end{pmatrix} \\ &= (-)^N \text{Pf} \begin{pmatrix} \partial_1 & \partial_0 + P' + \frac{r}{2}\Delta \\ \partial_0 - P' - \frac{r}{2}\Delta & -\partial_1 \end{pmatrix}. \end{aligned} \quad (5.26)$$

Therefore changing the sign of P' can in general only preserve the modulus of the Pfaffian if the Wilson

⁹Nevertheless, the *squared* SLAC derivative can be defined unambiguously for periodic fields with an even number of lattice points.

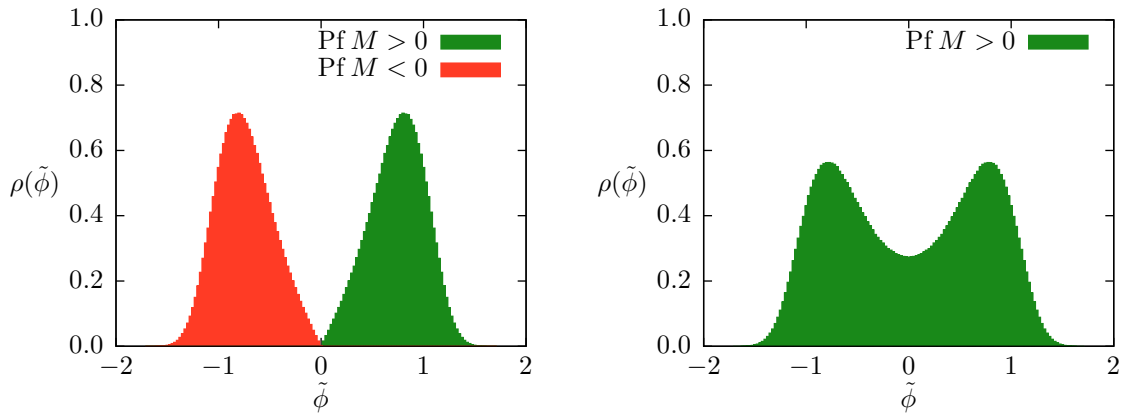


Figure 5.7: Probability density of the volume averaged bosonic field for periodic boundary conditions on a 9×9 lattice (left panel) and thermal boundary conditions on an 8×9 lattice (right panel) at coupling $\hat{f} = 100$ and $\hat{\lambda} = 0.1$. The histograms are computed (with a statistics of $6 \cdot 10^6$ configurations) separately for fixed sign $\text{Pf } M$.

parameter r changes its sign, too. Since the lattice theory is only defined with fixed r the \mathbb{Z}_2 symmetry will be broken by the Wilson term, similar to the $\mathcal{N} = 2$ Wess-Zumino model. For that reason the discretisation based on the SLAC derivative extends the works [37, 103, 111] by implementing the \mathbb{Z}_2 symmetry of the continuum model on the lattice.

5.2.3 Symmetries, boundary conditions, and ground states

The static properties under the \mathbb{Z}_2 symmetry that depend on the boundary conditions for the dynamical fermions can be directly related to the ground state structure of the full model. In the case of broken \mathbb{Z}_2 symmetry one ground state is naturally located in the range of positive $\tilde{\phi} = N^{-1} \sum_x \phi_x$ while the other one has its support at negative $\tilde{\phi}$. The analysis of $\text{sign Pf } M$ reveals that in exactly one of these states the sign changes under changing the boundary conditions. By the change in fermionic boundary conditions the partition function will acquire an insertion of $(-1)^{N_F}$ which exactly implies the existence of one bosonic and one fermionic ground state.

As this is only a static analysis these relations have also been checked in the dynamical ensemble with (small scale) lattice simulations based on periodic and antiperiodic temporal boundary conditions for the fermions at couplings $\hat{\lambda} = 0.1$ and $\hat{f} = 100$ (see Fig. 5.7). The different boundary conditions at finite temperature imply that the functional forms of both histograms need not necessarily coincide. However, all configurations with $\tilde{\phi} > 0$ keep $\text{sign Pf } M$ under a change of fermionic boundary conditions, such that the bosonic ground state is located at $\tilde{\phi} > 0$, while the fermionic has a support $\tilde{\phi} < 0$. These relations have been checked at further couplings $\hat{f} \in [10, 100]$ and $\text{sign } \tilde{\phi} \cdot \text{sign Pf } M > 0$ is found on *every* configuration. Similar to the broken supersymmetric quantum mechanics in Chapter 2 it is necessary to use thermal boundary conditions to have a well defined measure.¹⁰

This choice of thermal boundary conditions has further implications for the analysis of supersymmetry breaking. Apart from the *explicit* supersymmetry breaking introduced in the lattice theory by the finite lattice spacing and finite volume there is a further explicit breaking introduced by the finite temperature. For that reason an analysis of the *spontaneous* supersymmetry breaking in the continuum theory will involve the limit of infinite volume (“thermodynamic limit”), vanishing temperature, and

¹⁰The Pfaffian is found to be strictly positive for finite temperature simulations with several couplings on lattices up to 20×21 . However, for even larger lattices the measurement of the Pfaffian is extremely time consuming and a representative statistics has not been generated.

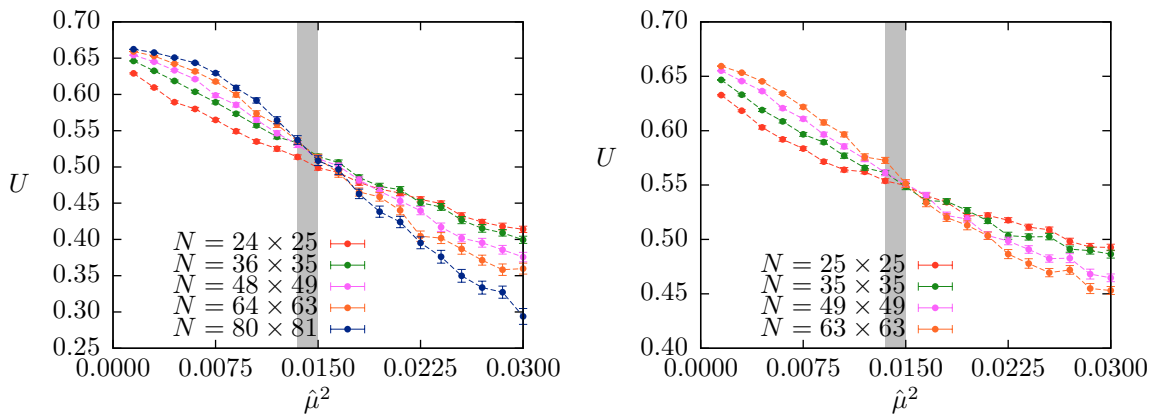


Figure 5.8: Binder cumulants for thermal (left panel) and supersymmetry preserving (right panel) boundary conditions determined at fixed $\hat{\lambda} = 0.3$ and varying $\hat{\mu}^2$ (with a statistic of 10^4 configurations). The shaded area denotes the error bounds of the critical $\hat{\mu}^2$.

vanishing lattice spacing of the lattice theory.

5.2.4 \mathbb{Z}_2 breaking

The numerical survey of the phase diagram starts in analogy to the quenched case with the determination of the phase transition associated to the \mathbb{Z}_2 breaking. The binder cumulant U is thus computed for different volumes at fixed lattice spacing with thermal boundary conditions. However, a direct comparison to results with periodic boundary conditions (without reweighting) turns out to be insightful. For $\hat{\lambda} = 0.3$ the intersection point of the Binder cumulants is independent of the chosen boundary conditions (see Fig. 5.8). This behaviour is explained by the ground state structure at infinite lattice volume. In the \mathbb{Z}_2 broken phase (for small $\hat{\mu}^2$) the system resides in only one ground state with fixed sign $\text{Pf } M$. In that case periodic boundary conditions are impossible and expectation values should not be affected from a change in boundary conditions. For that reason it is quite safe to approach the phase transition from the \mathbb{Z}_2 broken region and extract a critical coupling from a crossing of Binder cumulants *at the edge* of the phase. Nevertheless, *reweighted* expectation values are undefined for periodic boundary conditions in the \mathbb{Z}_2 symmetric phase and the unweighted values may only be used to guide the eye over the phase transition point.

The phase transition has also been determined for two further lattice spacings with thermal boundary conditions (see Fig. 5.9) and the results for every $\hat{\lambda}$ are in full agreement with a critical coupling of $f_c = 21.1(1.1)$. At this point the achieved numerical precision is not sufficient to resolve any running of the critical coupling with the finite lattice spacing mainly because of the accessible lattice sizes. Therefore the determined critical couplings are taken as the continuum critical coupling of the \mathbb{Z}_2 breaking with a broken phase for $f > f_c$ and \mathbb{Z}_2 restoration for $f < f_c$.

5.2.5 Supersymmetry breaking

As found in Sec. 5.2.3 the $\mathcal{N} = 1$ Wess-Zumino model with the chosen prepotential possesses one bosonic and one fermionic ground state which are related through the \mathbb{Z}_2 symmetry. Therefore the spontaneously broken \mathbb{Z}_2 symmetry goes at hand with one definite ground state which will be the supersymmetric one because its partner state is not present in the physical spectrum at infinite volume. On the other hand, if \mathbb{Z}_2 is unbroken there need not be a supersymmetric ground state. So in contrast to the supersymmetric quantum mechanics a restored \mathbb{Z}_2 symmetry does *not necessarily exclude* a supersymmetric ground state and it is necessary to study supersymmetry breaking on its own.

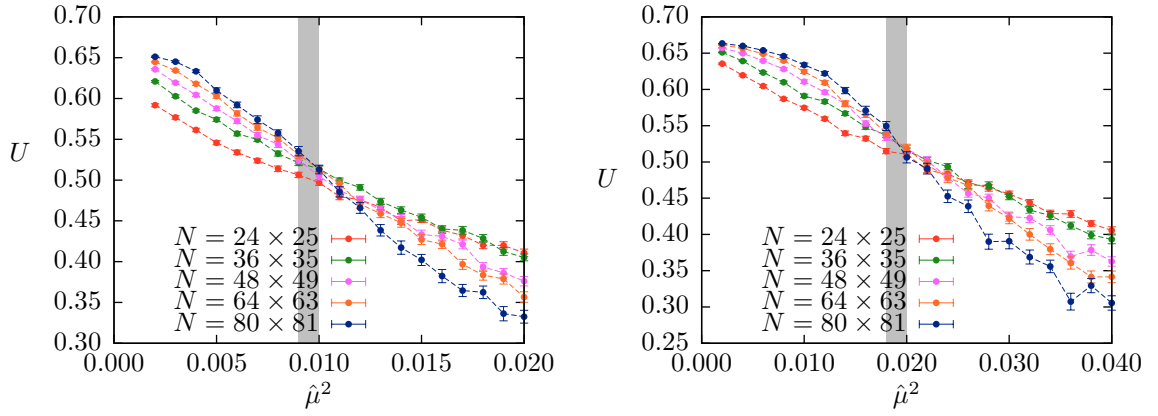


Figure 5.9: Binder cumulants for thermal boundary conditions determined at fixed $\hat{\lambda} = 0.2$ (left panel) and $\hat{\lambda} = 0.4$ (right panel) with a critical $\hat{\mu}^2$ indicated by the shaded area.

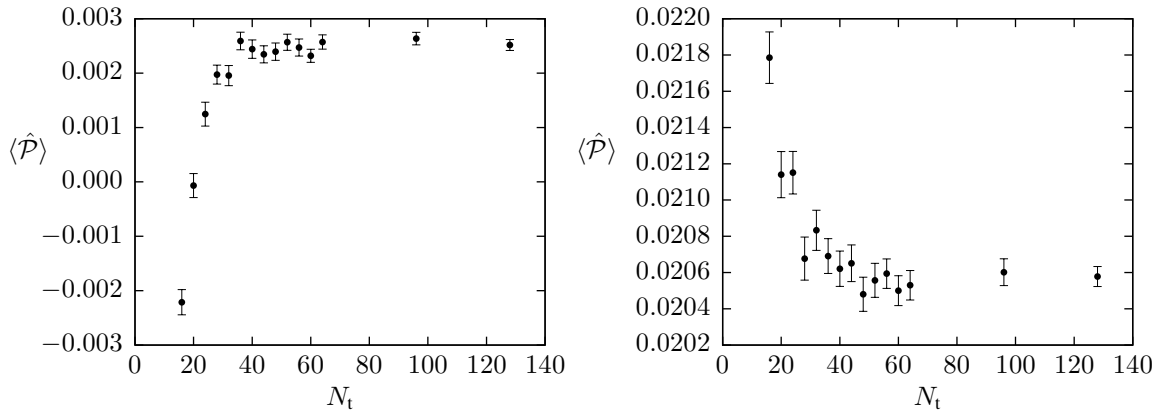


Figure 5.10: Prepotential $\langle \hat{\mathcal{P}} \rangle$ at fixed $\hat{\lambda} = 0.1$ and $N_s = 35$ for the \mathbb{Z}_2 broken phase with $\hat{f} = 100$ (left panel) and the \mathbb{Z}_2 symmetric phase with $f = 10$ (right panel).

The direct way to study supersymmetry breaking is given by Ward identities that are related to the supersymmetry transformation. If there is one broken Ward identity then supersymmetry is broken. The simplest Ward identity which is inherently related to the ground state energy is constructed from the transformation of the fermionic field,

$$\left\langle V^{-1} \int d^2x \delta\psi \right\rangle = \epsilon \left\langle V^{-1} \int d^2x P \right\rangle = 0 \quad \Leftrightarrow \quad \langle \mathcal{P} \rangle = 0$$

$$\text{with } \langle \mathcal{P} \rangle = \langle \hat{\mathcal{P}} \rangle / \sqrt{\hat{\lambda}}, \quad \hat{\mathcal{P}} = N^{-1} \sum_x \left(\frac{\hat{\mu}_0^2}{\sqrt{2\hat{\lambda}}} + \sqrt{\frac{\hat{\lambda}}{2}} \phi^2 \right). \quad (5.27)$$

In that way the dimensionless prepotential \mathcal{P} serves as an indicator for supersymmetry breaking. However, supersymmetry in the chosen discretisation is explicitly broken by the finite lattice spacing, finite temperature, and finite volume. Therefore dynamical supersymmetry breaking can only be examined the limit of infinite lattice volume, $N \rightarrow \infty$, in combination with the continuum limit $a \rightarrow 0$.

The first limit to study here is the limit of vanishing temperature at fixed lattice spacing ($\hat{\lambda} = 0.1$) and fixed spatial volume ($N_s = 35$). Simulations have been performed at $\hat{f} = 100$ (\mathbb{Z}_2 unbroken) and $\hat{f} = 10$ (\mathbb{Z}_2 broken) and the results indicate (see Fig. 5.10) that for $N_t \gtrsim N_s$ the finite temperature corrections become negligible for both phases. Therefore, in the following, lattice geometries are chosen to be nearly quadratic with $N_t = N_s \pm 1$. But already at this point the prepotential is one order of magnitude larger in the \mathbb{Z}_2 symmetric phase than in the \mathbb{Z}_2 broken phase.

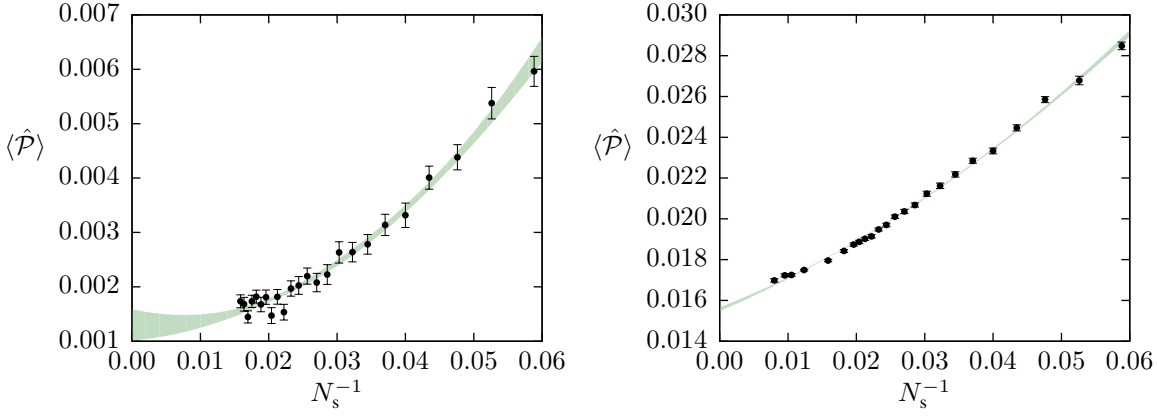


Figure 5.11: Extrapolation of $\langle \hat{\mathcal{P}} \rangle$ to infinite volume at fixed $\hat{\lambda}$ and couplings $\hat{f} = 100$ (left panel) and $\hat{f} = 10$ (right panel). Depending on the lattice size from 10^4 up to $5 \cdot 10^5$ configurations have been used.

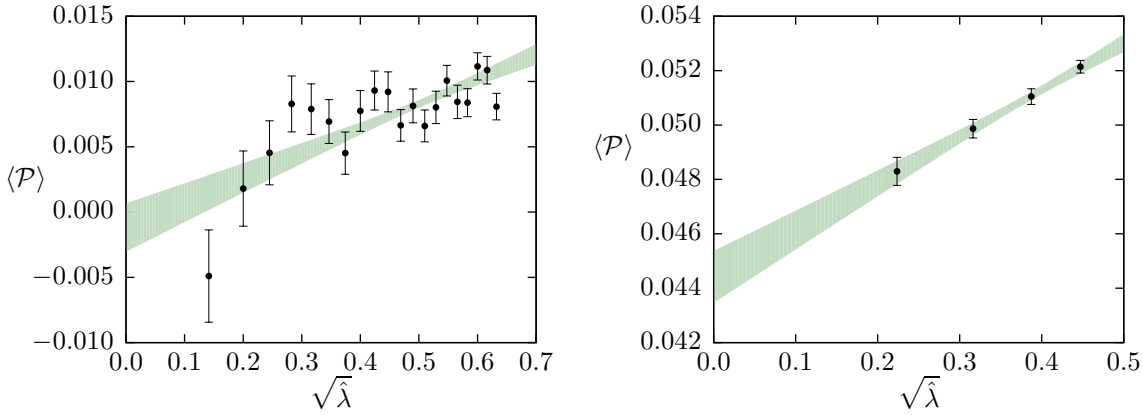


Figure 5.12: For the \mathbb{Z}_2 broken case ($f = 100$, left panel) the Ward identity is fulfilled with $\langle \mathcal{P} \rangle = -0.0012(19)$. For restored \mathbb{Z}_2 symmetry at $f = 10$ (right panel) $\langle \mathcal{P} \rangle = 0.0444(10)$ is obtained.

Now that the finite temperature effects are under control the infinite volume limit can be carried out. Here, the infinite volume limit is taken *before* the continuum limit to finally work out the effect of the finite lattice spacing. To accomplish an extrapolation the data at fixed finite lattice spacing is fitted to a functional form

$$\langle \hat{\mathcal{P}} \rangle(N_s) = A + BN_s^{-1} + CN_s^{-2}. \quad (5.28)$$

and extrapolated to $N_s \rightarrow \infty$. For most of the couplings \hat{f} lattices with $N_s \in \{25, 27, 31, 35, 43, 63\}$ are used. The two fine grained examples for $\hat{\lambda} = 0.1$ and $\hat{f} \in \{10, 100\}$ in Fig. 5.11 illustrate the validity of the chosen extrapolation formula.

The last limit to take is the continuum limit. In the simplest case corrections are of $\mathcal{O}(a)$ and a linear extrapolation to the continuum limit is possible. The extrapolation is performed at each coupling $f \in \{10, 12.5, 16, 20, 25, 40, 100\}$ and is shown in the limiting cases of the present study, at $f = 10$ and $f = 100$, in Fig. 5.12 where the validity of a linear extrapolation is visible. In these cases a complete coincidence between restored \mathbb{Z}_2 symmetry and spontaneously broken supersymmetry is present. All continuum extrapolated Ward identities in the considered coupling range are eventually shown in Fig. 5.13 and listed in Tab. 5.2.

The calculation of the dimensionless prepotential that serves as Ward identity by Eq. (5.27) has shown that after taking all necessary limiting procedures supersymmetry is broken whenever the \mathbb{Z}_2 symmetry is restored. Nevertheless, one inconsistency shows up for f slightly above the critical coupling of \mathbb{Z}_2 breaking (approximately $f \in [f_c, 27]$). In that region the \mathbb{Z}_2 symmetry is broken while

the Ward identity is not fulfilled. This is in contradiction with the fact that a broken \mathbb{Z}_2 symmetry strictly implies a restored supersymmetry after all limits have been taken. Thus an analysis of possible systematic errors is in order.

Firstly the used extrapolation formulae for the specific limits may not be sufficient in every case. Secondly, close to the critical coupling at fixed $\hat{\lambda}$ where a second order phase transition (related to an infinite continuum λ) with diverging correlation length occurs, the considered lattice volumes may still be too small to be in the applicability range for an infinite volume extrapolation with Eq. (5.28). Thirdly the ordering of limits may be of importance. As it has been found in the supersymmetric quantum mechanics and the $\mathcal{N} = 2$ Wess-Zumino model the sign problem that arises from the fermionic part of the action becomes worse for larger volumes at fixed lattice spacing and is weakened in the continuum limit at fixed physical volume. Although the sign problem is completely absent for small lattices sign $\text{Pf } M$ has not been computed for the larger lattices due to the accessible computer power and the numerical complexity of $\mathcal{O}(N^3)$. Therefore sign problems cannot be excluded for large lattice volumes and an extrapolation to infinite volume before the continuum limit has been taken may turn out to be insufficient if no reweighting with sign $\text{Pf } M$ is used.

Even with taking these possible systematic errors into account a supersymmetry breaking phase transition is confirmed where the corresponding critical coupling coincides with that of the \mathbb{Z}_2 phase transition. Nevertheless, the Binder cumulant technique for the \mathbb{Z}_2 symmetry breaking provides a more reliable way to determine the critical coupling because the extrapolation does not directly involve (possibly wrong) extrapolation formulae.

5.2.6 Masses

Ward identities are a fundamental indicator for the restoration of supersymmetry. Since the phase structure is settled further physical observables are of interest. Amongst them masses of particles, or the energy difference between the ground state and the first excited state, to be specific, are the most fundamental ones as has already been seen in the previous models. Here, one expects a fundamentally different behaviour of the masses in the distinct phases [101]. In the supersymmetric phase a degeneracy between the (finite) bosonic and fermionic mass is expected, similar to the $\mathcal{N} = 2$ Wess-Zumino model. For broken supersymmetry a *goldstino* should arise as massless fermionic mode while the physical spacetime volume serves as a regulator for the bosonic mass, which itself eventually vanishes in the infinite volume limit.

The analysis starts with the \mathbb{Z}_2 broken phase at a fixed coupling of $f = 100$. In this phase it is necessary to project the (finite volume) lattice simulations onto one ground state to mimic the sup-

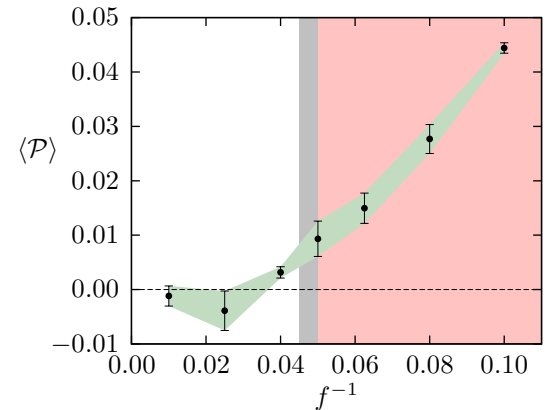


Figure 5.13: Dimensionless prepotential \mathcal{P} over inverse coupling f^{-1} . The region shaded in red indicates the \mathbb{Z}_2 restored coupling range where supersymmetry is broken while the region shaded in gray gives the error bound for the \mathbb{Z}_2 phase transition.

f	$\langle \mathcal{P} \rangle$
100	-0.0012(19)
40	-0.0039(36)
25	0.0032(11)
20	0.0093(33)
16	0.0150(28)
12.5	0.0277(27)
10	0.0444(10)

Table 5.2: Dimensionless prepotential \mathcal{P} after extrapolation to the limit of vanishing temperature, infinite volume, and vanishing lattice spacing (in given order).

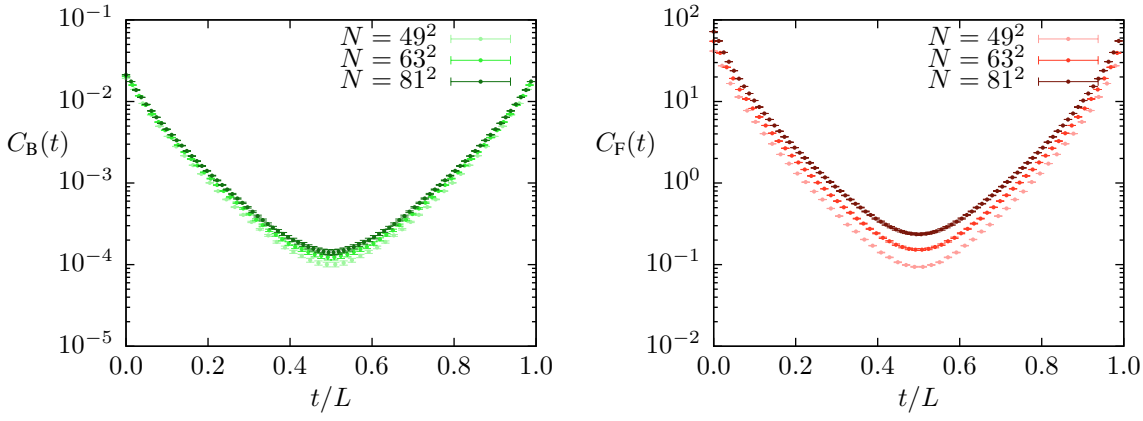


Figure 5.14: Connected bosonic (left panel) and fermionic (right panel) correlator in the \mathbb{Z}_2 broken phase ($f = 100$) at fixed physical volume $L\sqrt{\lambda} = 39.8$ for different lattice spacings.

$N_s = 49$	$N_s = 63$	$N_s = 81$	cont.		$N_s = 49$	$N_s = 63$	$N_s = 81$	cont.
0.379(2)	0.379(4)	0.383(4)	0.389(10)	$L\sqrt{\lambda} = 19.9$	0.300(1)	0.294(2)	0.291(2)	0.277(4)
0.295(4)	0.293(5)	0.293(5)	0.289(12)	$L\sqrt{\lambda} = 28.2$	0.276(1)	0.263(2)	0.262(2)	0.237(5)
0.267(6)	0.262(8)	0.261(7)	0.251(20)	$L\sqrt{\lambda} = 34.5$	0.270(1)	0.261(2)	0.252(2)	0.225(5)
0.238(10)	0.228(12)	0.231(10)	0.218(30)	$L\sqrt{\lambda} = 39.8$	0.270(1)	0.254(3)	0.245(2)	0.204(6)

Table 5.3: Bosonic (left half) and fermionic (right half) masses $m_{B/F}/\sqrt{\lambda}$ for fixed physical volumes $L\sqrt{\lambda}$ and varying lattice spacing together with the continuum extrapolation at coupling $f = 100$.

pression of tunnelling events in the infinite volume limit.¹¹ This is the same technique as analysed in Sec. 3.2.7 for the $\mathcal{N} = 2$ Wess-Zumino model and it is absolutely necessary to finally extrapolate the obtained masses to the infinite volume limit. Since a projection to one ground state is performed it is *not required* to stick to thermal boundary conditions as discussed in Sec. 5.2.4. Thus, in order to remove the supersymmetry breaking introduced by a finite temperature, periodic boundary conditions are used to obtain correlators and masses in the \mathbb{Z}_2 broken phase. Furthermore only square lattices are investigated to simplify the comparison of different lattice spacings and physical volumes.

Masses are extracted from the correlators

$$C_B(t) = N_s^{-2} \sum_{x,x'} \langle \phi_{(t,x)} \phi_{(0,x')} \rangle \quad \text{and} \quad C_F(t) = N_s^{-2} \sum_{\alpha,x,x'} \langle \bar{\psi}_{\alpha,(t,x)} \psi_{\alpha,(0,x')} \rangle \quad (5.29)$$

using a cosh fit in a range $t \in [L/3, 2L/3]$. It is obvious that the correlators at fixed physical volume depend on the lattice spacing (in Fig. 5.14 the fermionic correlator shows larger discretisation errors) and extracted masses must therefore be extrapolated to the continuum limit. The continuum value is reached via a linear extrapolation that has already been used successfully for the continuum extrapolation of results based on the SLAC derivative in an unbroken supersymmetric quantum mechanics in [41]. The results based on $N_s \in \{49, 63, 81\}$ for the bosonic and fermionic mass at four different physical volumes are provided together with the continuum extrapolation in Tab. 5.3 and are shown in Fig. 5.15 (left panel) for finite lattice spacings. Finally an infinite volume extrapolation of the continuum results is necessary. Although one finds that the bosonic masses approach the fermionic partners at larger volumes, as predicted by supersymmetry, their statistical accuracy is not sufficient for a reliable extrapolation. Therefore only the fermionic masses are extrapolated linearly (see Fig. 5.15, right panel) to the infinite volume limit, resulting in $m_F/\sqrt{\lambda} = 0.14(1)$. Unfortunately, the bosonic mass

¹¹Here the configurations are projected without loss of generality to the bosonic ground state.

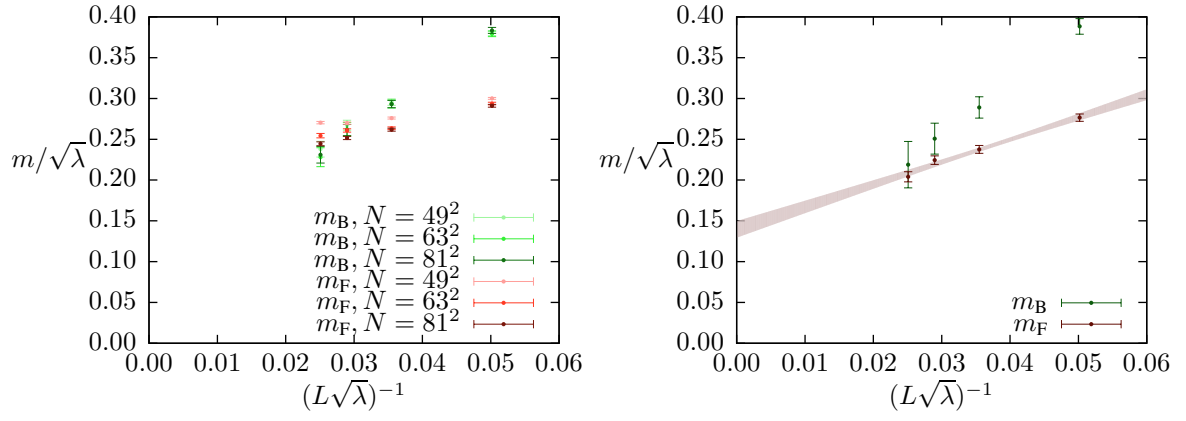


Figure 5.15: Left panel: Masses at finite lattice spacing at coupling $f = 100$. Right panel: Continuum extrapolated masses together with the error bounds of an extrapolation of the fermionic mass to the infinite volume limit (shaded area). 10^6 configurations have been used for each data point.

can only be assumed to take the same limit. Eventually a note concerning the finiteness of the mass is in order at this point. The breaking of the *discrete* \mathbb{Z}_2 symmetry does not imply the existence of Goldstone bosons and a finiteness of the mass is *not excluded*. In contrast, for a restored \mathbb{Z}_2 symmetry there will be a breaking of the *continuous supersymmetry* and it is expected to observe goldstinos.

The analysis of masses is therefore continued in the phase of broken supersymmetry where the \mathbb{Z}_2 symmetry is restored. In this phase it is unavoidable to use thermal boundary conditions since bosonic and fermionic ground state participate equally well in the path integral with unsuppressed tunnelling even at infinite volume. Goldstinos will, similar to the broken supersymmetric quantum mechanics, show up as massless modes in $C'_F(t) = N_s^{-2} \sum_{\alpha, x, x'} \langle \bar{\psi}_{1,(t,x)} \psi_{1,(0,x')} - \bar{\psi}_{2,(t,x)} \psi_{2,(0,x')} \rangle$, the spinor component combination that yields a cosh form for thermal boundary conditions. At $\hat{f} = 10$ the correlator has been computed at varying physical volume with fixed lattice size and for fixed physical volume with varying lattice spacing (see Fig. 5.16).¹² A constant part of the correlator is clearly visible and independent of the physical volume or lattice spacing. This is an unambiguous sign of a goldstino.

To complete the physical picture bosonic masses are calculated. These are expected to vanish in the infinite volume limit as predicted from functional methods in [101]. Again, the *connected* bosonic

¹²The fluctuations showing up in the correlator can be traced back to the non-locality of the SLAC derivative. They will decrease in the continuum limit, as visible in Fig. 5.16 (right panel).

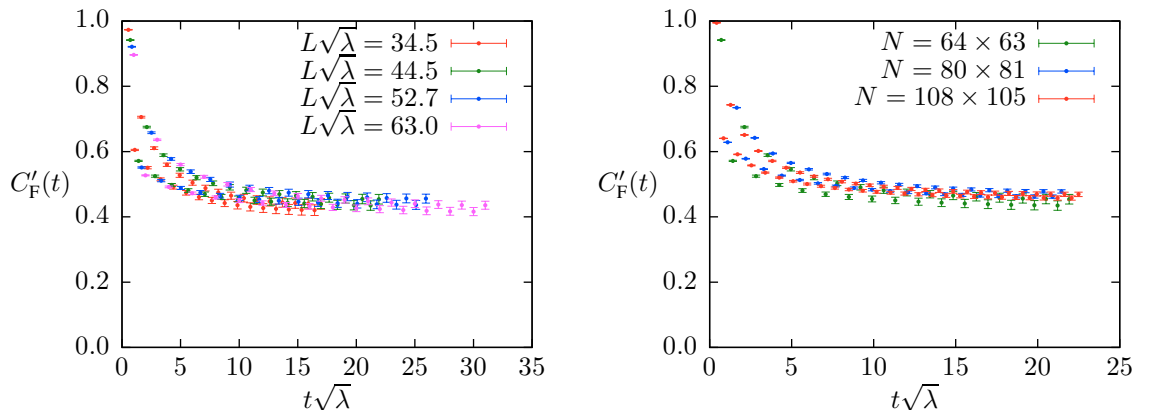


Figure 5.16: Fermionic correlators at coupling $f = 10$ for different physical volumes on a 64×63 lattice (left panel) and for different lattice sizes on a fixed physical volume $L\sqrt{\lambda} = 44.5$ (right panel). For symmetry reasons only the $t/L < 0.5$ range is shown.

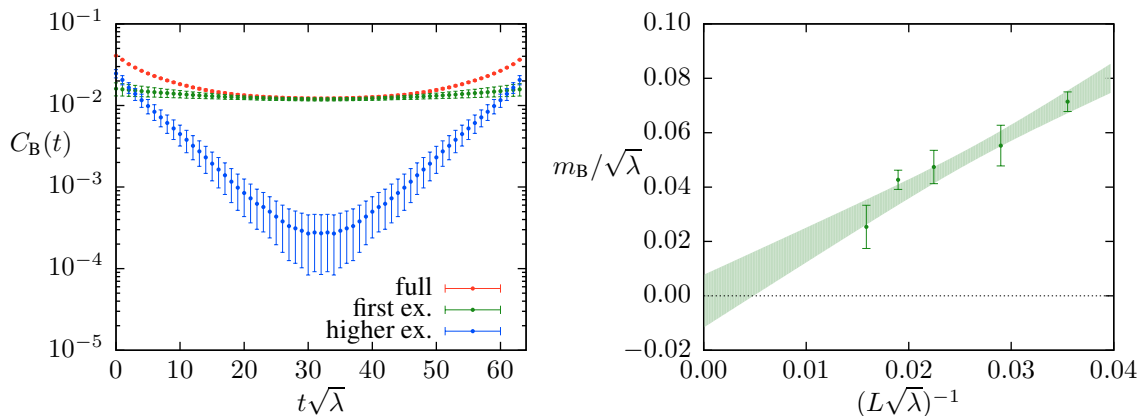


Figure 5.17: *Left panel: Bosonic correlator at coupling $f = 10$ on a 64×63 lattice for fixed physical volume $L\sqrt{\lambda} = 63$ where the contributions of first and higher excited states have been separated. Right panel: Bosonic mass of the first excited state on 64×63 lattices and the infinite volume extrapolation (shaded area) for $f = 10$.*

correlator at $f = 10$ is computed and it is found to be composed of a part with nearly vanishing mass, corresponding to the first excited state, and a part that arises from higher excited states (see Fig. 5.17, left panel).¹³ The masses of the first excited state are now extrapolated (linearly) to infinite volume (see Fig. 5.17, right panel). Here, only constant lattice sizes $N = 64 \times 63$ are used and the continuum limit is not carried out. However, it has been checked for $L\sqrt{\lambda} = 44.5$ on lattice sizes $N = 80 \times 81$ and $N = 108 \times 105$ that the discretisation errors are still below the statistical errors. The infinite volume extrapolation is in agreement with $m_B \propto L^{-1}$ with an extrapolated value of $m_B/\sqrt{\lambda} = -0.002(10)$, i.e. the bosonic mass vanishes after the infrared regulator is removed coinciding with [101].

5.3 Conclusions

The analysis of the $\mathcal{N} = (1, 1)$ Wess-Zumino model in two dimensions aimed at observing and understanding dynamical supersymmetry breaking from first principles. A lattice regularisation based on the SLAC derivative is used and the choice of this regularisation is justified utilising the quenched model where a complete agreement of the obtained critical coupling with the reference value [106] is found.

With this discretisation the \mathbb{Z}_2 symmetry breaking is analysed and a renormalised continuum coupling is defined. For the first time a regulator independent critical coupling is determined from lattice simulations. From the computation of a Ward identity a complete coincidence between the restoration of \mathbb{Z}_2 symmetry and the dynamical breaking of supersymmetry is obtained. The computation of masses in the continuum limit for different physical volumes completes the analysis and agrees with the picture of a finite and equal bosonic and fermionic mass in the supersymmetric phase and the occurrence of a massless goldstino for broken supersymmetry.

In future works it may be checked on the Ward identities by taking the infinite volume limit *after* the continuum limit has been carried out to suppress possible systematic errors arising from the sign problem. Masses of higher excited states could be within reach by using improved correlators. Finally a completely independent calculation with the presented techniques based on another discretisation is desirable, where a formulation based on Wilson fermions [37] is again a natural choice. However, in that case one must ensure that a spontaneous breaking of the \mathbb{Z}_2 symmetry is not influenced by the explicit \mathbb{Z}_2 symmetry breaking induced by the Wilson mass term.

¹³The exponential decay of higher excited states is also visible for $t\sqrt{\lambda} < 10$ in the fermionic correlator, cf. Fig. 5.16.

Nonlinear sigma models

Nonlinear sigma models in two dimensions have long been used as testing ground for strongly coupled gauge theories [42, 112]. They are scale invariant on the classical level and asymptotically free at the quantum level. The ubiquitous $\mathbb{C}P^N$ models possess regular instanton solutions, the topological charges of which yield lower BPS-bounds on the action, they have a chiral anomaly when coupled to fermions, generate a dynamical mass by non-perturbative effects at zero temperature and a thermal mass $\propto g^2 T$ at finite temperature. They have numerous interesting applications to condensed matter physics, e.g. (anti)ferromagnetism, Hall effect, Kondo effect (for a review see [113]), and have also been used to study the sphaleron induced fermion-number violation at high temperature [114].

Supersymmetric nonlinear sigma models with $\mathbb{C}P^N$ and S^N target space have been introduced as supersymmetric extension of the corresponding bosonic models [115–117] with $U(N + 1)$ and $O(N + 1)$, respectively, target space symmetry.¹ The supersymmetric $O(N)$ sigma models are invariant under one supersymmetry. $\mathbb{C}P^N$ spaces admit a Kähler structure such that the two dimensional $\mathbb{C}P^N$ models admit a supersymmetric extension with two supersymmetries. Additionally the $O(3)$ and $\mathbb{C}P^1$ model are completely equivalent so that even for S^2 target space two supersymmetries are present. For both classes of target spaces it was analysed in [15] that these models are free of dynamical supersymmetry breaking. E.g. for the $O(3)$ model there are two bosonic ground states that imply a non-vanishing Witten index which ensures a zero energy ground state invariant under supersymmetry.

The scope of this chapter is twofold. In the first half the topological properties of bosonic $\mathbb{C}P^N$ sigma models with twisted boundary conditions are investigated. Zero modes of minimally coupled and supersymmetric fermions in the background of instantons are constructed. The second half is devoted to the analysis of the supersymmetric $O(3)$ model on the lattice. Basic concepts are introduced in the context of the quenched model. Eventually a target space invariant lattice formulation of the full model based on the SLAC derivative is simulated and supersymmetry restoration is discussed.

6.1 Instantons and fermionic zero modes in twisted $\mathbb{C}P^N$ models

In this section $\mathbb{C}P^N$ models are considered at finite temperature, i.e. *Euclidean models* with imaginary time having period $\beta = 1/k_B T$. These models possess instanton solutions with finite action and the dimension of the moduli space in a given instanton sector depends on the topology of the Euclidean spacetime. For example, on the two-torus the charge- k instantons of $\mathbb{C}P^N$ depend on as many collective parameters as the instantons of $\mathbb{C}P^{N+1}$ with one charge less [118]. For the present analytical investigations space is not compactified such that spacetime is a cylinder.

For suitable field variables the selfduality equation for $\mathbb{C}P^N$ instantons reduces to Cauchy-Riemann conditions such that all instantons are known explicitly for the plane, cylinder, and torus. On the plane they are given by rational functions of the complex coordinate z and on the cylinder by suitable periodic generalisations thereof, see below.

In [119] the twisted $O(3)$ model is introduced (which is equivalent to the $\mathbb{C}P^1$ model) and it is shown that generically the unit charged instantons in this model dissociate into two fractional charged constituents, sometimes called ‘instanton quarks’. Again there is a close analogy to the corresponding situation in Yang-Mills theories, where instantons with nontrivial holonomy along the compact

¹Interestingly, the common naming scheme denotes $\mathbb{C}P^N$ models by their target space but $O(N)$ models by their global symmetry.

direction of a four dimensional cylinder possess magnetic monopoles as constituents [120–123].

Here, [119] will be extended in several directions. First the $k(N+1)$ constituents of $\mathbb{C}P^N$ instantons with charge k and twisted boundary conditions are constructed and their positions, sizes, and fractional charges will be related to the collective parameters of the instantons. Then, the zero modes of the Dirac operator will be calculated and analysed for minimally coupled fermions with quasi-periodic boundary conditions in the background of the twisted instantons. Similar to the case of four dimensional Yang-Mills theories with 1 (or 2) compact dimensions [124–126] these zero modes can be used as tracers for the instanton constituents; they are localised to the latter, to which constituent depends on the boundary condition. The Dirac operator for the supersymmetric extension of the $\mathbb{C}P^N$ models is given by the linearised field equation for the fermions. Also the zero modes of this operator will be calculated.

The analytic studies will be supplemented by numerical simulations. By standard lattice cooling techniques instantons and their constituents can be extracted from a given (thermalised) configuration.² Furthermore the zero modes of the overlap Dirac operator are calculated and analysed on partially cooled configurations.

6.1.1 The $\mathbb{C}P^N$ model in the continuum and on the lattice

The two dimensional $\mathbb{C}P^N$ model [133, 134] can be formulated in terms of a complex $(N+1)$ -vector $u = (u_0, \dots, u_N)^T$ subject to the constraint $u^\dagger u = 1$. The Euclidean action is given by

$$S = \frac{2}{g^2} \int d^2x (D_\mu u)^\dagger D_\mu u, \quad D_\mu = \partial_\mu - iA_\mu. \quad (6.1)$$

It is invariant under local $U(1)$ gauge transformations

$$u_j(x) \mapsto e^{i\lambda(x)} u_j(x), \quad A_\mu(x) \mapsto A_\mu(x) + \partial_\mu \lambda(x), \quad (6.2)$$

as well as global transformations

$$u_j(x) \mapsto \mathcal{U}_{jl} u_l(x) \quad (6.3)$$

with a constant matrix $\mathcal{U} \in U(N+1)$. The gauge field A_μ can be eliminated from the action by using its algebraic equation of motion,

$$A_\mu = -iu^\dagger \partial_\mu u. \quad (6.4)$$

The integer-valued instanton number,

$$Q = \int d^2x q(x) \quad \text{with} \quad q(x) = \frac{1}{2\pi} \epsilon_{\mu\nu} \partial_\mu A_\nu(x), \quad (6.5)$$

can be interpreted as the quantised magnetic flux in a fictitious third dimension. At infinity u must approach a pure gauge, $u(x) \rightarrow e^{i\lambda(x)} c$ and Q is just the winding number of the map $x \rightarrow e^{i\lambda(x)}$ at infinity, an element of the first homotopy group of $U(1)$.

Configurations minimising the action in $S \geq 4\pi|Q|/g^2$ are called (*anti*-)instantons. They fulfil first

²How the corresponding instanton constituents in Yang-Mills theories emerge in the process of cooling/smearing has been studied in [127–132].

order *self-duality equations*. In homogeneous coordinates v_j with

$$u_j = \frac{v_j}{|v|}, \quad j = 0, \dots, N, \quad (6.6)$$

the self-duality equations read

$$\partial_\mu v_j = \mp i \epsilon_{\mu\nu} \partial_\nu v_j, \quad (6.7)$$

which simply are Cauchy-Riemann conditions with respect to the complex coordinate $z = x_1 + ix_0$. The most general instanton solution with instanton number $Q = k \in \mathbb{N}$ can thus be written with $\{v_j(z)\}$, a set of polynomials of z with no common root and maximum degree k . The topological charge density of an instanton configuration then reads

$$q(x) = \frac{1}{4\pi} \Delta \ln |v(z)|^2. \quad (6.8)$$

Lattice formulation

For the bosonic model the lattice regularisation can be obtained as described in [135, 136]. After introducing the matrix-valued gauge invariant field

$$P(x) = u(x)u^\dagger(x), \quad (6.9)$$

which projects onto the one dimensional subspace spanned by u , one finds

$$\text{tr} [\partial_\mu P \partial_\mu P] = 2 \partial_\mu u^\dagger \partial_\mu u + 2 (u^\dagger \partial_\mu u)^2 = g^2 \mathcal{L}. \quad (6.10)$$

This equation, valid for the model defined on a continuous spacetime, is discretised naively with the forward derivative, $\partial_\mu P \mapsto P_{x+\hat{\mu}} - P_x$, such that

$$\text{tr} [\partial_\mu P \partial_\mu P] \mapsto 2d - 2 \sum_\mu \text{tr} [P_x P_{x+\hat{\mu}}]. \quad (6.11)$$

Therefore, the action, up to an irrelevant additive constant, takes the form

$$S = -\frac{2}{g^2} \sum_{x,\mu} \text{tr} [P_x P_{x+\hat{\mu}}] = -\frac{2}{g^2} \sum_{x,\mu} |u_x^\dagger u_{x+\hat{\mu}}|^2. \quad (6.12)$$

The simulations of the lattice models have been performed with the help of an overrelaxation algorithm [136]. In addition, to investigate the topological properties, the lattice configurations have been cooled [137]. For a given configuration one *cooling step* consists of minimising the action locally on a randomly chosen site x . This is achieved by constructing $Q_x = \sum_\mu (P_{x+\hat{\mu}} + P_{x-\hat{\mu}})$ and replacing u_x by the normalised eigenvector corresponding to the largest eigenvalue of Q_x . A *cooling sweep* corresponds to one cooling step per lattice site on average. Using this procedure the instanton constituents naturally emerge from the locally fluctuating fields.

For the topological charge on the lattice the geometric definition of [138] is used that leads to an integer-valued instanton number. This definition and the chosen lattice action are sufficient for the analysis of global topological properties in the vicinity of classical configurations. Thus, results are

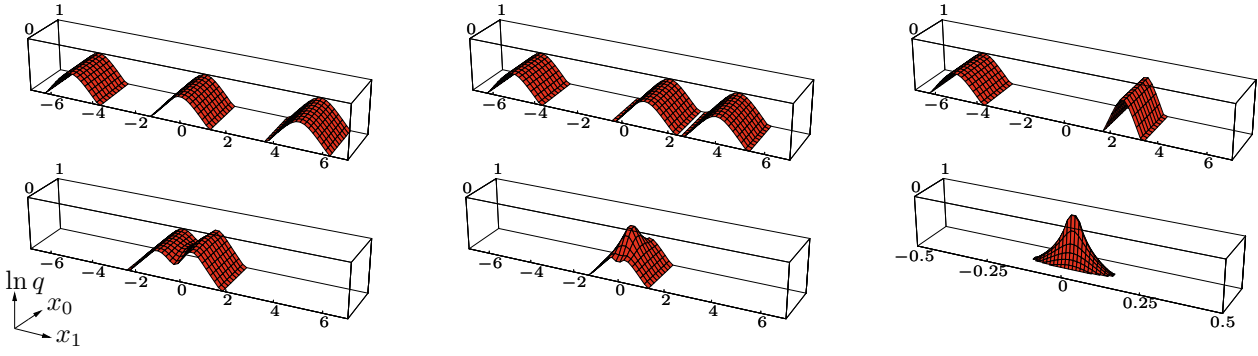


Figure 6.1: *Logarithm of the topological density for the 1-instanton solution of the $\mathbb{C}P^2$ model (see (6.8) and (6.20)) with symmetric constituents, $\mu_1 = \mu_2 = \mu_3 = 1/3$ (cut off below e^{-5}). The parameters λ_i are chosen such that the constituents are localised according to (6.23) from left to right at $(a_1, a_2, a_3) = (-5, 0, 5), (-5, 1, 4), (-5, 7, -2)$ (first line) and $(-1, 0.5, 0.5), (0, 0, 0), (3, -1, -2)$ (second line). Note that the x_1 -range has been changed in the lower right panel.*

not affected by the improper scaling behaviour of the dynamical $\mathbb{C}P^N$ models with $N \leq 2$ [139].

6.1.2 Instantons at finite temperature

For a quantum system at inverse temperature β one identifies $z \sim z + i\beta$. Since β is the only length scale in the problem all lengths are measured in units of β . In particular the coordinates become dimensionless, $z \sim z + i$ is identified. Periodic k -instanton solutions (‘calorons’) are then given by [140, 141]

$$v_{\text{per}}(z) = b^{(0)} + b^{(1)}e^{2\pi z} + \dots + b^{(k)}e^{2\pi k z}. \quad (6.13)$$

By a global $U(N+1)$ symmetry transformation one can rotate v_{per} such that the constant (and per assumption non-vanishing) vector $b^{(k)} \in \mathbb{C}^{N+1}$ points in the 0-direction, $b_j^{(k)} = b_0^{(k)} \delta_{j0}$.

The *twisted model* is only quasi-periodic in the imaginary time direction. This means that the components v_j of v are periodic up to phases $e^{2\pi i \mu_j}$ with $\mu_j \in [0, 1)$, i.e., the vectors v and u are periodic up to a diagonal element of the global symmetry $U(N+1)$. The $U(N+1)$ -invariants like $|v|$ and A_μ and hence also q stay periodic. Without loss of generality the phases are assumed to be ordered according to $\mu_0 \leq \mu_1 \leq \dots \leq \mu_N$.

For the general solutions of the twisted model the Fourier ansatz

$$v_j(z) = e^{2\pi \mu_j z} \sum_{s=-\infty}^{\infty} b_j^{(s)} e^{2\pi s z} \quad (6.14)$$

is considered where the coefficients $b_j^{(s)}$ are demanded to be non-vanishing only for a finite range of s (for each component j). This is because the corresponding maximum and minimum of the powers

$$\kappa_{\max} = \max_{j,s: b_j^{(s)} \neq 0} (s + \mu_j), \quad \kappa_{\min} = \min_{j,s: b_j^{(s)} \neq 0} (s + \mu_j) \quad (6.15)$$

then yield a finite topological charge Q . According to (6.8) one has to compute the following surface integrals

$$Q = \frac{1}{4\pi} \int_0^\beta dx_0 \partial_1 \ln |v|^2 \Big|_{x_1 \rightarrow -\infty}^{x_1 \rightarrow \infty} = \kappa_{\max} - \kappa_{\min} \in \mathbb{N}_0 + \{\mu_j - \mu_l \mid j, l = 0, \dots, n\}. \quad (6.16)$$

Hence the total topological charge in the twisted model can have a fractional part, whose values are restricted by the boundary conditions. By a global transformation κ_{\min} is enforced to be taken on in the 0th component and by a (non-periodic) local transformation one further sets $\mu_0 = 0$ and $\kappa_{\min} = 0$, such that $Q = \kappa_{\max}$. According to Eq. (6.6), these powers also govern the asymptotic values of the fundamental fields u_j .

The following analysis will mainly cover *twisted instantons* with integer-valued instanton number $Q = k \in \mathbb{N}$. They are obtained by $\kappa_{\max} = k$ taken on in the 0th component, i.e., the highest coefficient $b^{(k)}$ points in the 0-direction, $b_j^{(k)} = b_0^{(k)} \delta_{j0}$. Thus one can obtain the components v_j by multiplying each component $v_{\text{per},j}$ from (6.13) with $\exp(2\pi\mu_j z)$, which yields

$$v(z) = \Omega v_{\text{per}}(z), \quad \Omega = \text{diag} \left(e^{2\pi\mu_0 z}, \dots, e^{2\pi\mu_N z} \right). \quad (6.17)$$

For $N = 1$ the known twisted unit charged instanton solution [119] can be recovered in terms of the gauge invariant field

$$\frac{v_1(z)}{v_0(z)} = \frac{b_1^{(0)} e^{2\pi\omega z}}{b_0^{(0)} + b_0^{(1)} e^{2\pi z}}, \quad (6.18)$$

where $\mu_0 = 0$ and $b_1^{(1)} = 0$ is used and μ_1 is denoted by ω .

One-instanton sector

Firstly solutions with unit charge $Q = k = 1$ are considered in order to explore the topological density of the instantons. v is multiplied by a constant such that $b_0^{(0)} = 1$ and afterwards the Euclidean time x_0 is shifted such that $b_0^{(1)}$ becomes real and non-negative. For these choices the density $|v|^2$ only depends on the absolute values $\lambda_j = |b_j^{(0)}|$ with $j = 0, 1, \dots, N$. If, in addition, one defines $\lambda_{N+1} = |b_0^{(1)}|$ and $\mu_{N+1} = 1$, then it can be written in the condensed form

$$|v(z)|^2 = \sum_{i=0}^{N+1} \lambda_i^2 e^{4\pi\mu_i x_1} + 2\lambda_{N+1} e^{2\pi x_1} \cos(2\pi x_0). \quad (6.19)$$

The corresponding topological charge density splits into $N + 1$ constituents at most. For $\mathbb{C}P^2$ this is illustrated in Fig. 6.1 which shows $\ln q(x)$ for various choices of the parameters λ_i .

For the general $\mathbb{C}P^N$ models the occurrence of the constituents can be understood geometrically. To see this more clearly

$$|v(z)|^2 = \sum_{i=0}^{N+1} e^{p_i(x_1)} + 2e^{\tilde{p}(x_1)} \cos(2\pi x_0), \quad (6.20)$$

is considered with

$$p_i(x_1) = 4\pi\mu_i x_1 + 2 \ln \lambda_i, \quad \tilde{p}(x_1) = 2\pi x_1 + \ln \lambda_{N+1}. \quad (6.21)$$

In particular

$$p_0(x_1) = 0, \quad p_{N+1}(x_1) = 4\pi x_1 + 2 \ln \lambda_{N+1} = 2\tilde{p}(x_1). \quad (6.22)$$

Now the graphs of these $N + 3$ linear functions are compared, see Fig. 6.2 for three examples in the $\mathbb{C}P^2$ model amounting to five exponential terms.

The dominant contribution to $|v|^2$ in (6.20) at a fixed point x_1 comes from the exponential term whose graph is above the lines defined by the other exponential terms. Hence $\ln |v|^2$ is piecewise linear

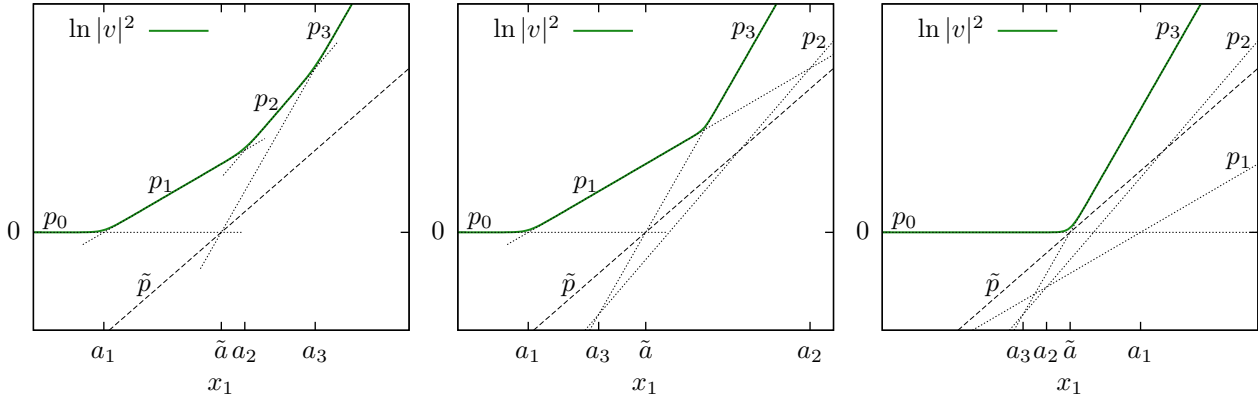


Figure 6.2: $\ln |v|^2$ and exponents p_i and \tilde{p} as a function of x_1 , see Eqs. (6.20) and (6.21), in the $\mathbb{C}\mathbb{P}^2$ model. Left panel: $(a_1, a_2, a_3) = (-5, 1, 4)$, what leads to three well-separated constituents (equivalent to second example in Fig. 6.1). Middle panel: $(a_1, a_2, a_3) = (-5, 7, -2)$, where the second and third constituent merged (equivalent to third example in Fig. 6.1). Right panel: $(a_1, a_2, a_3) = (3, -1, -2)$, where the time-dependent \tilde{p} -term becomes relevant (equivalent to sixth example in Fig. 6.1).

in the direction x_1 up to exponentially small corrections that are maximal in transition regions, where the highest lying graphs intersect.

Note that for a strictly linear $\ln |v|^2$ the topological density $q \propto \Delta \ln |v|^2$ would vanish exactly, whereas at cusps generated by intersections of linear parts the topological density would be a Dirac delta distribution.³ As this is a good approximation to the actual $\ln |v|^2$, it follows that the topological density of the twisted instantons *splits into constituents* localised at the intersection points of the lines. Because of the ordering of the μ 's, the slopes of the linear functions p_i are ordered as well. Note that for $x_1 < -1/(2\pi\mu_1) \ln \lambda_1$ the term $\exp(p_0)$ dominates such that $\ln |v| \approx 0$ on the left of all constituents. Correspondingly, $\ln |v| \approx 4\pi x_1$ on the right of all constituents.

The maximum number of constituents is obtained, if all consecutive graphs intersect separately and above the rest of the graphs, respectively. More precisely said, the twisted instanton of $\mathbb{C}\mathbb{P}^N$ splits into $N + 1$ constituents, if, and only if, $a_1 \ll a_2 \ll \dots \ll a_{N+1}$,⁴ whereas a_i is the intersection point of the lines p_{i-1} and p_i ,

$$a_i = -\frac{\ln(\lambda_i/\lambda_{i-1})}{2\pi(\mu_i - \mu_{i-1})}, \quad i = 1, \dots, N + 1, \quad (6.23)$$

i.e., in particular the twist parameters μ_i are distinct, $0 = \mu_0 < \mu_1 < \dots < \mu_N < \mu_{N+1} = 1$. These positions a_i are arbitrary provided the corresponding λ -parameters are chosen according to

$$\ln \lambda_i = -2\pi \sum_{l=1}^i (\mu_l - \mu_{l-1}) a_l \quad \text{with} \quad \mu_0 = 0. \quad (6.24)$$

Now, the case of the well-separated constituents is discussed. In the neighbourhood of the intersection point a_i of the lines p_{i-1} and p_i one approximates

$$|v(z)|^2 \approx \lambda_{i-1}^2 e^{4\pi\mu_{i-1}x_1} + \lambda_i^2 e^{4\pi\mu_i x_1}, \quad (6.25)$$

³In 3+1 dimensional Yang-Mills theory a similar singular localisation can be obtained in the far-field limit [125, 142].

⁴Thereby the condition $a_{i-1} \ll a_i$ needs not to be taken too literally. It is sufficient, if a_{i-1} is not close to a_i , whereas the required distance is determined by the slopes of $p_i - p_{i-1}$ and $p_{i-1} - p_{i-2}$.

for x_1 not too far from the constituent i ,

$$\frac{1}{2}(a_{i-1} + a_i) \leq x_1 \leq \frac{1}{2}(a_i + a_{i+1}), \quad i = 1, \dots, N + 1. \quad (6.26)$$

For $i = 1$ the lower bound for x_1 is $-\infty$ and for $i = N + 1$ the upper bound is $+\infty$. The contribution to the topological density of the i th constituent is

$$q_{\text{const},i}(x) \approx \frac{\pi(\mu_i - \mu_{i-1})^2}{\cosh^2[2\pi(\mu_i - \mu_{i-1})(x_1 - a_i)]}. \quad (6.27)$$

This shape is the same for all \mathbb{CP}^N models, cf. [119] for the \mathbb{CP}^1 case. The constituent decays exponentially with characteristic length $2\pi(\mu_i - \mu_{i-1})$ (measured in units of β) away from its position a_i . It has a fractional topological charge $Q_{\text{const},i} = \mu_i - \mu_{i-1}$ and these charges add up to 1 as they should. In terms of the linear graphs the fractional topological charge is proportional to the difference of slopes of the lines that meet (which also would give the amplitude of the delta distribution mentioned above), and the total charge is the sum of all slope differences, which indeed bend the graph from p_0 with slope 0 to p_{N+1} with slope 4π eventually.

Neighbouring constituents can merge adding up the fractional topological charges. This can be understood as ‘pulling down’ the line that connects the two constituents in the graph of $\ln|v|^2$, in other words by choosing the corresponding parameter λ_i small (cf. Fig. 6.2, middle panel).

Under which circumstances does the time-dependence of $|v|^2$ contained in the last term of Eq. (6.20), which is proportional to $\exp \tilde{p}(x_1)$, play a role? Since the three graphs of p_0 , p_{N+1} and \tilde{p} intersect at the point $(\tilde{a}, 0)$ with $2\pi\tilde{a} = -\ln \lambda_{N+1}$ one finds

$$\tilde{p}(x_1) \leq \max\{p_0(x_1), p_{N+1}(x_1)\}, \quad (6.28)$$

such that the time-dependent \tilde{p} -term can contribute to the sum in (6.20) only in the neighbourhood of \tilde{a} . Furthermore, all other lines have to lie below $(\tilde{a}, 0)$.⁵ As the slopes of the $p_i(x_1)$, $i = 1, \dots, N$ are between 0 and 1, these graphs are never dominant once they are below $(\tilde{a}, 0)$. This means that only one transition point occurs. Hence time-dependence of the instanton appears iff the topological charge is concentrated in one lump (which can be thought of as all constituents merged, cf. Fig. 6.2, right panel).

The case of non-distinct μ 's can be understood by considering the limit $\mu_j \rightarrow \mu_{j-1}$ for some j 's. Then the corresponding constituent becomes flatter and broader, in the limit it will be invisible and ‘massless’ (i.e., without topological charge/action; this has been ‘eaten’ by the constituent $j + 1$). In this spirit also the periodic solution⁶ is recovered with $\mu_0 = \mu_1 = \dots = \mu_N = 0$. The resulting topological density then consists of only one constituent with unit charge, which can, but does not have to be time-dependent (depending on where the invisible, massless constituents are localised). This can be demonstrated by means of Fig. 6.2 (left panel), i.e., based on the case of well-separated constituents: The limit is taken by sending the slopes of the graphs of p_1 and p_2 to 0. If all positions a_i are kept constant (by adjusting the λ -parameters), then $p_{1,2} \rightarrow 0$ (as functions) and the resulting topological density of the periodic solution is equivalent to the case of all constituents merged in the

⁵If one of the other lines p_i lies well above that point, then the topological density becomes to a good approximation static.

⁶In Yang-Mills theories this amounts to the Harrington-Shepard caloron [143].

twisted model, cf. Fig. 6.1 (lower right panel) and Fig. 6.2 (right panel). If the limit is taken with all λ -parameters kept constant (i.e., by sending the positions $a_{1,2}$ to $-\infty$), then $p_{1,2} \rightarrow 2 \ln \lambda_{1,2}$ can lie well above 0 in the limit and the topological density remains static, though it consists of only one unit charged constituent.

Finally, it is also possible to generate solutions with topological charge less than 1 from these instantons. Technically one has to avoid the asymptotics $\ln |v| \approx 4\pi x_1$ for large x_1 .⁷ Hence, if the corresponding parameter $\lambda_{N+1} = |b_0^{(1)}|$ is vanishing (in the Fourier ansatz there is no integer phase $e^{2\pi z}$), then the total topological charge of the configuration is less than 1. A phase with $\kappa_{\max} < 1$ then gives the total topological charge (i.e., governs the asymptotics for large x_1). Also these configurations consist of constituents with the same formulae for locations, sizes and charges. The number of constituents varies from N down to 1, depending on how many of the remaining parameters λ are zero (in the graph the corresponding lines and intersection points are missing).

Interestingly, all these configurations have in common that the constituents in them are *ordered along the noncompact direction*. This has already been observed in [119] and substantiated by topological considerations. Here it can best be understood from Eq. (6.23). The fractional charge of the i th constituent, $\mu_i - \mu_{i-1}$, is fixed by the twist in the boundary condition. These charges can be realised in isolation only if the ordering of their positions, $a_1 \ll \dots \ll a_{N+1}$, applies. If some a_i do not obey this ordering, then constituents emerge with the sum of the individual fractions as their topological charge. In other words, ‘pulling a constituent through a neighbouring one’ results not in a different ordering but in joining the constituents to a bigger one, cf. Fig. 6.1 (upper and lower right panels).

Notice that by giving up the choice $\kappa_{\min} = 0$ the constituents can be rearranged cyclically; this can become relevant on the lattice, where x_1 is naturally periodic.

This ordering is of course related to the selfduality which dictates that all solutions are functions of $x_1 + ix_0$; antiselfdual solutions will have the opposite ordering. Therefore this phenomenon may be particular to 1 + 1 Euclidean dimensions.

k -instanton sector

The general twisted instanton solution of Eqs. (6.13) and (6.17) with integer-valued topological charge k corresponds to the norm

$$|v(z)|^2 = \sum_{i=0}^{k(N+1)} e^{p_i(x_1)} + 2 \sum_{s=1}^k \sum_{i=0}^{(k-s)(N+1)} e^{\tilde{p}_i^{(s)}(x_1)} \cos(2\pi s x_0 + \varphi_{i+s(N+1)} - \varphi_i), \quad (6.29)$$

where one introduces

$$\begin{aligned} p_i(x_1) &= 4\pi \mu_i x_1 + 2 \ln \lambda_i, \\ \tilde{p}_i^{(s)}(x_1) &= 2\pi(2\mu_i + s)x_1 + \ln(\lambda_i \lambda_{i+s(N+1)}) = \frac{1}{2} [p_i(x_1) + p_{i+s(N+1)}(x_1)]. \end{aligned} \quad (6.30)$$

Two indices of $b_j^{(s)}$ can be encoded into one, $i = s(N+1) + j$, and

$$\lambda_i = |b_j^{(s)}|, \quad \varphi_i = \arg(b_j^{(s)}), \quad \mu_i = \mu_j + s \quad (6.31)$$

⁷Still, the gauge where $\kappa_{\min} = 0$ is used and hence the asymptotics for small x_1 is kept.

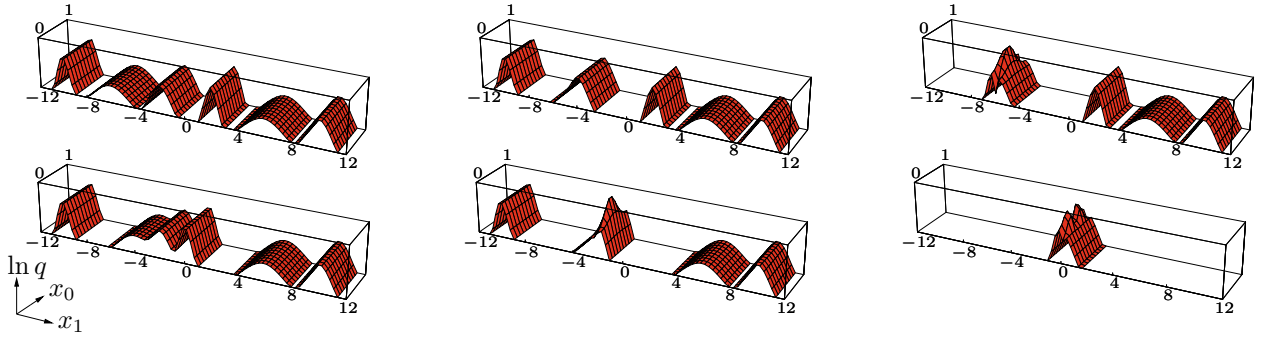


Figure 6.3: *Logarithm of the topological density for the charge-2 instanton of $\mathbb{C}P^2$, with non-symmetric constituents, $\mu_1 = 0.55$, $\mu_2 - \mu_1 = 0.15$, $1 - \mu_2 = 0.3$. The positions of the constituents from left to right are $(a_1, a_2, a_3, a_4, a_5, a_6) = (-10, -6, -2, 2, 6, 10)$, $(-10, -4, -4, 2, 6, 10)$, $(-6, -6, -6, 2, 6, 10)$ (first line) and $(-10, -4, -2, 0, 6, 10)$, $(-10, -2, -2, -2, 6, 10)$, $(0, 0, 0, 0, 0, 0)$ (second line).*

is defined, where $s = 0, \dots, k$, $j = 0, \dots, N$. To arrive at (6.29) the constant vector $b^{(k)}$ is transformed into the 0-direction. Similarly as for the one-instanton solution the constituents are localised at the transition points of the piecewise linear function $|v(z)|^2$. The topological density thus splits into at most $k(N + 1)$ constituents. Well-separated constituents are static and exponentially localised at a_i , $i = 1, \dots, k(N + 1)$, given in an analogous manner as in the 1-instanton case, cf. Eq. (6.23). The constituents carry the fractional charge $\mu_i - \mu_{i-1}$ and from the periodicity of the μ 's in Eq. (6.31) follows that they are again ordered, see also Fig. 6.3 (upper left panel).

Again one finds

$$\tilde{p}_i^{(s)}(x_1) \leq \max \{p_i(x_1), p_{i+s(N+1)}(x_1)\}, \quad (6.32)$$

since the three graphs of p_i , $p_{i+s(N+1)}$ and $\tilde{p}_i^{(s)}$ all intersect at

$$\tilde{a}_i^{(s)} = -\frac{\ln(\lambda_{i+s(N+1)}/\lambda_i)}{2\pi s}. \quad (6.33)$$

Therefore the time-dependent term containing $\tilde{p}_i^{(s)}$ only contributes to the sum in (6.29) if the $s(N + 1)$ constituents at the positions $a_{i+1}, \dots, a_{i+s(N+1)}$ merge to one constituent with integer charge s . The integer s thus determines the maximal frequency of the emerging constituent measured in units of the smallest possible frequency. This behaviour is illustrated in Fig. 6.3 for 2-instanton solutions of the $\mathbb{C}P^2$ model. Note that the freedom φ_i of choosing the complex phase of the parameters $b_j^{(s)}$ enters only as shifts in the time dependence, Eq. (6.29).

Cooling of lattice data

Charge-one instantons of the $\mathbb{C}P^2$ model containing up to the maximal number of three constituents are reproduced with a cooling of lattice data. The simulations have been performed on a 6×100 (temporal \times spatial) lattice at coupling $g^{-2} = 2$. In the spatial direction periodic boundary conditions are imposed whereas in the temporal direction the v_j are twisted with prescribed μ_j . Then a particular configuration is cooled. During the cooling procedure configurations with $|k| = 1$ and two or more well separated constituents are fairly stable even with this type of unimproved cooling (at least up to 10^5 cooling sweeps). Nevertheless, also the typical annihilation of selfdual and antiselfdual constituents is observed. Only a small fraction of configurations is cooled to a state with *three* clearly separated constituents. One of these is shown in Fig. 6.4 at three different cooling stages. More often one ends

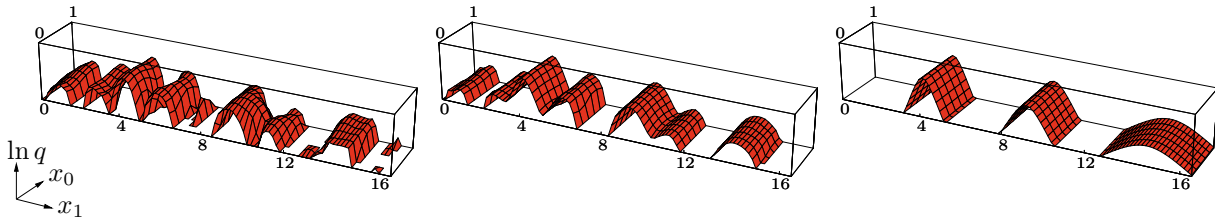


Figure 6.4: The cooling procedure is applied to a $\mathbb{C}P^2$ configuration of the Monte-Carlo ensemble with twists $\mu_1 = 0.15$, $\mu_2 - \mu_1 = 0.5$, $1 - \mu_2 = 0.35$. Three stable constituents emerge after several cooling sweeps (10, 25, 500 from left to right). Here only the positive part of q is shown.

up with only *two* constituents. These results indicate that in a dynamical simulation topological objects with fractional charge (given by the twist parameters μ_j) may be as relevant as they are in Yang-Mills theories.

6.1.3 Zero modes of the Dirac operator

Minimal coupling to fermions

The bosonic $\mathbb{C}P^N$ model is extended by introducing a massless Dirac fermion ψ , for the time being minimally coupled, such that the action has the form

$$S = \int d^2x \left((D_\mu u)^\dagger D_\mu u + i\bar{\psi}\gamma^\mu D_\mu \psi \right). \quad (6.34)$$

Here the chiral representation of the γ -matrices is used for which $\gamma_* = i\gamma^0\gamma^1$ is diagonal,

$$\gamma^0 = \begin{pmatrix} 0 & i \\ -i & 0 \end{pmatrix}, \quad \gamma^1 = \begin{pmatrix} 0 & 1 \\ 1 & 0 \end{pmatrix}, \quad \gamma_* = \begin{pmatrix} -1 & 0 \\ 0 & 1 \end{pmatrix}. \quad (6.35)$$

Splitting the Dirac spinor into chiral components $\psi = (\varphi, \chi)^\top$ the Dirac equation in the background of a self-dual configuration splits into the Weyl equations

$$\begin{aligned} (\partial - u^\dagger \partial u) \varphi &= |v| \partial (|v|^{-1} \varphi) = 0, \\ (\bar{\partial} - u^\dagger \bar{\partial} u) \chi &= |v|^{-1} \bar{\partial} (|v| \chi) = 0, \end{aligned} \quad (6.36)$$

where ∂ and $\bar{\partial}$ denote the derivatives with respect to the complex coordinates $z = x_1 + ix_0$ and $\bar{z} = x_1 - ix_0$. It follows that the zero modes have the form

$$\varphi(x) = f(\bar{z}) |v| \quad \text{and} \quad \chi(x) = \frac{g(z)}{|v|} \quad (6.37)$$

with (anti-)holomorphic functions $f(\bar{z})$ and $g(z)$. Similarly as for the bosonic fields quasi-periodic boundary conditions for the fermion field are imposed,

$$\psi(x_0 + 1, x_1) = e^{2\pi i \zeta} \psi(x_0, x_1) \quad \text{with} \quad \zeta \in [0, 1). \quad (6.38)$$

The functions f, g can be expanded in Fourier series,

$$\begin{aligned}\varphi(x) &= \sum_{s=-\infty}^{\infty} \alpha^{(s)} |v| e^{2\pi(s+\zeta)\bar{z}}, \\ \chi(x) &= \sum_{s=-\infty}^{\infty} \beta^{(s)} e^{2\pi(s+\zeta)z} / |v|.\end{aligned}\tag{6.39}$$

These modes are only square integrable on the cylinder if the coefficients $\alpha^{(s)}, \beta^{(s)}$ and the twist parameter ζ fulfil certain constraints. Recall that the asymptotic behaviour of the general solution with charge $Q = \kappa_{\max}$ ($\kappa_{\min} = 0$ is used) is

$$\lim_{x_1 \rightarrow -\infty} |v| = 1 \quad \text{and} \quad \lim_{x_1 \rightarrow \infty} |v| \propto e^{2\pi Q x_1}.\tag{6.40}$$

Therefore there are no normalisable left-handed zero modes φ .⁸ The quantum number s of the right-handed zero modes is constrained by $0 < s + \zeta < Q$.

This immediately leads to the *index theorem* for right-handed zero modes. For integer topological charge two cases for the fermionic phases ζ must be distinguished:

$$\begin{aligned}\zeta = 0 : & \quad Q - 1 \text{ zero modes,} \\ \zeta \in (0, 1) : & \quad Q \text{ zero modes.}\end{aligned}\tag{6.41}$$

For fractional topological charge the floor function $\lfloor \cdot \rfloor : \mathbb{R} \rightarrow \mathbb{Z}$ and the fractional part $\{\cdot\} : \mathbb{R} \rightarrow [0, 1)$ are introduced such that $Q = \lfloor Q \rfloor + \{Q\}$. It follows

$$\begin{aligned}\zeta = 0 : & \quad \lfloor Q \rfloor \text{ zero modes,} \\ \zeta \in (0, \{Q\}) : & \quad \lfloor Q \rfloor + 1 \text{ zero modes,} \\ \zeta \in [\{Q\}, 1) : & \quad \lfloor Q \rfloor \text{ zero modes.}\end{aligned}\tag{6.42}$$

Now the localisation properties of the (right-handed) zero modes in the background of the instanton with integer charge $Q = k$ are investigated. They have the explicit form

$$|\chi^{(s)}(x)|^2 = e^{4\pi(s+\zeta)x_1 - \ln|v|^2}, \quad s = 0, \dots, k-1,\tag{6.43}$$

with $|v|^2$ from (6.29). It is helpful to first consider well-separated constituents for which $\ln|v|^2$ becomes time-independent and piecewise linear,

$$\ln|v(z)|^2 \approx \{p_i(x_1) = 4\pi\mu_i x_1 + 2 \ln \lambda_i \mid a_i < x_1 < a_{i+1}\},\tag{6.44}$$

as described in Sec. 6.1.2. Clearly, the zero mode has maximal amplitude at points where $\ln|v|^2 - 4\pi(s + \zeta)x_1$ is minimal. At these x_1 the vertical distance between the graphs of the approximately piecewise linear function $\ln|v|^2$ and the linear function $4\pi(s + \zeta)x_1$ is minimal. For $s + \zeta$ in the interval (μ_{i-1}, μ_i) the minimum is at $x_1 = a_i$ where the graphs of p_{i-1} and p_i intersect. The situation is depicted in Fig. 6.5.

⁸For anti-instantons with negative topological charge the left-handed modes become normalisable.

Hence, for generic values of ζ the zero mode is *localised at one constituent*. The profile of the zero mode is symmetric about the constituent i for the particular value $s + \zeta = \frac{1}{2}(\mu_{i-1} + \mu_i)$,

$$|\chi^{(s)}(x)|^2 \propto \frac{1}{\cosh [2\pi(\mu_i - \mu_{i-1})(x_1 - a_i)]}. \quad (6.45)$$

Interestingly, the profile is almost constant between the i th and $(i + 1)$ th constituent for $\zeta = \mu_i$. These ‘bridges’ can be understood by the fact that in this region the graphs of $\ln |v|^2$ and $4\pi(s + \zeta)x_1$ are parallel (up to exponentially small corrections) at these values of s and the fermionic phase ζ .

Altogether the zero modes walk along the ordered set of constituents when changing the fermionic phase ζ . With phases at the bounds $\zeta = 0$ resp. $\zeta = 1$ (or $\zeta = \{Q\}$ for configurations with fractional charge) the zero modes become constants asymptotically. In other words, these zero modes have ‘bridges’ coming from $-\infty$ resp. reaching out to $+\infty$ and hence are not normalisable.

Similar arguments apply if two or more constituents merge. A few examples are given in Fig. 6.6.

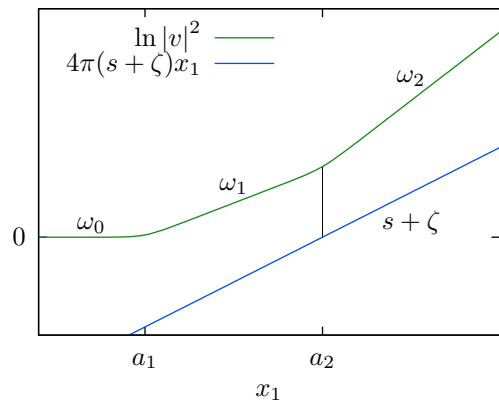


Figure 6.5: Piecewise linear function $\ln |v|^2$ and linear function $4\pi(s + \zeta)x_1$ for the example of $s + \zeta \in (\mu_1, \mu_2)$. For $x_1 < a_1$ the slope of $\ln |v|^2$ is $4\pi\mu_0 = 0$, for $a_1 < x_1 < a_2$ it is $4\pi\mu_1$, for $a_2 < x_1$ it is $4\pi\mu_2$. The vertical distance between the graphs is minimal at a_2 where the zero mode is localised.

Zero modes on the lattice

Using the overlap operator [144] with quasi-periodic boundary conditions for the $U(1)$ gauge field it is possible to analyse its zero modes [145] in the background given by the cooled lattice configurations. In general the overlap operator is given in terms of the Dirac-Wilson operator D_W by

$$D_{\text{ov}} = 1 - \gamma_* \text{sign}(H), \quad H = \gamma_*(\sigma - D_W) \quad (6.46)$$

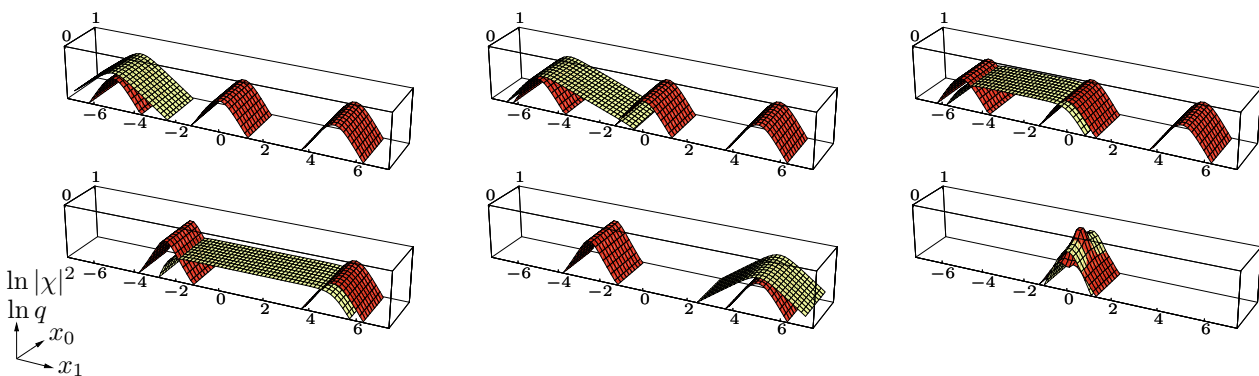


Figure 6.6: Minimally coupled fermionic zero modes (yellow) in the background of 1-instanton constituents (red) of the CP^2 model with symmetric constituents, $\mu_1 = \mu_2 - \mu_1 = 1 - \mu_2 = 1/3$. In the first line the constituents are well-separated at $(a_1, a_2, a_3) = (-5, 0, 5)$, in the second line from left to right they are at $(-2.5, -2.5, 5)$, $(-2.5, -2.5, 5)$, $(0, 0, 0)$, i.e., two respectively three constituents have merged. The fermionic twist is $\zeta = 1/6, 1/4, 1/3$ (first line) and $2/3, 5/6, 1/2$ (second line).

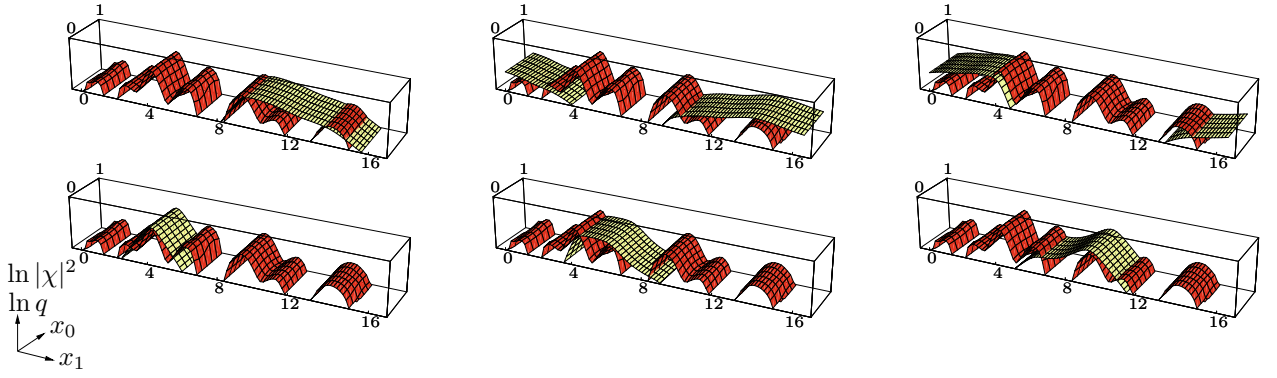


Figure 6.7: Fermionic zero modes of the overlap operator for the $\mathbb{C}P^2$ model with twists $\mu_1 = 0.15$, $\mu_2 - \mu_1 = 0.5$, $1 - \mu_2 = 0.35$ after application of 25 cooling sweeps (compare to Fig. 6.4, middle panel). The fermionic twist is $\zeta = 0, 0.075, 0.15$ (first line) and $\zeta = 0.4, 0.65, 0.825$ (second line).

with a shift parameter $\sigma \in (0, 2)$. For the present computations $\sigma = 1$ was used. Even for moderately cooled configurations do the zero modes of D_{ov} reflect the position of the fully cooled instanton constituents for specific boundary conditions (see Fig. 6.7). Therefore the lattice results are in full agreement with the analytical results and in addition the fermionic zero modes are excellent tracers for instanton constituents on mildly cooled configurations.

Supersymmetric coupling to fermions

The supersymmetric $\mathbb{C}P^N$ model [117, 146] contains $N + 1$ Dirac fermion fields ψ_j , $j = 0, \dots, N$, in addition to the complex scalar fields u_j . Its action is

$$S = \int d^2x \left((D_\mu u)^\dagger (D_\mu u) + i\bar{\psi}\gamma^\mu D_\mu \psi + \frac{1}{4} \left((\bar{\psi}\psi)^2 - (\bar{\psi}\gamma_*\psi)^2 - (\bar{\psi}\gamma^\mu\psi)(\bar{\psi}\gamma_\mu\psi) \right) \right), \quad (6.47)$$

where u and ψ are constrained by

$$u^\dagger u = 1, \quad u^\dagger \psi = \bar{\psi} u = 0. \quad (6.48)$$

Introducing Weyl spinors, $\psi = (\varphi, \chi)^\top$, the model is invariant under the on-shell $\mathcal{N} = (2, 2)$ supersymmetry transformations

$$\begin{aligned} \delta u &= \varepsilon_1 \varphi - \varepsilon_2 \chi, \\ \delta \varphi &= +2i\bar{\varepsilon}_1 \bar{D}u - \bar{\varepsilon}_1 (\bar{\varphi}\varphi)u + \bar{\varepsilon}_2 (\bar{\chi}\varphi)u, \\ \delta \chi &= -2i\bar{\varepsilon}_2 Du + \bar{\varepsilon}_2 (\bar{\chi}\chi)u - \bar{\varepsilon}_1 (\bar{\varphi}\chi)u, \end{aligned} \quad (6.49)$$

with the covariant derivatives

$$D = \partial - u^\dagger \partial u \quad \text{and} \quad \bar{D} = \bar{\partial} - u^\dagger \bar{\partial} u \quad (6.50)$$

and anticommuting parameters $\varepsilon_{1,2}$ satisfying $\varepsilon_2^* = \bar{\varepsilon}_1$ and $\varepsilon_1^* = \bar{\varepsilon}_2$. Both spinors φ and χ have $N + 1$ components.

The *linearised* Dirac equation in an external u -field splits into two Weyl equations,

$$(1 - uu^\dagger) D\varphi = 0 \quad \text{and} \quad (1 - uu^\dagger) \bar{D}\chi = 0. \quad (6.51)$$

For an instanton background with $u = v(z)/|v|$ the Weyl equations simplify to

$$(1 - P_v) \partial (|v|^{-1} \varphi) = (1 - P_v) \bar{\partial} (|v| \chi) = 0, \quad (6.52)$$

where P_v projects onto the holomorphic $v(z)$,

$$P_v = uu^\dagger = \frac{vv^\dagger}{|v|^2}. \quad (6.53)$$

It follows that a left-handed solution reads

$$\varphi(x) = |v| f(\bar{z}), \quad (6.54)$$

where $f(\bar{z})$ is an arbitrary vector of anti-holomorphic functions orthogonal to v . None of these solutions is normalisable. With the help of $P_v \bar{\partial} P_v = \bar{\partial} P_v$ one shows that a right-handed solution has the form

$$\chi(x) = \frac{1}{|v|} (1 - P_v) g(z), \quad (6.55)$$

where $g(z)$ is a vector of holomorphic functions. In order not to break supersymmetry g must fulfil the same boundary conditions as the instanton solution v . Therefore, the choice of fermionic twists is very limited here. Each function g can be constructed by linear combination of the basis elements $\{g^{(j,s)}\}$ defined by

$$g^{(j,s)}(z) = e^{2\pi(s+\mu_j)z} e_j, \quad j = 0, \dots, N, \quad s \in \mathbb{Z}, \quad (6.56)$$

where e_j is the unit vector pointing in direction j . For the corresponding zero modes the squared norm is

$$|\chi^{(j,s)}|^2 = \frac{e^{4\pi(s+\mu_j)x_1}}{|v|^4} \sum_{l \neq j}^n |v_l|^2. \quad (6.57)$$

Normalisability of the zero mode in the k -instanton background requires

$$s = \begin{cases} 0, 1, \dots, k & \text{for } j = 0, \\ 0, 1, \dots, k-1 & \text{for } j = 1, \dots, N. \end{cases} \quad (6.58)$$

In the case of well-separated instanton constituents one can approximate

$$|\chi^{(i)}|^2 \approx \frac{1}{|v|^4} \sum_{l \bmod (N+1) \neq i}^{k(N+1)} e^{p_l(x_1) + 4\pi\mu_i x_1}, \quad (6.59)$$

where $\chi^{(i)} = \chi^{(j,s)}$ is introduced for $i = s(N+1) + j$. The linear functions $p_l(x_1)$ are given in (6.30). Again the maximum of $|\chi^{(i)}|$ is easily found by considering the graphs of the linear functions $2p_l(x_1)$ and $p_l(x_1) + 4\pi\mu_i x_1$. In a logarithmic plot both the numerator and denominator of $|\chi^{(i)}|$ are piecewise

linear. For $x_1 < a_i$ the slope of the numerator is larger and for $x_1 > a_{i+1}$ the slope of the denominator is larger. This is illustrated in Fig. 6.8. Simple geometric arguments about these graphs reveal, that the zero modes $\chi^{(i)}$ with $0 < i < k(N+1)$ split into two constituents located at a_i and a_{i+1} , which have the same amplitude, but decay with different lengths. The zero modes $\chi^{(0)}$ and $\chi^{(k(N+1))}$ have only one maximum at a_1 and $a_{k(N+1)}$, respectively. Some examples are plotted in Fig. 6.9. The general right-handed zero mode has the form

$$\chi = \sum_{i=0}^{k(n+1)} \beta_i \chi^{(i)}. \quad (6.60)$$

Its (squared) norm splits into $k(n+1)$ or less constituents. They have the same analytic form proportional to $\cosh^{-2} [2\pi Q_{\text{const},i}(x_1 - a_i)]$ and are located at the same positions a_i as the instanton constituents.

There exists always a particular zero mode, whose (squared) norm is proportional to the topological density

$$q = \frac{1}{4\pi} \Delta \ln |v|^2 = \frac{1}{\pi} \frac{|v|^2 |\partial v|^2 - |v^\dagger \partial v|^2}{|v|^4}. \quad (6.61)$$

Namely, since the squared norm of χ in (6.55) is

$$|\chi|^2 = \frac{|v|^2 |g|^2 - |v^\dagger g|^2}{|v|^4}, \quad (6.62)$$

the exact relation

$$|\chi(x)|^2 = \pi q(x) \quad (6.63)$$

is obtained for the zero mode with $g = \partial v$, which means that $\beta_i \propto \mu_i \lambda_i$ in Eq. (6.60).

The occurrence of this particular zero mode can also be understood as follows: Any instanton background breaks half of the supersymmetry, namely the one generated by the parameter $\bar{\varepsilon}_2$. If

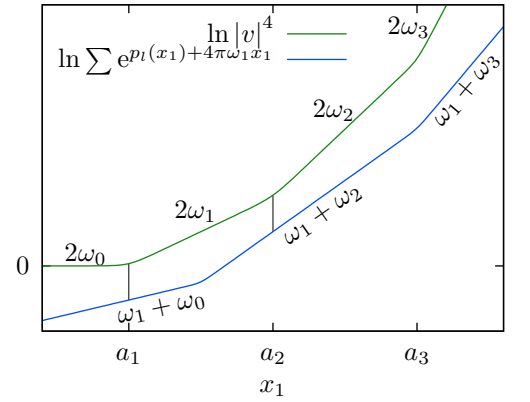


Figure 6.8: Logarithm of denominator and numerator of $|\chi^{(1)}|^2$ in (6.59). The zero mode has two maxima of equal amplitude at a_1 and a_2 .

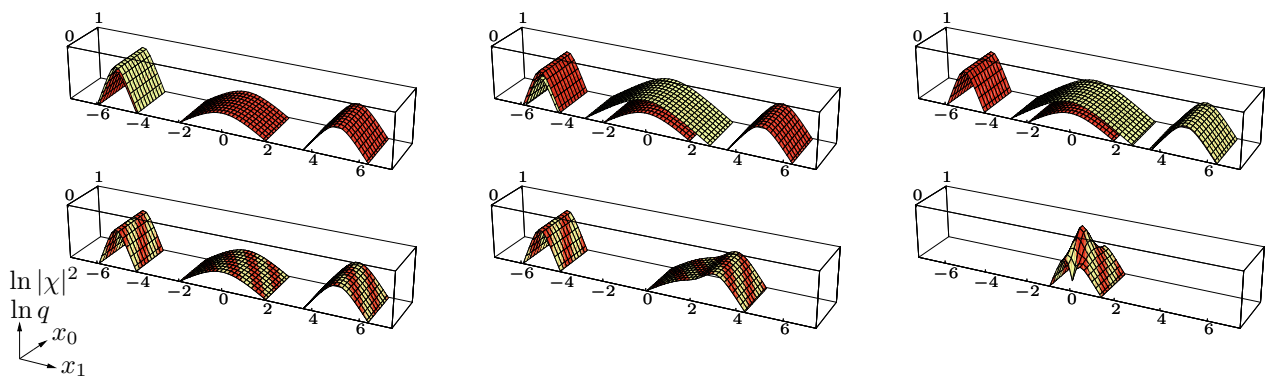


Figure 6.9: Supersymmetrically coupled fermionic zero modes (yellow) in the background of 1-instanton constituents (red) in the $\mathbb{C}P^2$ model with twist parameters $\mu_1 = 0.55$, $\mu_2 - \mu_1 = 0.15$, $1 - \mu_2 = 0.3$. In the first line the zero modes $\chi^{(0)}$, $\chi^{(1)}$ and $\chi^{(2)}$ (from left to right) with instanton locations $(a_1, a_2, a_3) = (-5, 0, 5)$. In the second line the half-BPS state χ_{inst} with instanton locations $(-5, 0, 5)$, $(-5, 2, 3)$, $(0, 0, 0)$ (from left to right).

the configuration $u_{\text{inst}} = v(z)/|v|$, $\psi_{\text{inst}} = 0$ is transformed with the broken symmetry then $\delta\psi_{\text{inst}}$ is inevitably a zero mode of the Dirac operator because the action is invariant under the supersymmetry transformation. In this way a non-vanishing right-handed zero mode

$$\delta\chi_{\text{inst}} = -2i\bar{\varepsilon}_2 Du \propto \frac{1}{|v|} (1 - P_v) \partial v, \quad (6.64)$$

is obtained that is a zero mode with $g \propto \partial v$. Except for irrelevant prefactors, this is exactly the zero mode whose squared norm is equal to the topological density of the instanton.

6.1.4 Conclusions

Integer-charged instantons were constructed and analysed for twisted \mathbb{CP}^N models on a cylinder. The twisted instantons with charge k support $k(N+1)$ constituents. If these constituents are well-separated then they become static lumps. The fractional charges and the shapes of the constituents' topological profile are governed by the phases in the boundary condition (and the scale β). The constituent positions are related to the collective parameters of the twisted instanton and hence free up to the demand that for all constituents to be present their positions must be ordered.

Neighbouring constituents can merge adding up their charges. If at least $N+1$ constituents merge then the resulting lump becomes time-dependent. For a composite object containing multiples of $N+1$ constituents time-dependent terms with higher frequencies contribute, respectively.

The analytic findings are in complete agreement with the corresponding numerical ones. The latter were obtained by cooling lattice configurations of the twisted model with a non-vanishing topological charge.

All fermionic zero modes in the background of the twisted instantons have been determined. This has been achieved for minimally coupled fermions satisfying quasi-periodic boundary conditions in the Euclidean time direction. Similarly as for gauge theories, the zero modes are localised at the positions of the constituents and they may jump from one constituent to the neighbouring one if the boundary conditions for the fermions are changed. Again the analytical findings have been compared to numerical results. To that aim the zero modes of the overlap Dirac operator are determined for lattice configurations with different degrees of cooling. Again analytical and numerical results fully agree, in close analogy with the corresponding situation for $SU(N)$ Yang-Mills theories. Even without much cooling the zero modes detect the constituents of the fully cooled configurations.

In the supersymmetric \mathbb{CP}^N model the Dirac fermions transform according to the fundamental representation of the global $U(N+1)$ symmetry group. The linearised field equations for the $N+1$ fermion flavours define a supersymmetric Dirac operator. The square integrable zero modes of this operator were studied and they generically split into $k(N+1)$ constituents with maxima at the locations of the instanton constituents. There exists always a particular zero mode whose norm squared is equal to the topological charge density of the supporting instanton. This zero mode is generated by the half-broken supersymmetry.

The results are in close parallel to the corresponding findings in $SU(N)$ gauge theories. But since twisted instantons, their constituents and the fermionic zero modes in \mathbb{CP}^N models are much simpler than in gauge theories the results may be useful to shed further light on the relevant degrees of freedom in strongly coupled models at finite temperature. The next natural step would be to include quantum

fluctuations about twisted instantons to study the quantum corrections to the constituent picture.

In the $SU(N)$ gauge theory there is a beautiful construction of the constituents based on the Nahm transform [120]. A similar construction, with Nahm transform as introduced in [118], may further simplify the construction of instanton constituents for twisted $\mathbb{C}P^N$ models.

6.2 Supersymmetric $O(3)$ sigma model on the lattice

For general N , the supersymmetric $O(N)$ sigma model can be constructed from a Hermitian superfield

$$\Phi = n + i\bar{\alpha}\psi + i\frac{1}{2}(\bar{\alpha}\alpha)f \quad (6.65)$$

with N (flavour) components. n and f are real N -component scalar fields, ψ denotes N Majorana spinor components and α is a constant Majorana spinor. Here, the Majorana basis is taken, such that

$$\gamma_0 = \begin{pmatrix} 1 & 0 \\ 0 & -1 \end{pmatrix}, \quad \gamma_1 = \begin{pmatrix} 0 & -1 \\ -1 & 0 \end{pmatrix}, \quad C = \begin{pmatrix} 0 & -1 \\ 1 & 0 \end{pmatrix}, \quad (\bar{\psi}_1, \bar{\psi}_2)_a = (\psi_1, \psi_2)_a C. \quad (6.66)$$

with ‘ a ’ as flavour index of ψ_a . The Lagrangian is given by

$$\mathcal{L} = \frac{1}{2g^2} (\partial_\mu n \cdot \partial^\mu n + i\bar{\psi} \cdot (\not{\partial}\psi) - f \cdot f) \quad (6.67)$$

and is invariant under global $O(N)$ transformations

$$n \rightarrow Rn, \quad \psi \rightarrow R\psi, \quad f \rightarrow Rf \quad \text{with} \quad R \in O(3). \quad (6.68)$$

The nonlinearity, that turns the free (massless) model into an interacting model with dynamical mass generation, is introduced by imposing the constraint $\Phi \cdot \Phi = 1$. In terms of the component fields this constraint reads

$$n \cdot n = 1, \quad n \cdot \psi = 0, \quad n \cdot f = i\frac{1}{2}\bar{\psi} \cdot \psi. \quad (6.69)$$

There is no kinetic term for the auxiliary field f and it may be integrated out, which results in $f = i\frac{1}{2}(\bar{\psi} \cdot \psi)n$. The path integral is thus given in terms of dynamical fields by⁹

$$\mathcal{Z} = \int \mathcal{D}n \mathcal{D}\psi \delta(n \cdot n - 1) \delta(n \cdot \psi) e^{-S[n, \psi]} \\ \text{with} \quad S = \frac{1}{2g^2} \int d^2x (\partial_\mu n \cdot \partial^\mu n + i\bar{\psi} \cdot (\not{\partial}\psi) + \frac{1}{4}(\bar{\psi} \cdot \psi)^2). \quad (6.70)$$

The $\mathcal{N} = (1, 1)$ supersymmetry that arises from the superfield formulation is then given by

$$\delta n = i\bar{\epsilon}\psi, \quad \delta\psi = \gamma^\mu \epsilon \partial_\mu n + i\epsilon \frac{1}{2}(\bar{\psi} \cdot \psi)n. \quad (6.71)$$

Further the constraints (6.69) are invariant under this supersymmetry transformation. Alternatively this model can be written in $\mathbb{C}P^1$ form and is then given by the corresponding action (6.47) with constraints (6.48). In either case the fields obey nonlinear constraints which prevent the fermions from

⁹For the time being field independent prefactors of the path integral \mathcal{Z} are omitted.

being integrated out naively. To solve these constraints a stereographic projection of the superfields can be performed and the model (with holonomic fermions) is given in terms of unconstrained fields ω (complex scalar) and Ψ (Dirac fermion) by the action [42]

$$S = \frac{2}{g^2} \int d^2x \rho^2 \left(\partial_\mu \bar{\omega} \partial_\mu \omega - \frac{i}{2} \bar{\Psi} \not{\partial} \Psi + \frac{i}{2} \partial_\mu \bar{\Psi} \gamma^\mu \Psi + i \rho \bar{\Psi} \gamma^\mu \Psi (\bar{\omega} \partial_\mu \omega - \omega \partial_\mu \bar{\omega}) + \rho^2 (\bar{\Psi} \Psi)^2 \right) \quad (6.72)$$

with measure $\rho = (1 + \bar{\omega} \omega)^{-1}$ and path integral $\mathcal{Z} = \int \mathcal{D}\omega \mathcal{D}\Psi \rho^{-2} e^{-S[\omega, \Psi]}$.¹⁰ This \mathbb{CP}^1 formulation explicitly implements a $\mathcal{N} = (2, 2)$ supersymmetry, which is the case for all two dimensional nonlinear sigma models with Kähler target space [147]. Independent of the formulation there is a spontaneous breaking of the \mathbb{Z}_2 chiral symmetry

$$\psi \rightarrow C\psi \quad \Rightarrow \quad i\bar{\psi} \cdot \psi \rightarrow -i\bar{\psi} \cdot \psi, \quad (6.73)$$

and the two corresponding ground states are the *supersymmetric* bosonic ground states [15].

Using a construction based on a ‘twisted’ form of the continuum action¹¹ with *nilpotent* supercharge an explicit lattice realisation corresponding to the action (6.72) with one preserved (scalar) supersymmetry has been given in [43, 44], which allows for a generalisation to generic \mathbb{CP}^N target spaces and supersymmetric nonlinear sigma models in four dimensions. This lattice construction makes use of the Wilson derivative and therefore introduces soft supersymmetry breaking terms which vanish in the continuum limit. Further this discretisation will break the \mathbb{Z}_2 chiral symmetry and, more importantly, the target space $O(3)$ symmetry. It is the purpose of this section to investigate the problems arising from the broken target space symmetry and to give a lattice regularisation of the supersymmetric $O(3)$ nonlinear sigma model with intact target space symmetry.

6.2.1 Quenched model

To put the regularisation of the full supersymmetric model on solid grounds the applied techniques are exemplified in the bosonic sector of the theory. For the specific case of the bosonic $O(3)$ nonlinear sigma model with action

$$S = \frac{1}{2g^2} \int d^2x \partial_\mu n \cdot \partial^\mu n \quad (6.74)$$

and constraint $n \in S^2$, i.e. $n \cdot n = 1$, there have been lots of algorithmic advances, e.g. powerful cluster algorithms [148] that are applicable for generic $O(N)$ models. Although the naive generalisation of cluster algorithms for generic \mathbb{CP}^N models will not cure the problem of critical slowing down [149] recent formulations based on the strong coupling expansion [150, 151] also allow for an efficient simulation with these target spaces. By using the specialised algorithms precise numerical results have been obtained, e.g. for the renormalised zero momentum four-point coupling [152] and the step scaling function of the finite volume mass gap [153, 154] where exact continuum results have been computed by the thermodynamic Bethe ansatz [155].

The pitfall of these highly efficient lattice techniques is, that a generalisation to include the fermionic dynamics is not straightforward. For that reason the present analysis sticks to a formulation that is suitable for simulations with the hybrid Monte-Carlo algorithm as discussed in Chapter 4.

¹⁰The factor ρ^{-2} in the path integral measure arises from integrating out the auxiliary fields after constructing the model in the superfield formalism.

¹¹This is not to be confused with the twisted boundary conditions in the previous section.

Naive ambiguities and target space invariance of the lattice regularisation

The fermionic constraint $n \cdot \psi = 0$ in the constrained formulation forbids to naively integrate out the fermionic degrees of freedom. Therefore a prescription in terms of unconstrained variables allows for a straightforward treatment of the fermions in the full model. Based on the action (6.72) the corresponding formulation of the bosonic sector is given by the path integral

$$\mathcal{Z} = \int \mathcal{D}\omega \rho^2 e^{-S[\omega]}, \quad S = 2g^{-2} \int d^2x \rho^2 \partial_\mu \omega \partial^\mu \bar{\omega} \quad (6.75)$$

for a complex scalar ω and measure factor $\rho = (1 + \omega\bar{\omega})^{-1}$. The relation to the original field n is given by

$$n = \rho \begin{pmatrix} 2 \operatorname{Re} \omega \\ 2 \operatorname{Im} \omega \\ 1 - \omega\bar{\omega} \end{pmatrix}, \quad \omega = \frac{n_1 + i n_2}{1 + n_3} \quad (6.76)$$

where w arises from a stereographic projection of the unit sphere to the complex plane. If now a regularisation using a nearest neighbour interaction is applied, the lattice action is given by

$$S = 2g^{-2} \sum_{\langle xy \rangle} \rho_{xy}^2 |\omega_x - \omega_y|^2. \quad (6.77)$$

At this point an ambiguity in defining ρ_{xy}^2 arises. ρ_{xy}^2 must interpolate between ρ_x^2 and ρ_y^2 , where both become identical in the continuum limit. Naively, such an interpolation may be based on the arithmetic mean, $\rho_{xy}^2 = \frac{1}{2}(\rho_x^2 + \rho_y^2)$. However, if one performs a variable transformation of the standard action $S = \frac{1}{2g^2} \sum_{\langle xy \rangle} (n_x - n_y)^2$ in the formulation based on the constrained n -field, the geometric mean $\rho_{xy}^2 = \rho_x \rho_y$ is revealed and the underlying global $O(3)$ symmetry of the continuum model is explicitly preserved. By analytical means [102] this continuous global symmetry cannot be broken spontaneously in two dimensions such that $\langle \tilde{n} \rangle = 0$ with volume averaged field $\tilde{n} = V^{-1} \sum_x n$.

To analyse a possible breaking of the $O(3)$ symmetry in the formulation based on the arithmetic mean simulations for both lattice prescriptions have been performed.¹² It is shown in Fig. 6.10 that the

¹²For a simulation with the hybrid Monte-Carlo algorithm the factor ρ^2 of the path integral measure of Eq. (6.75) has

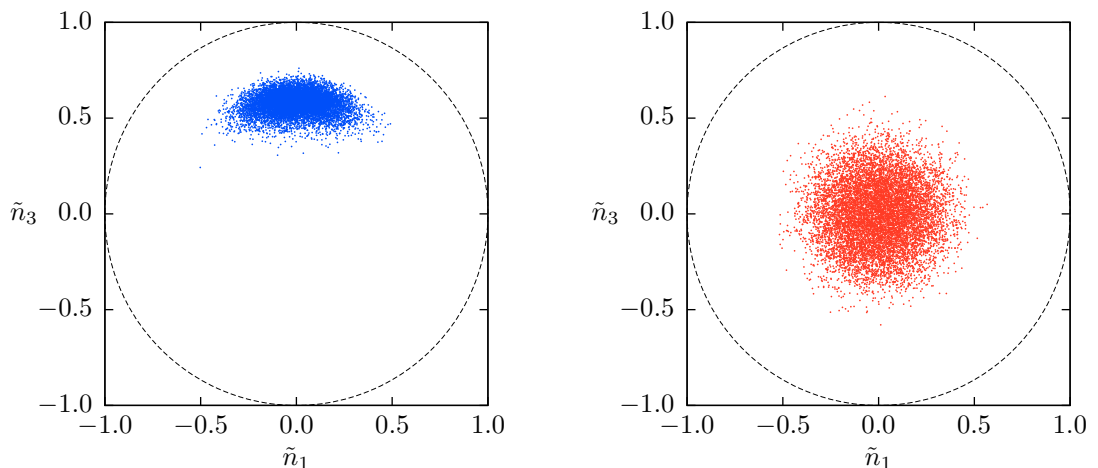


Figure 6.10: Scatter plot (projected to the \tilde{n}_1 - \tilde{n}_3 plane) of the averaged field \tilde{n} for a lattice discretisation based on the arithmetic mean (left panel) and geometric mean (right panel) at $g^{-2} = 1$ and lattice size $N = 10 \times 10$.

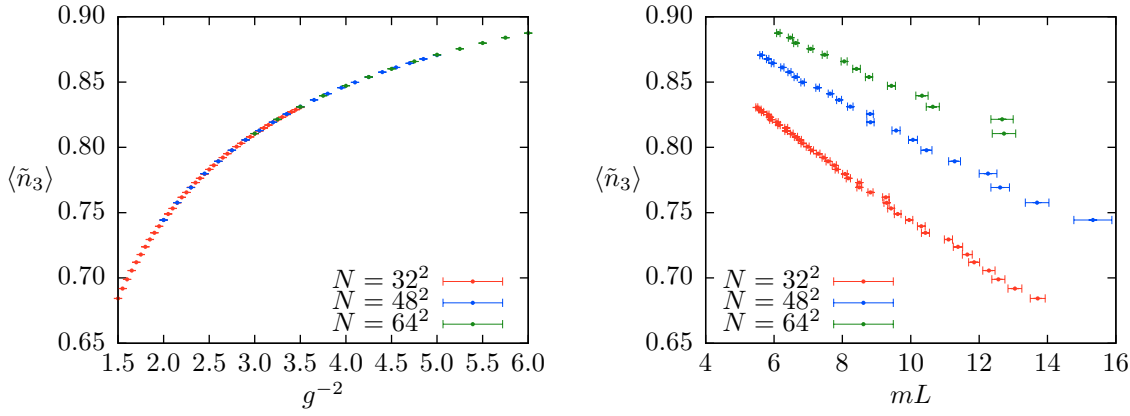


Figure 6.11: The value of $\langle \tilde{n}_3 \rangle$ as indicator for a broken global $O(3)$ symmetry for three lattice volumes plotted over the coupling g^{-2} (left panel) and physical box size (right panel).

lattice prescription based on the geometric mean indeed gives $O(3)$ symmetric results whereas for the arithmetic mean only a $O(2)$ symmetry around the \tilde{n}_3 axis is found, which is a direct consequence of the global $U(1)$ symmetry $\omega \rightarrow e^{i\phi}\omega$. Nevertheless, in the naive continuum limit both prescriptions are expected to coincide. To investigate this issue Monte-Carlo simulations of the model based on the arithmetic mean have been carried out with different lattice sizes N and at different couplings g^{-2} . A restoration of the $O(3)$ symmetry would be indicated by a vanishing $\langle \tilde{n}_3 \rangle$ in the continuum limit. For the considered coupling range $\langle \tilde{n}_3 \rangle$ is found to be independent of the lattice volume such that the result is assumed to be free of finite size effects (see Fig. 6.11, left panel). By fitting the correlator

$$C_B(t) = N_s^{-2} \text{Re} \left\langle \sum_{x,x'} \omega_{(t,x')} \bar{\omega}_{(0,x)} \right\rangle \quad (6.78)$$

to $C_B(t) \propto \cosh(ma(\hat{t} - N_t/2))$ the mass $mL = maN_s$ measured in units of the physical box length can be extracted.¹³ The analysis of $\langle \tilde{n}_3 \rangle$ at fixed physical box size mL in the continuum limit (see Fig. 6.11, right panel) clearly shows that $\langle \tilde{n}_3 \rangle$ grows to a value close to 1 in the limit of fine lattice spacings, i.e. for large N and large g^{-2} . Therefore it is *impossible* to reach the correct $O(3)$ symmetric continuum limit for a regularisation based on the arithmetic mean.

This observation implies that a restoration of the $O(3)$ symmetry *must* be checked in any lattice simulation which is based on a formulation that breaks the global target space symmetry on the lattice. In [43, 44] this symmetry restoration has not been checked explicitly and it will be analysed here in the context of the full supersymmetric model in Sec. 6.2.2 how crucial the breaking of the target space symmetry for the proposed model with an intact supersymmetry on the lattice really is.

Although a straightforward discretisation based of the action (6.75) with unconstrained field ω may break the target space symmetry it is still possible in the bosonic $O(N)$ model to derive a lattice regularised form with unconstrained field that is invariant under the $O(N)$ symmetry. This is reached by discretising the constrained continuum formulation to arrive at a lattice action

$$S = \frac{1}{2g^2} \sum_{x,y} n_x^\top K_{xy} n_y. \quad (6.79)$$

¹³been pulled into the action, $S \rightarrow S - 2 \sum_x \ln \rho_x$.

¹³Due to the $U(1)$ symmetry $\langle \omega \rangle = 0$, and an unconnected part of the correlator $C_B(t)$ vanishes.

with kinetic operator K_{xy} . Afterwards the constraint is solved using $n = \rho \begin{pmatrix} 2w \\ 1 - w^\top w \end{pmatrix}$ with $w \in \mathbb{R}^{N-1}$ and $\rho = (1 + w^\top w)^{-1}$.¹⁴ The resulting action

$$S = \frac{1}{2g^2} \sum_{x,y} \rho_x \rho_y (4w_x^\top K_{xy} w_y + (1 - w_x^\top w_x) K_{xy} (1 - w_y^\top w_y)) \quad (6.80)$$

directly shows the need for ρ_{xy} to be given by the geometric mean and turns into (6.77) if a forward derivative is used to construct K_{xy} while the path integral $\mathcal{Z} = \int Dw \rho^2 e^{-S[w]}$ again includes the measure factor ρ^2 .¹⁵

Universality and the SLAC derivative

The SLAC derivative has been proven to be useful in the context of the Wess-Zumino models and supersymmetric quantum mechanics. Because regularisations based on the SLAC derivative show only small lattice artefacts and do *not break* the \mathbb{Z}_2 chiral symmetry explicitly this derivative shall also be used for the supersymmetric nonlinear sigma model. Since it is not obvious a priori if the SLAC derivative can be used for models with curved target space it will be tested if a known continuum result, namely the scaling of the finite volume mass gap, can be reproduced.

As a quantity accessible even at a finite volume the step scaling function introduced in [153] is computed. At finite spatial volume N_s the mass gap $m(N_s)L$ can be computed by using periodic boundary conditions and a large temporal extent. On every finite lattice the step scaling function Σ is then computed according to

$$\Sigma(2, u, N_s^{-1}) = m(2N_s)2L|_{m(N_s)L=u} \quad (6.81)$$

where the condition $m(N_s)L = u$ determines the bare coupling g^{-2} that is used on both spatial volumes N_s and $2N_s$. This step scaling function is expected to have an universal continuum limit $\sigma(2, u) = \Sigma(2, u, 0) = \lim_{N_s \rightarrow \infty} \Sigma(2, u, N_s^{-1})$ and the precise numerical results so far [150, 154] coincide with this universality. Here, this quantity is reproduced with the SLAC derivative at the popular point

$$u_0 = 1.0595 \quad \text{with} \quad \sigma(2, u_0) = 1.261210. \quad (6.82)$$

Using the SLAC derivative the regularised action is given by

$$S = -\frac{1}{2g^2} \sum_{x,y} n_x^\top (\partial_\mu^{\text{SLAC}})_{xy}^2 n_y \quad (6.83)$$

and the corresponding formulation in terms of unconstrained fields may be derived from Eq. (6.80). However, a simulation is directly possible in terms of the constrained n -field. Since the action is not given by nearest neighbour interactions a cluster algorithm is not applicable and the hybrid Monte-Carlo algorithm will be used instead. For that purpose the field $n \in S^2$ is rewritten by $n = Rn_0$ with a fixed $n_0 \in S^2$ and $R \in SO(3)$ such that the path integral turns into $\mathcal{Z} = \int DR e^{-S[R]}$.¹⁶ The simulation

¹⁴For the $O(3)$ model it is again possible to use a complex scalar $\omega = w_1 + iw_2$.

¹⁵By a similar construction the CP^N model can also be reformulated in terms of unconstrained fields while keeping the full $U(n)$ symmetry.

¹⁶The measure of the path integral is not affected by this variable transformation, i.e. a distribution of R according to

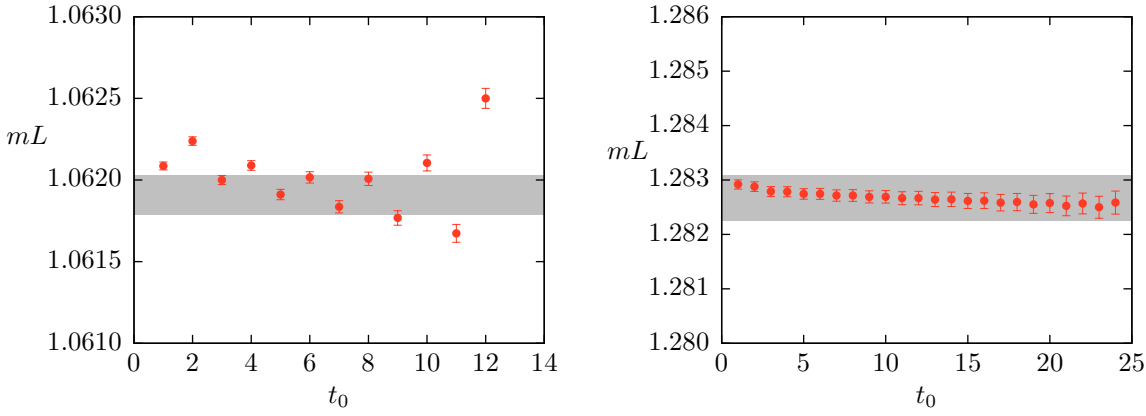


Figure 6.12: Mass gap extracted from a logarithmic cosh fit of the correlator (6.84) in a range $\hat{t} \in [t_0, N_t - t_0]$ for $N_s = 6$ (left panel) and $N_s = 12$ (right panel) at coupling $g^{-2} = 1.309$ for fixed $N_t = 6N_s$. The shaded area denotes the usual accuracy of results at other g^{-2} .

is then implemented with group valued dynamical fields R , the momenta of the ‘Hamiltonian’ used for the hybrid Monte-Carlo algorithm will be elements of the Lie algebra $so(3)$.

The $O(3)$ invariant correlator is naturally defined as

$$C(t) = N_s^{-2} \sum_{x, x'} n_{(t, x')} \cdot n_{(0, x)} \quad (6.84)$$

and the mass is extracted via a fit to

$$C(t) \propto \cosh(ma \cdot (\hat{t} - N_t/2)) \quad (6.85)$$

on a logarithmic scale, to take into account contributions from \hat{t} ’s in the vicinity of $N_t/2$ for a suppression of influences from higher excited states. However, reliable high-precision results can only be determined if possible systematic errors are under control. To actually see the contribution of higher excited states, one is interested in the extracted mass as a function of t_0 where the fit is performed over a range $\hat{t} \in [t_0, N_t - t_0]$ for fixed N_t and N_s . This effect is analysed for $N_s \in \{6, 12\}$ and $N_t = 6N_s$ for a coupling $g^{-2} = 1.309$, which is quite close to the the point of interest (6.82), with extremely large statistics of about $5 \cdot 10^9$ configurations, distributed over 1 000 replica. The results (see Fig. 6.12) show that for the larger lattice the contribution of higher excited states is well below the usual statistical accuracy that is used for most of the results given below (about $2 \cdot 10^8$ configurations). For the smaller lattice there are two competing effects: For small t_0 a contribution of higher states is well visible whereas for large t_0 the fluctuations arising from the non-locality of the SLAC derivative begin to grow. Therefore the optimal choice, that leads to systematic errors at the order of statistical ones, is given by $t_0 = N_s$ and will be used in the following. The second possible systematic error is given by the finite N_t . For N_t too small a thermal contribution to the mass gap will be present. This effect is investigated by keeping $t_0 = N_s$ fixed but varying N_t , see Fig. 6.13 for $N_s \in \{6, 12\}$. For the smaller lattice the contributions at small N_t are more pronounced and become negligible for $N_t > 6N_s$ while for the larger lattice $N_t > 5N_s$ is sufficient. To be unaffected by these systematic errors $N_t = 8N_s$ ($N_t = 6N_s$) is used for the smaller (larger, respectively) lattice of each step scaling computation.

the Haar measure on $SO(3)$ will gain a flat distribution of $n = Rn_0$ on S^2 . Only an irrelevant constant measure factor corresponding to the local $U(1)$ symmetry, that leaves Rn_0 invariant, is obtained.

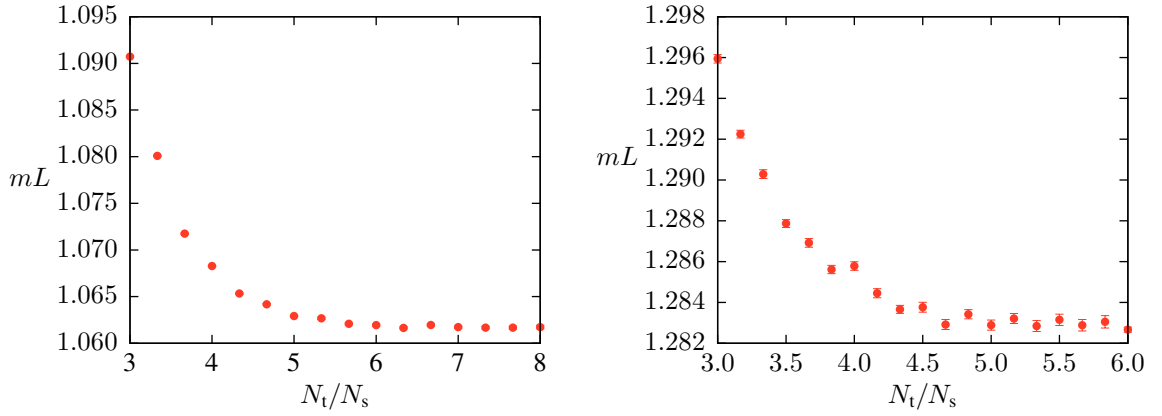


Figure 6.13: Mass gap extracted from a logarithmic cosh fit of the correlator (6.84) in a range $\hat{t} \in [N_s, N_t - N_s]$ for $N_s = 6$ (left panel) and $N_s = 12$ (right panel) at coupling $\beta = 1.309$ for different N_t/N_s .

With the systematic errors under control it is possible to compute the step scaling function in the continuum limit. For that reason the couplings are tuned to provide nearly a mass gap according to u_0 on the smaller lattice with sizes $N_s \in \{4, 6, 8, 10, 12, 16, 20\}$. The corresponding $\Sigma(2, u, N_s^{-1})$ are plotted over u for a subset of these N_s in Fig. 6.14 (left panel), and a linear interpolation based on eight different coupling g^{-2} allows for the extraction of $\Sigma(2, u_0, N_s^{-1})$ at the point $u_0 = 1.0595$ (cf. Tab. 6.1 for explicit values). By applying Symanzik's theory of lattice artefacts it has been calculated in [154] that finite a corrections are of order $\mathcal{O}(a^2(\ln a)^3)$ and appear *nearly linear* for a large range of computationally accessible lattice sizes [156]. For that reason an extrapolation to $a = 0$ based on the formula

$$\Sigma(2, u_0, N_s^{-1}) = \sigma(2, u_0) + A \cdot \left(\frac{B}{N_s}\right)^2 \left(\ln \frac{B}{N_s}\right)^3 \quad (6.86)$$

is used. Only the results for $N_t = 4$ have been omitted because of the large systematic errors introduced by the fluctuations arising from the SLAC derivative for large lattice spacings. The extrapolation is shown in Fig. 6.14 (right panel) and a value of $\sigma(2, u_0) = 1.2604(13)$ is extracted in complete agreement with the exactly known result in the continuum limit of Eq. (6.82). Therefore a discretisation of the (bosonic) $O(3)$ nonlinear sigma model with the SLAC derivative is feasible and may also be used for the full supersymmetric model.

N_s	$\Sigma(2, u_0, N_s^{-1})$	g^{-2}
4	1.28914(19)	1.22906(6)
6	1.27938(18)	1.31071(5)
8	1.27368(34)	1.36526(9)
10	1.27049(31)	1.40622(8)
12	1.26742(33)	1.43903(8)
16	1.26587(35)	1.48986(8)
20	1.26416(70)	1.52870(12)

Table 6.1: Value of the step scaling function $\Sigma(2, u_0, N_s^{-1})$ after interpolating to $u_0 = 1.0595$ for different spatial lattice sizes N_s and corresponding g^{-2} at which $m(N_s)L = u_0$ is reached.

6.2.2 Supersymmetric model

It has been found in the setting of the quenched model that a broken target space symmetry in the lattice formulation may prohibit the restoration of this symmetry in the continuum limit of the quantum theory even though in the (naive) classical continuum limit the symmetry is recovered. For that reason there is need for a reinvestigation of the supersymmetry preserving lattice formulation of [43, 44] with an emphasis on that restoration. To be unaffected by this broken global symmetry a formulation of the supersymmetric $O(3)$ nonlinear sigma model will be constructed on the lattice that is explicitly invariant under the global $O(3)$ symmetry. Eventually the dynamics of this formulation is investigated with the SLAC derivative.

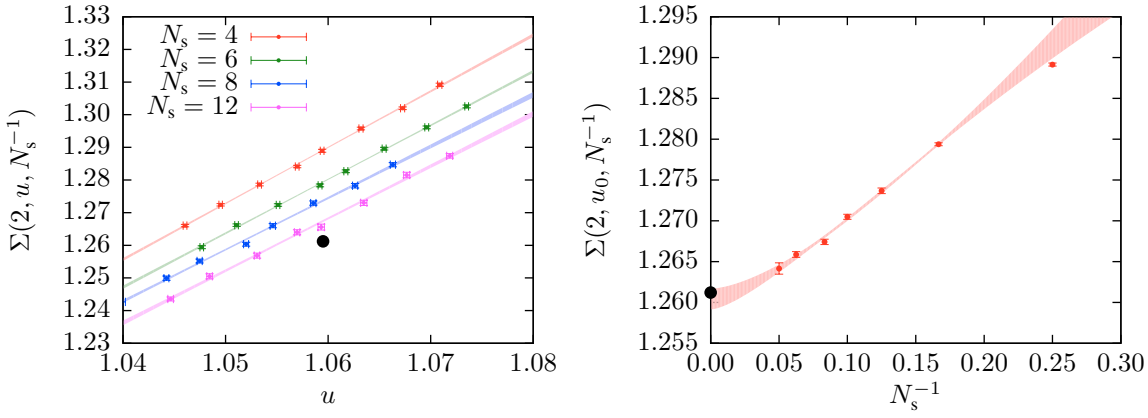


Figure 6.14: Left panel: Step scaling function for lattices with spatial size $N_s \in \{4, 6, 8, 12\}$. Shaded regions indicate error bounds of a linear interpolation. Right panel: Continuum limit of the step scaling function for $u_0 = 1.0595$. The shaded area indicates the error bounds of a fit according to Eq. (6.86), where the value for $N_s^{-1} = 0.25$ has been omitted. The black dot marks the continuum value given in Eq. (6.82).

Drawbacks of a Q exact lattice formulation

The formulation of [43, 44] is constructed by starting from the $\mathbb{C}P^1$ formulation of the $O(3)$ sigma model. It has been possible to give a Q exact formulation where Q denotes the generator of a ‘twisted’ supersymmetry. Furthermore it has been checked for a restoration of corresponding Ward identities and for a non-vanishing chiral condensate. These results imply that supersymmetry is restored although the used Wilson mass breaks supersymmetry softly. The explicit action and path integral are given after a Hubbard-Stratonovich transformation [157], to get rid of the four fermion interaction, in terms of complex scalars $\omega = \omega_1 + i\omega_2$, $\sigma = \sigma_1 + i\sigma_2$ and Dirac fermion Ψ by

$$\mathcal{Z} = \int Dw D\sigma D\Psi \rho^{-2} e^{-S[\omega, \sigma, \Psi]} \quad \text{with} \quad (6.87)$$

$$S = \underbrace{\frac{2}{g^2} \sum_x (\rho_x^2 (\Delta_+^s \omega)_x (\Delta_-^s \bar{\omega})_x + \rho_x^2 (m_W \omega)_x (m_W \bar{\omega})_x + \frac{1}{2} \sigma_x \bar{\sigma}_x)}_{=S_B} + \frac{2}{g^2} \bar{\Psi} M[\omega, \sigma] \Psi.$$

The fermion matrix is given in the chiral basis by

$$M[\omega, \sigma] = \begin{pmatrix} \frac{\rho^2}{2} m_W - \rho^3 \bar{\omega} (m_W \omega) + \text{h.c.} & \rho^2 (\Delta_+^s - 2\rho \bar{\omega} (\Delta_+^s \omega) + \sigma) \\ \rho^2 (\Delta_-^s + 2\rho \omega (\Delta_-^s \bar{\omega}) - \bar{\sigma}) & \frac{\rho^2}{2} m_W - \rho^3 \bar{\omega} (m_W \omega) + \text{h.c.} \end{pmatrix}. \quad (6.88)$$

Further the definitions $m_W = \frac{1}{2} (\Delta_+^+ \Delta_-^- + \Delta_-^+ \Delta_+^-)$, $\Delta_\pm = \Delta_1 \pm i\Delta_2$, and $\Delta_\mu^s = \frac{1}{2} (\Delta_\mu^+ + \Delta_\mu^-)$ are used, where Δ^\pm denotes the usual forward and backward derivative operators. To not break supersymmetry periodic boundary conditions must be used also for the fermions. The difference to a straightforward discretisation is given by an *improvement term* ΔS that vanishes in the continuum theory, similar to the case of the Nicolai improved action in the $\mathcal{N} = 2$ Wess-Zumino model,

$$\Delta S = \frac{4}{g^2} \sum_x \rho_x^2 (\Delta_1^s \omega_2 \Delta_2^s \omega_1 - \Delta_1^s \omega_1 \Delta_2^s \omega_2). \quad (6.89)$$

For the simulation of this model the hybrid Monte-Carlo algorithm with the naive fermionic action

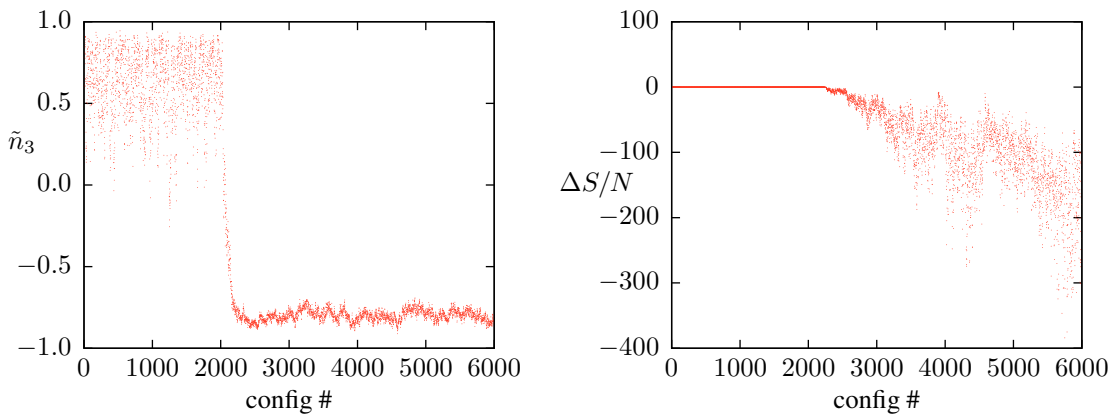


Figure 6.15: Monte-Carlo timeline of \tilde{n}_3 (left panel) and ΔS (right panel) for a simulation of the lattice model (6.87) at coupling $g^{-2} = 1.5$ on an 8×8 lattice.

is used. This has the advantage that no additional fluctuations and possible instabilities, that arise from an approximation of the fermion determinant by pseudo-fermions, overshadow potential conceptual shortcomings of the lattice formulation.

In close analogy to the $\mathcal{N} = 2$ Wess-Zumino model (see Sec. 3.2.1) the improvement term is analysed for a lattice size of $N = 8 \times 8$ at coupling $g^{-2} = 1.5$. During the whole simulation a value of $S_B \approx 2N$ is found (with statistical fluctuations of about 10%) in accordance with the simplest Ward identity [44], which is a consequence of the (nearly, up to the Wilson mass) lattice supersymmetry. However, the Monte-Carlo timelines of \tilde{n}_3 (as defined in the quenched model in Eq. (6.76)) and ΔS can shed some light on the influence of the improvement term on the dynamics, see Fig. 6.15. At a certain point in the simulation the value of \tilde{n}_3 freezes out and the improvement term starts growing largely negative.¹⁷ Just as for the Nicolai improved Wess-Zumino model the simulation is driven away from the continuum physics, where ΔS must vanish, into an unphysical phase.¹⁸ This implies that the severe problems of a supersymmetrically improved action must be taken into account also for simulation of supersymmetric sigma models. For that reason only configurations from the physical phase with nearly vanishing improvement term should be taken into account for the computation of expectation values. But similar to the Wess-Zumino model it has been found that tunnelling events to the unphysical phase are hampered for larger lattices and larger g^{-2} , i.e. in the continuum limit. Nevertheless, from these observations it may be proposed that similar effects could arise in other lattice models with exact supersymmetry that are constructed from a (Q exact) twisting procedure, e.g. two dimensional $\mathcal{N} = 2$ super Yang-Mills [158].

But why did this instability not show up in the results of [44]? The explanation may lie in the used rational hybrid Monte-Carlo algorithm. As explained in Sec. 4.4 spectral bounds must be chosen to cover the spectrum of $M^\dagger M$. Typically these are obtained by test runs with rather pessimistic bounds and *small statistics*, such that only the physical phase with $\Delta S \approx 0$ is present. But for the simulation that is shown in Fig. 6.15 the lowest eigenvalue of $M^\dagger M$ decreases by a factor of 10^{-5} when entering the unphysical phase.¹⁹ For that reason the rational hybrid Monte-Carlo algorithm with spectral bounds that are not applicable to the whole simulation will be an *inexact* algorithm and will give an arbitrarily

¹⁷Every other part of the bosonic action S_B is positive definite.

¹⁸On the configurations before the simulation breaks down the normalised improvement term $\Delta S/N$ fluctuates around zero with a width of about 0.002.

¹⁹The largest eigenvalue of $M^\dagger M$ is kept at the same order of magnitude in the unphysical phase.

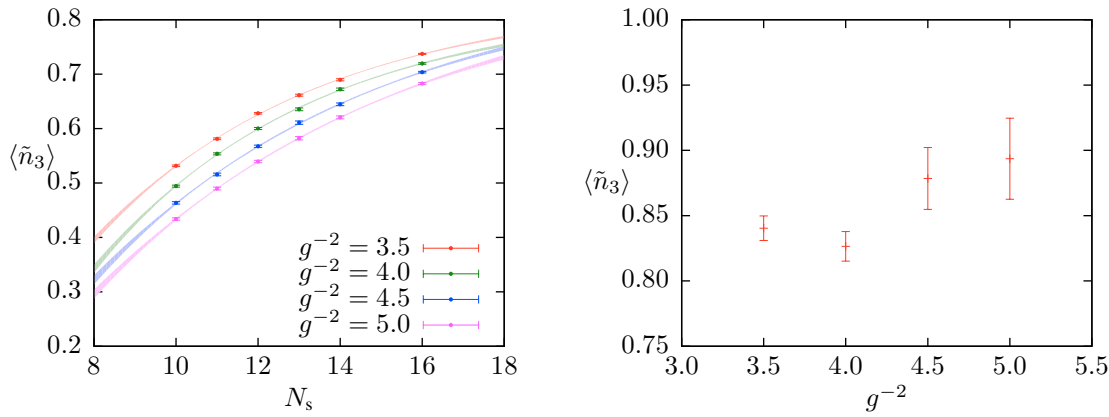


Figure 6.16: Left panel: $\langle \tilde{n}_3 \rangle$ for different lattice volumes $N = N_s^2$ at four couplings g^{-2} . The infinite volume extrapolation according to Eq. (6.90) is indicated by the shaded areas. Right panel: Infinite volume values of $\langle \tilde{n}_3 \rangle$ for different g^{-2} .

small acceptance rate for the unphysical configurations that dominate the path integral. Furthermore $\text{sign det } M$ is not positive definite and a *deflated* rational hybrid Monte-Carlo algorithm is necessary to get reliable expectation values (cf. Fig. 4.8).

These results imply that for a reasonable measurement of $\langle \tilde{n}_3 \rangle$ large couplings g^{-2} must be used in order to suppress the unphysical phase. Since the continuum limit is reached for $g \rightarrow 0$ measurements will be affected by finite size corrections. On this observable the corrections are assumed to vanish exponentially with growing volume,

$$\langle \tilde{n}_3 \rangle (N_s) = \langle \tilde{n}_3 \rangle (\infty) + Ae^{-BN_s}, \quad (6.90)$$

such that a fit to this functional form for $N_s \in \{10, 11, 12, 13, 14, 16\}$ and corresponding lattice volumes $N = N_s^2$ reveals the infinite volume value for $g^{-2} \in \{3.5, 4.0, 4.5, 5.0\}$, see Fig. 6.16 (left panel). Although $\langle \tilde{n}_3 \rangle$ shrinks for fixed N_s and growing g^{-2} , the infinite volume values tend to grow for larger g^{-2} , see Fig. 6.16 (right panel). Therefore the $O(3)$ symmetry will *not* be restored in the infinite volume continuum limit of the lattice model (6.87).

All these results have a crucial implication. Although the formulation (6.87) may restore the full $\mathcal{N} = (2, 2)$ supersymmetry on the lattice, the resulting continuum model is *not* the supersymmetric $O(3)$ (or \mathbb{CP}^1 , equivalently) model because the global $O(3)$ symmetry, that cannot be broken spontaneously in the continuum model [102], is *not restored* in the continuum limit. Therefore it is necessary to construct a lattice formulation that explicitly implements the $O(3)$ target space symmetry.

$O(3)$ invariant lattice formulation

To get rid of the constraints (6.69) in the path integral formulation (6.70) with a three-component Hermitian superfield Φ as defined in Eq. (6.65), the stereographic projection is generalised to superspace by using a two-component Hermitian superfield

$$\Upsilon = w + i\bar{\alpha}\chi + i\frac{1}{2}(\bar{\alpha}\alpha)g \quad \text{with} \quad \Phi = \frac{1}{1 + \Upsilon^\dagger\Upsilon} \begin{pmatrix} 2\Upsilon \\ 1 - \Upsilon^\dagger\Upsilon \end{pmatrix}. \quad (6.91)$$

By this construction the superspace constraint $\Phi \cdot \Phi = 1$ is identically fulfilled and the action is rewritten (in the continuum, after integrating out the auxiliary field g) to

$$S = \frac{2}{g^2} \int d^2x \rho^2 (\partial_\mu w \cdot \partial^\mu w + i\bar{\chi} \cdot \not{\partial} \chi + 2i\rho(\bar{\chi} \cdot w)\gamma^\mu(\partial_\mu w \cdot \chi) - 2i\rho(\bar{\chi} \cdot \partial_\mu w)\gamma^\mu(w \cdot \chi) + 4(\bar{\chi} \cdot \chi)^2) \quad (6.92)$$

with $\rho = (1 + w^\top w)^{-1}$ and path integral $\mathcal{Z} = \int \mathcal{D}u \mathcal{D}\chi \rho^{-2} e^{-S[w,\chi]}$. However, a straightforward discretisation of this expression will *not necessarily ensure* the underlying $O(3)$ symmetry in the continuum.

To arrive at an $O(3)$ invariant lattice regularisation the constrained formulation (6.70) is directly discretised,

$$\mathcal{Z} = \int \mathcal{D}n \mathcal{D}\psi \prod_x (\delta(n_x \cdot n_x - 1) \delta(n_x \cdot \psi_x)) e^{-S[n,\psi]} \quad \text{with} \quad S = \frac{1}{2g^2} \sum_{x,y} (n_x^\top K_{xy} n_y + i\bar{\psi}_x^\top M_{xy} \psi_y + \frac{1}{4}(\bar{\psi}_x^\top \delta_{xy} \psi_y)^2), \quad (6.93)$$

where ‘ ψ^\top ’ denotes ‘transpose in flavour space’. The (derivative) operators K and M can be specified later under the condition that they approach $-\partial_\mu \partial^\mu$ and $\not{\partial}$, respectively, in the continuum limit. Now the stereographic projection of superfields (6.91) is used, which implies the transformation of the component fields *on each lattice site* according to

$$n = \rho \begin{pmatrix} 2w \\ 1 - w^\top w \end{pmatrix}, \quad \psi = \rho \begin{pmatrix} 2\chi - 4\rho(w^\top \chi)u \\ -4\rho(w^\top \chi) \end{pmatrix} = e^i(w)\chi_i \quad (6.94)$$

with (flavour) basis vectors e^i . An orthonormal basis can be constructed by taking $E^i = (2\rho)^{-1}e^i$ and the fermionic field is then given by $\psi = E^i \lambda_i$, $\lambda_i = 2\rho \chi_i$. Using this variable transformation the path integral $\mathcal{Z} = \int \mathcal{D}w \mathcal{D}\lambda \rho^2 e^{-S[w,\lambda]}$ is given in terms of unconstrained fields by the action

$$S = \frac{1}{2g^2} \sum_{x,y} \left(4\rho_x w_x^\top K_{xy} w_y \rho_y + \rho_x (1 - w_x^\top w_x) K_{xy} (1 - w_y^\top w_y) \rho_y \right. \\ \left. + i\bar{\lambda}_x^\top ((\mathbb{1}_2 - 2w_x w_x^\top \rho_x) M_{xy} (\mathbb{1}_2 - 2w_y w_y^\top \rho_y) + 4\rho_x w_x M_{xy} w_y^\top \rho_y) \lambda_y + \frac{1}{4}(\bar{\lambda}_x^\top \delta_{xy} \lambda_y)^2 \right). \quad (6.95)$$

With a Hubbard-Stratonovich transformation it is possible to eliminate the four fermion interaction by introducing a (real) auxiliary scalar field σ . The path integral $\mathcal{Z} = \int \mathcal{D}w \mathcal{D}\sigma \mathcal{D}\lambda \rho^2 e^{-S[w,\lambda,\sigma]}$ is then given by the action

$$S = \frac{1}{2g^2} \sum_{x,y} \left(4\rho_x w_x^\top K_{xy} w_y \rho_y + \rho_x (1 - w_x^\top w_x) K_{xy} (1 - w_y^\top w_y) \rho_y + \sigma_x \delta_{xy} \sigma_y \right. \\ \left. + i\bar{\lambda}_x^\top ((\mathbb{1}_2 - 2w_x w_x^\top \rho_x) (M_{xy} + \delta_{xy} \sigma_x) (\mathbb{1}_2 - 2w_y w_y^\top \rho_y) + 4\rho_x w_x (M_{xy} + \delta_{xy} \sigma_x) w_y^\top \rho_y) \lambda_y \right). \quad (6.96)$$

At each lattice point the vectors $\{n, E^i\}$ form an orthonormal basis and may be composed as columns of a $SO(3)$ matrix $R = (n, E^1, E^2)$. However, the vectors E^i as constructed above are only a specific choice for the basis of fermionic fields and may be redefined by a (local) $SO(2)$ rotation. Therefore

the local basis is given by a (now general) $SO(3)$ matrix R , such that

$$n = Rn_0, \quad (E^1, E^2) = R\kappa \quad \text{with} \quad n_0 = \begin{pmatrix} 1 \\ 0 \\ 0 \end{pmatrix}, \quad \kappa = \begin{pmatrix} 0 & 0 \\ 1 & 0 \\ 0 & 1 \end{pmatrix}, \quad (6.97)$$

and the path integral becomes in terms of new dynamical variables $R \in SO(3)$

$$\mathcal{Z} = \int DR D\sigma D\lambda e^{-S}, \quad S = \frac{1}{2g^2} \sum_{x,y} (n_0^\top R_x^\top K_{xy} R_y n_0 + \sigma_x \delta_{xy} \sigma_y + i\lambda_x^\top \underbrace{\kappa^\top R_x^\top C(M_{xy} + \delta_{xy} \sigma_x) R_y \kappa}_{Q_{xy}} \lambda_y). \quad (6.98)$$

By changing the dynamical fields from w to R the measure factor ρ^2 in the path integral is absorbed in the Haar measure on $SO(3)$. This renders the structure of the lattice action rather simple by the cost of introducing a local $SO(2)$ freedom to choose the basis vectors E^i . Integrating out the (now unconstrained) Majorana fermions λ leads to a path integral

$$\mathcal{Z} = \int DR D\sigma \text{sign Pf } Q e^{-S_B - \ln |\text{Pf } Q|}, \quad S_B = \frac{1}{2g^2} \sum_{x,y} (n_0^\top R_x^\top K_{xy} R_y n_0 + \sigma_x \delta_{xy} \sigma_y) \quad (6.99)$$

and simulations are performed in the sign quenched ensemble, i.e. $\text{sign Pf } Q$ is dropped from the simulations and must be handled by reweighting afterwards. In this formulation the invariance of the path integral under the local $SO(2)$ transformation is manifest. The bosonic action is unaffected under $\kappa \rightarrow \kappa S$ with $S \in SO(2)$ and $Q_{xy} \rightarrow Q'_{xy} = S_x^\top Q_{xy} S_y$. This also leaves the Pfaffian invariant by using Eq. (5.24),

$$\text{Pf } Q' = \left(\prod_x \det S_x \right) \text{Pf } Q = \text{Pf } Q. \quad (6.100)$$

Technically, the effective fermionic action is rewritten according to $\ln |\text{Pf } Q| = \frac{1}{2} \ln \det Q$ and the hybrid Monte-Carlo algorithm with naive fermionic action is used, such that the Hamiltonian evolution of the group valued R field is similar to the quenched case.

Now that the formulation is completely $O(3)$ symmetric the operators M and K need to be specified. Motivated by the results for the Wess-Zumino models and the supersymmetric quantum mechanics, the regularisation here is build upon the SLAC derivative, i.e.

$$K_{xy} = - \sum_{z,\mu} (\partial_\mu^{\text{SLAC}})_{xz} (\partial_\mu^{\text{SLAC}})_{zy}, \quad M_{xy} = (\gamma^\mu \partial_\mu^{\text{SLAC}})_{xy}. \quad (6.101)$$

With this discretisation it can be shown similar to Sec. 5.2.2 that bosonic action and Pfaffian are unchanged under $\sigma \rightarrow -\sigma$, which translates (by integrating out the σ field) into the explicit realisation of the chiral \mathbb{Z}_2 symmetry on the lattice.²⁰

Supersymmetry breaking on the lattice

Although the $O(3)$ symmetry is now explicitly realised in the lattice formulation, supersymmetry is broken by the discretisation. This happen in two places in the path integral representation of Eq. (6.93).

²⁰In contrast to the situation in the $\mathcal{N} = 1$ Wess-Zumino model this symmetry does *not* depend on the fermionic boundary conditions (or the lattice size) because of the *two* Majorana flavours.

Firstly the supersymmetry transformation (see Eq. (6.71)) of the action is given by

$$\delta S = -\frac{1}{2g^2} \sum_x [(\bar{\psi}_x \cdot \psi_x) \bar{\epsilon} \gamma^\mu ((\partial_\mu^{\text{SLAC}} \psi)_x \cdot n_x + \psi_x \cdot (\partial_\mu^{\text{SLAC}} n)_x)] \neq 0, \quad (6.102)$$

which would vanish in the continuum according to

$$(\partial_\mu \psi) \cdot n + \psi \cdot (\partial_\mu n) = \partial_\mu (\psi \cdot n) = 0. \quad (6.103)$$

Secondly the supersymmetry transformation is not compatible with one constraint in (6.69),

$$\delta(n_x \cdot \psi_x) = \gamma^\mu \epsilon n_x \cdot (\partial_\mu n)_x \neq 0 \quad (6.104)$$

In both cases the non-invariance under the supersymmetry transformation can be traced back to the failure of the Leibniz rule on the lattice. Therefore, in the following the focus lies on the restoration of supersymmetry in the continuum limit of the proposed lattice model.

Sign of the Pfaffian

To check if the sign quenched approximation is applicable simulations on lattice sizes ranging from 5×5 to 11×11 have been performed over a coupling range $g^{-2} \in [0.4, 1.2]$. The results that are based on 10^5 configurations per data point (see Fig. 6.17) indicate that the average sign of the Pfaffian is quite small for smaller g^{-2} , which is equivalent to coarse lattices. Also the sign problem worsens for larger lattice volumes at fixed coupling. In these cases the probability based (sign quenched) Monte-Carlo sampling will *not* correspond to the relevant configurations in an unquenched ensemble and statistical errors on reweighted measurements will become rather large. Nevertheless, with the the standard Monte-Carlo techniques simulations are only possible without taking the sign into account, such that a reweighting becomes unavoidable. Technically, this sign problem prohibits the simulation on large lattices anyway, so that there is no need to introduce pseudo-fermions. But still the Pfaffian sign is only given in terms of the bare coupling g . The dependence on the physical volume and the physical lattice spacing can only be given in terms of a mass that sets the physical scale.

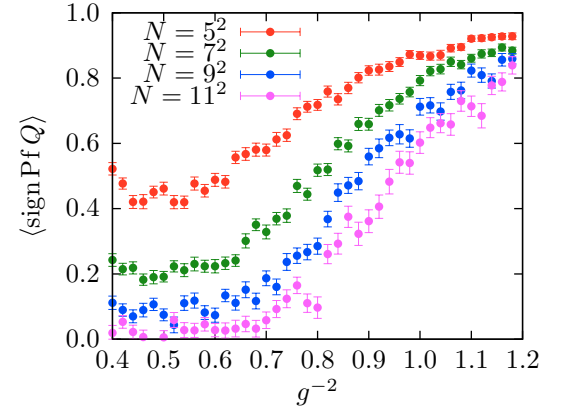


Figure 6.17: Average sign of the Pfaffian for different couplings g^{-2} on lattices sizes ranging from 5×5 to 11×11 .

Chiral symmetry breaking

For unconstrained fermionic fields the $O(3)$ invariant chiral condensate $\langle i\bar{\psi}_x \cdot \psi_x \rangle$ would be given directly by the diagonal elements of the inverse fermion matrix. Here, the fields ψ are subject to constraints. Nevertheless, the same relation is also revealed in terms of the unconstrained fermions λ ,

$$\begin{aligned} \langle i\bar{\psi}_x \cdot \psi_x \rangle &= \mathcal{Z}^{-1} \int Dn D\sigma D\psi \delta(n \cdot \psi) \delta(n \cdot n - 1) (i\bar{\psi}_x \cdot \psi_x) e^{-S} \\ &= \mathcal{Z}^{-1} \int DR D\sigma D\lambda \underbrace{i\bar{\lambda}_x^T \kappa^T R_x^T R_x \kappa}_{\mathbb{1}_2} \lambda_x e^{-S_B - \frac{i}{2g^2} \lambda^T Q \lambda} = \langle i\bar{\lambda}_x \cdot \lambda_x \rangle = g^2 \langle \text{tr}_{f,s}(CQ_{xx}^{-1}) \rangle. \end{aligned} \quad (6.105)$$

with ‘ $\text{tr}_{f,s}$ ’ as trace over flavour and spinor indices.

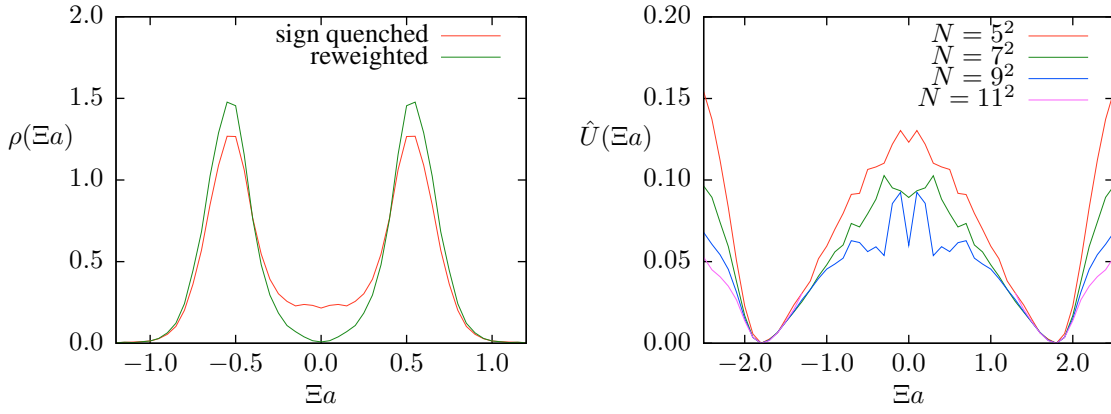


Figure 6.18: *Left panel: Probability density of the volume averaged chiral condensate for lattice size 9×9 at a bare coupling $g^{-2} = 1$ in the sign quenched and reweighted ensemble. Right panel: Constraint effective potential (normalised to $\min_{(\Xi a)} \hat{U}(\Xi a) = 0$) of the chiral condensate for different lattice volumes at $g^{-2} = 0.64$ computed using up to $3 \cdot 10^7$ configurations.*

The \mathbb{Z}_2 chiral symmetry (6.73) is expected to be broken spontaneously in the infinite volume limit [15] and the supersymmetric ground states correspond to the two ground states of this broken symmetry. A discretisation based on the SLAC derivative ensures this chiral symmetry on the lattice by the cost of having a non-local derivative. Therefore $\langle i\bar{\psi} \cdot \psi \rangle$ will vanish for every finite lattice volume and is therefore not sufficient to trace a broken symmetry. Instead, this symmetry breaking is analysed by histograms of the volume averaged chiral condensate $\Xi a = N^{-1} \sum_x \bar{\psi}_x \cdot \psi_x$. Fig. 6.18 (left panel) clearly shows a double peak structure of the chiral condensate distribution $\rho(\Xi a)$, coinciding with the two ground states. The reweighting process reveals that a cancellation between positive and negative Pfaffians happens mostly for $\Xi a \approx 0$. In the analysis of the constraint effective potential $\hat{U}(\Xi a) = -\ln(\rho(\Xi a))/N$ for several lattice volumes at fixed coupling (see Fig. 6.18, right panel) no running of the two minima is visible, such that there will be a spontaneous chiral symmetry breaking in the infinite volume limit of the lattice model.

Fermionic masses

The theory has no intrinsic mass scale given as parameter of the Lagrangian. However there is a relation between mass gap and bare coupling by dimensional transmutation. Further in the $\overline{\text{MS}}$ scheme it is possible to compute the mass gap [159, 160] in relation to $\Lambda_{\overline{\text{MS}}}$. In the $\mathcal{N} = 1$ Wess-Zumino model it has been found that the fermionic mass is less affected by finite size effects than the bosonic mass. For that reason the fermionic mass is used to set the physical scale, i.e. the physical box length and the lattice spacing, in the lattice regularised theory.²¹

In analogy to the bosonic case (6.84) the $O(3)$ symmetric fermionic correlator is constructed as

$$\begin{aligned} \langle i\bar{\psi}_x \cdot \psi_y \rangle &= \mathcal{Z}^{-1} \int Dn D\sigma D\psi \delta(n \cdot \psi) \delta(n \cdot n - 1) (i\bar{\psi}_x \cdot \psi_y) e^{-S} \\ &= \mathcal{Z}^{-1} \int DR D\sigma D\lambda i\bar{\lambda}_x^T \kappa^T R_x^T R_y \kappa \lambda_y e^{-S_B - \frac{i}{2g^2} \lambda^T Q \lambda} = g^2 \langle \text{tr}_{f,s}(R_x \kappa C Q_{xy}^{-1} \kappa^T R_y^T) \rangle. \end{aligned} \quad (6.106)$$

The corresponding timeslice correlator is given by $C_F(t) = N_s^{-2} \sum_{xx'} \langle i\bar{\psi}_{(t,x)} \cdot \bar{\psi}_{(0,x')} \rangle$. To measure the mass in *one* of the ground states the configurations are projected, without loss of generality, to the

²¹Supersymmetry and the degeneracy of bosonic and fermionic mass is broken by the finite lattice spacing and the finite box size. Therefore the restoration of equal masses must be checked in the corresponding limits.

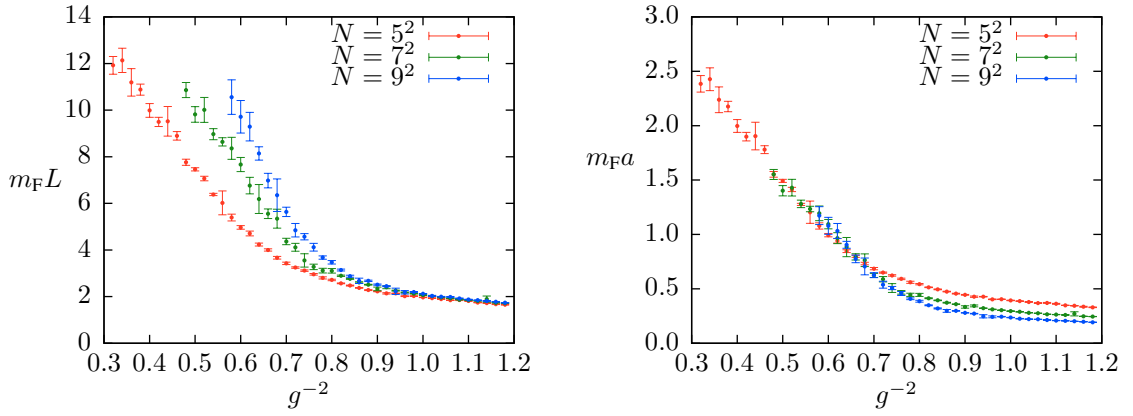


Figure 6.19: Fermionic masses in units of the box length (left panel) and lattice spacing (right panel) for different lattice volumes and bare couplings g^{-2} computed using up to $2 \cdot 10^7$ configurations.

sector with $\Xi > 0$.²² Using these definitions the fermionic masses are obtained by a cosh fit to the correlator over the range $\hat{t} \in]0, N_t[$. A comparison of the fermionic masses for different lattice sizes (see Fig. 6.19) reveals that finite size effects on $m_F a$ are below the statistical error bars if $m_F L \gtrsim 5$.

With this mass scale at hand it is now possible to give $\langle \text{sign Pf } Q \rangle$ over the physical volume $m_F L$. The results are shown in Fig. 6.20 and imply that for the present lattice sizes the sign problem worsens when the lattice spacing is refined at fixed volume $m_F L$. In contrast to the Wess-Zumino models, where the sign problem becomes weaker in the continuum limit, for the $O(3)$ sigma model the sign problem becomes severe in the continuum limit at fixed physical volume. This turns out to be a technical problem making simulations close to continuum limit at fixed physical volume exceptionally hard, so that the present analysis is only based on rather small lattice sizes.

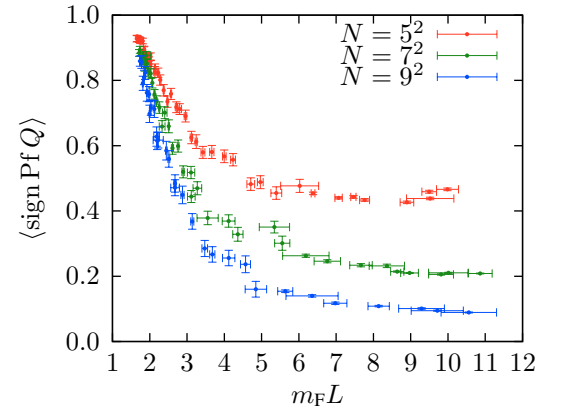


Figure 6.20: Average sign of the Pfaffian over the physical volume in units of the fermionic mass at different lattice sizes.

Bosonic masses

As supersymmetry predicts the degeneracy of bosonic and fermionic mass it is important to check if they match up in the lattice simulations. The bosonic masses $m_B L$ are extracted similar to the quenched case from the $O(3)$ invariant correlator (6.84) via a cosh fit over the range $\hat{t} \in]0, N_t[$. Further the bosonic correlator is unaffected by a change in σ , such that no projection to one ground state is necessary. After the bosonic masses are determined a comparison of bosonic and fermionic mass at different couplings and lattice sizes reveals a possible restoration of the degenerate spectrum. Calculations have been performed on lattice sizes $N \in \{5^2, 7^2, 9^2\}$ over a coupling range $g^{-2} \in [0.4, 1.2]$. The direct comparison is shown in Fig. 6.21 (left panel) and the results seem to be disappointing at first sight. The bosonic masses lie considerably below the fermionic partners and for larger lattices this trend becomes even more pronounced. However, this does not necessarily imply that supersymmetry will be broken in the continuum limit. As was found in the $\mathcal{N} = 2$ Wess-Zumino model, for a supersymmetric theory with a spontaneously broken \mathbb{Z}_2 symmetry the masses will split in the strongly coupled limit at finite physical box sizes. E.g. for a coupling at the edge of the applicability of one-

²²Technically this is achieved by flipping the sign of σ for configurations with $\Xi < 0$, such that $\Xi \rightarrow -\Xi$.

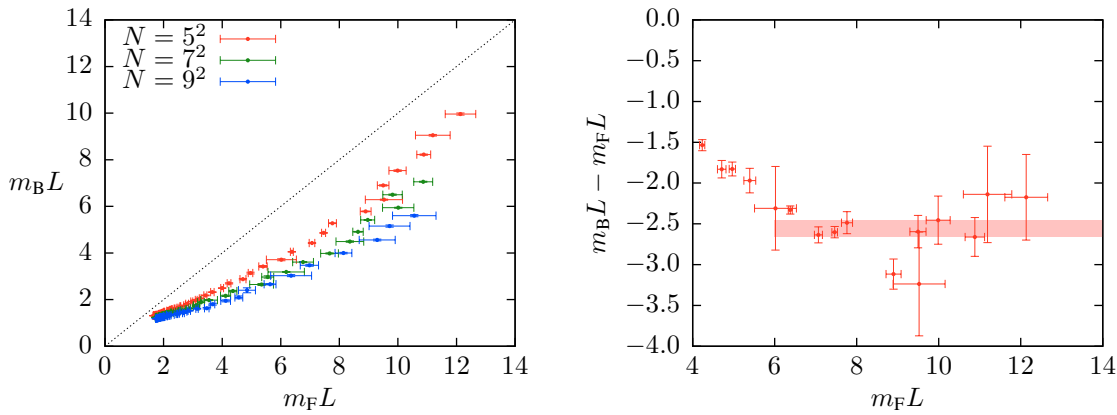


Figure 6.21: *Left panel: Direct comparison of bosonic and fermionic mass in units of the box size for three different lattice sizes. The dotted line denotes the case $m_F = m_B$. Right panel: Difference $m_B L - m_F L$ for varying box size $m_F L$ on a 5×5 lattice. The shaded area denotes a fit according to Eq. (6.107) for $m_F L > 6$.*

loop perturbation theory with a box size $m_F L \approx 10$ a 20% splitting with a smaller bosonic mass is observed (see Fig. 3.15) although one supersymmetry is implemented on the lattice. From that point of view the supersymmetric $O(3)$ nonlinear sigma model is similar to a very strongly coupled $\mathcal{N} = 2$ Wess-Zumino model. The finite size effects may be even larger and a mass splitting of much more than 20% is not surprising for $m_F L < 10$. Only an analysis of the mass ratio m_B/m_F in the large volume limit can uncover a restoration of degenerate masses. This is exemplarily shown for the results on the 5×5 lattice in Fig. 6.21 (right panel). Despite the fact that lattice artefacts are rather large the basic concept becomes clear. In the limit of large volumes a relation

$$m_B L = m_F L - \Delta M \quad \Rightarrow \quad \frac{m_B}{m_F} = 1 - \frac{\Delta M}{m_F L} \quad (6.107)$$

with constant ΔM is found such that the ratio tends to 1 and the masses will be degenerate in the infinite volume limit.²³

But still the accessible physical volumes at larger lattices do not allow for a reliable extrapolation of the corresponding ΔM and no continuum limit can be taken at the moment. Therefore it is an open question if Eq. (6.107) also applies in the continuum limit and supersymmetry will be restored. For that reason a simple Ward identity is considered than allows for a more direct investigation of supersymmetry restoration.

Path integral based Ward identity

Similar to the Ward identity for the action that is given in [44] an equivalent formulation can be constructed for the present lattice model. Starting from the path integral in the continuum,

$$\mathcal{Z} = \int \mathcal{D}n \mathcal{D}\psi \mathcal{D}f \delta(n \cdot n - 1) \delta(n \cdot \psi) \delta(n \cdot f - i\frac{1}{2}\bar{\psi} \cdot \psi) e^{-S[n,\psi,f]}$$

$$\text{with } S = \frac{1}{2g^2} \int d^2x (\partial_\mu n \cdot \partial^\mu n + i\bar{\psi} \cdot (\not{\partial}\psi) - f \cdot f), \quad (6.108)$$

²³For the 5×5 lattice a fit to Eq. (6.107) for $m_F L > 6$ gives $\Delta M = 2.56(10)$.

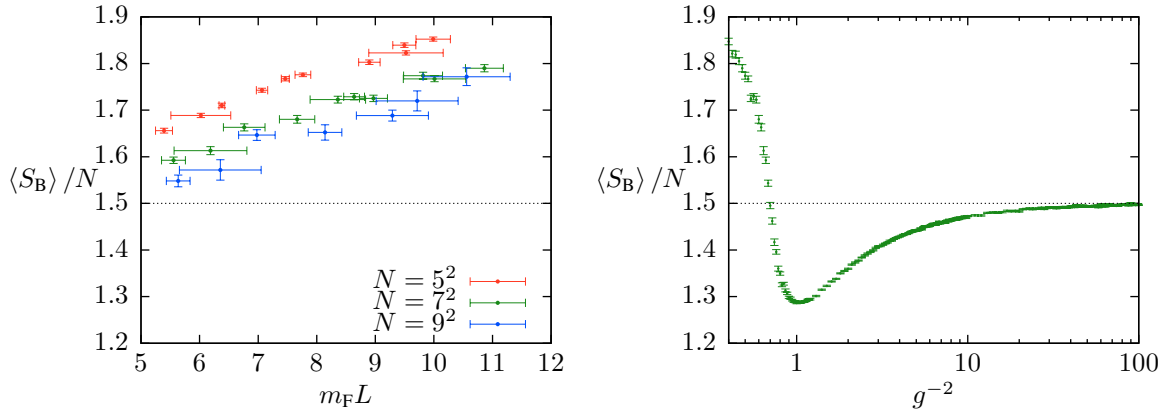


Figure 6.22: Normalised action $\langle S_B \rangle / N$, which will take the value 1.5 if supersymmetry is restored in the continuum limit as required by the Ward identity (6.112). Left panel: Measurements for different lattice sizes at a range of physical volumes $5 < m_F L < 11$. Right panel: Results for fixed lattice volume $N = 7 \times 7$ and couplings $g^{-2} \in [0.4, 100]$ that reach the regime of small physical volumes (small g).

Q exactness is given by the twisted supercharge of [44] in the continuum, such that $S = \frac{1}{2g^2} Q\Lambda$ with $Q^2 = 0$. This implies the continuum Ward identity

$$\frac{\partial \ln \mathcal{Z}}{\partial (g^{-2})} = \langle -\frac{1}{2} Q\Lambda \rangle = 0, \quad (6.109)$$

since action *and* measure are invariant under the symmetry transformation provided by Q . After putting the theory on the lattice, integrating out the constrained auxiliary field f , and introducing the unconstrained field σ to cancel the four fermion interaction (in that order) one is left with a path integral,

$$\mathcal{Z} = g^N \int DR D\sigma D\lambda e^{-S[R,\sigma,\lambda]} \quad (6.110)$$

with N as number of lattice sites and action given in Eq. (6.98).²⁴ Here, the coupling dependent part is important, such that only constant numerical factors may be dropped. The corresponding Ward identity then turns into

$$\frac{\partial \ln \mathcal{Z}}{\partial (g^{-2})} = -\frac{Ng^2}{2} - g^2 \langle S_B \rangle + \frac{g^2}{2} \dim Q. \quad (6.111)$$

If the theory is supersymmetric under Q the Ward identity is given by combining the continuum result (6.109) with the lattice result (6.111),

$$\langle S_B \rangle = \frac{3}{2} N, \quad (6.112)$$

with S_B defined in Eq. (6.99). To see a possible restoration of supersymmetry in the continuum limit the bosonic action has been calculated for three lattice sizes in a coupling range where finite size effects should be negligible, i.e. for $m_F L > 5$.

The results that are shown in Fig. 6.22 (left panel) reveal that for the smallest (5×5) lattice Eq. (6.112) is violated as much as 10% for $m_F L \approx 5$ and up to 20% at $m_F L \approx 10$. Therefore the Ward identity violation grows for coarser lattice spacings. However, in the continuum limit at a fixed physical volume $m_F L$ the Ward identity tends to be restored. Additionally one can explore the small volume regime of this theory by sending $g \rightarrow 0$ at fixed lattice volume to reach the continuum limit with small lattice spacings. This has been performed on a 7×7 lattice for a large range of couplings

²⁴The factor g^N in front of the path integral stems from the Gaussian integrals that need to be carried out (for f) or introduced (for σ).

$g^{-2} \in [0.4, 100]$, see Fig. 6.22 (right panel). Here the Ward identity is explicitly restored in the limit of large g^{-2} and small lattice spacing.

Altogether the Ward identity tends to be restored in the continuum limit at fixed physical volumes and is explicitly restored at small physical volumes. Although the used lattice sizes are rather small these observations imply that a supersymmetric continuum limit can be reached and that the non-degeneracy of bosonic and fermionic mass is a finite size effect, which is also present in the continuum theory. However, to come to a definite answer to the question of supersymmetry restoration simulations on larger lattices would be necessary to show at least that $\langle S_B \rangle / N$ does not undershoot and drop below 1.5 in the continuum limit at fixed $m_F L$.

6.2.3 Conclusions

It has been demonstrated for the quenched model that the target space $O(3)$ symmetry must be ensured in the lattice discretisation. Even in the continuum limit of the lattice model there is no restoration of the target space symmetry and a spontaneous magnetisation occurs in contradiction to the Mermin-Wagner theorem [102]. To ensure the applicability of the SLAC derivative for a curved target space the step scaling function has been verified in the continuum limit to high precision.

The analysis of the Q exact model of [44] reveals that the $O(3)$ symmetry will *not* be restored if it is broken by the discretisation in the supersymmetric model. Further the instabilities at coarse lattices in a lattice model with an exact supersymmetry, that have been found in the $\mathcal{N} = 2$ Wess-Zumino model, are also recovered in this setting.

By using a stereographic projection it has been demonstrated that a discretisation of the supersymmetric $O(3)$ nonlinear sigma model is possible, which ensures the bosonic and fermionic constraint as well as the target space symmetry. Using the SLAC derivative for bosonic and fermionic degrees of freedom the chiral \mathbb{Z}_2 symmetry is implemented on the lattice and the spontaneous breaking is only caused by dynamical effects. The theoretically predicted ground state structure has been checked with histogram methods and two ground states, corresponding to the spontaneously broken chiral symmetry, are found.

The bosonic and fermionic masses have been computed and they disagree considerably, which can be traced back to finite size effects that cause a mass splitting in strongly coupled theories with spontaneously broken \mathbb{Z}_2 symmetry. An analysis of a Ward identity based on the bosonic action shows explicitly that supersymmetry is restored at small physical volumes and indicates that the Ward identity will be fulfilled in the continuum limit at finite (large) physical volume.

Although the results are very encouraging so far there is one pitfall remaining. The sign problem becomes worse in the continuum limit and a simulation on larger lattices will be exceptionally hard. Further elaborate methods based on pseudo-fermions are not efficient since the sign of the Pfaffian must still be computed for a reweighting of observables. However, the $O(3)$ invariant formulation does not specify the used derivative operators. It may turn out that a formulation based on the overlap operator (to ensure the chiral symmetry) possesses a less severe sign problem and does therefore allow for larger lattice sizes and a precise investigation of the supersymmetry restoration in the continuum limit. Eventually the construction of an $O(3)$ invariant formulation with one exact supersymmetry on the lattice might be possible, which will ensure a supersymmetric and $O(3)$ symmetric continuum limit.

Chapter 7

Summary and outlook

In this work different supersymmetric models were studied on the lattice with an emphasis on the ground state structure, supersymmetry restoration in the continuum limit of the corresponding lattice models, and spontaneous supersymmetry breaking.

A supersymmetric quantum mechanics with dynamically broken supersymmetry was analysed with a lattice model built upon a discretisation with the SLAC derivative. Observables that are computed via Monte-Carlo simulations of the lattice regularised theory are in full agreement with results from the diagonalised Hamiltonian. Bosonic and fermionic ground state can be distinguished on the lattice by the impact of changing the fermionic boundary conditions on the sign of the fermion determinant. A massless fermionic excitation was found that corresponds to the Goldstone fermion of the dynamically broken supersymmetry. By a projection to one ground state it was possible to compute the energy gap between ground state and first excited state. Due to the broken supersymmetry Ward identities are *not fulfilled* and will additionally be affected by a finite temperature. The whole analysis demonstrates that a complete treatment of theories with dynamically broken supersymmetry on the lattice is possible. Ground state structure, observables, and the low lying energy spectrum were determined reliably. Additionally *no counterterms* are necessary to obtain the correct continuum theory.

In the study of the $\mathcal{N} = 2$ Wess-Zumino model three different lattice derivatives have been compared. For coarse lattices and large couplings the improvement term, that is introduced to implement one exact supersymmetry on the lattice, leads to an *unstable* behaviour of the lattice model, irrespective of the chosen derivative. In the weak coupling regime the continuum extrapolation of the coupling dependent renormalised mass coincides with perturbation theory. More importantly, all different lattice prescriptions approach the same continuum result. The SLAC derivative shows the smallest lattice artefacts and allows for much larger couplings in the Nicolai improved versions of the model. Results in the intermediate coupling regime, at the edge of the applicability range of one-loop perturbation theory, were obtained and (small) deviations from perturbative results were found. Only in that coupling region supersymmetrically improved and unimproved formulations lead to different results, where in the improved version lattice artefacts are suppressed. Although one supersymmetry is explicitly realised in the improved lattice models a broken Ward identity is found for larger couplings, which can be traced back to the measurement process, during which a projection to one ground state may be necessary. This procedure to mimic an infinite volume ground state structure with a broken \mathbb{Z}_2 symmetry amounts to supersymmetry breaking terms in the action and only \mathbb{Z}_2 invariant observables are insensitive to this artificial supersymmetry breaking. Altogether the coupling region up to the breakdown of one-loop perturbation theory is completely under control and reliable results can be obtained. The most promising way to go beyond the perturbative region is given by Nicolai improved actions with the SLAC derivative on larger lattice sizes than studied here and at even larger physical volumes to suppress instabilities of the improvement term and finite volume effects.

In the $\mathcal{N} = 1$ Wess-Zumino model with the chosen prepotential a supersymmetry breaking phase transition was confirmed with a regularisation based on the SLAC derivative. For the first time the corresponding renormalised critical coupling was determined and a regulator independence of this coupling was demonstrated in the quenched model. At the phase transition a restoration of the \mathbb{Z}_2 symmetry goes at hand with the spontaneous breaking of supersymmetry. Supersymmetry restoration

was examined with a Ward identity in the continuum, infinite volume, and zero temperature limit. Bosonic and fermionic masses were determined at one specific coupling in the supersymmetric phase and a massless fermionic mode, a goldstino, was found for spontaneously broken supersymmetry while the bosonic mass vanishes with growing physical volume. Although the physical picture of this model is now completely determined a few systematic uncertainties concerning the ordering of limits still remain and need to be clarified in future works. Eventually a completely independent calculation using another lattice regularisation is needed to directly confirm the independence of the given renormalised critical coupling on the used discretisation of the full supersymmetric model.

Instanton constituents of twisted $\mathbb{C}P^N$ nonlinear sigma models on a cylinder were constructed and their fractional charges were related to the phases of the twisted boundary conditions. The instanton structure that emerges from lattice cooling techniques is in agreement with the analytical findings. For minimally and supersymmetrically coupled fermions the zero modes of the Dirac operator in the background of twisted instantons were determined. Even on incompletely cooled lattice configurations these zero modes are tracers for the instanton constituents, in coincidence with the analytical results.

In the supersymmetric $O(3)$ nonlinear sigma model the relevance of an intact target space symmetry in the lattice model has been demonstrated and a previously suggested lattice formulation was found to break this symmetry even in the continuum limit. A lattice formulation that explicitly implements the global $O(3)$ symmetry was constructed independently of the used lattice derivative. To ensure the applicability of the SLAC derivative for an $O(3)$ target space the step scaling function of the finite volume mass gap has been verified in the continuum limit to high precision. Thus, the supersymmetric $O(3)$ nonlinear sigma model was studied using an explicitly $O(3)$ invariant lattice prescription with the SLAC derivative, that ensures the chiral \mathbb{Z}_2 symmetry of the continuum model. The theoretically predicted ground state structure is confirmed by the constraint effective potential of the chiral condensate. Bosonic and fermionic masses are found to disagree, which can be understood, similarly to the $\mathcal{N} = 2$ Wess-Zumino model, from finite volume effects. A specific Ward identity tends to be restored in the continuum limit at fixed physical volume and is explicitly restored in the limit of small physical volumes. Unfortunately, the sign problem hinders the simulations from approaching the continuum limit at fixed physical volume. Although the present formulation may in principle have a well behaved supersymmetric continuum limit, this problem makes simulations exceptionally time consuming. Only discretisations with a different derivative operator may show a better behaved sign problem.

In most of the considered models the SLAC derivative has proven to be successfully applicable, which can be traced back to the absence of gauge fields in these models. Therefore it may be advantageous to consider the SLAC derivative as an interesting alternative to Ginsparg-Wilson fermions in simulations of the four dimensional $\mathcal{N} = 1$ Wess-Zumino model [161].

Supersymmetrically improved lattice actions inevitably include periodic boundary conditions for fermionic field which lead to a severe sign problem in supersymmetric theories with a spontaneously broken supersymmetry. Therefore the applicability of the improvement program to these theories becomes questionable. Further there are two examples with unbroken supersymmetry, namely the $\mathcal{N} = 2$ Wess-Zumino model and the supersymmetric $\mathbb{C}P^1$ nonlinear sigma model, where the supersymmetrically improved lattice models possess an inherent instability. Thus, it may be proposed that these instabilities can (in principle) occur in every supersymmetric lattice model that is constructed from a nilpotent (scalar) supercharge and only further investigations may shed light on this issue.

-
- [1] H. Weyl, *Electron and gravitation*, Z. Phys. **56** (1929) 330.
- [2] E. Fermi, *Quantum theory of radiation*, Rev. Mod. Phys. **4** (1932) 87.
- [3] C.-N. Yang and R. L. Mills, *Conservation of isotopic spin and isotopic gauge invariance*, Phys. Rev. **96** (1954) 191.
- [4] S. L. Glashow, *Partial Symmetries of Weak Interactions*, Nucl. Phys. **22** (1961) 579.
- [5] A. Salam and J. C. Ward, *Electromagnetic and weak interactions*, Phys. Lett. **13** (1964) 168.
- [6] S. Weinberg, *A Model of Leptons*, Phys. Rev. Lett. **19** (1967) 1264.
- [7] H. Fritzsch, M. Gell-Mann and H. Leutwyler, *Advantages of the Color Octet Gluon Picture*, Phys. Lett. **B47** (1973) 365.
- [8] K. Kodama et al. (DONUT), *Observation of tau-neutrino interactions*, Phys. Lett. **B504** (2001) 218 [arXiv:hep-ex/0012035].
- [9] S. R. Coleman and J. Mandula, *All possible symmetries of the S matrix*, Phys. Rev. **159** (1967) 1251.
- [10] R. Haag, J. T. Lopuszanski and M. Sohnius, *All Possible Generators of Supersymmetries of the S Matrix*, Nucl. Phys. **B88** (1975) 257.
- [11] J. Wess and B. Zumino, *A lagrangian model invariant under supergauge transformations*, Phys. Lett. **B49** (1974) 52.
- [12] S. Dimopoulos and H. Georgi, *Softly Broken Supersymmetry and SU(5)*, Nucl. Phys. **B193** (1981) 150.
- [13] J. R. Ellis, J. S. Hagelin, D. V. Nanopoulos, K. A. Olive and M. Srednicki, *Supersymmetric relics from the big bang*, Nucl. Phys. **B238** (1984) 453.
- [14] G. Hiller and M. Schmaltz, *Solving the strong CP problem with supersymmetry*, Phys. Lett. **B514** (2001) 263 [arXiv:hep-ph/0105254].
- [15] E. Witten, *Constraints on Supersymmetry Breaking*, Nucl. Phys. **B202** (1982) 253.
- [16] L. O’Raifeartaigh, *Spontaneous Symmetry Breaking for Chiral Scalar Superfields*, Nucl. Phys. **B96** (1975) 331.
- [17] E. Witten, *Dynamical breaking of supersymmetry*, Nucl. Phys. **B188** (1981) 513.
- [18] M. Creutz, *Monte Carlo Study of Quantized SU(2) Gauge Theory*, Phys. Rev. **D21** (1980) 2308.
- [19] S. Dürr et al., *Ab-Initio Determination of Light Hadron Masses*, Science **322** (2008) 1224 [arXiv:0906.3599].
- [20] A. Feo, *Predictions and recent results in SUSY on the lattice*, Mod. Phys. Lett. **A19** (2004) 2387 [arXiv:hep-lat/0410012].

- [21] J. Giedt, *Deconstruction and other approaches to supersymmetric lattice field theories*, Int. J. Mod. Phys. **A21** (2006) 3039 [arXiv:hep-lat/0602007].
- [22] T. Takimi, *Relationship between various supersymmetric lattice models*, JHEP **07** (2007) 010 [arXiv:0705.3831].
- [23] P. H. Damgaard and S. Matsuura, *Lattice supersymmetry: Equivalence between the link approach and orbifolding*, JHEP **09** (2007) 097 [arXiv:0708.4129].
- [24] S. Catterall, *From twisted supersymmetry to orbifold lattices*, JHEP **01** (2008) 048 [arXiv:0712.2532].
- [25] J. W. Elliott, J. Giedt and G. D. Moore, *Lattice four-dimensional $N=4$ SYM is practical*, arXiv:0806.0013.
- [26] J. Giedt, *Progress in four-dimensional lattice supersymmetry*, Int. J. Mod. Phys. **A24** (2009) 4045 [arXiv:0903.2443].
- [27] M. G. Endres, *Dynamical simulation of $N=1$ supersymmetric Yang-Mills theory with domain wall fermions*, Phys. Rev. **D79** (2009) 094503 [arXiv:0902.4267].
- [28] K. Demmouche et al., *Simulation of 4d $N=1$ supersymmetric Yang-Mills theory with Symanzik improved gauge action and stout smearing*, arXiv:1003.2073.
- [29] K. G. Wilson, *Quarks and Strings on a Lattice*, New Phenomena In Subnuclear Physics. Part A. Proceedings of the First Half of the 1975 International School of Subnuclear Physics, Erice, Sicily, July 11 - August 1, 1975, ed. A. Zichichi, Plenum Press, New York, 1977, p. 69, CLNS-321.
- [30] H. B. Nielsen and M. Ninomiya, *Absence of Neutrinos on a Lattice. 1. Proof by Homotopy Theory*, Nucl. Phys. **B185** (1981) 20.
- [31] H. B. Nielsen and M. Ninomiya, *Absence of Neutrinos on a Lattice. 2. Intuitive Topological Proof*, Nucl. Phys. **B193** (1981) 173.
- [32] H. B. Nielsen and M. Ninomiya, *No go theorem for regularizing chiral fermions*, Phys. Lett. **B105** (1981) 219.
- [33] P. H. Ginsparg and K. G. Wilson, *A Remnant of Chiral Symmetry on the Lattice*, Phys. Rev. **D25** (1982) 2649.
- [34] P. H. Dondi and H. Nicolai, *Lattice supersymmetry*, Nuovo Cim. **A41** (1977) 1.
- [35] J. Giedt and E. Poppitz, *Lattice supersymmetry, superfields and renormalization*, JHEP **09** (2004) 029 [arXiv:hep-th/0407135].
- [36] I. Montvay, *Tuning to $N=2$ supersymmetry in the $SU(2)$ adjoint Higgs-Yukawa model*, Nucl. Phys. **B445** (1995) 399 [arXiv:hep-lat/9503009].

- [37] M. F. L. Golterman and D. N. Petcher, *A local interactive lattice model with supersymmetry*, Nucl. Phys. **B319** (1989) 307.
- [38] S. Catterall, D. B. Kaplan and M. Unsal, *Exact lattice supersymmetry*, Phys. Rept. **484** (2009) 71 [arXiv:0903.4881].
- [39] G. Bergner, F. Bruckmann and J. M. Pawłowski, *Generalising the Ginsparg-Wilson relation: Lattice Supersymmetry from Blocking Transformations*, Phys. Rev. **D79** (2009) 115007 [arXiv:0807.1110].
- [40] G. Bergner, *Complete supersymmetry on the lattice and a No-Go theorem: A simulation with intact supersymmetries on the lattice*, JHEP **01** (2010) 024 [arXiv:0909.4791].
- [41] G. Bergner, T. Kästner, S. Uhlmann and A. Wipf, *Low-dimensional supersymmetric lattice models*, Annals Phys. **323** (2008) 946 [arXiv:0705.2212].
- [42] V. A. Novikov, M. A. Shifman, A. I. Vainshtein and V. I. Zakharov, *Two-Dimensional Sigma Models: Modeling Nonperturbative Effects of Quantum Chromodynamics*, Phys. Rept. **116** (1984) 103.
- [43] S. Catterall and S. Ghadab, *Lattice sigma models with exact supersymmetry*, JHEP **05** (2004) 044 [arXiv:hep-lat/0311042].
- [44] S. Catterall and S. Ghadab, *Twisted supersymmetric sigma model on the lattice*, JHEP **10** (2006) 063 [arXiv:hep-lat/0607010].
- [45] T. Kästner, G. Bergner, S. Uhlmann, A. Wipf and C. Wozar, *Two-Dimensional Wess-Zumino Models at Intermediate Couplings*, Phys. Rev. **D78** (2008) 095001 [arXiv:0807.1905].
- [46] C. Wozar, G. Bergner, T. Kästner, S. Uhlmann and A. Wipf, *Numerical Investigation of the 2D $N=2$ Wess-Zumino Model*, PoS **LATTICE2008** (2008) 234 [arXiv:0809.2176].
- [47] T. Kästner, *Supersymmetry on a space-time lattice*, Ph.D. thesis, Friedrich Schiller University of Jena (2008).
- [48] G. Bergner, *Symmetries and the methods of quantum field theory: Supersymmetry on a space-time lattice*, Ph.D. thesis, Friedrich Schiller University of Jena (2009).
- [49] W. Brendel, F. Bruckmann, L. Janssen, A. Wipf and C. Wozar, *Instanton constituents and fermionic zero modes in twisted $CP(n)$ models*, Phys. Lett. **B676** (2009) 116 [arXiv:0902.2328].
- [50] L. Janssen, *Instantons and fermionic zero modes in the supersymmetric $CP(N)$ model (in german)*, diploma thesis, Friedrich Schiller University of Jena (2008).
- [51] M. Creutz and B. Freedman, *A statistical approach to quantum mechanics*, Ann. Phys. **132** (1981) 427.

- [52] S. Catterall and E. Gregory, *A lattice path integral for supersymmetric quantum mechanics*, Phys. Lett. **B487** (2000) 349 [arXiv:hep-lat/0006013].
- [53] M. Beccaria, G. Curci and E. D'Ambrosio, *Simulation of supersymmetric models with a local Nicolai map*, Phys. Rev. **D58** (1998) 065009 [arXiv:hep-lat/9804010].
- [54] T. Kästner, G. Bergner, S. Uhlmann, A. Wipf and C. Wozar, *Supersymmetric lattice models in one and two dimensions*, PoS **LAT2007** (2007) 265 [arXiv:0709.0822].
- [55] J. Giedt, R. Koniuk, E. Poppitz and T. Yavin, *Less naive about supersymmetric lattice quantum mechanics*, JHEP **12** (2004) 033 [arXiv:hep-lat/0410041].
- [56] I. Kanamori, H. Suzuki and F. Sugino, *Euclidean lattice simulation for the dynamical supersymmetry breaking*, Phys. Rev. **D77** (2008) 091502 [arXiv:0711.2099].
- [57] I. Kanamori, F. Sugino and H. Suzuki, *Observing dynamical supersymmetry breaking with euclidean lattice simulations*, arXiv:0711.2132.
- [58] A. Wipf, *Non-perturbative methods in supersymmetric theories*, arXiv:hep-th/0504180.
- [59] A. Kirchberg, J. D. Lange and A. Wipf, *From the Dirac operator to Wess-Zumino models on spatial lattices*, Ann. Phys. **316** (2005) 357 [arXiv:hep-th/0407207].
- [60] S. D. Drell, M. Weinstein and S. Yankielowicz, *Strong coupling field theories. 2. Fermions and gauge fields on a lattice*, Phys. Rev. **D14** (1976) 1627.
- [61] L. H. Karsten and J. Smit, *The vacuum polarization with SLAC lattice fermions*, Phys. Lett. **B85** (1979) 100.
- [62] L. O'Raifeartaigh, A. Wipf and H. Yoneyama, *The constraint effective potential*, Nucl. Phys. **B271** (1986) 653.
- [63] S. Catterall and S. Karamov, *Exact lattice supersymmetry: the two-dimensional $N=2$ Wess-Zumino model*, Phys. Rev. **D65** (2002) 094501 [arXiv:hep-lat/0108024].
- [64] S. Elitzur, E. Rabinovici and A. Schwimmer, *Supersymmetric models on the lattice*, Phys. Lett. **B119** (1982) 165.
- [65] D. B. Kaplan, E. Katz and M. Unsal, *Supersymmetry on a spatial lattice*, JHEP **05** (2003) 037 [arXiv:hep-lat/0206019].
- [66] H. Nicolai, *On a new characterization of scalar supersymmetric theories*, Phys. Lett. **B89** (1980) 341.
- [67] R. Frezzotti, P. A. Grassi, S. Sint and P. Weisz (Alpha), *Lattice QCD with a chirally twisted mass term*, JHEP **08** (2001) 058 [arXiv:hep-lat/0101001].
- [68] J. Giedt, *R-symmetry in the Q-exact (2,2) 2d lattice Wess-Zumino model*, Nucl. Phys. **B726** (2005) 210 [arXiv:hep-lat/0507016].

- [69] S. Cecotti and L. Girardello, *Functional measure, topology and dynamical supersymmetry breaking*, Phys. Lett. **B110** (1982) 39.
- [70] A. Hasenfratz et al., *Finite size effects and spontaneously broken symmetries: The case of the $O(4)$ model*, Z. Phys. **C46** (1990) 257.
- [71] A. Hasenfratz et al., *Goldstone bosons and finite size effects: A Numerical study of the $O(4)$ model*, Nucl. Phys. **B356** (1991) 332.
- [72] M. Gockeler and H. Leutwyler, *Constraint correlation functions in the $O(N)$ model*, Nucl. Phys. **B361** (1991) 392.
- [73] G. E. Moore, *Cramming more components onto integrated circuits*, Electronics **19** (1965) 114.
- [74] M. Creutz, L. Jacobs and C. Rebbi, *Experiments with a Gauge Invariant Ising System*, Phys. Rev. Lett. **42** (1979) 1390.
- [75] J. M. Bulava et al., *Excited State Nucleon Spectrum with Two Flavors of Dynamical Fermions*, Phys. Rev. **D79** (2009) 034505 [arXiv:0901.0027].
- [76] N. Metropolis, A. W. Rosenbluth, M. N. Rosenbluth, A. H. Teller and E. Teller, *Equation of state calculations by fast computing machines*, J. Chem. Phys. **21** (1953) 1087.
- [77] S. Duane, A. D. Kennedy, B. J. Pendleton and D. Roweth, *Hybrid Monte Carlo*, Phys. Lett. **B195** (1987) 216.
- [78] U. Wolff, *Cluster simulation of relativistic fermions in two space- time dimensions*, Nucl. Phys. **B789** (2008) 258 [arXiv:0707.2872].
- [79] U. Wenger, *Efficient simulation of relativistic fermions via vertex models*, Phys. Rev. **D80** (2009) 071503 [arXiv:0812.3565].
- [80] I. P. Omelyan, I. M. Mryglod and R. Folk, *Symplectic analytically integrable decomposition algorithms: classification, derivation, and application to molecular dynamics, quantum and celestial mechanics simulations*, Computer Physics Communications **151** (2003) 272.
- [81] R. Toral and A. L. Ferreira, *Generalized hybrid Monte Carlo*, arXiv:hep-lat/9409014.
- [82] S. Catterall and S. Karamov, *Testing a Fourier accelerated hybrid monte carlo algorithm*, Phys. Lett. **B528** (2002) 301 [arXiv:hep-lat/0112025].
- [83] P. Gerhold, *Upper and lower Higgs boson mass bounds from a chirally invariant lattice Higgs-Yukawa model*, arXiv:1002.2569.
- [84] M. A. Clark and A. D. Kennedy, *The RHMC algorithm for 2 flavors of dynamical staggered fermions*, Nucl. Phys. Proc. Suppl. **129** (2004) 850 [arXiv:hep-lat/0309084].
- [85] M. A. Clark, *The Rational Hybrid Monte Carlo Algorithm*, Ph.D. thesis, University of Edinburgh (2005).

- [86] M. A. Clark and A. D. Kennedy, *Accelerating dynamical fermion computations using the rational hybrid Monte Carlo (RHMC) algorithm with multiple pseudofermion fields*, Phys. Rev. Lett. **98** (2007) 051601 [arXiv:hep-lat/0608015].
- [87] W. Fraser, *A survey of methods of computing minimax and near-minimax polynomial approximations for functions of a single independent variable*, J. ACM **12** (1965) 295.
- [88] M. A. Clark and A. D. Kennedy (2005), <http://www.ph.ed.ac.uk/~mike/remez>.
- [89] R. Frezzotti and K. Jansen, *A polynomial hybrid Monte Carlo algorithm*, Phys. Lett. **B402** (1997) 328 [arXiv:hep-lat/9702016].
- [90] R. Frezzotti and K. Jansen, *The PHMC algorithm for simulations of dynamical fermions. I: Description and properties*, Nucl. Phys. **B555** (1999) 395 [arXiv:hep-lat/9808011].
- [91] R. Frezzotti and K. Jansen, *The PHMC algorithm for simulations of dynamical fermions. II: Performance analysis*, Nucl. Phys. **B555** (1999) 432 [arXiv:hep-lat/9808038].
- [92] B. Jegerlehner, *Krylov space solvers for shifted linear systems*, arXiv:hep-lat/9612014.
- [93] R. B. Lehoucq, D. C. Sorensen and C. Yang, *ARPACK Users' Guide: Solution of Large-Scale Eigenvalue Problems with Implicitly Restarted Arnoldi Methods*, SIAM, 1998.
- [94] W. E. Arnoldi, *The principle of minimized iterations in the solution of the matrix eigenvalue problem*, Quarterly of Applied Mathematics **9** (1951) 17.
- [95] J. B. Kogut and D. K. Sinclair, *The RHMC algorithm for theories with unknown spectral bounds*, Phys. Rev. **D74** (2006) 114505 [arXiv:hep-lat/0608017].
- [96] J. Bartels and J. B. Bronzan, *Supersymmetry on a lattice*, Phys. Rev. **D28** (1983) 818.
- [97] J. Ranft and A. Schiller, *Hamiltonian monte carlo study of (1+1)-dimensional models with restricted supersymmetry on the lattice*, Phys. Lett. **B138** (1984) 166.
- [98] M. Beccaria, M. Campostrini and A. Feo, *Supersymmetry breaking in two dimensions: The lattice $n = 1$ wess-zumino model*, Phys. Rev. **D69** (2004) 095010 [arXiv:hep-lat/0402007].
- [99] M. Beccaria, G. F. De Angelis, M. Campostrini and A. Feo, *Phase diagram of the lattice Wess-Zumino model from rigorous lower bounds on the energy*, Phys. Rev. **D70** (2004) 035011 [arXiv:hep-lat/0405016].
- [100] C. Wetterich, *Exact evolution equation for the effective potential*, Phys. Lett. **B301** (1993) 90.
- [101] F. Synatschke, H. Gies and A. Wipf, *Phase Diagram and Fixed-Point Structure of two dimensional $N=1$ Wess-Zumino Models*, Phys. Rev. **D80** (2009) 085007 [arXiv:0907.4229].
- [102] N. D. Mermin and H. Wagner, *Absence of ferromagnetism or antiferromagnetism in one-dimensional or two-dimensional isotropic Heisenberg models*, Phys. Rev. Lett. **17** (1966) 1133.

- [103] S. Catterall and S. Karamov, *A lattice study of the two-dimensional Wess-Zumino model*, Phys. Rev. **D68** (2003) 014503 [arXiv:hep-lat/0305002].
- [104] S.-J. Chang, *The Existence of a Second Order Phase Transition in the Two-Dimensional ϕ^4 Field Theory*, Phys. Rev. **D13** (1976) 2778.
- [105] W. Loinaz and R. S. Willey, *Monte Carlo simulation calculation of critical coupling constant for continuum $\phi^4(2)$* , Phys. Rev. **D58** (1998) 076003 [arXiv:hep-lat/9712008].
- [106] D. Schaich and W. Loinaz, *An improved lattice measurement of the critical coupling in ϕ^4_2 theory*, Phys. Rev. **D79** (2009) 056008 [arXiv:0902.0045].
- [107] K. Binder, *Finite size scaling analysis of Ising model block distribution functions*, Z. Phys. **B43** (1981) 119.
- [108] D. Kadoh and H. Suzuki, *Supersymmetric nonperturbative formulation of the WZ model in lower dimensions*, Phys. Lett. **B684** (2010) 167 [arXiv:0909.3686].
- [109] I. Montvay, *Majorana fermions on the lattice*, arXiv:hep-lat/0108011.
- [110] X. Jia and S. Chakravarty, *Quantum dynamics of an Ising spin chain in a random transverse field*, Phys. Rev. **B74** (2006) 172414 [arXiv:cond-mat/0607703].
- [111] S. Catterall and S. Karamov, *A two-dimensional lattice model with exact supersymmetry*, Nucl. Phys. Proc. Suppl. **106** (2002) 935 [arXiv:hep-lat/0110071].
- [112] A. M. Polyakov, *Interaction of Goldstone Particles in Two-Dimensions. Applications to Ferromagnets and Massive Yang-Mills Fields*, Phys. Lett. **B59** (1975) 79.
- [113] A. M. Tsvetik, *Quantum Field Theory in Condensed Matter*, Cambridge University Press, 1995.
- [114] E. Mottola and A. Wipf, *Unsuppressed Fermion Number Violation at High Temperature: an $O(3)$ Model*, Phys. Rev. **D39** (1989) 588.
- [115] P. Di Vecchia and S. Ferrara, *Classical Solutions in Two-Dimensional Supersymmetric Field Theories*, Nucl. Phys. **B130** (1977) 93.
- [116] E. Witten, *A Supersymmetric Form of the Nonlinear Sigma Model in Two- Dimensions*, Phys. Rev. **D16** (1977) 2991.
- [117] A. D'Adda, M. Lüscher and P. Di Vecchia, *Confinement and Chiral Symmetry Breaking in CP^{n-1} Models with Quarks*, Nucl. Phys. **B152** (1979) 125.
- [118] M. Aguado, M. Asorey and A. Wipf, *Nahm transform and moduli spaces of CP^N -models on the torus*, Annals Phys. **298** (2002) 2 [arXiv:hep-th/0107258].
- [119] F. Bruckmann, *Instanton constituents in the $O(3)$ model at finite temperature*, Phys. Rev. Lett. **100** (2008) 051602 [arXiv:0707.0775].

- [120] T. C. Kraan and P. van Baal, *Periodic instantons with non-trivial holonomy*, Nucl. Phys. **B533** (1998) 627 [arXiv:hep-th/9805168].
- [121] K. Lee and C. Lu, *SU(2) calorons and magnetic monopoles*, Phys. Rev. **D58** (1998) 025011 [arXiv:hep-th/9802108].
- [122] F. Bruckmann, D. Negradi and P. van Baal, *Instantons and constituent monopoles*, Acta Phys. Polon. **B34** (2003) 5717 [arXiv:hep-th/0309008].
- [123] F. Bruckmann, *Topological objects in QCD*, Eur. Phys. J. ST **152** (2007) 61 [arXiv:0706.2269].
- [124] M. Garcia Perez, A. Gonzalez-Arroyo, C. Pena and P. van Baal, *Weyl-Dirac Zero-Mode for Calorons*, Phys. Rev. **D60** (1999) 031901 [arXiv:hep-th/9905016].
- [125] F. Bruckmann, D. Negradi and P. van Baal, *Constituent monopoles through the eyes of fermion zero-modes*, Nucl. Phys. **B666** (2003) 197 [arXiv:hep-th/0305063].
- [126] C. Ford and J. M. Pawłowski, *Doubly periodic instanton zero modes*, Phys. Lett. **B626** (2005) 139 [arXiv:hep-th/0505214].
- [127] M. Garcia Perez, A. Gonzalez-Arroyo, A. Montero and P. van Baal, *Calorons on the Lattice: A New Perspective*, JHEP **06** (1999) 001 [arXiv:hep-lat/9903022].
- [128] E.-M. Ilgenfritz, B. V. Martemyanov, M. Müller-Preussker, S. Shcheredin and A. I. Veselov, *On the topological content of SU(2) gauge fields below T_c* , Phys. Rev. **D66** (2002) 074503 [arXiv:hep-lat/0206004].
- [129] F. Bruckmann, E.-M. Ilgenfritz, B. V. Martemyanov and P. van Baal, *Probing for instanton constituents with ϵ -cooling*, Phys. Rev. **D70** (2004) 105013 [arXiv:hep-lat/0408004].
- [130] E.-M. Ilgenfritz, B. V. Martemyanov, M. Müller-Preussker and A. I. Veselov, *The monopole content of topological clusters: Have KvB calorons been found?*, Phys. Rev. **D71** (2005) 034505 [arXiv:hep-lat/0412028].
- [131] E.-M. Ilgenfritz, M. Müller-Preussker and D. Peschka, *Calorons in SU(3) lattice gauge theory*, Phys. Rev. **D71** (2005) 116003 [arXiv:hep-lat/0503020].
- [132] V. G. Bornyakov, E. M. Ilgenfritz, B. V. Martemyanov and M. Müller-Preussker, *The dyonic picture of topological objects in the deconfined phase*, Phys. Rev. **D79** (2009) 034506 [arXiv:0809.2142].
- [133] H. Eichenherr, *SU(N) Invariant Nonlinear Sigma Models*, Nucl. Phys. **B146** (1978) 215.
- [134] A. D'Adda, M. Lüscher and P. Di Vecchia, *A $1/n$ Expandable Series of Nonlinear Sigma Models with Instantons*, Nucl. Phys. **B146** (1978) 63.
- [135] P. Di Vecchia, A. Holtkamp, R. Musto, F. Nicodemi and R. Pettorino, *Lattice CP^{N-1} models and their large N behavior*, Nucl. Phys. **B190** (1981) 719.

- [136] U. Wolff, *Scaling topological charge in the CP^3 spin model*, Phys. Lett. **B284** (1992) 94 [arXiv:hep-lat/9205001].
- [137] B. Berg, *Dislocations and topological background in the lattice $O(3)$ sigma model*, Phys. Lett. **B104** (1981) 475.
- [138] B. Berg and M. Lüscher, *Definition and Statistical Distributions of a Topological Number in the Lattice $O(3)$ Sigma Model*, Nucl. Phys. **B190** (1981) 412.
- [139] M. Lüscher, *Does the Topological Susceptibility in Lattice Sigma Models Scale According to the Perturbative Renormalization Group?*, Nucl. Phys. **B200** (1982) 61.
- [140] I. Affleck, *The Role of Instantons in Scale Invariant Gauge Theories (II). The Short-Distance Limit*, Nucl. Phys. **B171** (1980) 420.
- [141] A. Actor, *Temperature Dependence of the CP^{N-1} Model and the Analogy with Quantum Chromodynamics*, Fortsch. Phys. **33** (1985) 333.
- [142] F. Bruckmann and P. van Baal, *Multi-caloron solutions*, Nucl. Phys. **B645** (2002) 105 [arXiv:hep-th/0209010].
- [143] B. J. Harrington and H. K. Shepard, *Periodic euclidean solutions and the finite temperature Yang-Mills gas*, Phys. Rev. **D17** (1978) 2122.
- [144] H. Neuberger, *More about exactly massless quarks on the lattice*, Phys. Lett. **B427** (1998) 353 [arXiv:hep-lat/9801031].
- [145] F. Niedermayer, *Exact chiral symmetry, topological charge and related topics*, Nucl. Phys. Proc. Suppl. **73** (1999) 105 [arXiv:hep-lat/9810026].
- [146] E. Witten, *Instantons, the Quark Model, and the $1/n$ Expansion*, Nucl. Phys. **B149** (1979) 285.
- [147] B. Zumino, *Supersymmetry and Kahler Manifolds*, Phys. Lett. **B87** (1979) 203.
- [148] U. Wolff, *Collective Monte Carlo Updating for Spin Systems*, Phys. Rev. Lett. **62** (1989) 361.
- [149] S. Caracciolo, R. G. Edwards, A. Pelissetto and A. D. Sokal, *Wolff type embedding algorithms for general nonlinear sigma models*, Nucl. Phys. **B403** (1993) 475 [arXiv:hep-lat/9205005].
- [150] U. Wolff, *Simulating the All-Order Strong Coupling Expansion III: $O(N)$ sigma/loop models*, Nucl. Phys. **B824** (2010) 254 [arXiv:0908.0284].
- [151] U. Wolff, *Simulating the All-Order Strong Coupling Expansion IV: $CP(N-1)$ as a loop model*, Nucl. Phys. **B832** (2010) 520 [arXiv:1001.2231].
- [152] J. Balog et al., *Comparison of the $O(3)$ bootstrap sigma-model with the lattice regularization at low energies*, Phys. Rev. **D60** (1999) 094508 [arXiv:hep-lat/9903036].

- [153] M. Lüscher, P. Weisz and U. Wolff, *A Numerical method to compute the running coupling in asymptotically free theories*, Nucl. Phys. **B359** (1991) 221.
- [154] J. Balog, F. Niedermayer and P. Weisz, *The puzzle of apparent linear lattice artifacts in the 2d non-linear sigma-model and Symanzik's solution*, Nucl. Phys. **B824** (2010) 563 [arXiv:0905.1730].
- [155] J. Balog and A. Hegedus, *TBA equations for excited states in the $O(3)$ and $O(4)$ nonlinear sigma-model*, J. Phys. **A37** (2004) 1881 [arXiv:hep-th/0309009].
- [156] M. Hasenbusch, P. Hasenfratz, F. Niedermayer, B. Seefeld and U. Wolff, *Nonstandard cutoff effects in the nonlinear sigma model*, Nucl. Phys. Proc. Suppl. **106** (2002) 911 [arXiv:hep-lat/0110202].
- [157] J. Hubbard, *Calculation of partition functions*, Phys. Rev. Lett. **3** (1959) 77.
- [158] F. Sugino, *A lattice formulation of super Yang-Mills theories with exact supersymmetry*, JHEP **01** (2004) 015 [arXiv:hep-lat/0311021].
- [159] J. M. Evans and T. J. Hollowood, *The Exact mass gap of the supersymmetric CP^{n-1} sigma model*, Phys. Lett. **B343** (1995) 198 [arXiv:hep-th/9409142].
- [160] J. M. Evans and T. J. Hollowood, *The Exact mass gap of the supersymmetric $O(N)$ sigma model*, Phys. Lett. **B343** (1995) 189 [arXiv:hep-th/9409141].
- [161] C. Chen, E. Dzienkowski and J. Giedt, *Lattice Wess-Zumino model with Ginsparg-Wilson fermions: One-loop results and GPU benchmarks*, arXiv:1005.3276.

Zusammenfassung

Symmetrien bilden die Grundfesten der modernen theoretischen Physik und führten zu der Entwicklung des Standardmodells der Teilchenphysik, welches erfolgreich die Physik auf Energieskalen unterhalb von 1 TeV beschreibt. Da jede weitere Symmetrie einer Theorie zu einer Einschränkung der möglichen Streuamplituden führt, kommt als einzige Erweiterung von Poincaré-Symmetrie und internen Symmetrien nur eine Supersymmetrie in Frage, welche Teilchen mit ganzzahligem Spin und Teilchen mit halbzahligem Spin verknüpft. Mit Hilfe von supersymmetrischen Erweiterungen des Standardmodells können dessen offene Probleme, wie z.B. das Hierarchieproblem, das Auftreten von Dunkler Materie oder das starke CP-Problem, gelöst oder zumindest abgeschwächt werden.

Supersymmetrische Modelle mit ungebrochener Supersymmetrie implizieren eine Entartung von bosonischen und fermionischen Massen. Da jedoch keine Anzeichen einer solchen Entartung in den bisherigen Experimenten sichtbar sind, kann Supersymmetrie, wenn überhaupt, nur in einer gebrochenen Form vorhanden sein. Nichtsdestotrotz ist eine Supersymmetrie-Algebra vorhanden, welche auch im gebrochenen Fall Auswirkungen auf experimentelle Resultate hat. Es sind unter anderem auch diese Effekte, welche am Large Hadron Collider in den kommenden Jahren untersucht werden sollen, so dass es nötig ist, nicht-störungstheoretische Methoden zur Verfügung zu haben, mit denen sich supersymmetrische Theorien untersuchen lassen.

Eine herausragende Stellung unter den nicht-störungstheoretischen Methoden nimmt die Gitter-Regularisierung ein, mit deren Hilfe heutzutage ab-initio-Rechnungen des Hadronen-Spektrums in der Quantenchromodynamik möglich sind. Daher wäre es wünschenswert, wenn sich dieses mächtige Werkzeug auch für supersymmetrische Theorien verwenden ließe. Jedoch spielen Symmetrien auch in gitterregularisierten Feldtheorien eine wichtige Rolle. Wenn eine Symmetrie der Kontinuumstheorie auf dem Gitter nicht vorhanden ist, dann ist es möglich, dass diese im Kontinuumslimites ebenso verletzt wird. Bestimmte Symmetrien jedoch lassen sich auf dem Gitter direkt implementieren (z.B. Eichsymmetrien) oder aber kontrolliert brechen (z.B. die chirale Symmetrie masseloser Fermionen), so dass diese Symmetrien auch im Kontinuumslimites gesichert sind.

Im Falle der Supersymmetrie, welche die Poincaré-Algebra erweitert, müssten mit vollständig implementierter Supersymmetrie auf dem Gitter auch beliebige (infinitesimale) Translationen Teil der Symmetriegruppe des Gitters sein, was im Widerspruch zum Vorhandensein eines endlichen Gitterabstandes steht, der nur endliche Translationen als Symmetrietransformation erlaubt. Somit ist eine vollständige Realisierung der Kontinuums-Supersymmetrie-Algebra auf dem Gitter unmöglich und Supersymmetrien können im Allgemeinen nur durch eine Feinjustage von Kopplungen der Gittertheorie im Kontinuumslimites wiederhergestellt werden. Da dies bereits nicht-triviale Kenntnisse über die zu untersuchende Theorie voraussetzt, wurden verschiedenen Ansätze entwickelt, um solche eine Feinjustage zu vermeiden. Einer davon basiert auf der Möglichkeit, in Theorien mit erweiterter Supersymmetrie einen (skalaren) Teil davon explizit auf dem Gitter zu realisieren, so dass man die volle Supersymmetrie im Kontinuumslimites automatisch erhält.

In der vorliegenden Arbeit werden verschiedene supersymmetrische Modelle in einer und zwei Raumzeit-Dimensionen untersucht, welche wesentliche Bestandteile von realistischeren Theorien, wie z.B. dem minimalen supersymmetrischen Standardmodell, beinhalten. Durch die separate Untersuchung der einzelnen Aspekte ist es möglich die Vor- und Nachteile der jeweils verwendeten Gittermethoden herauszuarbeiten. Zusätzlich erlaubt die niedrige Dimensionalität sehr präzise numerische Studien, welche konzeptuelle und technische Probleme bei der Behandlung von supersymmetrischen

Theorien auf dem Gitter aufdecken können.

Am Beginn der Untersuchung von supersymmetrischen Theorien auf dem Gitter steht das eher pädagogische Beispiel einer supersymmetrischen Quantenmechanik mit dynamisch gebrochener Supersymmetrie. Hieran wird die grundlegende Anwendbarkeit von Gittermethoden auf Theorien mit dynamisch gebrochener Supersymmetrie verifiziert. Dabei werden fundamentale Konzepte erläutert, die auch in den weiteren untersuchten Modellen zur Anwendung kommen. Referenzwerte für Observablen können durch Diagonalisierung der Hamilton-Operatoren gewonnen werden, so dass ein Verständnis der Supersymmetriebrechung auf einer gesicherten Basis geschieht. Die zugehörige Gitterformulierung basiert auf der nichtlokalen SLAC-Ableitung, welche sich in vorherigen Untersuchungen an einer ungebrochenen supersymmetrischen Quantenmechanik als besonders nützlich erwiesen hat. Anschließend an eine Untersuchung der Grundzustandsstruktur wird dargestellt, wie sich das tiefliegende Energiespektrum der Theorie aus Korrelatoren bestimmen lässt, wobei sich die energetische Entartung der Grundzustände im konstanten Anteil des fermionischen Korrelators widerspiegelt. Abschließend wird eine Ward-Identität untersucht, welche auf Grund der gebrochenen Supersymmetrie nicht erfüllt ist und zusätzlich noch durch endliche Temperaturen beeinflusst wird. All diese Resultate können dabei ohne Feinjustage der Kopplungen der Gittertheorie gewonnen werden, so dass die explizite Supersymmetriebrechung im Kontinuumslimes der Gittertheorie verschwindet und nur eine spontane Brechung zurückbleibt.

Das $\mathcal{N} = 2$ Wess-Zumino-Modell in $1 + 1$ Dimensionen stellt die dimensional reduzierte Version des vierdimensionalen $\mathcal{N} = 1$ Wess-Zumino-Modells dar. Es basiert auf einem holomorphen Superpotential, so dass die Supersymmetrie nicht spontan gebrochen werden kann. An diesem Modell werden fünf verschiedene Gitterformulierungen verglichen, von denen drei eine explizite Realisierung eines Teils der vollen Supersymmetrie auf dem Gitter darstellen. Dies wird durch einen Improvement-Term erreicht, welcher jedoch zu Instabilitäten in den zugehörigen Gittermodellen führen kann. Für schwache Kopplungen werden Kontinuumsextrapolationen von Massen mit störungstheoretischen Resultaten verglichen, wobei die SLAC-Ableitung die geringsten Gitterartefakte aufweist. Es können Resultate am Rande des Gültigkeitsbereiches der 1-Loop-Störungstheorie gewonnen werden, wobei sich nur dort supersymmetrisch verbesserte Formulierungen signifikant von den Standardformulierungen unterscheiden. Obwohl in den verbesserten Modellen eine Supersymmetrie explizit realisiert ist, kann bei großen Kopplungen eine Brechung von Ward-Identitäten auftreten. Dies wird durch Details des Messprozesses erklärt, im Rahmen dessen die Grundzustandsstruktur im unendlichen Volumen simuliert wird. Somit wird das Modell bis hin zu Kopplungen, an denen die 1-Loop-Störungstheorie zusammenbricht, ausführlich dargestellt, und es wird aufgezeigt, wie man Erkenntnisse darüber hinaus gewinnen kann.

Die Durchführung von hochpräzisen Messungen stellt selbst in zweidimensionalen Theorien eine große numerische Aufgabe dar. Daher werden die algorithmischen Verbesserungen, die im Verlaufe dieser Arbeit benutzt wurden, am Beispiel des $\mathcal{N} = 2$ Wess-Zumino-Modells exemplarisch dargestellt. In diesem Zusammenhang zeigt sich, dass der etablierte „Rational Hybrid Monte-Carlo“-Algorithmus nicht direkt auf die vorhandenen Modelle angewendet werden kann, sondern Modifikationen erfordert, welche eine exakte Behandlung der kleinsten Eigenwerte der Fermion-Matrix mit einschließen.

Die Minimalversion einer supersymmetrischen Feldtheorie mit supersymmetriebrechendem Phasenübergang ist durch das $\mathcal{N} = 1$ Wess-Zumino-Modell in $1 + 1$ Dimensionen gegeben. In einer

Regularisierung, welche auf der SLAC-Ableitung beruht, wird zum ersten Mal eine renormierte kritische Kopplung bestimmt, wobei deren Regulatorunabhängigkeit am bosonischen Part des Modells verifiziert wird. Am zugehörigen Phasenübergang geht eine Wiederherstellung der \mathbb{Z}_2 -Symmetrie des Modells mit der Brechung der Supersymmetrie einher. Die Wiederherstellung der Supersymmetrie in der supersymmetrischen Phase wird mit Hilfe einer Ward-Identität untersucht, wobei der Grenzfall eines unendlichen Volumens, verschwindender Temperatur und des Übergangs zum Kontinuum beachtet werden muss. Bosonische und fermionische Massen werden an einer ausgewählten Kopplung in der supersymmetrischen Phase bestimmt. Das physikalische Bild dieses Modells wird komplettiert durch die Existenz einer masselosen fermionischen Mode, des Goldstinos, in der Phase spontan gebrochener Supersymmetrie.

Die letzte Modellklasse dieser Arbeit bilden (supersymmetrische) nichtlineare Sigma-Modelle. Diese beinhalten Merkmale von nichtabelschen Eichtheorien, wie z.B. asymptotische Freiheit, dynamische Massenerzeugung und die Anwesenheit von topologischen Objekten. Im Hinblick auf die letztgenannte Eigenschaft wird die Instantonen-Struktur von bosonischen nichtlinearen $\mathbb{C}P^N$ -Sigma-Modellen mit getwisteten Randbedingungen konstruiert und die gebrochenzahligen Ladungen werden zu den Phasenparametern der Randbedingungen in Beziehung gesetzt. Die Struktur, welche beim „Kühlen“ von Gitterkonfigurationen entsteht, deckt sich mit den theoretischen Resultaten. Für minimal und supersymmetrisch gekoppelte Fermionen werden die Nullmoden des Dirac-Operators im Hintergrund der getwisteten Instantonen bestimmt. Die Untersuchung des Dirac-Operators auf dem Gitter zeigt, dass die Nullmoden auch in einer dynamischen Theorie als Indikator für Instanton-Konstituenten dienen.

Die Arbeit schließt mit einer Analyse des supersymmetrischen nichtlinearen $O(3)$ -Sigma-Modells auf dem Gitter. Die Relevanz einer intakten Targetraum-Symmetrie auf dem Gitter wird gezeigt. Jedoch bricht eine bekannte Gitterformulierung dieses Modells die $O(3)$ -Symmetrie sowohl auf dem Gitter als auch im Kontinuumsimes. Daher wird eine gitterregularisierte Version des Modells unter expliziter Beibehaltung der $O(3)$ -Symmetrie konstruiert. Mit Hilfe der SLAC-Ableitung, welche die chirale Symmetrie auch auf dem Gitter erhält, kann die analytisch vorhergesagte Grundzustandsstruktur verifiziert werden. Bosonische und fermionische Massen werden bestimmt, wobei zu deren Analyse Einflüsse des endlichen physikalischen Volumens beachtet werden müssen. Die Wiederherstellung der Supersymmetrie wird im Grenzfall kleiner Gitterkonstanten bei festgehaltenem physikalischen Volumen und im Grenzfall extrem kleinen physikalischen Volumens durch die Messung einer Ward-Identität bestätigt.

Danksagung

Ich möchte mich bei all denen bedanken, die zum Gelingen dieser Doktorarbeit beigetragen haben.

Für die gute Betreuung und Zusammenarbeit bedanke ich mich besonders bei Prof. Dr. Andreas Wipf, der mit Weitblick die nötigen Impulse zu dieser Arbeit gab und mir ein unabhängiges und freies Forschen ermöglichte.

Von ebenso großer Bedeutung war auch die Zusammenarbeit mit den weiteren Mitgliedern der Arbeitsgruppe. Besonders hervorzuheben sind dabei Dr. Tobias Kästner und Dr. Georg Bergner. Mit ihnen gemeinsam erfolgte die numerische Umsetzung der Wess-Zumino-Modelle und viele gute Ideen entwickelten wir in unseren Diskussionen. Ich bedanke mich bei Lukas Janssen. Mit ihm führte ich die Arbeiten an den $\mathbb{C}P^N$ -Modellen durch. Björn Wellegehausen danke ich für unsere Arbeiten an G_2 -Eichtheorien und Diskussionen zu Algorithmen. Bei Franziska Synatschke bedanke ich mich für die Gespräche über Wess-Zumino- und Sigma-Modelle, sowie bei Raphael Flore für die gemeinschaftliche Konstruktion einer $O(3)$ -invarianten Formulierung des supersymmetrischen Sigma-Modells.

Weiter bedanke ich mich bei Dr. Falk Bruckmann für unsere Arbeit an den $\mathbb{C}P^N$ -Modellen. Mein Dank gilt auch Dr. Philipp Gerhold und Dr. habil. Karl Jansen für Gespräche über Algorithmen für Modelle mit Yukawa-Wechselwirkung, wovon ich in der Simulation der Wess-Zumino-Modelle profitierte. Prof. Dr. Urs Wenger und Prof. Dr. Uwe-Jens Wiese danke ich für Diskussionen über grundlegende Fragen in Modellen mit spontaner Supersymmetrie-Brechung.

Der Studienstiftung des deutschen Volkes danke ich für die weitreichende finanzielle Unterstützung.

Mein größter Dank gilt Claudia und Henrike, meiner kleinen Familie. Sie mussten vor allem im letzten Jahr große Entbehrungen auf sich nehmen, um mir die Fertigstellung dieser Arbeit zu ermöglichen. Viele gemeinsame Tage sind uns dadurch unwiederbringlich verloren gegangen. Trotz alledem haben sie mich in dieser Zeit mit aller Kraft unterstützt, und sie haben mindestens den gleichen Anteil an dieser Arbeit wie ich selbst.

Ehrenwörtliche Erklärung

Ich erkläre hiermit ehrenwörtlich, dass ich die vorliegende Arbeit selbständig, ohne unzulässige Hilfe Dritter und ohne Benutzung anderer als der angegebenen Hilfsmittel und Literatur angefertigt habe. Die aus anderen Quellen direkt oder indirekt übernommenen Daten und Konzepte sind unter Angabe der Quelle gekennzeichnet. Ergebnisse, die in Zusammenarbeit mit den Mitgliedern des Lehrstuhles für Quantenfeldtheorie in Jena und anderen Kooperationen entstanden sind, sind in der Arbeit entsprechend benannt.

Weitere Personen waren an der inhaltlich-materiellen Erstellung der vorliegenden Arbeit nicht beteiligt. Insbesondere habe ich hierfür nicht die entgeltliche Hilfe von Vermittlungs- bzw. Beratungsdiensten (Promotionsberater und andere Personen) in Anspruch genommen. Niemand hat von mir unmittelbar oder mittelbar geldwerte Leistungen für Arbeiten erhalten, die im Zusammenhang mit dem Inhalt der vorgelegten Dissertation stehen.

Die Arbeit wurde bisher weder im In- noch im Ausland in gleicher oder ähnlicher Form einer anderen Prüfungsbehörde vorgelegt.

Die geltende Promotionsordnung der Physikalisch-Astronomischen Fakultät ist mir bekannt.

Ich versichere ehrenwörtlich, dass ich nach bestem Wissen die reine Wahrheit gesagt und nichts verschwiegen habe.

Jena, 30.06.2010

Christian Wozar

Lebenslauf

Name Christian Wozar
geboren am 13. September 1981 in Lauterbach (Hessen)
Familienstand verheiratet, eine Tochter

Schule

1987 – 1992 Freiherr-vom-Stein-Schule, Herbstein
1992 – 2001 Alexander-von-Humboldt-Gymnasium, Lauterbach
2001 Abitur

Studium

WS 2001/02 – SS 2002 Diplomstudium (Physik, Informatik), TU Darmstadt
WS 2002/03 – SS 2003 Diplomstudium (Physik, Informatik, Mathematik), TU Darmstadt
September 2003 Vordiplome (Physik, Informatik, Mathematik), TU Darmstadt
WS 2003/04 – SS 2004 Diplomstudium (Physik, Mathematik), FSU Jena
WS 2004/05 – WS 2006/07 Diplomstudium (Physik), FSU Jena
November 2006 Diplom (Physik), FSU Jena
seit Dezember 2006 Doktorand am Theoretisch-Physikalischen Institut, FSU Jena

Jena, 30.06.2010

Christian Wozar

Publikationen

- [CW01] C. Wozar, T. Kästner, A. Wipf, T. Heinzl und B. Pozsgay, *Phase Structure of $Z(3)$ -Polyakov-Loop Models*, Phys. Rev. D **74** (2006) 114501 [arXiv:hep-lat/0605012].
- [CW02] A. Wipf, T. Kästner, C. Wozar und T. Heinzl, *Generalized Potts-models and their relevance for gauge theories*, SIGMA **3** (2007) 006 [arXiv:hep-lat/0610043].
- [CW03] F. Synatschke, A. Wipf und C. Wozar, *Spectral sums of the Dirac-Wilson operator and their relation to the Polyakov loop*, Phys. Rev. D **75** (2007) 114003 [arXiv:hep-lat/0703018].
- [CW04] C. Wozar, T. Kästner, A. Wipf und T. Heinzl, *Inverse Monte-Carlo determination of effective lattice models for $SU(3)$ Yang-Mills theory at finite temperature*, Phys. Rev. D **76** (2007) 085004 [arXiv:0704.2570].
- [CW05] C. Wozar, T. Kästner, S. Uhlmann, A. Wipf und T. Heinzl, *$Z(3)$ Polyakov Loop Models and Inverse Monte-Carlo Methods*, PoS **LAT2007** (2007) 341 [arXiv:0708.4146].
- [CW06] T. Kästner, G. Bergner, S. Uhlmann, A. Wipf und C. Wozar, *Supersymmetric lattice models in one and two dimensions*, PoS **LAT2007** (2007) 265 [arXiv:0709.0822].
- [CW07] T. Kästner, G. Bergner, S. Uhlmann, A. Wipf und C. Wozar, *Two-Dimensional Wess-Zumino Models at Intermediate Couplings*, Phys. Rev. D **78** (2008) 095001 [arXiv:0807.1905].
- [CW08] C. Wozar, T. Kästner, B. H. Wellegehausen, A. Wipf und T. Heinzl, *Inverse Monte-Carlo and Demon Methods for Effective Polyakov Loop Models of $SU(N)$ -YM*, PoS **LATTICE2008** (2008) 257 [arXiv:0808.4046].
- [CW09] C. Wozar, G. Bergner, T. Kästner, S. Uhlmann und A. Wipf, *Numerical Investigation of the 2D $N=2$ Wess-Zumino Model*, PoS **LATTICE2008** (2008) 234 [arXiv:0809.2176].
- [CW10] W. Brendel, F. Bruckmann, L. Janssen, A. Wipf und C. Wozar, *Instanton constituents and fermionic zero modes in twisted $CP(n)$ models*, Phys. Lett. B **676** (2009) 116 [arXiv:0902.2328].
- [CW11] B. H. Wellegehausen, A. Wipf und C. Wozar, *Effective Polyakov Loop Dynamics for Finite Temperature $G(2)$ Gluodynamics*, Phys. Rev. D **80** (2009) 065028 [arXiv:0907.1450].
- [CW12] B. H. Wellegehausen, A. Wipf und C. Wozar, *Casimir Scaling and String Breaking in $G(2)$ Gluodynamics*, arXiv:1006.2305.